UNIVERSITY OF SOUTHAMPTON

FACULTY OF ENGINEERING, SCIENCE AND MATHEMATICS

School of Engineering Sciences

Numerical Studies of the Flow around an Airfoil at Low Reynolds Number

by

Lloyd Edward Jones

Thesis for the degree of Doctor of Philosophy

January 2008

ABSTRACT

UNIVERSITY OF SOUTHAMPTON
FACULTY OF ENGINEERING, SCIENCE AND MATHEMATICS
SCHOOL OF ENGINEERING SCIENCES

DOCTOR OF PHILOSOPHY

NUMERICAL STUDIES OF THE FLOW AROUND AN AIRFOIL AT LOW REYNOLDS NUMBER

by Lloyd Edward Jones

A study of the flow around airfoils at low-Reynolds numbers has been performed, by a combination of direct numerical simulation (DNS) and linear stability analysis. The behaviour of laminar separation bubbles formed on a NACA-0012 airfoil at $Re_c = 5 \times 10^4$ and incidence 5° is investigated. Initially volume forcing is introduced in order to promote transition to turbulence. After obtaining sufficient data from this forced case, the explicitly added disturbances are removed and the simulation run further. With no forcing the turbulence is observed to 'self-sustain', with increased turbulence intensity in the reattachment region. A comparison of the forced and unforced cases shows that the forcing improves the aerodynamic performance whilst requiring little energy input. Linear stability analysis of the time-averaged flowfield is performed, however no absolute instability is observed that could explain the presence of self sustaining turbulence. A series of simplified DNS are presented that illustrate a three-dimensional instability of the two-dimensional vortex shedding that occurs naturally. The instability leads to exponential growth in time at fixed streamwise locations, and a mechanism for its growth is proposed. The fact that this transition process is independent of upstream disturbances has implications for modelling separation bubbles. A further DNS, of a laminar separation bubble formed on a NACA-0012 airfoil at incidence 7° clearly exhibits sustained transition to turbulence via the proposed instability mechanism, and illustrates that the effect of a modest increase in airfoil incidence upon separation bubble behaviour appears slight in comparison to that of the addition of forcing. For all airfoil flows the transition/reattachment region of the separation bubble was observed to be a significant contributor to airfoil self-noise. Numerical simulations of the response of the time-averaged flowfield to small perturbations, intended to complement linear stability analysis, illustrate that for two dimensional cases in the range $5° \leq \alpha \leq 8.5°$ the time-averaged flowfield is unstable due to an acoustic feedback instability, whereby hydrodynamic disturbances convecting over the trailing edge generate upstream traveling acoustic waves, which ultimately generate further downstream travelling hydrodynamic disturbances. As the cycle repeats, the amplitude of both hydrodynamic instabilities and acoustic waves increases. It is suggested that an acoustic feedback loop of this type may act as a frequency selection mechanism for naturally occurring vortex shedding observed in two-dimensions.

Contents

List of Figures

List of Tables

DECLARATION OF AUTHORSHIP

I, Lloyd Edward Jones, declare that the thesis entitled Numerical Studies of the Flow around an Airfoil at Low Reynolds number and the work presented in it are my own. I confirm that:

- this work was done wholly or mainly while in candidature for a research degree at this University;
- where any part of this thesis has previously been submitted for a degree or any other qualification at this University or any other institution, this has been clearly stated;
- where I have consulted the published work of others, this is always clearly attributed;
- where I have quoted from the work of others, the source is always given. With the exception of such quotations, this thesis is entirely my own work;
- I have acknowledged all main sources of help;
- where the thesis is based on work done by myself jointly with others, I have made clear exactly what was done by others and what I have contributed myself;
- parts of this work have been published as:

Jones, L., Sandberg, R. & Sandham, N. 2006 Direct numerical simulation of an airfoil with unsteady wake. *Proceedings of ECCOMAS CFD 2006, European Conference on Computational Fluid Dynamics.*

Jones, L., Sandberg, R. & Sandham, N. 2007 Direct numerical simulation of the Flow around a NACA-0012 airfoil. *5th International Symposium on Turbulence and Shear Flow Phenomena.*

Jones, L., Sandberg, R. & Sandham, N. 2007 Direct numerical simulations of forced and unforced separation bubbles on an airfoil at incidence. *J Fluid Mech.* (in submission)

Signed: ....

Date: ....

Acknowledgements

I would like to thank Professor Neil Sandham for the excellent supervision and guidance provided throughout the course of this study. I would also like to thank Dr Richard Sandberg who was a valuable source of inspiration throughout.

Symbols and abbreviations

Roman symbols

a, b	Carpenter boundary scheme coefficients
a_1,b_1,c_1,c_2	entropy splitting variables
c	speed of sound
C_i	temporal derivatives of characteristic waves
C_{Df}	skin-friction drag coefficient
C_{DP}	pressure drag coefficient
C_D	total drag coefficient, i.e. C_{DP}+C_{Df}
c_f	skin-friction coefficient
c_g	group-velocity
C_L	lift-coefficient
C_P	pressure-coefficient
c_{ph}	phase-speed
D	dispersion relation operator
D_i	characteristic boundary treatment variables
$\mathbf{D}$	Carpenter boundary scheme derivative operator
$\mathbf{D^2}$	Carpenter boundary scheme second derivative operator
e	internal energy, $e = T/\gamma(\gamma - 1)M^2$
E_t	total energy, $E_t = \rho(e + \frac{1}{2}u_iu_i)$
$\mathbf{E}, \mathbf{F}, \mathbf{G}$	inviscid flux vector terms
F_i	forcing amplitude function
f	frequency
f_1, f_2	entropy splitting variables
$\mathbf{F_n}$	normal Euler fluxes
J	Jacobian
$\mathbf{J}, \mathbf{K}, \mathbf{L}$	split Euler flux matrices
$k_1 - k_4$	Runge-Kutta sub-step variables
i	the square root of -1
L_z	computational domain width
N	disturbance N-factor

N_x,N_y,N_z	number of grid-points in x, y and z-directions respectively
p	pressure
Pr	Prandtl number
$\mathbf{P}, \mathbf{Q}$	Carpenter boundary scheme matrix terms
Q	Second invariant of the velocity gradient tensor
$\mathbf{Q}$	Vector of conservative variables
q_i	conduction term of the energy equation
Q_i	the conduction and work terms of the energy equation
R	computational domain radius
R	gas constant, $p/\rho T$
Re_c	Reynolds number based on airfoil chord
$\mathbf{R}, \mathbf{S}, \mathbf{T}$	viscous vector terms
s	airfoil surface coordinate
s	entropy
St	Strouhal number
S_f	Direct Fourier transform of f
t	time
T	temperature
u,v,w	cartesian velocities
u',v',w'	fluctuating components of cartesian velocities
u_τ	friction velocity, $u_\tau = \sqrt{\frac{\nu}{Re}\frac{du}{dy}_w}$
W	computational domain wake length
$\mathbf{W}$	entropy transformation vector
x, y, z	cartesian coordinates

Greek symbols

α	angle of airfoil incidence to the free-stream flow
α	complex wavenumber, $\alpha = \frac{2\pi}{\lambda}$
β	entropy splitting constant
β	spanwise wavenumber, $\beta = 2\pi/\lambda_z$
γ	ratio of specific heats, c_p/c_v
δ^*	boundary layer displacement thickness
δ_{ij}	Kronecker delta, equal to 1 when $i = j$ and equal to zero when $i \neq j$
Δt	time-step
ϵ	convergence criteria variable for spatial stability algorithm
η	wall-normal curvilinear coordinate
θ	boundary layer momentum thickness

λ	wavelength
λ_i	velocity of characteristic waves
μ	dynamic viscosity
ν	kinematic viscosity
ξ	streamwise curvilinear coordinate
ρ	fluid density
σ	exponential growth rate
τ_{ij}	shear-stress tensor
ϕ	phase angle
ψ	entropy function
ω	complex frequency, $\omega = 2\pi f$

Other symbols

∇	divergence operator
$\overline{f}$	mean of f
$\widetilde{f}$	Favre average of f
f'	fluctuating part of f $(f - \overline{f})$

Subscripts

i,j,k	tensor indices
D	drag
e	value at edge of the boundary layer
f	skin-friction
i	imaginary part
P	pressure
r	real part
r	reference (free-stream) value
w	value at wall
∞	free-stream value

Abbreviations

3DF	the three-dimensional airfoil simulation at $\alpha = 5°$, with explicitly added forcing
3DU	the unforced the three-dimensional airfoil simulation at $\alpha = 5°$

3D7	the unforced three-dimensional airfoil simulation at $\alpha = 7^\circ$
CFD	computational fluid dynamics
DNS	direct numerical simulation
LCBC	local characteristic boundary condition
LES	large eddy simulation
LST	linear stability theory
PDF	probability density function
RANS	Reynolds-averaged Navier–Stokes
RMS	root-mean-square
TS	Tollmien–Schlicting
ZCBC	zonal characteristic boundary condition

Chapter 1

Introduction

1.1 Low Reynolds number aerodynamics

Interest in low Reynolds number aerodynamics has increased in recent years, primarily due to the development of small autonomous aircraft commonly referred to as unmanned or micro air vehicles (UAV's or MAV's). Current goals for the development of MAV's are a maximum dimension of 15cm and an expected cruise velocity of 15-80km/h, yielding an operational Reynolds number range of $Re = 42,000 - 225,000$ (Torres & Mueller, 2001). Larger UAV's at very high altitude will also tend to operate in a low Reynolds number regime due to the increase in kinematic viscosity. For example, at an altitude of 24km the kinematic viscosity of air will have reduced by a factor of 22 compared to that at sea level, and the Reynolds number will have decreased by the same factor. Wind turbines and turbine cascades also operate in the low Reynolds number regime, since the velocity at the root of the blade will be substantially lower than that at the tip, and represent another focus of low Reynolds number research.

Historically, low Reynolds number aerodynamics has not received as much interest as aerodynamics at higher Reynolds number, thus experimental and numerical data are commonly only available for high to moderate Reynolds number flow. For example, generating airfoil lift and drag data requires more sensitive instrumentation at lower Reynolds number, and so the large amount of experimental airfoil data publicly available does not typically extend to low Reynolds number (Mueller, 1999). This problem is compounded by the fact that low Reynolds number aerodynamics is dominated by different physical behaviour compared to aerodynamics at high Reynolds number, and hence knowledge of the performance of an airfoil geometry at low Reynolds numbers does not necessarily extrapolate well to high Reynolds number, and vice versa.

At low Reynolds numbers transitional behaviour and the effect of boundary layer separation can be critical to airfoil performance. Airfoil boundary layers will typically remain laminar for a large percentage of the airfoil chord, whereas at high Reynolds numbers the boundary layer will undergo transition to turbulence near the airfoil leading edge and the boundary layer will be mostly turbulent. The transition process, and hence location, is more sensitive at low Reynolds numbers and must be predicted accurately in order to determine aerodynamic performance. This contrasts with high Reynolds number flows where transition is often not modelled at all, for example in traditional computational fluid dynamics (CFD) based on the Reynolds-averaged Navier–Stokes (RANS) equations. Since boundary layers remain laminar for a greater streamwise extent, laminar separation is more common at low Reynolds numbers, and the resultant separated shear-layer may also remain laminar for a significant extent before transition to turbulence occurs. Upon transition the increased wall-normal momentum transfer typically means that the boundary layer reattaches, followed by a developing turbulent boundary layer. The resultant structure formed by laminar separation, transition to turbulence and reattachment is termed a laminar separation bubble (LSB) and is a classic hallmark of low Reynolds number flows.

Differences in behaviour between high Reynolds number and low Reynolds number fluid flow are often significant. Critically, this means that the industry standard tool for predicting fluid flows at high Reynolds numbers, RANS based CFD, does not perform well in the low Reynolds number regime, since large regions of laminar flow are often present. Additionally, the reattachment process is highly dependent on transition and the subsequent turbulent behaviour, and has been found to be difficult to model accurately with RANS based CFD (Yuan, Xu & Khalid, 2004). Methods such as direct numerical simulation (DNS) and large eddy simulation (LES), whilst accurately capturing the physics present, are not suitable for use as design tools due to the high computational cost. Effectively, the state of the art for low Reynolds number airfoil design currently consists of viscous-inviscid interaction (VII) solvers (Selig, Gopalarathnam, Giguere & Lyon, 2001), in particular the Profoil/Eppler code, and XFoil. Both programs solve using a panel method for the potential flow, however they differ in their approach when solving for the boundary layer. The Eppler code (Eppler & Somers, 1980) uses a non-coupled integral boundary layer method, with empirically derived transition criterion dependent on momentum thickness, shape factor and local flow conditions. On the other hand, XFoil's integral boundary layer method is coupled to the potential flow solution and uses an empirically derived e^n transition criterion (Drela & Giles, 1987), hence XFoil represents a more advanced approach. The Eppler code cannot predict separation at all, whereas the XFoil code does attempt to predict limited separated regions but cannot predict stall with any accuracy. Both codes essentially provide a steady-state two-dimensional solution, thus unsteady effects will be ignored. More recently efforts have also been made to integrate the e^n transition prediction method into RANS based simulations (Yuan *et al.*, 2007; Windte *et al.*, 2006) with some success, and the technique appears promising. Potential problems with this method are that the reattachment behaviour, and the developing turbulent boundary layer are difficult to model accurately, and will be sensitive to the turbulence model used. Also, the ability of the technique to model the experimentally observed sudden bubble 'bursting' is not yet proven.

It appears therefore, that current design tools for low Reynolds number aerodynamics are not entirely satisfactory, and that there is a lack of publicly available experimental data at low Reynolds number. This means that experimental studies are still critically important for MAV development. Perhaps the biggest challenge for low Reynolds number airfoil design is the accurate prediction of laminar separation bubble behaviour. Whilst VII solvers may predict the presence of separation bubbles, the 'bursting' of bubbles into extended separated regions, or the onset of sudden stall, is not predicted. Furthermore, separation bubble models employed by VII solvers assume that the bubble is a fundamentally steady structure, whereas studies have shown that separation bubbles are far from steady. If advances can be made in understanding the physics of laminar separation bubbles, they may potentially lead to improvements in low Reynolds number design tools.

1.2 Separation bubbles

As outlined in section 1.1, the accurate modelling of their behaviour represents a considerable challenge in predicting airfoil performance at low Reynolds numbers. The first recorded observation of a laminar separation bubble was by Jones (1938), in a study of the stalling process of airfoils. The initial observation was followed by a series of experimental studies of the fundamental structure of separation bubbles, as reviewed by Young & Horton (1966). Bubble behaviour at near-stall conditions was subsequently investigated by Gault (1957), who defined three types of stall depending upon the separation behaviour of the boundary layer near stall; leading edge, trailing edge and thin airfoil stall. Gault observed that the presence and behaviour of a separation bubble can potentially have a strong influence on airfoil stalling characteristics. Horton (1968) was the first to describe the time-averaged structure of a laminar separation bubble, resulting in the classical model of a separation bubble illustrated in figure 1.1.

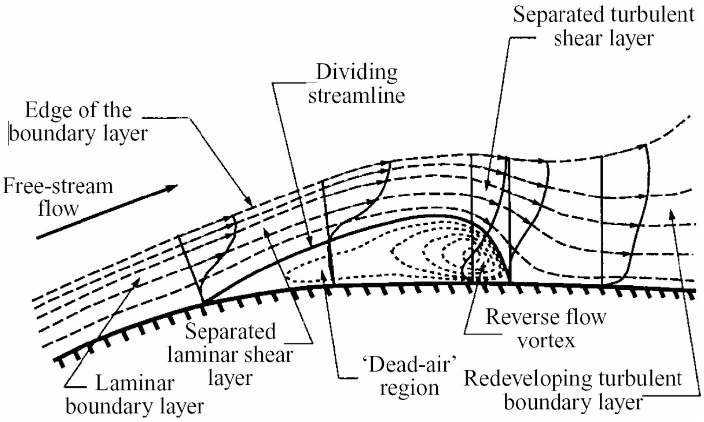

Figure 1.1: The structure of a laminar separation bubble, as described by Horton (1968).

In the classical model a laminar separation bubble forms when, under the influence of an adverse pressure gradient, the boundary layer separates, forming a free shear layer which is highly unstable. The separated shear layer undergoes rapid transition to turbulence, and subsequent reattachment. Just downstream of the separation point, within the bubble, the fluid velocity is close to zero and thus this region is denoted the 'dead air' region. Just upstream of the reattachment point a vortical structure is present, associated with the circulation of air within the bubble, called the 'reverse-flow vortex'. This steady model of a separation bubble, where the only time dependent behaviour is the transition to turbulence and subsequent turbulent behaviour downstream, became the widely accepted model.

Owen & Klanfer (1953) classified bubbles of this type as either 'short' bubbles or 'long' bubbles. Short bubbles were defined as possessing bubble length approximately 10^2 times the displacement thickness at the separation point, whereas long separation bubbles were defined as being of order 10^4 times the displacement thickness at the separation point. Perhaps more importantly, short separation bubbles are defined as having little effect on the external potential flow, whereas long bubbles have a marked impact, e.g completely altering the circulation around an airfoil. Where a short separation bubble suddenly changes state to that of a long separation bubble, or indeed to a fully separated state with no reattachment, the process is termed bubble 'bursting' and is the mechanism behind thin airfoil stall as defined by Gault (1957). Gaster (1966) investigated a large number of bubbles on a flat surface, produced by placing an inverted airfoil above the plate. This experimental configuration allowed the investigation of separation bubbles formed under a variety of conditions, by varying the location and incidence of the airfoil. From these experiments a two parameter bursting criterion was produced. Gaster observed that bubble bursting can occur either as a steady increase in bubble length with some change in free-stream conditions or as a sudden near-discontinuous event, but the parameters governing this behaviour were not determined. Gaster's experimental results were subsequently used by Horton (1969), to produce a semi empirical model for bubble growth and bursting, based upon the concept of a steady separation bubble. Horton's model gave predictions for the transition location and momentum thickness distribution, as well as overall bubble length, and provided a benchmark for the development of subsequent models. However, despite refinements such as modelling the dependency on background turbulence levels (Roberts, 1980), the use of the e^n transition prediction method (Ingen, 1985) and the modelling of low Reynolds number effects (Shum & Marsdent, 1994), present day models do not adequately predict bubble bursting or unsteady behaviour. More recently, advances in understanding the physics of separation bubbles have been made by numerical studies.

1.2.1 Numerical separation bubble studies

Subsequent to Gaster's experiments and Horton's models, some of the most important advances in the understanding of separation bubbles, particularly with regard to unsteady behaviour, have been made via numerical methods, primarily by directly solving the Navier–Stokes equations, with no modelling.

The first numerical simulations of separation bubbles were limited either to two-dimensional analysis, or else only studied primary/linear instability and did not resolve transition. Pauley, Moin & Reynolds (1990) conducted one of the earliest attempts, and considered only the two-dimensional incompressible Navier–Stokes equations. A separation bubble was induced on a flat plate via the application of transpiration to an upper boundary, and at low adverse pressure gradient the bubble produced was observed to be thin and steady. With increasing adverse pressure gradient, oscillations were observed within the bubble, and above a critical adverse pressure gradient periodic vortex shedding was observed to occur from the separated shear layer. Despite the strong unsteadiness, time-averaged velocity contours looked qualitatively similar to those of Gaster and Horton. The length of the separated region was found to increase with increasing adverse pressure gradient until the onset of vortex shedding, after which the length of the separated region was found to decrease with further increase in adverse pressure gradient. Pauley *et al.* therefore suggested that the short and long separation bubbles observed by Gaster may in fact be steady and unsteady separation bubbles respectively. A study by Pauley (1994) investigated the development of three-dimensionality due to the introduction of 3D velocity perturbations to the earlier case studied by Pauley *et al.* (1990). Only the initial response to these disturbances was studied however, and the simulations did not resolve transition to turbulence. Similarly, Rist (1994) performed direct numerical simulations of a laminar separation bubble subject to combinations of both two-dimensional and three-dimensional disturbances. The study focused on instability behaviour, and it was found that oblique disturbances yielded the most realistic flow parameters and transition behaviour. Again, full transition to turbulence was not resolved. It was not until the studies of Alam & Sandham (2000) and Spalart & Strelets (2000) that transition to turbulence in a separation bubble was fully resolved.

Alam & Sandham (2000) investigated a short separation bubble on a flat surface. The bubble was induced via suction on the upper boundary, and unsteadiness was introduced by the addition of a disturbance strip upstream of the separation point. The study found that, unlike three-dimensional simulations, two-dimensional simulations could not adequately capture the characteristics of the separation bubble. The three-dimensional simulations exhibited transition to turbulence, and thus the transition process could be investigated in detail. Transition was found to occur within the shear layer, via amplification of oblique modes followed by a Λ-vortex induced breakdown. The boundary layer reattached as turbulent flow, with the turbulent behaviour being most energetic away from the wall, and relaxation to log-law boundary layer profiles taking several bubble lengths downstream. For the case in question, it was determined that reverse flow greater than 15% would be required in order to sustain an absolute instability, whereas reverse flow was actually only 4-8%. As a result, it was stated that the transition process was entirely due to the presence of convective instability.

In the same year Spalart & Strelets (2000) conducted DNS of a laminar separation bubble, formed by the same method as Alam & Sandham, for the purpose of assessing turbulence models. No unsteadiness was introduced and inflow disturbances were less than 0.1%, however transition to turbulence was still observed. As a result the study stated that entry-region disturbances (TS-waves) could be discarded as the mechanism behind transition, however the study also stated that magnitude of reverse flow present was unlikely to be sufficient to sustain absolute instability. Transition was observed by ‘wavering of the separated shear layer, followed by the formation of Kelvin-Helmholtz vortices, instantly becoming three-dimensional with no clear regions of primary, secondary or tertiary instability'. No Λ-vortices were observed, and thus the transition process was markedly different to that of Alam & Sandham. Spalart & Strelets suggested that the flow is independent of upstream disturbances.

Subsequent to the first fully resolved studies in 2000 several further numerical simulations of separation bubbles have been conducted. Yang & Voke (2001) conducted LES of a separation bubble induced by a surface curvature change. In contrast to previous three-dimensional studies, the bubble exhibited shedding of spanwise-coherent vortices, appearing nominally similar to that observed by Pauley *et al.* (1990) in two-dimensions. Two-dimensional unsteadiness was found to originate in the free shear layer, and three-dimensional motions were found to develop as a result of small spanwise disturbances. The instantaneous reattachment position was observed to move over a distance of 50% of the mean bubble length and thus, in contrast to classical models, the bubble was highly unsteady. Wissink & Rodi (2002) also observed quasi-periodic vortex shedding, in a DNS study of a separation bubble induced on a flat plate. As the vortices travelled downstream they were observed to break down into smaller structures and ultimately turbulence.

An alternative approach was carried out by Marxen, Lang, Rist & Wagner (2003), who performed a combined DNS and experimental study (including particle image velocimetry and laser doppler anemometry), with flow parameters chosen to enable comparison. Periodic two-dimensional disturbances were introduced upstream of separation, and three-dimensionality was introduced via a spanwise array of spacers. The separated shear layer was observed to roll up to form vortices, appearing similar to the study of Wissink & Rodi (2002), which subsequently broke down to turbulence. The same configuration was studied further by Lang, Rist & Wagner (2004) and again by Marxen, Rist & Wagner (2004) in order to quantify the respective roles of two-dimensional and three-dimensional disturbances. Marxen *et al.* concluded that transition was driven by convective amplification of a two-dimensional TS wave, which also determined the length of the bubble, and that the dominant mechanism behind transition is an absolute secondary instability in a manner first proposed by Maucher, Rist & Wagner (1997).

Baragona (2004) also performed a combined numerical and experimental study of separation bubbles including DNS, although the DNS did not resolve the transition process and subsequent turbulence. Experimental results again revealed laminar vortex shedding from a separated shear layer, undergoing transition to turbulence downstream of the shedding location. The vortex shedding was found to strongly influence both the transition process and subsequent turbulent boundary layer, however the study concluded that for the cases under consideration the addition of TS-like disturbances was necessary in order to reproduce experimental results.

More recently Marxen & Henninsdon (2007) attempted to investigate bubble bursting behaviour via DNS. A separation bubble was induced on a flat plate by means of an imposed pressure distribution and periodic disturbances were introduced via a disturbance strip, resulting in transition to turbulence. The bubble was observed to shorten significantly. Having formed a short bubble the disturbance input was then removed, at which point the bubble grew in length, achieving a 'long' bubble state. Transition was still observed however, and the transition location did not change significantly upon removal of disturbances; the bubble length increased because the location of turbulent reattachment moved downstream. The physical mechanism behind different forms of separation bubble bursting as observed by Gaster (1966) was not investigated in great detail, however the study implicitly illustrates that background turbulence levels may play some role. Further studies by Wissink & Rodi (2003) and Wissink, Michelassi & Rodi (2004) have investigated separation bubbles formed under the influence of oscillating external flow, and in the case of Wissink *et al.* with the addition of heat transfer. These studies are more relevant to turbomachinery, and will not be discussed in detail.

To summarise, it appears that separation bubble behaviour is complex and far from universal in nature. Depending on the flow parameters separation bubbles may or may not exhibit vortex shedding or coherent structures, and studies alternately attribute transition to convective instability, absolute instability or to some form of secondary absolute instability. Furthermore, it has been suggested both that the addition of TS-type disturbances is necessary to accurately reproduce experimental data (Baragona, 2004), and alternately that bubble behaviour is independent of upstream disturbances (Spalart & Strelets, 2000). It is apparent that stability characteristics of separation bubbles are not well defined in all cases, and hence better understanding of instability mechanisms present may potentially help to explain the differences in behaviour observed in numerical studies.

1.2.2 Hydrodynamic instability and separation bubbles

From the discussion of numerical separation bubble studies in section 1.2.1 it is apparent that if the stability characteristics of separation bubbles were better understood, it is likely that their physical behaviour could be better predicted. A discussion of the role of instability mechanisms in separation bubbles follows.

The concepts of absolute and convective instability were first identified in the context of fluid dynamics by Gaster (1963, 1968), and are fundamental to much of the discussion regarding stability characteristics of separation bubbles (for a review of absolute instability, including earlier studies see Huerre & Monkewitz, 1990). The difference between convective and absolute instability may be explained by considering a one-dimensional system, perturbed at location $x = 0$. The perturbation may either grow or decay in time, and will convect as it does so. The resultant behaviour is defined in three ways. If the perturbation decays with time the system is stable. If the perturbation grows in time, but the convection of the perturbation is such that the perturbation amplitude at $x = 0$ decays in time, the system is said to be convectively unstable (figure 1.2, left). As time increases the system will return to its initial condition in the vicinity of $x = 0$. Convective instability is the mechanism by which Tollmien-Schlicting (TS) waves are amplified. If the perturbation grows in time, and both the temporal growth rate and perturbation velocity are such that the perturbation amplitude grows temporally at $x = 0$, the system is said to be absolutely unstable (figure 1.2, right). The perturbation will grow in amplitude and ultimately contaminate the entire system. The presence of absolute instability has been confirmed both for shear-layers (Huerre & Monkewitz, 1985) and bluff body wakes (Hannemann & Oertel, 1989), and in the latter case has been found to trigger the onset of bluff body vortex shedding.

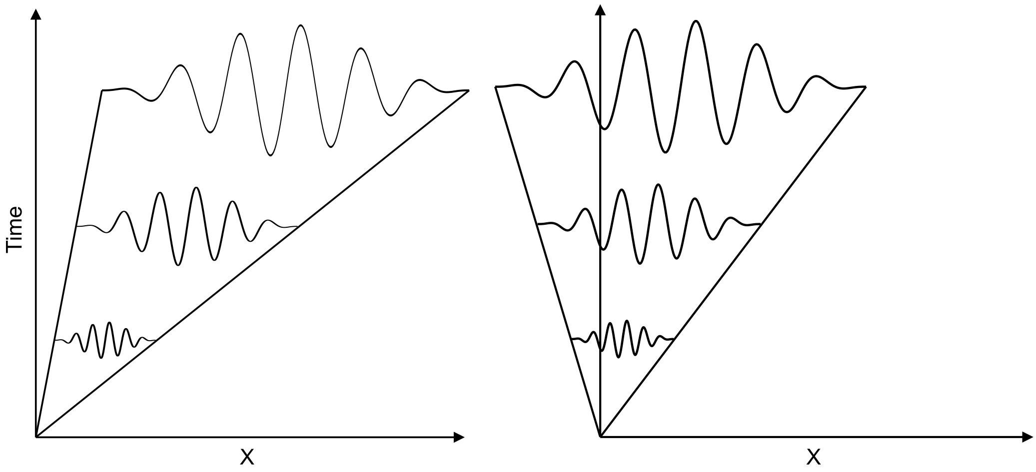

Figure 1.2: X/T plot illustrating convective instability (left) and absolute instability (right).

It is well known that perturbations will be rapidly amplified by convective instability in separated shear layers; convective growth rates for separation bubbles have been accurately reproduced via both linear stability analysis (Bestek, Gruber & Fasel, 1989) and parabolic stability equation (PSE) analysis (Theofilis, 2000). The role of absolute instability in separation bubble flow is less well defined however. Several studies have attempted to answer the question as to whether absolute instability will occur in separation bubbles, and if so what criteria govern its onset. One method of determining the stability characteristics of separation bubbles is via linear stability analysis of time-averaged velocity profiles, either constructed analytically or extracted from numerical simulations. Hammond & Redekopp (1998) and Rist & Maucher (2002) both performed stability analysis of analytic profiles, and both studies found absolute instability to occur, dependent on certain parameters. Hammond & Redekopp (1998) found the onset of local absolute instability to be dependent on both the maximum reverse flow and the height of the reverse flow region, and found that for profiles at $Re_{\delta^*} = 10^3$, a minimum reverse flow velocity of 20% was required to observe local absolute instability. Hammond & Redekopp further suggested that although local absolute instability may be observed for reverse flow of 20%, a global response would only be expected if reverse flow approaching 30% was present. Rist & Maucher (2002) observed similar behaviour regarding the onset of local absolute instability, and highlighted that both the height and intensity of the shear layer are also important onset parameters. There is no guarantee however, that analytic profiles sustaining absolute instability will occur in real situations. The simulations of Alam & Sandham (2000) and Spalart & Strelets (2000) are a case in point. Alam & Sandham performed linear stability velocity profiles fitted to data extracted from DNS of a laminar separation bubble formed on a flat plate. Alam & Sandham found that reverse flow greater than 15% would be required in order to sustain absolute instability, compared to an observed reverse flow of only 4-8%. As a result, it was concluded that the transition process was driven by convective instability. Spalart & Strelets (2000) conducted DNS of a laminar separation bubble induced on a flat plate, however again the authors suggested that magnitude of reverse flow present was unlikely to be sufficient to sustain absolute instability. Hence neither study observed reverse flow large enough to sustain absolute instability as determined by analysis of analytic profiles. Similarly, an earlier study by Allen & Riley (1995), performing stability analysis on velocity profiles extracted from a RANS simulation, observed only convective instability for all cases under investigation. A global self-sustained response was observed by Marquillie & Ehrenstein (2003), from a separation bubble formed behind a bump on a flat plate, although only when 'geometrically stabilised' by adding a second bump at the rear of the bubble. Although such behaviour is of interest, the resultant bubble cannot be said to resemble that formed on, for example, an airfoil however. In this configuration reverse flow approaching 30% of the freestream velocity was observed, and the global response took the form of periodic oscillation, originating at the rear of the bubble.

As well as classical linear stability analysis, recently advances have been made with 'global' (also termed 'BiGlobal') stability analysis (Theofilis, 2003). As explained in section 2.4, classical linear stability analysis considers the growth of normal-mode perturbations on one-dimensional velocity profiles. For the spatial problem, a perturbation frequency is specified, and a corresponding wavelength and one-dimensional eigenvector, describing the disturbance structure, is returned. When performing 'BiGlobal' analysis a spanwise wavenumber is specified, and a temporal growth-rate and two-dimensional eigenvector describing the disturbance structure is returned. When applied to the case of a laminar separation bubble (Theofilis, 2000) temporally unstable global modes have been observed that are not predictable by classical linear stability analysis. However the growth rates are small compared to that of convective instabilities present, hence it is likely that transition will occur before such a global mode may amplify significantly. It is suggested however that the presence of global modes may be relevant to the phenomenon of vortex shedding observed in many simulations.

To summarise, it appears that unlike bluff body wakes the presence of local absolute instability has not been rigorously proven for either a numerically or experimentally produced separation bubble. Despite the lack of evidence for the presence of absolute instability in experimentally or numerically produced separation bubbles, self-sustained transition to turbulence has been observed in the absence of explicitly added disturbances (e.g., Spalart & Strelets, 2000). It is perhaps possible that the presence of absolutely unstable regions of flow leads to some form of secondary behaviour, e.g. vortex shedding or transition to turbulence, that prevents detection of the original absolute instability from time-averaged data, however the question remains as to whether absolute instability will occur in 'real' laminar separation bubbles, and if so what form the resultant global behaviour will take.

1.3 Airfoil studies

A discussion of laminar separation bubbles, and the role of instability mechanisms in separation bubble behaviour has illustrated that separation bubble behaviour appears to differ significantly from case to case, and that instability mechanisms present in separation bubbles are not well understood in all cases.

Continued advances in computing power mean that direct numerical simulations of airfoil configurations are now possible. The advantage of studying full airfoil configurations is that the bubble can interact strongly with the potential flow (in particular via the Kutta condition at the trailing edge), as opposed to subjecting the bubble to pre-determined flow conditions. The bubble will be closer in nature to those observed under flight conditions, and the influence of the bubble behaviour on the aerodynamic performance of the airfoil can be observed directly. To date, direct numerical simulations of airfoil flow have typically been limited either to two-dimensions, or else to very low Reynolds numbers. The use of modelling, such as in LES or DES, has however enabled studies of three-dimensional airfoil flow at moderate Reynolds numbers, with mixed success. In the following paragraph a discussion of airfoil DNS studies to date is presented, followed by a discussion of numerical studies of airfoil flow utilizing other numerical methods, that are relevant to the current study.

Several DNS studies of airfoil flow exist, primarily investigating the fundamental fluid behaviour present. Bouhadji & Braza (2003) performed a two-part DNS study of the two-dimensional flow around a NACA-0012 airfoil at zero degrees. In the first part of the study simulations were performed at a Reynolds number of $Re = 10^4$ based on airfoil chord whilst varying the Mach number from $M = 0.2$ to $M = 0.98$. The study found steady, symmetric flow around the airfoil in the range $M = 0.2 - 0.35$. Above $M = 0.35$ the wake was found to become unstable, and vortex shedding was observed downstream of the airfoil. Additionally, in the Mach number range $0.75 - 0.8$ a second lower frequency oscillation was observed in the lift coefficient, described as a transonic buffet effect. Above a critical Mach number in the range $0.9 - 0.95$ vortex shedding ceased, and the flow returned to a steady state. In the second part of the study simulations were run at $M = 0.85$ for a variety of Reynolds numbers in the range 500-10000, and the onset of wake vortex shedding was determined to be at $\mathrm{Re_c} = 2070$. A further paper by Bourdet, Bouhadji, Braza & Thiele (2003) presents two-dimensional results drawn from the previous studies and also extends the study to three dimensions. A spanwise perturbation of magnitude 1×10^{-4} was introduced, and three-dimensional instability was observed by the appearance and growth of w-velocity oscillations. Full transition to turbulence was not observed however, and only secondary instability was investigated. Hoarau, Braza, Ventikos, Faghani & Tzabiras (2003*a*) and Hoarau, Faghani, Braza, Perrin, Anne-Archard & Ruiz (2003*b*) both performed DNS of a NACA-0012 airfoil at 20° incidence. The study of Hoarau *et al.* (2003*a*) first documents the behaviour of the flow over the airfoil in two-dimensions as the Reynolds number is increased. In the first regime, $\mathrm{Re_c} = 800 - 2000$, a von-Kârman type instability was observed, with periodic vortex shedding. In the second regime, $\mathrm{Re_c} = 2000 - 10000$, a Kelvin-Helmholtz instability was observed in the separated shear layer, upstream of the von-Karman vortex shedding. The frequency of the Kelvin-Helmholtz instability was much higher than that associated with the von-Karman instability, and non-linear interaction between the two modes resulted in a more complex frequency spectrum. The simulation was extended to three-dimensions at $Re_c = 800$, with the addition of random perturbations in order to introduce three-dimensionality. A spanwise-periodic disturbance structure was observed to develop, appearing qualitatively similar to behaviour observed in bluff-body wakes, however full transition to turbulence was not studied. The study of Hoarau *et al.* (2003*b*) appears to draw from the same data and reaches primarily similar conclusions.

More recently DNS has been used as a tool to study the acoustic response of the flow around airfoils. Hatakeyama & Inoue (2006) and Tam & Ju (2006) performed two-dimensional DNS of airfoils at $\mathrm{Re_c} = 5000$ and $Re_c = 200000$ respectively, and since a compressible formulation was employed acoustic behaviour could be observed directly. In both cases the fluid flow was characterized by roll-up of the upper surface boundary layer into vortices, and sound waves were generated by acoustic scattering (Ffowcs Williams & Hall, 1970), as the vortices convected over the airfoil trailing edge. Tam & Ju however also observed the vortices themselves to act as sources of acoustic radiation. Kim, Lee & Fujisawa (2005) performed an incompressible LES of the three-dimensional flow around a NACA-0018 airfoil at $Re_c = 1 \times 10^9$ in order to investigate sources of tonal noise. The upper airfoil surface exhibited separation and transition, but the fluid dynamics were not extensively investigated beyond the context of explaining self-noise mechanisms. The results of the LES were used to predict the farfield sound spectrum via an acoustic analogy, and the study concluded that the primary source of tonal noise is expected to be interaction of periodic vortex shedding on the pressure side of the airfoil with the turbulent flow on the suction side.

The only three-dimensional DNS study of an airfoil at MAV flight conditions to date was carried out by Shan, Jiang & Liu (2005), who simulated the flow over a NACA-0012 airfoil at $\mathrm{Re_c} = 10^5$, $M = 0.2$ and 4° incidence. A precursory two-dimensional simulation exhibited boundary layer separation near the airfoil leading edge, and vortex shedding from the separated shear layer. The two-dimensional simulation was extended into three dimensions and progressed, with no artificial noise or perturbations being added, and transition to turbulence was observed to subsequently take place. The primary purpose of the study was to assess the use of pulsed jets as a separation control measure and, where unsteady blowing was applied, bypass transition was observed to take place and the bubble length reduced accordingly. The study did not study the fluid dynamics of the separation bubble extensively however, and uses only eight times more grid-points than Hoarau *et al.* (2003*a*) (6.9×10^6 *c.f* 8.7×10^5), despite an increase of a factor of 125 in Reynolds number. Other three-dimensional studies have been performed at MAV-type Reynolds numbers and above, however they have all employed some form of modelling in order to reduce the computational cost.

Mary & Sagaut (2002) performed LES of an ONERA 'A-airfoil' geometry with a separation bubble at Reynolds number $Re_c = 2.1 \times 10^6$, at $M = 0.15$ and incidence $\alpha = 13.3°$. The purpose was to demonstrate the ability of LES to successfully replicate the flow in question. Results were found to be strongly dependent on both the grid resolution and sub-grid scale (SGS) model used, and although the results compared moderately well with experimental data, significant differences were observed, particularly in root-mean-square (RMS) boundary layer quantities. By the airfoil trailing edge the boundary layer thickness was of similar size to the computational domain width however, which is likely to have constrained the behaviour. Schmidt & Thiele (2003) performed a detached-eddy simulation of the same case, alongside RANS based CFD studies. Perhaps surprisingly the DES simulations did not perform significantly better than the RANS simulations, and could not replicate unsteady behaviour, such as the Reynolds stress profiles, observed in experimental studies. Yuan, Xu, Khalid & Radespiel (2006) performed a parametric incompressible LES study of the flow over an SD7003 airfoil at $Re_c = 6 \times 10^4$, investigating the influence of both grid resolution and SGS model on results. The spanwise domain width was only 1.2% of the airfoil chord however, and used only four grid-points. Since the spanwise domain width was small in comparison to the separated boundary layer thickness it is unsurprising that the study observed markedly different behaviour when compared to experimental results, including a separation bubble that was 50% larger.

Kitsios, Kotapati, Mittal, Ooi, Soria & You (2006) performed a study of a NACA-0015 airfoil at $Re_c = 3 \times 10^5$ with the addition of a wall-normal zero-net-mass-flux jet at the leading edge. Both incompressible DNS and LES were performed, and the results compared to experimental data. The majority of discussion focuses on the two-dimensional case however, and certain differences to experimental results were observed. A similar study that is perhaps of more interest is that of You & Moin (2006). You & Moin performed LES of the flow around a NACA-0015 airfoil at the comparatively high Reynolds number of $Re_c \approx 9 \times 10^6$, both with and without the addition of synthetic jet control. Performing a numerical simulation at this Reynolds number appears to have been possible due to a combination of factors. Unstructured grids were employed, allowing strong grid-stretching, in combination with a modest computational domain size ($6c \times 2.5c \times 0.2c$) chosen to match an experimental configuration. In conjunction with LES this presumably led to the feasibility of using a comparatively low number of grid-points ($\sim 8 \times 10^6$). Additionally, the use of an incompressible code allowed an implicit time-marching scheme, and hence large time-steps. The time-averaged pressure coefficient and wake-profiles appear to compare well with experimental data, however unsteady behaviour and turbulent statistics were not presented. The addition of periodic blowing and suction was found to delay the onset of, presumably turbulent, separation due to increased wall-normal momentum transfer, and to increase airfoil performance significantly.

An alternative approach to modelling low Reynolds number airfoil flow was employed by Windte, Scholz & Radespiel (2006). Windte *et al.* attempted to predict transitional airfoil flow by coupling a RANS based solver to a transition prediction model. Two transition prediction methods were employed. For the first, boundary layer velocity profiles are analysed by a linear stability solver and the corresponding disturbance growth-rates are used to construct a spatial disturbance growth 'N-factor'. When the N-factor reaches some empirically defined threshold, transition is deemed to occur and the production terms of the active turbulence model are activated. The second case differs in that instead of performing linear stability analysis, the e^N method is used to determine the transition location. The test-case for the numerical method was an SD7003 airfoil geometry at $Re_c = 6 \times 10^4$, and numerical predictions were compared to experimental data for various angles of attack. Both methods proved to agree well with experimental data, with respect to both the time-averaged flowfield and force coefficients. A further study by Radespiel & Scholz (2007) used the same coupled RANS-LST method to investigate flapping airfoil flow. In order to account for changes in boundary layer stability characteristics due to unsteady flow, frequency dependent N-factors were computed accounting for disturbance history. Again, an SD7003 airfoil geometry was studied at $Re_c = 6 \times 10^4$, however this time the airfoil was subject to a sinusoidal plunge motion, and the numerical results were compared to phase-locked experimental data. Discrepancies could be observed in comparison to experimental results, particularly in the streamwise transition location, and force-coefficients were predicted less accurately than for steady cases. Overall however, the results were far more accurate than could be expected of traditional RANS based CFD and would not be able to be reproduced by panel methods or VII solvers based on steady flow.

A similar numerical method was employed by Lian & Shyy (2006), who apparently deemed the transition length, i.e. the distance between onset of secondary instability and breakdown to turbulence, of greater importance than Windte *et al.* (2006), since an empirical intermittency function was employed to model this behaviour. In contrast, Windte *et al.* argue that appropriate selection of the empirically determined transition N-factor makes such modelling unnecessary. The method was applied to the case of an airfoil in steady flow, and an airfoil in an unsteady flow, however unlike Radespiel & Scholz, the temporal history of disturbance growth was not considered for unsteady cases. Lian & Shyy instead argue that if the time taken for instability waves to be convectively amplified from the point of receptivity to transition is significantly smaller than the time-scale of changes to the global flow, an instantaneous application of the e^N method is valid. For the case of a rigid wing in gust flow, the method predicted hysteresis in the time-dependent force coefficients, and in the separation and periodic streamwise oscillation of the separation and transition points. Unfortunately the unsteady airfoil flow was not compared to experimental data, and hence the accuracy of unsteady measurements is not quantified. The method was also applied to the case of an airfoil where part of the surface was a flexible membrane, which was observed to undergo self-sustained oscillations.

Given the range of numerical airfoil studies discussed here it is apparent then that the application of DNS to airfoil flow is now feasible for two-dimensional flow, and allows accurate representation of both hydrodynamic and acoustic behaviour. Although LES has been performed of airfoils at Reynolds numbers greatly exceeding MAV flight conditions, the accuracy of such studies varies. Taking this into consideration, in conjunction with the dependency of the resultant flow on the SGS model used, LES does not appear a suitable tool for studying the fundamental fluid dynamics of separation bubbles. Coupled RANS-LST approaches appear quite promising, and have been proven to model both steady and unsteady transition with some success. It would be interesting to see to what extent such an approach is able to predict bubble bursting. Studies to date do not appear to have investigated the fundamental fluid dynamics of low Reynolds number airfoil flows with transition to turbulence, and no study of laminar separation bubbles on airfoils has yet been performed.

1.4 The current study

At present the physics of laminar separation bubbles are not fully understood and hence any improvement in understanding may potentially lead to improvements in prediction tools. Advances in computing power mean that it is now possible to perform direct numerical simulations of airfoil configurations, and hence it is now possible to perform direct numerical simulations of separation bubbles on airfoils. The focus of this study is therefore to investigate numerically the behavior of laminar separation bubbles formed on airfoils at incidence, at MAV-type flight conditions, with a view to improved understanding of the physics present. Particular aims of the study have been identified, as follows:

- To quantify the grid and domain requirements for DNS of airfoil geometries, and provide a reference for further airfoil simulations

- To capture numerically a laminar separation bubble on an airfoil at MAV-type flight conditions

- To investigate fully the physics of laminar separation bubbles formed on airfoils at incidence, including the transition process and subsequent turbulent behaviour, and the unsteady characteristics of the resultant flow.

- To investigate the effect of boundary layer disturbances on the transition process and resultant flow.

- To investigate fully the absolute/convective stability characteristics of laminar separation bubbles on airfoils at incidence, with a view to clarifying the stability mechanisms present.

- To investigate the acoustic response of the flow over airfoils with laminar separation bubbles.

1.5 Thesis structure

Chapter 2 details the governing equations and numerical implementation of the direct numerical simulations and stability solver used for the majority of results in this study. Chapters 3 and 4 present the results of preliminary two-dimensional simulations at $Re_c = 10^4$ and $Re_c = 5 \times 10^4$ respectively. Additionally, in chapter 3 stability analysis of a time averaged flow-field is performed which demonstrates the ability of the numerical methods to detect absolute instability. Three dimensional separation bubbles formed on airfoils at incidence are investigated in chapters 5 and 6. In chapter 5 the effect of explicitly adding boundary layer disturbances is investigated, whereas in chapter 6 the effect of a modest incidence change on separation bubble behaviour is investigated. In chapter 7 stability analysis is performed on the time-averaged flowfields of all three-dimensional simulations, and in chapter 8 a mechanism behind secondary absolute instability of vortex shedding, observed in three-dimensional simulations, is described. In chapter 9 the acoustic characteristics of all three-dimensional airfoil flows are discussed and, finally, conclusions and recommendations for further study are presented in chapter 10.

Chapter 2

Governing equations and numerical method

2.1 Introduction

This chapter details the equations that govern the fluid flows of interest, and the numerical methods employed to solve them. The numerical techniques employed may be broadly split into direct numerical simulations, and linear stability analysis.

Direct numerical simulations are performed using a method fundamentally similar to that employed by Lawal (2002), Morin (2002) and Krishnan (2005). The primary difference between the current investigation and these earlier studies is the modification of the computational code to allow the use of complex geometries; a C-type grid with data transfer across the wake cut is now used instead of a rectangular computational domain. This means that the airfoil trailing edge represents a singularity which must be treated in the appropriate numerical fashion. Although MAV's operate in the low Reynolds number low Mach number regime, a compressible code is used in order to compute the acoustic response of the flow. For the sake of completeness the numerical method is described fully here, including airfoil-specific post-processing. Linear stability analysis is performed using an incompressible Orr-Sommerfeld solver in conjunction with the cusp-map technique to determine the presence of absolute stability. An iterative method is employed to perform spatial stability analysis where required.

2.2 Direct numerical simulations

2.2.1 Governing equations

The compressible Navier–Stokes equations are written in curvilinear form as

$$\frac{\partial \mathbf{Q}}{\partial t}+\frac{\partial \mathbf{E}}{\partial \xi}+\frac{\partial \mathbf{F}}{\partial \eta}+\frac{\partial \mathbf{G}}{\partial z}=\frac{\partial \mathbf{R}}{\partial \xi}+\frac{\partial \mathbf{S}}{\partial \eta}+\frac{\partial \mathbf{T}}{\partial z}. \tag{2.1}$$

The conservative vector $\mathbf{Q}$, inviscid flux vectors $\mathbf{E}$, $\mathbf{F}$ and $\mathbf{G}$, and the viscous vector terms $\mathbf{R}$, $\mathbf{S}$ and $\mathbf{T}$ are defined as

$$\mathbf{Q}=\begin{pmatrix}\rho\\ \rho u\\ \rho v\\ \rho w\\ E_t\end{pmatrix},\quad \mathbf{E}=\begin{pmatrix}\rho U\\ \rho uU+p\xi_x\\ \rho vU+p\xi_y\\ \rho wU\\ (E_t+p)U\end{pmatrix} \tag{2.2}$$

$$\mathbf{F}=\begin{pmatrix}\rho V\\ \rho uV+p\eta_x\\ \rho vV+p\eta_y\\ \rho wV\\ (E_t+p)V\end{pmatrix},\quad \mathbf{G}=\begin{pmatrix}\rho w\\ \rho uw\\ \rho vw\\ \rho ww+p\\ (E_t+p)w\end{pmatrix} \tag{2.3}$$

$$\mathbf{R}=\begin{pmatrix}0\\ \tau_{xx}\xi_x+\tau_{xy}\xi_y\\ \tau_{yx}\xi_x+\tau_{yy}\xi_y\\ \tau_{zx}\xi_x+\tau_{zy}\xi_y\\ Q_x\xi_x+Q_y\xi_y\end{pmatrix},\quad \mathbf{S}=\begin{pmatrix}0\\ \tau_{xx}\eta_x+\tau_{xy}\eta_y\\ \tau_{yx}\eta_x+\tau_{yy}\eta_y\\ \tau_{zx}\eta_x+\tau_{zy}\eta_y\\ Q_x\eta_x+Q_y\eta_y\end{pmatrix},\quad \mathbf{T}=\begin{pmatrix}0\\ \tau_{xz}\\ \tau_{yz}\\ \tau_{zz}\\ Q_z\end{pmatrix}, \tag{2.4}$$

where ρ is the fluid density, u, v and w are velocity components in the Cartesian x, y and z directions, p is the pressure, and E_t is the total energy per unit volume, defined as

$$E_t=\rho e+\frac{1}{2}\rho(uu+vv+ww), \tag{2.5}$$

where

$$e=\frac{T}{\gamma(\gamma-1)M^2}. \tag{2.6}$$

Primitive variables are non-dimensionalised as follows

$$u_i=\frac{u_i^*}{u_r^*},\quad \rho=\frac{\rho^*}{\rho_r^*},\quad T=\frac{T^*}{T_r^*},\quad x_i=\frac{x_i^*}{c^*}, \tag{2.7}$$

and

$$\mu = \frac{\mu^*}{\mu_r^*}, \quad p = \frac{p^*}{\rho_r^* u_r^{*2}}, \quad e = \frac{e^*}{u_r^{*2}}, \quad t = \frac{t^* u_r^*}{c^*}, \tag{2.8}$$

where the superscript $*$ denotes dimensional variables, the subscript r denotes reference (free-stream) values and c^* is the airfoil chord.
Metric terms are defined as

$$\xi_x = \frac{y_\eta}{J}, \quad \xi_y = -\frac{x_\eta}{J}, \quad \eta_x = -\frac{y_\xi}{J}, \quad \eta_y = \frac{x_\xi}{J}, \tag{2.9}$$

noting that terms ξ_z and η_z are both equal to zero for computational grids with no spanwise variation, as used in the current study, and the Jacobian J is defined as

$$J = x_\xi y_\eta - x_\eta y_\xi. \tag{2.10}$$

The contravariant velocities U and V are defined as

$$U = \xi_x u + \xi_y v, \quad V = \eta_x u + \eta_y v, \tag{2.11}$$

and, assuming a Newtonian fluid, the stress terms τ_{ij} are defined as

$$\tau_{ij} = \frac{\mu}{Re}\left(\frac{\partial u_i}{\partial x_j} + \frac{\partial u_j}{\partial x_i}\right) - \frac{2}{3}\frac{\mu}{Re}\frac{\partial u_k}{\partial x_k}\delta_{ij}. \tag{2.12}$$

The terms Q_i comprise the conduction and work terms of the energy equation,

$$Q_i = -q_i + u_j \tau_{ij}, \tag{2.13}$$

where

$$q_i = \frac{-\mu}{(\gamma - 1)M^2 Re Pr}\frac{\partial T}{\partial x_i}. \tag{2.14}$$

Viscosity is calculated using Sutherland's law (White, 1991),

$$\mu = T^{3/2}\frac{1 + C}{T + C}, \; C = 0.368\dot{6}, \tag{2.15}$$

and finally, the perfect gas law relates p, ρ and T

$$p = \frac{\rho T}{\gamma M^2}. \tag{2.16}$$

2.2.2 Discretisation

Spatial scheme

fourth-order accurate central differences utilising a five-point stencil are used for spatial discretisation when evaluating interior derivatives, i.e. not at computational domain boundaries. First and second derivatives are given by

$$f' = \frac{f_{i-2} - 8f_{i-1} + 8f_{i+1} - f_{i+2}}{12\Delta s} \tag{2.17}$$

and

$$f'' = \frac{-f_{i-2} + 16f_{i-1} - 30f_i + 16f_{i+1} - f_{i+2}}{12\Delta s^2} \tag{2.18}$$

respectively, where Δs is a length scale defined as

$$\Delta s = (\frac{l}{n-1}), \tag{2.19}$$

where n is the number of points in the curvilinear direction of interest, and l is the domain length in the case of ξ derivatives and the domain half-height in the case of η derivatives. Fourth-order accuracy is extended to the domain boundaries by use of a Carpenter boundary scheme (Carpenter, Nordström & Gottlieb, 1999). The first derivative operator is $\mathbf{D}$, written as

$$\mathbf{D}\overline{u} = \frac{1}{\Delta s}\mathbf{P}^{-1}\mathbf{Q}\overline{u} \tag{2.20}$$

where Δs is defined in equation 2.19. For the fourth-order central difference scheme used in this study, the matrices $\mathbf{P}$ and $\mathbf{Q}$ are

$$\mathbf{P} = \begin{pmatrix} \frac{-(216b+2160a-2125)}{12960} & \frac{81b+675a+415}{540} & \frac{-(72b+720a+445)}{1440} & \frac{-(108b+756a+421)}{1296} \\ \frac{(81b+675a+415)}{540} & \frac{-(4104b+32400a+11225)}{4320} & \frac{(1836b+14580a+7295)}{2160} & \frac{-(216b+2160a+655)}{4320} \\ \frac{-(72b+720a+445)}{1440} & \frac{(1836b+14580a+7295)}{2160} & \frac{-(4104b+32400a+12785)}{4320} & \frac{(81b+675a+335)}{540} \\ -\frac{(108b+756a+421)}{1296} & \frac{-(216b+2160a+655)}{4320} & \frac{(81b+675a+335)}{540} & \frac{-(216b+2160a-12085)}{12960} \end{pmatrix} \tag{2.21}$$

and

$$\mathbf{Q} = \begin{pmatrix} -\frac{1}{2} & \frac{-(864b+6480a+305)}{4320} & \frac{(216b+1620a+725)}{540} & \frac{-(864b+6480a+3335)}{4320} & 0 & 0 \\ \frac{(864b+6480a+305)}{4320} & 0 & \frac{-(864b+6480a+2315)}{1440} & \frac{(108b+810a+415)}{270} & 0 & 0 \\ \frac{-(216b+1620a+725)}{540} & \frac{(864b+6480a+2315)}{1440} & 0 & \frac{-(864b+6480a+785)}{4320} & \frac{-1}{12} & 0 \\ \frac{(864b+6480a+3335)}{4320} & \frac{-(108b+810a+415)}{270} & \frac{(864b+6480a+785)}{4320} & 0 & \frac{2}{3} & \frac{-1}{12} \end{pmatrix}, \tag{2.22}$$

where

$$a = \frac{-(2177\sqrt{295369} - 1166427)}{25488} \tag{2.23}$$

and

$$b = \frac{(66195\sqrt{53}\sqrt{5573} - 35909375)}{101952}. \tag{2.24}$$

The derivative operator $\mathbf{D}$ is evaluated to machine accuracy at the start of each calculation, by multiplying $\mathbf{Q}$ by the inverse of $\mathbf{P}$. An analogous criterion proposed by Carpenter *et al.* (1999) is used for the second derivative. For the fourth-order central difference scheme used the second derivative operator may be written explicitly as

$$\mathbf{D^2} = \frac{1}{\Delta s^2} \begin{pmatrix} \frac{35}{12} & -\frac{26}{3} & \frac{19}{2} & -\frac{14}{3} & \frac{11}{12} \\ & & & & \\ \frac{11}{12} & -\frac{5}{3} & \frac{1}{2} & \frac{1}{3} & -\frac{1}{12} \\ & & & & \end{pmatrix}, \tag{2.25}$$

for the first two grid-points, noting that $\mathbf{D}^2 \neq \mathbf{D}.\mathbf{D}$.

Temporal scheme

The explicit fourth-order accurate Runge-Kutta scheme is used for time stepping, typically written as

$$\mathbf{Q}_{n+1} = \mathbf{Q}_n + \frac{1}{6}\Delta t\left(k_1 + 2k_2 + 2k_3 + k_4\right), \tag{2.26}$$

$$k_1 = \left(\frac{d(\mathbf{Q}_n)}{dt}\right)_{t=t_n}, \quad k_2 = \left(\frac{d(\mathbf{Q}_n + \frac{k_1}{2})}{dt}\right)_{t=t_n+\frac{\Delta t}{2}}, \tag{2.27}$$

$$k_3 = \left(\frac{d(\mathbf{Q}_n + \frac{k_2}{2})}{dt}\right)_{t=t_n+\frac{\Delta t}{2}}, \quad k_4 = \left(\frac{d(\mathbf{Q}_n + k_3)}{dt}\right)_{t=t_n+\Delta t}. \tag{2.28}$$

The code uses a low storage implementation, requiring only three data arrays. The array $\mathbf{Q}_{\text{old}}$ stores data from the previous time-step, and does not change throughout the time-stepping procedure. The array $\mathbf{Q}_{\text{store}}$ is used to effectively sum the variables k_1-k_4. The array $\mathbf{Q}_{\text{new}}$ is used to store the data needed to calculate variables k_1-k_4. Starting from the condition $\mathbf{Q}_{\text{store}} = 0$, the following four steps comprise the time stepping procedure:

$$1.\quad \mathbf{Q}_{\text{store}} = \mathbf{Q}_{\text{store}} + \frac{d\mathbf{Q}_{\text{old}}}{dt}, \qquad \mathbf{Q}_{\text{new}} = \mathbf{Q}_{\text{old}} + \frac{1}{2}\Delta t\frac{d\mathbf{Q}_{\text{old}}}{dt} \tag{2.29}$$

$$2.\quad \mathbf{Q}_{\text{store}} = \mathbf{Q}_{\text{store}} + 2\frac{d\mathbf{Q}_{\text{new}}}{dt}, \qquad \mathbf{Q}_{\text{new}} = \mathbf{Q}_{\text{old}} + \frac{1}{2}\Delta t\frac{d\mathbf{Q}_{\text{new}}}{dt} \tag{2.30}$$

$$3.\quad \mathbf{Q}_{\text{store}} = \mathbf{Q}_{\text{store}} + 2\frac{d\mathbf{Q}_{\text{new}}}{dt}, \qquad \mathbf{Q}_{\text{new}} = \mathbf{Q}_{\text{old}} + \Delta t\frac{d\mathbf{Q}_{\text{new}}}{dt} \tag{2.31}$$

$$4.\quad \mathbf{Q}_{\text{store}} = \mathbf{Q}_{\text{store}} + \frac{d\mathbf{Q}_{\text{new}}}{dt}, \qquad \mathbf{Q}_{\text{new}} = \mathbf{Q}_{\text{old}} + \frac{1}{6}\Delta t\frac{d\mathbf{Q}_{\text{store}}}{dt}, \tag{2.32}$$

where $\frac{d\mathbf{Q}}{dt}$ refers to the derivative of $\mathbf{Q}$ with respect to time, as evaluated by the DNS code. At the last step, $\mathbf{Q}_{\text{store}}$ is equal to $\frac{1}{\Delta t}(k_1 + 2k_2 + 2k_3 + k_4)$ and thus the expression for $\mathbf{Q}_{\text{new}}$ is equivalent to equation 2.26.

2.2.3 Entropy splitting

The split high-order-entropy-conserving-scheme (SHOEC) of Gerritsen & Olsson (1996, 1998) is applied to the Euler fluxes, in order to improve stability. The Euler fluxes in a curvilinear coordinate system are written as

$$\frac{d\mathbf{Q}}{dt} + \frac{d\mathbf{E}}{d\xi} + \frac{d\mathbf{F}}{d\eta} + \frac{d\mathbf{G}}{dz}, \tag{2.33}$$

with vector variables defined as in equations (2.2) and (2.3). The entropy variable transformation

$$\mathbf{W} = \mathbf{W}(\mathbf{Q}) \tag{2.34}$$

is introduced, where

$$\mathbf{W} = \frac{d\psi}{d\mathbf{Q}}. \tag{2.35}$$

The entropy function ψ is defined as

$$\psi = \rho h(s), \tag{2.36}$$

where

$$s = p\rho^{-\gamma} \tag{2.37}$$

is the entropy. The choice of $h(s)$ is restricted by a homogeneity requirement and a positive definite condition on the matrix $d\mathbf{Q}/d\mathbf{W}$, which can be satisfied by letting $h(s) = Ke^{\left(\frac{s}{\alpha+\gamma}\right)}$, where K and α are constants. With the homogeneity condition satisfied, the vector W can be written as

$$\mathbf{W} = \frac{p^*}{p}\left[E + \frac{\alpha-1}{\gamma-1},\ -\rho u,\ -\rho v,\ -\rho w,\ \rho\right]^T, \tag{2.38}$$

where p and p^* are related by

$$p^* = \frac{-K}{\beta}e^{\frac{s}{\alpha+\gamma}} = \frac{-K}{\beta}(p\rho^{-\gamma})^{1/(\alpha+\gamma)}. \tag{2.39}$$

The split form of the Euler fluxes is then written as

$$\frac{d\mathbf{Q}}{dt} + f_1\left(\frac{d\mathbf{E}}{d\xi} + \frac{d\mathbf{F}}{d\eta} + \frac{d\mathbf{G}}{dz}\right) + f_2\left(\frac{d\mathbf{E}}{d\mathbf{W}}\frac{d\mathbf{W}}{d\xi} + \frac{d\mathbf{F}}{d\mathbf{W}}\frac{d\mathbf{W}}{d\eta} + \frac{d\mathbf{G}}{d\mathbf{W}}\frac{d\mathbf{W}}{dz}\right) = 0, \tag{2.40}$$

where

$$f_1 = \frac{\beta}{\beta+1},\ \ f_2 = \frac{1}{\beta+1},\ \ \beta = \frac{\alpha+\gamma}{1-\gamma}. \tag{2.41}$$

Upper triangular parts of the matrices $\mathbf{E}$, $\mathbf{F}$ and $\mathbf{G}$ are defined as

$$\frac{d\mathbf{E}}{d\mathbf{W}} = \frac{1}{p^*}\mathbf{J},\ \ \frac{d\mathbf{F}}{d\mathbf{W}} = \frac{1}{p^*}\mathbf{K},\ \ \frac{d\mathbf{G}}{d\mathbf{W}} = \frac{1}{p^*}\mathbf{L}, \tag{2.42}$$

with matrix **J** written as

$$\begin{pmatrix} \alpha_1\rho U & \alpha_1\rho Uu-p\xi_x & \alpha_1\rho Uv+p\xi_y & \alpha_1\rho Uw & [\alpha_1 E_t+(b_1-1)p]U \\ & \alpha_1\rho Uu^2+p(-3u\xi_x+v\xi_y) & \alpha_1\rho Uuv+p(-v\xi_x+u\xi_y) & \alpha_1\rho Uuw-pw\xi_x & c_1Uu-\frac{p}{\rho}[E_t+p]\xi_x \\ & & \alpha_1\rho Uv^2+p(-u\xi_x+3v\xi_y) & \alpha_1\rho Uvw+pw\eta_y & c_1Uv-\frac{p}{\rho}[E_t+p]\xi_y \\ & & & (\alpha_1\rho w^2-p)U & [\alpha_1 E_t+(b-2)p]Uw \\ & & & & c_2U \end{pmatrix}, \tag{2.43}$$

matrix **K** written as

$$\begin{pmatrix} \alpha_1\rho V & \alpha_1\rho Vu-p\eta_x & \alpha_1\rho Vv+p\eta_y & \alpha_1\rho Vw & [\alpha_1 E_t+(b_1-1)p]V \\ & \alpha_1\rho Vu^2+p(-3u\eta_x+v\eta_y) & \alpha_1\rho Vuv+p(-v\eta_x+u\eta_y) & \alpha_1\rho Vuw+pw\eta_x & c_1Vu-\frac{p}{\rho}[E_t+p]\eta_x \\ & & \alpha_1\rho Vv^2+p(-u\eta_x+3v\eta_y) & \alpha_1\rho Vvw-pw\eta_y & c_1Vv-\frac{p}{\rho}[E_t+p]\eta_y \\ & & & (\alpha_1\rho w^2-p)V & [\alpha_1 E_t+(b-2)p]Vw \\ & & & & c_2V \end{pmatrix}, \tag{2.44}$$

and matrix **L** written as

$$\begin{pmatrix} \alpha_1\rho w & \alpha_1\rho uw & \alpha_1\rho vw & \alpha_1\rho w^2-p & [\alpha_1 E_t+(b_1-1)p]w \\ & w(\alpha_1\rho u^2-p) & \alpha_1\rho uvw & u(\alpha_1\rho w^2-p) & [\alpha_1 E_t+(b_1-2)p]uw \\ & & w(\alpha_1\rho v^2-p) & v(\alpha_1\rho w^2-p) & [\alpha_1 E_t+(b_1-2)p]vw \\ & & & w(\alpha_1 w^2-3p) & c_1w^2-(E_t+p)p/\rho \\ & & & & c_2w \end{pmatrix}, \tag{2.45}$$

with coefficients

$$a_1 = \frac{1-\alpha-\gamma}{\alpha},\ b_1 = \frac{1}{\alpha},\ c_1 = a_1E_t + (b_1-2)p, \tag{2.46}$$

$$c_2 = \frac{a_1{E_t}^2}{\rho} + p\left[2(b_1-1)\frac{E_t}{\rho} - \frac{1}{2}(u^2+v^2+w^2)\right] + \frac{p^2}{\rho}[b_1(1+\beta)-2] \tag{2.47}$$

The parameter β adjusts the weighting of the Euler fluxes between the original and split formulations. As $\beta \to \infty$ the original formulation of the Euler fluxes

Boundary	Physical description	Applied boundary condition
ξ^+	Outflow boundary	Zonal-characteristic
ξ^-	Outflow boundary	Zonal-characteristic
η^+	Freestream boundary	Integral-characteristic
η^-	Mixed: airfoil surface and wake connection	Adiabatic, no slip (airfoil)

Table 2.1: Description of domain boundaries, and details of applied boundary conditions.

is recovered. Preliminary airfoil simulations suggested a value of $\beta = 2$ provides adequate stability, hence this value was used throughout the current study.

2.2.4 Simulation geometry

Topology of the curvilinear C-type grids used is given in Figure 2.1. The wake length is denoted W and the domain radius is denoted R. The coordinate system is defined such that the airfoil trailing edge is located at $(x, y) = (1, 0)$. A NACA airfoil geometry is specified for two reasons. Firstly, the NACA-0012 airfoil geometry is commonly studied in the research community, and hence the current study may be more readily compared to existing work. Use of a 'standard' geometry also means that the current study may provide a reference point for future investigations of airfoil flow. Secondly, experiments investigating the acoustic response of the flow around a NACA-0012 airfoil are planned at the Institute of Sound and Vibration research (ISVR) at the University of Southampton, which will complement acoustic analysis of the simulations presented here.

2.2.5 Boundary conditions

Unphysical reflections from the domain boundaries can be reduced by the use of appropriate boundary conditions. Definitions of the domain boundaries and associated boundary conditions are given in table 2.1. At the freestream (η^+) boundary, where the only disturbances likely to reach the boundary will be in the form of linear waves, an integral characteristic boundary condition is applied. At the downstream exit boundary ($\xi^\pm$), which will be subject to the passage of coherent fluid structures generated by instability in the wake, a zonal characteristic boundary condition (ZCBC) is applied for increased effectiveness. Additionally, in certain simulations a simple buffer was applied at the free-stream boundary to further reduce reflections from linear (acoustic) waves.

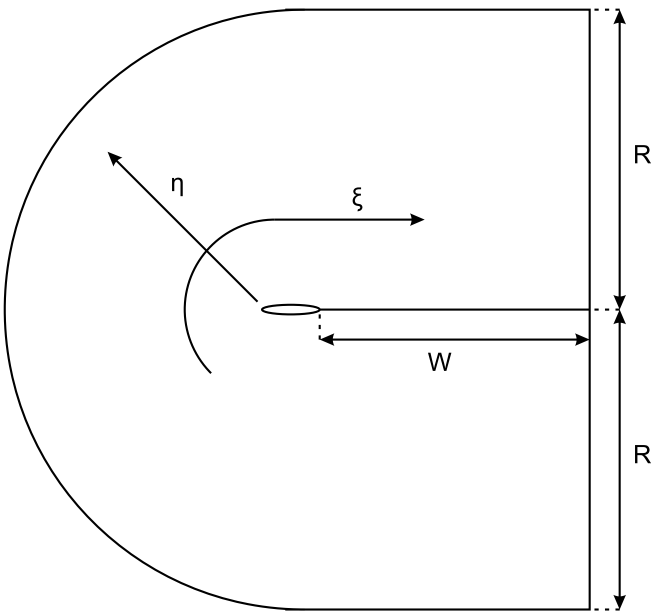

Figure 2.1: Domain topology for airfoil simulations.

Zonal characteristic boundary condition

The zonal characteristic boundary condition (Sandberg & Sandham, 2006) is based on similar principles to the local characteristic boundary condition (or LCBC, Thompson, 1987). The compressible Navier-Stokes equations are linearised, neglecting viscous terms. Using the method of characteristics, eigenvalues with associated eigenvectors can be determined. The resultant eigenvalues λ_i correspond to the characteristic velocities of pressure, vorticity or entropy waves. The sign of λ_i determines the direction of the associated wave, whether it is incoming or outgoing with respect to the boundary in question. The left-side eigenvectors L_i correspond to the rate of change of the wave amplitude. At the outflow boundary all incoming characteristic waves, those where $\lambda_i < 0$, are effectively removed by setting L_i to zero. All outgoing characteristic waves, where $\lambda_i > 0$, are left unchanged. The primary difference between the ZCBC and the LCBC is that for the local condition the treatment is applied only at domain boundaries. For the zonal condition the treatment is applied for a finite distance before the boundary, and is introduced with a smooth ramping function. The characteristic method is implemented as follows for the current code. For an arbitrary normal direction, normal derivatives of the normal Euler fluxes are defined as

$$\frac{d\mathbf{F_n}}{dn} = \frac{d\mathbf{F_n}}{d\xi}\frac{d\xi}{dn} + \frac{d\mathbf{F_n}}{d\eta}\frac{d\eta}{dn}, \tag{2.48}$$

where

$$\mathbf{F_n} = \begin{pmatrix} \rho u_n \\ \rho u u_n + p n_x \\ \rho v u_n + p n_y \\ \rho w u_n \\ (E_t + p) u_n \end{pmatrix}. \tag{2.49}$$

The normal derivatives are then subtracted from the previously computed right hand side of the Navier-Stokes equations,

$$\mathbf{RHS}' = \mathbf{RHS} - \frac{d\mathbf{F}_n}{dn} \tag{2.50}$$

and the temporal derivatives of the characteristic waves, C_i, are formed for the normal direction as

$$C_1 = (u_n - c)\left[-\rho c\left(n_x \frac{\partial u}{\partial n} + n_y \frac{\partial v}{\partial n}\right) + \frac{\partial p}{\partial n}\right], \ \ \lambda_1 = u_n - c \tag{2.51}$$

$$C_2 = u_n \left(n_y \frac{\partial u}{\partial n} - n_x \frac{\partial v}{\partial n}\right), \ \ \lambda_2 = u_n \tag{2.52}$$

$$C_3 = u_n \left(-c^2 \frac{\partial \rho}{\partial n} + \frac{\partial p}{\partial n}\right), \ \ \lambda_3 = u_n \tag{2.53}$$

$$C_4 = u_n \frac{\partial w}{\partial n}, \ \ \lambda_4 = u_n \tag{2.54}$$

$$C_5 = (u_n + c)\left[\rho c\left(n_x \frac{\partial u}{\partial n} + n_y \frac{\partial v}{\partial n}\right) + \frac{\partial p}{\partial n}\right], \ \ \lambda_5 = u_n + c. \tag{2.55}$$

The sign of λ_i determines whether the wave is incoming or outgoing. The rate of change of incoming characteristics is set to zero whilst outgoing characteristics are left unchanged. In the standard LCBC this is carried out only at the domain boundary, i.e.

$$\text{LCBC}: \begin{cases} \lambda_i < 0, & C'_i = 0 \\ \lambda_i > 0, & C'_i = C_i. \end{cases} \tag{2.56}$$

Using the current ZCBC method modification to the incoming characteristics is introduced smoothly, over a finite region adjacent to the domain boundary, using a cosine function,

$$\text{ZCBC}: \begin{cases} \lambda_i < 0, & C'_i = \frac{1}{2} C_i \left(1 + \cos \frac{\pi(x - x_{\text{start}})}{(x_{\text{out}} - x_{\text{start}})}\right) \\ \lambda_i > 0, & C'_i = C_i. \end{cases} \tag{2.57}$$

Intermediate variables D_1-D_5 are then formed from the modified characteristics ${C'}_1$-${C'}_5$, that will be used to reform the normal Euler fluxes:

$$D_1 = \frac{\frac{1}{2}{C'}_1 - {C'}_3 + \frac{1}{2}{C'}_5}{c^2} \tag{2.58}$$

$$D_2 = {C'}_2 n_y + \frac{n_x({C'}_5 - {C'}_1)}{2\rho c} \tag{2.59}$$

$$D_3 = -{C'}_2 n_x + \frac{n_y({C'}_5 - {C'}_1)}{2\rho c} \tag{2.60}$$

$$D_4 = {C'}_4 \tag{2.61}$$

$$D_5 = \frac{{C'}_3}{\rho^\gamma} \tag{2.62}$$

Using the intermediate variables, the normal Euler fluxes are reconstituted, incorporating the modified characteristics, with

$$\mathbf{F'_n} = \begin{pmatrix} D_1 \\ uD_1 + \rho D_2 \\ vD_1 + \rho D_3 \\ wD_1 + \rho D_4 \\ \left[\frac{c^2}{\lambda - 1} + \frac{1}{2}(u^2 + v^2 + w^2)\right] D_1 + \rho u D_2 + \rho v D_3 + \rho w D_4 + \frac{\rho^\gamma}{\gamma - 1} D_5 \end{pmatrix} \tag{2.63}$$

Finally, the modified normal Euler fluxes are added to the right hand side of the Navier-Stokes equations using

$$\mathbf{RHS} = \mathbf{RHS'} + \frac{d\mathbf{F'}_n}{dn}. \tag{2.64}$$

In comparison to a standard characteristic method, an increase in computational cost is incurred as the characteristic method is performed over a greater number of grid-points. Additionally, the region over which the method is applied is no longer physical and will no longer yield useful information. The method is however advantageous in that it uses no coefficients that need to be tuned for every application, and is proven to be more effective than alternative methods (Sandberg & Sandham, 2006).

2.2.6 Integral characteristic boundary condition

The integral characteristic boundary condition (Sandhu & Sandham, 1994) follows the same method as for the local characteristic boundary method, up until the formulation of the modified normal Euler fluxes. At this point, the derivatives of the normal Euler fluxes are integrated with respect to time using the fourth-order Runge-Kutta scheme (section 2.2.2). The time-integrated normal derivatives are then subtracted from target (freestream) values of the conservative variables, to enforce the freestream conditions on the boundary

$$\mathbf{F} = \mathbf{F}_{\text{freestream}} - \int \frac{d\mathbf{F'}_n}{dn} dt. \tag{2.65}$$

2.2.7 Freestream buffer

A simple buffer was applied at the free-stream boundary in certain cases, in order to further reduce reflections from linear waves. The buffer is active only over a finite region adjacent to the free-stream boundary, of width L_B. The buffer ramps the conservative variables $\mathbf{Q}$ towards the free-stream condition $\mathbf{Q}_\infty$, and varies in effectiveness from zero at the buffer onset to maximum effectiveness at the free-stream boundary. The conservative variables are modified as follows;

$$\mathbf{Q}' = \mathbf{Q} + \frac{1}{2} A \left(1 - \cos(\pi \frac{L_B - l}{L_B}) \right) (\mathbf{Q}_\infty - \mathbf{Q}) \tag{2.66}$$

where l is the distance normal to the free-stream boundary, and L_B the total buffer length. The strength of the buffer is determined by the parameter A. In all cases where a free-stream buffer was applied, A was specified as 0.05 and L_B was specified as 1.

A different form of buffer was employed for forced Navier–Stokes simulations; the buffer was applied ramping over a finite streamwise distance and ramps the conservative variables to the specified initial condition, not the freestream conditions. The conservative variables are modified in the following fashion;

$$\mathbf{Q}' = \mathbf{Q} + \frac{1}{2} A \left(1 - \cos(\pi \frac{x - x_{start}}{x_{end} - x_{start}}) \right) (\mathbf{Q}_{store} - \mathbf{Q}), \tag{2.67}$$

where $\mathbf{Q}_{store}$ is the initial value of the conservative variables, x_{start} is the streamwise buffer onset and x_{end} is the end of the ramping function. For $x < x_{start}$ the conservative variables are not modified, whereas for $x > x_{end}$ the conservative variables are modified as

$$\mathbf{Q}' = \mathbf{Q} + \frac{1}{2} A (\mathbf{Q}_{store} - \mathbf{Q}). \tag{2.68}$$

2.2.8 Airfoil surface boundary condition

At the airfoil surface an adiabatic, no slip condition is applied. The variables, u, v and w are set to zero, and the adiabatic thermal boundary condition is enforced by adjusting E_t such that

$$\frac{dT}{dn} = 0. \tag{2.69}$$

In order to enforce the adiabatic condition an iterative scheme is used. First, the condition

$$\frac{dT}{d\eta} = 0 \tag{2.70}$$

is applied at all points on the airfoil surface. This is achieved by calculating the temperature T from the conservative variables at all streamwise locations over the airfoil surface, and six grid-points into the freestream. The derivative at the airfoil surface may then be expressed as

$$\frac{dT}{d\eta_{j=1}} = D_{11}T_{j=1} + D_{21}T_{j=2} + D_{31}T_{j=3} + D_{41}T_{j=4} + D_{51}T_{j=5} + D_{61}T_{j=6} \tag{2.71}$$

where D_{ij} refers to locations in the derivative operator matrix D defined in section 2.2.2 as $\mathbf{P}^{-1}\mathbf{Q}$, and T_j refers to the temperature at wall normal grid-point j. Setting $\frac{dT}{d\eta_{j=1}}$ to zero and rearranging yields the expression for T at the airfoil surface

$$T_{j=1} = \frac{-1}{D_{11}}(D_{21}T_{j=2} + D_{31}T_{j=3} + D_{41}T_{j=4} + D_{51}T_{j=5} + D_{61}T_{j=6}) \tag{2.72}$$

This serves only as an initial estimate for the surface temperature, since the wall normal derivative of temperature depends also on the ξ derivative. New values for the surface temperature are then calculated using the iterative scheme

$$\frac{dT_{k+1}}{d\eta} = \frac{\frac{d\xi}{dn}}{\frac{d\eta}{dn}}\frac{dT_k}{d\xi},\ k = 1:5 \tag{2.73}$$

where

$$\frac{d\xi}{dn} = \frac{1}{J}\left(-n_y\frac{dx}{d\eta} + n_x\frac{dy}{d\eta}\right),\quad \frac{d\eta}{dn} = \frac{1}{J}\left(n_y\frac{dx}{d\xi} + n_x\frac{dy}{d\xi}\right) \tag{2.74}$$

and

$$n_x = \frac{-\frac{dy}{dxi}}{\sqrt{\left(\frac{dx}{d\xi}\right)^2 + \left(\frac{dy}{d\xi}\right)^2}}, \quad n_y = \frac{\frac{dx}{dxi}}{\sqrt{\left(\frac{dx}{d\xi}\right)^2 + \left(\frac{dy}{d\xi}\right)^2}} \tag{2.75}$$

Investigating the performance of the iterative scheme for airfoil flow at $Re_c = 10^4$ and $M = 0.6$ reveals that after 5 iterations $dT/dN < 10^{-12}$ at all locations on the airfoil surface.

2.2.9 Initial condition

Each simulation is initialised by setting freestream conditions throughout the domain,

$$\rho = 1, \;\; \rho u = 1, \;\; \rho v = 0, \;\; \rho w = 0, \;\; T = 1, \;\; E_t = \frac{\rho T}{\gamma(\gamma - 1)M^2} + \frac{1}{2}\rho(u^2 + v^2 + w^2) \tag{2.76}$$

and imposing a simple parabolic boundary layer over the airfoil to satisfy the surface boundary condition. The simulation is then run until transient effects are deemed to have passed, based on inspection of time dependent behaviour of quantities such as lift-coefficient, before data capture and analysis begin.

2.2.10 Volume forcing

Low amplitude forcing is applied in certain simulations in order to excite instabilities in the flow, and is implemented using the following method. Curvilinear coordinate quantities ξ_{force} and η_{force} are defined as

$$\xi_{\text{force}} = \frac{(\xi - \xi_{\text{start}})}{(\xi_{\text{end}} - \xi_{\text{start}})}, \quad \eta_{\text{force}} = \frac{(\eta - \eta_{\text{start}})}{(\eta_{\text{end}} - \eta_{\text{start}})}, \tag{2.77}$$

where ξ_{start} and η_{start} are the coordinates specifying the beginning of the forcing area, while ξ_{end} and η_{end} are coordinates specifying the end of the forcing area. Thus ξ_{force} and η_{force} both vary from zero to one. Ramping functions F_ξ and F_η are then formulated such that, when differentiated with respect to the appropriate curvilinear coordinate, a smooth cosine function results. Consider first the function F_ξ, which defines the forcing amplitude in the ξ direction and is only differentiated in the ξ direction. Outside the region $0 < \eta_{\text{force}} < 1$, F_ξ is defined as zero whereas within the region $0 < \eta_{\text{force}} < 1$, F_ξ possesses finite values. This creates a discontinuity in the η direction, but the function is differentiated only with respect to ξ and there will be no discontinuity in $\frac{dF_\xi}{d\xi}$. Setting F_ξ to zero outside the region $0 < \eta_{\text{force}} < 1$ is necessary in order to ensure $\frac{dF_\xi}{d\xi} = 0$ outside the forcing area. Within the region $0 < \eta_{\text{force}} < 1$ the function is defined as

$$\xi_{\text{force}} > 1, \;\; F_\xi = \frac{A\text{sin}(2\pi f t + \phi)\,(1 - \cos(2\pi\eta_{\text{force}}))}{2} \tag{2.78}$$

$$0 < \xi_{\text{force}} < 1, \;\; F_\xi = \frac{A\text{sin}(2\pi f t + \phi)\,\left(\xi_{\text{force}} - \frac{1}{2\pi}\text{sin}(2\pi\xi_{\text{force}})\right)(1 - \cos(2\pi\eta_{\text{force}}))}{2} \tag{2.79}$$

$$\xi_{\text{force}} < 0, \;\; F_\xi = 0 \tag{2.80}$$

where A is a user-specified coefficient controlling the forcing amplitude, f is the temporal frequency of the forcing, t is the non-dimensional time and ψ is the phase of the forcing. This results in smooth variation of F_ξ with ξ_{force}, with resultant derivative $\frac{dF_\xi}{d\xi}$ taking the form of a single cosine wave over the forcing region, and being zero elsewhere (figure 2.2).

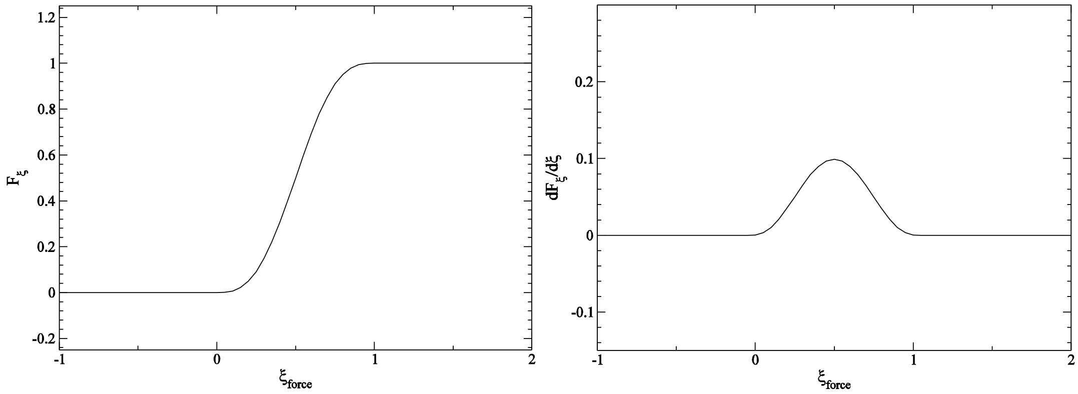

Figure 2.2: Variation of F_ξ with ξ_{force} (left), and variation of $\frac{dF_\xi}{d\xi}$ with ξ_{force} (right).

An equivalent function F_η defines the forcing amplitude in the η direction and is formulated in a similar fashion. Everywhere outside the region $0 < \xi_{\text{force}} < 1$, the function F_η is zero in order to ensure $\frac{dF_\eta}{d\eta}$ is also zero. Within the region $0 < \xi_{\text{force}} < 1$, F_η is defined as follows:

$$\eta_{\text{force}} > 1, \;\; F_\eta = \frac{A\text{sin}(2\pi f t + \phi)\,(1 - \cos(2\pi\xi_{\text{force}}))}{2} \tag{2.81}$$

$$0 < \eta_{\text{force}} < 1, \;\; F_\eta = \frac{A\text{sin}(2\pi f t + \phi)\,(1 - \cos(2\pi\xi_{\text{force}}))\left(\eta_{\text{force}} - \frac{1}{2\pi}\text{sin}(2\pi\eta_{\text{force}})\right)}{2} \tag{2.82}$$

$$\eta_{\text{force}} < 0, \;\; F_\eta = 0 \tag{2.83}$$

The function F_η and derivative $\frac{dF_\eta}{d\eta}$ are smooth functions that behave in the same manner as the ξ equivalent (figure 2.2), but in the η direction. Cartesian derivatives of the ramping functions F_x, and F_y are then formed by

$$\frac{dF}{dy} = \frac{dF_\eta}{d\eta}\frac{dx}{d\xi} - \frac{dF_\xi}{d\xi}\frac{dx}{d\eta} \tag{2.84}$$

$$\frac{dF}{dx} = \frac{dF_\xi}{d\xi}\frac{dy}{d\eta} - \frac{dF_\eta}{d\eta}\frac{dy}{d\xi} \tag{2.85}$$

noting that

$$\frac{dF_\xi}{d\xi} = \frac{dF_\eta}{d\eta} = \frac{A\text{sin}(2\pi f t + \phi)\,(1 - \cos(2\pi\xi_{\text{force}}))\,(1 - \cos(2\pi\eta_{\text{force}}))}{2} \tag{2.86}$$

Finally, $\frac{dF}{dy}$ is added to the right hand side of the x-momentum equation and $\frac{dF}{dx}$ is subtracted from the right hand side of the y-momentum equation, giving

$$\frac{d\rho u}{dt} = \frac{d\rho u}{dt} + \frac{dF}{dy}, \quad \frac{d\rho v}{dt} = \frac{d\rho v}{dt} - \frac{dF}{dx}. \tag{2.87}$$

Where forcing is required in a 3D simulation, a spanwise dependency is introduced, and the forcing amplitude varies as

$$\cos\left(2\pi n \frac{k-1}{N_z - 1}\right), \tag{2.88}$$

where k is the spanwise grid-point, N_z is the total number of spanwise grid-points and n is the spanwise wavenumber. When used in conjunction with cartesian grids the method is divergence free. For the case of curvilinear grids, as used here, the method is not identically divergence free, however in practice the forcing method appears to produce negligible acoustic perturbations, especially when compared to those occurring naturally as a result of hydrodynamic behaviour.

2.2.11 Validation

The code is based upon an existing code that has been previously validated for compressible turbulent plane channel flow (Sandham *et al.*, 2002), and more recently has been demonstrated to accurately represent the development of hydrodynamic instabilities (Sandberg *et al.*, 2006). The code used in the current study is different in that it is applied to a curvilinear C-type grid with wake connection, however the same metric terms were used in previous versions of the code. The use of an airfoil geometry necessitates special treatment of grid-points in the vicinity of the trailing edge, for which the dependency of simulation results on trailing edge treatment is quantified in section 2.2.15. The dependency of simulation results on boundary conditions has previously been quantified (Jones *et al.*, 2006), and the influence of both grid resolution and domain size upon simulation results has also been quantified in sections 4.3.1 and 4.3.2.

2.2.12 Parallel implementation

The computational domain is divided equally amongst the total number of processors used, such that each processor is responsible for a unique sub-domain. Each processor is denoted an integer identification number, ranging from 0 to $n_{\mathrm{pr}} - 1$, where n_{pr} is the total number of processors used. Processor 0 is located at the $\xi = 0$, $\eta = 0$ boundary. Further processors are then allocated moving first in the ξ direction, then the η direction as indicated in figure 2.3. In order to evaluate the fourth-order central difference scheme, given that a five point stencil is used, each processor requires data from adjacent processors.Each processor sub-domain is therefore extended in each direction by two grid-points. These extra cells are denoted 'halo' cells, and are filled with data from the first and second grid-points of adjacent processor sub-domains before evaluating derivatives, as illustrated in figure 2.4.

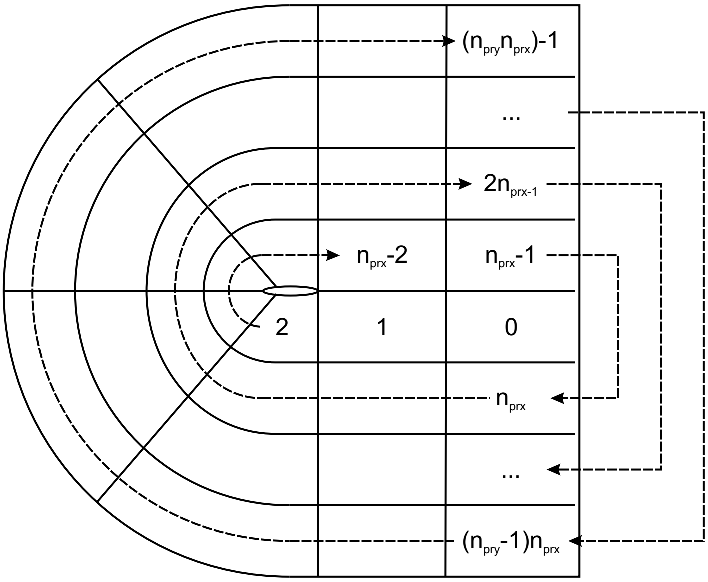

Figure 2.3: Distribution and numbering of processors within the computational domain.

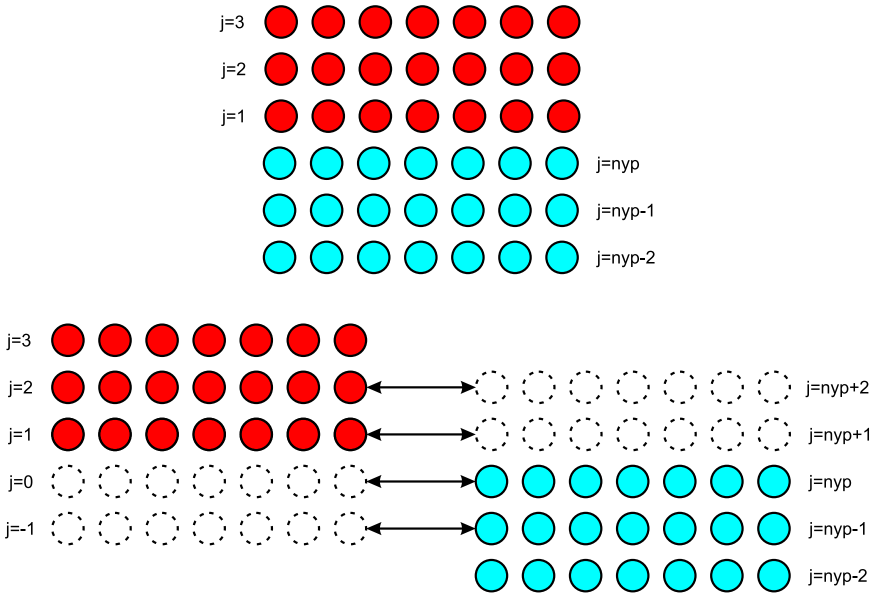

Figure 2.4: Illustration of data transfer between halo cells.

2.2.13 Wake connection

In contrast to the standard processor sub-domain interface, a processor on the wake dividing line will share the row of points on the dividing line with the adjacent processor across the wake-cut, as illustrated in figure 2.5. The grid-points on the dividing line are duplicated and the governing equations at these points are calculated by both processors. In order to evaluate derivatives across the wake, data transfer is employed using two halo cells, in a similar fashion as for other processor boundaries. However, when performing data transfer across the wake, halo cells will be filled with data from the second and third grid-points of the adjacent processor, as illustrated in figure 2.6. This differs from non-wake data transfer, where only the first and second grid-points are used. Since grid-points on the wake dividing line are duplicated, if the flow quantities on one side of the wake cut were to differ from those on the other side of the wake cut the discrepancy would persist indefinitely, and each processor would effectively be solving different equations for the same grid-points. In order to prevent this from occurring, for example due to round-off error, data for grid-points on the wake dividing line are averaged across the wake cut at specified intervals. Typically the interval for wake-averaging is every 5000 iterations.

2.2.14 Metric terms

Metric terms are calculated to machine accuracy at the start of the simulation using the spatial scheme described in section 2.2.2. When filling halo cells by

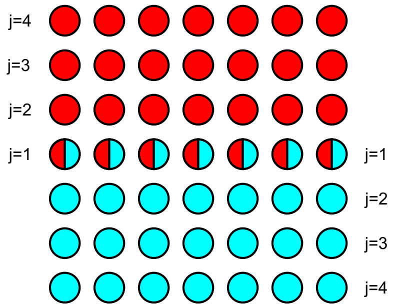

Figure 2.5: Illustration of grid-points shared between adjacent processors across the wake cut.

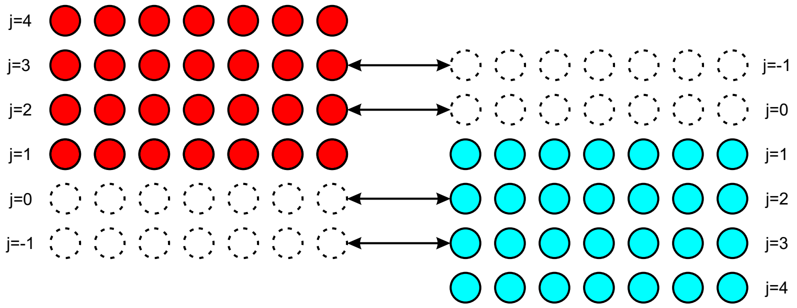

Figure 2.6: Illustration of the data transfer process across the wake cut.

transferring data across the wake dividing line, first derivative metric quantities must be multiplied by -1 to account for the discontinuous change in direction of ξ and η with respect to x and y.

2.2.15 Trailing edge treatment

The first two physical locations downstream of the trailing edge each consist of two grid-points, one on each side of the wake dividing line. When evaluating ξ derivatives, each of these coincident grid-points will use data from different five-point stencils. This can be observed in figure 2.7, where the points $\mathrm{TE}+1$ and $\mathrm{TE}+2$ use different derivative stencils depending on which side of the wake the derivative is evaluated. The coincident grid-points clearly represent the same physical location, and it would be unphysical to allow the possibility of the two coincident points possessing differing fluid properties. Therefore, derivatives in the direction at the two points downstream of the trailing edge, where the stencil can encompass points on either side of the airfoil, are evaluated by averaging data at points on the airfoil across both sides of the airfoil itself. This enforces the same fluid properties for both grid points.

Attempts have been made to quantify the influence of the airfoil trailing edge treatment. Grid refinement studies have been performed for two-dimensional simulations in chapter 4, section 4.3.1 which included varying grid resolution in the vicinity of the trailing edge. Additionally, the effect of using an alternative trailing edge treatment was investigated. The two-dimensional simulation at $Re_c = 5 \times 10^4$, $M = 0.4$ and $\alpha = 5^\circ$ presented in chapter 4, section 4.4 was selected as the test-case. After running the simulation for 40 non-dimensional time units using the trailing-edge treatment outlined above, an alternative trailing edge treatment was implemented and the simulation run further. The simulation was run for 15 non-dimensional time units to allow any transient effects to pass, before taking statistical data for a further 10 time units, or 29 vortex-shedding cycles. The alternative trailing-edge treatment consisted of applying the Carpenter boundary scheme to the first four points downstream of the trailing edge, and employing no averaging of derivatives across the wake cut. The time-dependent lift-coefficient and the Fourier transformed lift coefficient are plotted for both cases in figure 2.8. The global behaviour appears similar for both cases; the mean-lift coefficient changes by less than 0.3%, and the Fourier transformed lift-coefficient exhibits the same tonal structure and amplitudes, although the spectrum is less distinct due to the shorter time-series used. Thus the global behaviour appears to be independent of the trailing edge treatment.

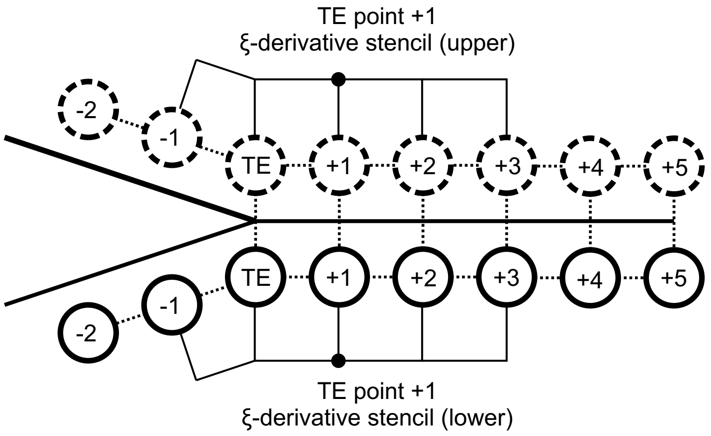

Figure 2.7: ξ derivative stencils in the vicinity of the trailing edge point.

2.2.16 Grid generation

Grid generation for high-order non-dissipative codes is non-trivial, and achieved by an iterative approach. The presence of under resolved flow phenomena results in numerical oscillations, particularly in sensitive quantities such as density gradient. By analysing simulation results, locations of poor resolution may be identified by such oscillations. A new grid is then generated, with the purpose of improving the resolution in the necessary locations, and the flow-field data are interpolated onto the new grid. The simulation is then run on the new grid

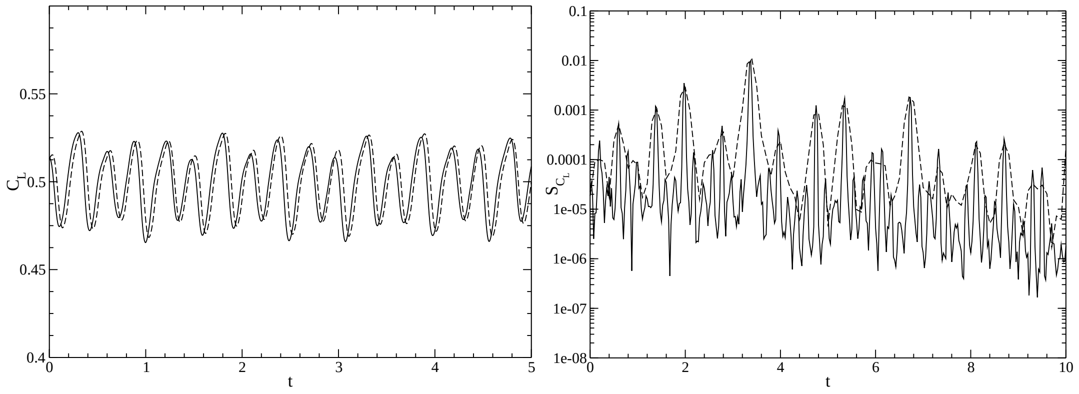

Figure 2.8: Time-dependent lift-coefficient (left), and Fourier transformed lift-coefficient (right) for the two-dimensional case at $Re_c = 5 \times 10^4$, $M = 0.4$ and $\alpha = 5°$, treating the trailing edge with central differences and wake-cut averaging (—) and with a Carpenter scheme and no averaging (− −).

and the results are analysed in order to assess whether resolution issues have been eliminated. The process can be repeated as often as necessary, and avoids the need for continually starting simulations from scratch, with the associated computational cost of waiting for transient effects to pass. In order to minimise the possibility of discontinuities in the metric terms, the grid-point distribution for connectors such as the airfoil surface and the downstream boundary are generated using a polynomial mapping technique. A connector specified with N control points will be mapped using $N - 1$ polynomial distributions of grid-points. At the interfaces between polynomials, the second derivative metric terms are always set to zero ensuring continuity in the second derivative metric terms. All grids are generated using the program Gridgen by Pointwise$^{\text{TM}}$.

2.2.17 Calculation of aerodynamic coefficients

Aerodynamic coefficients are found by integrating the appropriate force over the airfoil surface. The lift-coefficient is calculated as

$$C_L = \frac{1}{\frac{1}{2}\rho_\infty u_\infty^2} \int_{s=0}^{s=s_{total}} -S(p_{\eta=0} - p_\infty)|\sin\theta| ds, \tag{2.89}$$

where the subscript ∞ refers to free-stream conditions and the subscript $\eta = 0$ refers to quantities taken at the airfoil surface. The local surface inclination with respect to the cartesian axes, θ, is defined as $\tan^{-1}(\frac{dy}{dx}_{\eta=0})$, and the surface coordinate is denoted s. S is a function specified in order to maintain the correct sign of the lift contribution depending on whether the expression is evaluated on the upper or lower airfoil surface, and is defined as

$$S = 1 \text{ for } \frac{dx}{d\xi} > 0, \qquad S = -1 \text{ for } \frac{dx}{d\xi} < 0. \tag{2.90}$$

The pressure-drag coefficient and skin-friction drag coefficient are calculated as

$$C_{DP} = \frac{1}{\frac{1}{2}\rho_\infty u_\infty^2} \int_{s=0}^{s=s_{total}} p_{\eta=0} \text{sin}\theta \, ds \tag{2.91}$$

and

$$C_{Df} = \frac{1}{\frac{1}{2}\rho_\infty u_\infty^2} \int_{s=0}^{s=s_{total}} \mu \left[\left(\frac{du}{dy}_{\eta=0} \right) \cos\theta - S \left(\frac{dv}{dx}_{\eta=0} \right) |\sin\theta| \right] ds \tag{2.92}$$

respectively, where S is defined in the same manner as for the lift-coefficient. The total drag coefficient is found by summing the constituent coefficients,

$$C_D = C_{DP} + C_{Df}. \tag{2.93}$$

2.2.18 Calculation of integral boundary layer parameters

Extracting integral boundary layer properties, such as momentum and displacement thickness, from airfoil simulations is non-trivial. Boundary layer profiles are likely to possess a local edge velocity exceeding the free-stream velocity, and thus difficulties arise deciding on a reference velocity and integration limits. In order to bypass these problems a method of deriving boundary layer parameters from the mean vorticity field is used. First, a pseudo velocity is formed by integrating spanwise vorticity in the wall normal direction,

$$\tilde{u}(n) = \int_0^n \omega_z dn. \tag{2.94}$$

Outside the boundary layer, where the velocity gradient is zero, vorticity is also zero and hence the pseudo velocity reaches a constant value in the free-stream. Boundary layer parameters such as kinematic displacement thickness and momentum thickness are then formed using the pseudo velocity instead of using a true tangential velocity obtained from the simulation:

$$\delta_k^* = \int_{n=0}^{n=\infty} \left(1 - \frac{\tilde{u}}{\tilde{u}_\infty} \right) dn \tag{2.95}$$

$$\theta_k = \int_{n=0}^{n=\infty} \frac{\tilde{u}}{\tilde{u}_\infty} \left(1 - \frac{\tilde{u}}{\tilde{u}_\infty} \right) dn \tag{2.96}$$

The reference velocity, $\tilde{u}_\infty$, is the freestream pseudo velocity found by integrating spanwise vorticity into the freestream, not the true free-stream velocity. This method does not require extraction of edge velocities or ad-hoc specification of the boundary layer thickness. The only variable is the distance to which the spanwise vorticity is integrated. In practice the method is robust to variation of integration length, as illustrated in figure 2.9. Typically spanwise vorticity will be integrated to 60% of the wall-normal number of grid-points when extracting boundary layer parameters.

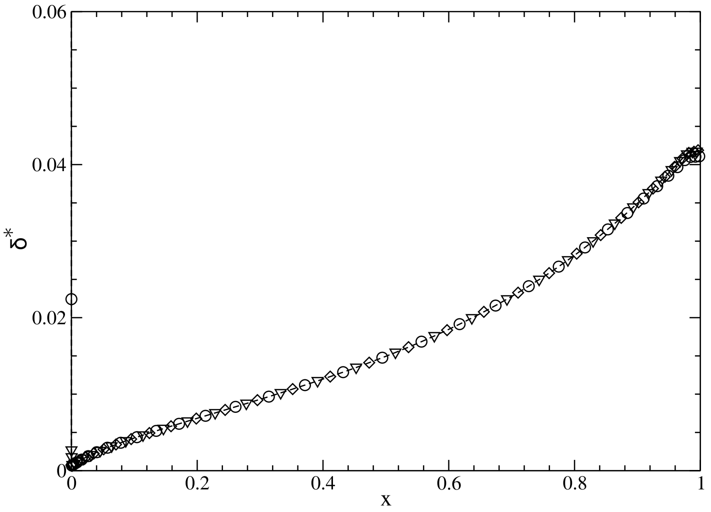

Figure 2.9: Variation of time averaged δ^* distribution with wall normal integration distance, $Re_c = 10\times10^4$, $M = 0.6$, showing δ^* integrated to 65 (○), 130 (◇) and 195 (▽ – – ▽) grid-points. Total number of wall normal grid-points is 259.

2.3 Fourier transforms

Fourier transforms of pressure series are computed at several points in this study. In all cases the mean of the time-series is subtracted before computing the spectra, and in certain cases windowing and segmenting is employed to improve the quality of spectra. Segmenting is applied as follows. Given a time-series of length T, an integer number of segments, N, is specified. The time series is then divided into N segments, each overlapping by 50%, hence the segments will be of length $\Delta T = 2T/(N+1)$. Fourier transforms are performed for each segment individually before ensemble averaging the resultant spectra. Hanning windowing is another technique employed to improve the quality of spectra, and essentially involves multiplying the time-series by a cosine function that ramps to zero at either end of the time-series. For a time series of length T, the Hanning function is defined as

$$f = 0.5 \left[1 - \cos \left(\frac{2}{\pi} tT \right) \right] . \tag{2.97}$$

In order to compensate for the reduction in signal amplitude, the resultant spectrum is multiplied by $1/\overline{f}$ i.e. 2. When computing power spectra, the spectra are multiplied by $1/\overline{f^2}$ i.e. 8/3.

2.4 Linear stability analysis

2.4.1 Governing equations

Linear stability analysis is used to predict the response of boundary layer profiles to small amplitude perturbations. Assuming incompressible flow, which is reasonable at the Mach numbers considered in this study, boundary layer disturbances are assumed to take the form of two-dimensional travelling waves such that

$$u_i' = \hat{u}_i(y) \mathrm{e}^{\mathrm{i}(\alpha x - \omega t)} . \tag{2.98}$$

The variable α is the complex wavenumber (defined as $\alpha = 2\pi/\lambda$, where λ is the disturbance wavelength) and ω is the complex frequency of the travelling wave (defined as $\omega = 2\pi f$, where f is the disturbance frequency). Wall normal variation is accounted for in the function $\hat{u}_{\mathrm{i}}(y)$, and the phase velocity is given by $c_{ph} = \omega/\alpha$. The amplitude of instability waves varies as

$$e^{\omega_{\mathrm{i}} t - \alpha_{\mathrm{i}} x} , \tag{2.99}$$

found by expanding (2.98), hence the imaginary part of the wavenumber (-α_{i}) corresponds to the spatial growth rate and the imaginary part of the frequency (ω_{i}) corresponds to the temporal growth rate.

A parallel baseflow is considered, for which $\overline{u} = f(y)$, $\overline{v} = 0$, $d\overline{u}/dx = 0$. Velocity and pressure are decomposed into mean and fluctuating quantities, i.e. $u_i = \overline{u_i} + u_i'$, $p = \overline{p} + p'$, and the incompressible Navier–Stokes equations are written for the decomposed variables. The equations for the base flow (i.e. with fluctuating quantities omitted) are subtracted, and fluctuating quantities are considered to be small, hence multiples of fluctuating quantities are removed. Assuming perturbations of the form given in (2.98), substituting into the Navier–Stokes equations and rearranging leads to the well known Orr–Sommerfeld equation, which may be written as

$$(\overline{u} - C_{ph}) \left(\frac{d^2\hat{v}}{dy^2} - \alpha^2\hat{v} \right) - \frac{d^2\overline{u}}{dy^2}\hat{v} = -\frac{i\nu}{\alpha} \left(\alpha^4\hat{v} - 2\alpha^2\frac{d^2\hat{v}}{dy^2} + \frac{d^4\hat{v}}{dy^4} \right). \tag{2.100}$$

A full derivation of the Orr-Sommerfeld equation is given in Drazin & Reed (1981). To solve the Orr–Sommerfeld equation, a velocity profile $\overline{u} = f(y)$ is specified, hence $\overline{u}(y)$ and $d^2\overline{u}/dy^2$ are known. The Orr-Sommerfeld equation then represents an eigenvalue problem of the form $\mathbf{A}\hat{v} = \mathbf{B}\hat{v}$, with $\hat{v}$ as the eigenvector, which yields non-trivial solutions for only certain values of α and c_{ph}. The eigenvalue problem can be solved in two ways. Either a real ω can be specified and a complex α computed, denoted spatial linear stability analysis, or a real α can be specified and a complex ω computed, denoted temporal linear stability analysis. The code used throughout this study solves the Orr-Sommerfeld equation as a temporal problem, however use of the iterative scheme detailed in section 2.4.2 allows spatial analysis to be performed.

2.4.2 Numerical method

Grids and data fitting

Grids used for linear stability analysis are not required to be as fine as for DNS, particularly in regions with little variation in mean fluid velocity. Therefore, in order to avoid unnecessary computational cost, linear stability analysis are performed upon computational grids that are not the same as that of the original DNS. The grid-point distribution varies depending on whether the analysis is of a wake or boundary layer profile, however in both cases the velocity profile is fitted from the old (DNS) grid on to the new grid using cubic spline interpolation, thus providing data values at locations between physical grid-points of the original data set.

Spatial analysis algorithm

When considering external aerodynamics it is typically more relevant to consider the spatial problem, where a frequency ω is specified and a wavenumber α computed, rather than the temporal problem. To solve the spatial problem using a temporal code an iterative scheme is employed. First we specify the complex frequency that we wish to solve for, ω_{in}. We then try to find the appropriate complex wavenumber, α_{out}, such that when the Orr-Sommerfeld equation is solved using this value of α_{out} we return our original complex frequency ω_{in}.

The process is as follows. Given a complex frequency ω_{in} for which we wish to find the corresponding α_{out}, the first step is to make an approximate estimate of α_{out}. In order to do this we first estimate a phase speed,

$$c_{ph} = 0.5, \tag{2.101}$$

for example, and then the approximate wavenumber estimate, α_1, may be computed as

$$\alpha_1 = \omega_{in}/c_{ph}. \tag{2.102}$$

A second wavenumber, α_2, is specified, by adding a small increment to the first, as

$$\alpha_2 = \omega_{in}/c_{ph} + 1 \times 10^{-3}(1+i). \tag{2.103}$$

The associated complex frequencies for both α_1 and α_2 may then be found by solving the Orr-Sommerfeld equation,

$$\omega_1 = f(\alpha_1, \overline{u}(y)), \tag{2.104}$$

$$\omega_2 = f(\alpha_2, \overline{u}(y)). \tag{2.105}$$

We are now in a position to commence the iteration sequence. At the start of the scheme we have two α/ω pairs; (α_1, ω_1), and (α_2, ω_2). At each iteration the derivative $d\omega/d\alpha$ is computed, and used to calculate a more accurate estimate for α_{out}. The new α/ω pair are stored, and (α_1, ω_1) discarded and the process is repeated until $\omega_2 = \omega_{in}$ to a specified level of accuracy. The method may be written as follows:

```
while ($|\omega_2 - \omega_{in}| > \epsilon$)
    $\left(\frac{d\omega}{d\alpha}\right) = \frac{\omega_2 - \omega_1}{\alpha_2 - \alpha_1}$
    $\alpha_{new} = (\omega_{in} - \omega_2)\left(\frac{d\omega}{d\alpha}\right)^{-1} + \alpha_2$
    $\omega_{new} = f(\alpha_{new}, \overline{u}(y))$
    $\alpha_1 = \alpha_2$
    $\omega_1 = \omega_2$
    $\alpha_2 = \alpha_{new}$
    $\omega_2 = \omega_{new}$
end while
```

The convergence criteria here is that $|\omega - \omega_{in}| < \epsilon$, where ϵ is a user-specified parameter. For the current study $\epsilon = 10^{-6}$. The initial estimate for α given by

(2.102) is quite crude hence, if analysis of a number of frequencies or velocity profiles is being performed, the value of α from the previous computation will instead be used as the initial estimate.

2.4.3 Numerics for boundary layer profiles

Discretisation

For boundary layer profiles, grid resolution is required to be fine in the vicinity of $y = 0$, where strong velocity gradients are present, and is allowed to coarsen with increasing y as freestream conditions are reached. A geometric discretisation is specified in order to achieve this, of the form

$$y_{j+1} = y_j + a(1 + s), \tag{2.106}$$

where a is the grid spacing at the first point, $y = 0$, and s determines the percentage increase in cell size with distance from the wall. In all cases 200 grid-points were used, in conjunction with values $s = 0.055$ and $a = 1.30 \times 10^{-4}$. For validation purposes the most unstable eigenmode for a Blasius boundary layer profile at $Re_{\delta^*} = 1500$, $\alpha = 0.2$ was determined, and the resultant value for ω was found to agree with the results of Gaster (1978) to the 5th digit for the real part and the 6th digit for the imaginary part.

Derivative scheme

In all cases 6th order compact difference stencils are used (Lele, 1992) to compute derivatives, including metric terms. Sufficient resolution for the derivative scheme is indicated by smooth derivatives of velocity profiles, up to and including the fourth derivative.

Spatial integration

When calculating the spatial growth of instability waves, wave amplitudes are required to be integrated spatially. Given an initial disturbance amplitude A_1, and a disturbance amplitude A_2 at an arbitrary downstream location, the disturbance N factor is defined as $N = \ln\left(\frac{A_2}{A_1}\right)$. Hence, considering equation 2.99, $N = N_{x=0} - \alpha_{\mathrm{i}} x$ and $-\alpha_{\mathrm{i}}$ is the spatial growth rate of the N-factor. The N factor is integrated using an Euler scheme, as

$$N_{x+\Delta x} = N_x - \alpha_{\mathrm{i}} \Delta x. \tag{2.107}$$

2.4.4 Numerics for wake profiles

For wake profiles, grid resolution is again required to be fine in the vicinity of $y = 0$, where strong velocity gradients are present, and to coarsen with increasing y. Additionally, metric terms must be smooth across the line $y = 0$ up to and including the fourth derivative. In order to achieve this, grid-points are distributed using a cosh function.

First we consider only half of the wake. We define N_y as the number of grid-points in this half of the wake and L_y as the half-height of the wake profile. Hence we require $y(0) = 0$ and $y(N_y) = L_y$. The following function is used to compute the cell size distribution of the grid,

$$\triangle y(j) = \cosh\left[\left(2\pi\frac{(j-1)}{(N_y-1)}\right)^r\right], \tag{2.108}$$

where r is a stretching parameter specified as $r = 1.6$ in order to provide a desirable distribution of grid-points. Equation 2.108 yields arbitrary initial cell sizes and so appropriate scaling must be applied to ensure $y(N_y) = L_y$. The appropriate scaling factor is computed numerically by dividing the half-wake height by the sum of all $\triangle y$, yielding

$$A = \frac{L_y}{\Sigma_{j=1}^{N_y}\triangle y(j)}. \tag{2.109}$$

Coordinates are then defined as

$$y(j) = y(j-1) + A\triangle y(j), \tag{2.110}$$

specifying $y(0) = 0$, hence $y(N_y) = L_y$ as required. The opposite half of the wake grid is a mirror image of the first. Since the cell size distribution is determined by a cosh function, metric terms will be derivatives of a cosh function and thus continuous across $y = 0$. The total number of grid-points is specified as $N = 2N_y - 1$, and the total height of the wake profile is $2L_y$. Hence only odd numbers of grid-points are used. The coordinates of the grid are redefined such that $y(1) = -L_y$, $y(N) = L_y$. In all cases 201 grid-points were used.

2.4.5 Cusp-map technique for locating absolute instability

A simple criterion for the presence of absolute instability is the existence of an instability wave possessing zero group velocity, $c_g = 0$, and a positive temporal growth rate, $\omega_i > 0$. The cusp-map technique is a method of looking for the presence of absolute instability based on these criteria, and is the temporal equivalent of Briggs method (Briggs, 1964). A full description of both Briggs method and the cusp-map method is found in Schmid, Henningson & Jankowski (2002), a brief description necessary to interpret the results follows. Use of a temporal method is preferable in order to avoid the additional computational expense of using the iterative spatial scheme defined in section 2.4.2.

Given that a dispersion relation D, in this case the Orr-Sommerfeld equation, relates α and ω,

$$D(\alpha, \omega) = 0, \tag{2.111}$$

points in the complex ω plane will map to points in the complex α plane and vice versa. The presence of a saddle point in the complex α plane represents a point where $c_g = 0$, since for a saddle point

$$D(\alpha, \omega) = 0, \qquad \frac{\partial D(\alpha, \omega)}{\partial \alpha} = 0 \tag{2.112}$$

and hence

$$c_g = \frac{\partial \omega}{\partial \alpha} = \frac{\partial D}{\partial \alpha} / \frac{\partial D}{\partial \omega} = 0. \tag{2.113}$$

Where a saddle point occurs in the complex α plane, a branch point will occur in the complex ω plane. Essentially, the cusp-map method is a systematic procedure for locating saddle and branch point pairs, and hence instability waves with $c_g = 0$. Lines of constant α_r are plotted in the complex α plane, and then mapped via the dispersion relation to the complex ω plane. A branch point in the complex ω plane may be readily observed as a 'cusp' where contours in the complex ω plane first cross themselves (figure 2.10). The presence of a branch point represents an instability wave with $c_g = 0$. If the branch point is in the lower half of the complex ω plane (i.e. $\omega_i < 0$), the stationary wave is absolutely stable. If the branch point is in the upper half of the complex ω plane (i.e. $\omega_i > 0$), the stationary wave is absolutely unstable.

The method is employed in the current study as follows. First, for the profile of interest, the Orr-Sommerfeld equation is solved for a range of real α, in order to determine the envelope of unstable (real) wavenumbers. The upper and lower limits of this envelope are denoted α_{r1} and α_{r2}. A second sweep is then performed over a range of both α_r and α_i, forming an equidistant grid in the complex α plane (figure 2.10, left). The upper and lower α_r values are chosen as α_{r1} and α_{r2}. The upper and lower limits of α_i are chosen intuitively, for the first attempt, and then refined. The associated map in the complex ω plane will either contain a cusp (figure 2.10, right), or else the process can be repeated making adjustments to α in order to locate a cusp. Once a cusp is found, it may be tracked as the boundary layer profile slowly varies, and the corresponding α and ω noted.

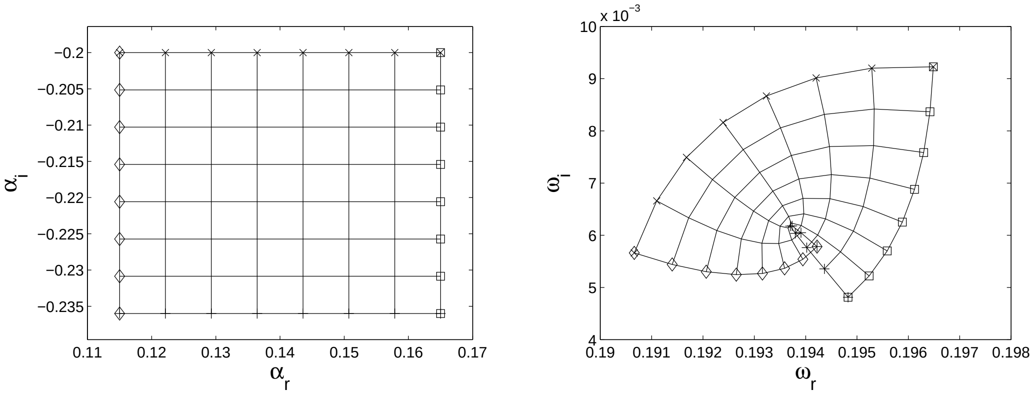

Figure 2.10: Equidistant grid in the complex α plane (left) and its corresponding map into the complex ω plane (right) , revealing a cusp associated with $c_g = 0$ and $\omega_i > 0$, as determined for shear layer profile given by equation 2.114 with R=1.35.

Use of the Orr-Sommerfeld solver in conjunction with the cusp-map method to determine the presence of absolute instability has been validated for analytic wake profiles given in Huerre & Monkewitz (1985), described by the equation

$$u(y) = 1 + R \tanh\left(\frac{y}{2}\right). \tag{2.114}$$

The variation of ω_i with R, determined using the Orr-Sommerfeld solver in conjunction with the cusp-map method and setting the Reynolds number to $Re_\theta = 10^6$, is plotted in figure 2.11 in the vicinity of $\omega_i = 0$. Transition from convective to absolute instability was found to occur at $R = 1.3156$, compared to $R = 1.315$ as reported by Huerre & Monkewitz using an inviscid approach. For the profile $R = 1.315$, values $\omega_i = -1.266 \times 10^{-4}$ and $\omega_r = 1.921 \times 10^{-1}$ were determined, compared to $\omega_i = 0$ and $\omega_r = 1.92 \times 10^{-1}$ as reported by Huerre & Monkewitz.

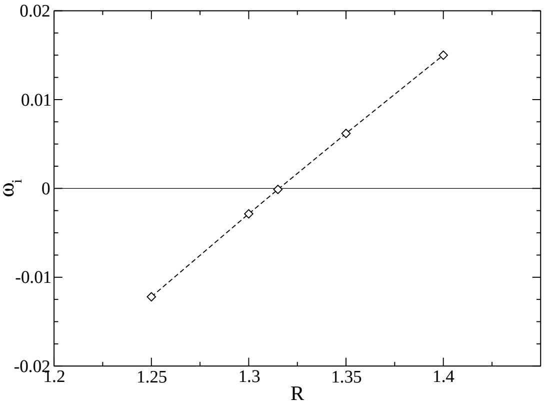

Figure 2.11: Variation with R of complex ω associated with $c_g = 0$, for profiles given in Huerre & Monkewitz (1985).

Chapter 3

Two-dimensional studies of the flow around an airfoil at Reynolds number 10,000[1]

3.1 Introduction

In this chapter the flow around an airfoil at $Re_c = 10^4$ is investigated by both numerical simulation and stability analysis. Although in reality no aircraft operates at $Re_c = 10^4$, simulations at this Reynolds number allow validation of the numerical method by comparison both to similar studies and alternative prediction methods, whilst being comparatively cheap to run in terms of computational time. Furthermore, the effect of the domain size on the potential flow around the airfoil may be investigated cheaply at this Reynolds number. The results of studies at $Re_c = 10^4$ can then be used to plan simulations at higher Reynolds numbers.

3.2 Domain size selection

Before simulations can be performed with confidence, an appropriate size for the computational domain must be determined. The computational domain must be sufficiently large not to constrain the potential flow around the airfoil, whilst not being so large as to incur unnecessary computational expense.

Three comparatively cheap 2D airfoil simulations were run on three different grids, denoted D1, D2 and D3, in order to quantify the effect of domain size. The simulations were all run at zero degrees incidence, $Re_c = 10^4, M = 0.6$, and the size of the computational domain was varied. Details of the domains

---

[1] See also Jones *et al.* (2006)

Grid	D1	D2	D3
R	3.3	5.3	7.95
W	5	5	8
N_ξ	1181	1181	2361
N_η	245	259	274
N_{foil}	201	201	201
N_{wake}	982	982	2162

Table 3.1: Domain and grid dimensions for cases D1-D3.

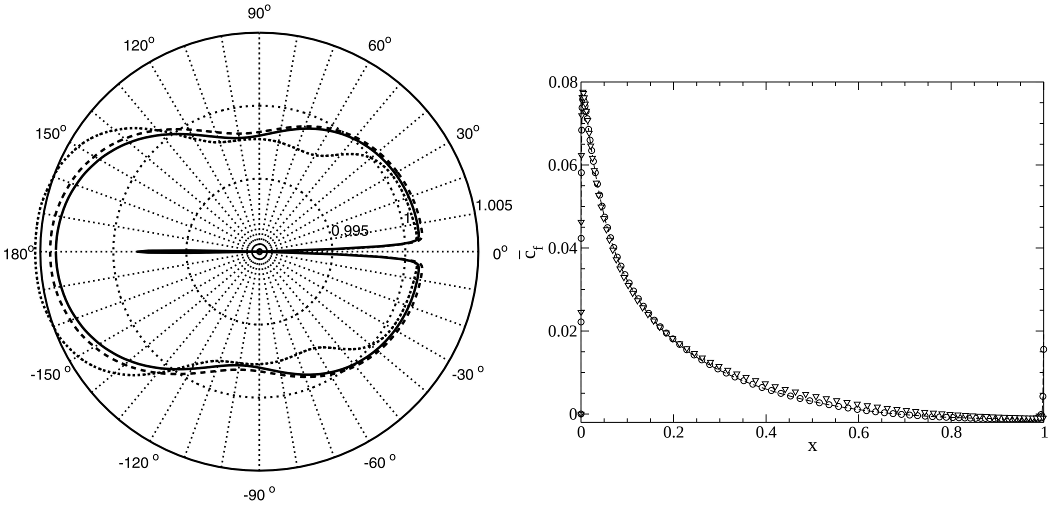

Figure 3.1: Azimuthal variation of $\frac{p}{p_\infty}$ at 3 chords radius from the trailing, over the range 0.99 to 1.005 for grids D1 (···), D2 (−−) and D3 (—)) (left) and time-averaged c_f distributions for grids D1 (▽), D2 (−−) and D3 (○) (right).

and grids used are given in table 3.1. The larger domain sizes were generated by adding grid-points to grid D1, whilst leaving original grid-points unchanged. Flowfield statistics were taken for 60 time units upon achieving a periodic state of behaviour.

The azimuthal variation of mean pressure at a fixed radius of 3 chords about the trailing edge is plotted in figure 4.8 (left). It can be seen that whilst there is marked difference between grid D1 and D2, there is little difference in pressure distribution between grids D2 and D3. Plotting time-averaged skin-friction ($\overline{c_f}$) distributions yields a similar result (figure 4.8, right). Any further increase in domain size will incur even smaller changes.

It appears then that a minimum radius of 5.3 chords is adequate to capture the potential flow of the test-case with the current code. Therefore all simulations at $Re_c = 10^4$ are run using grid D2 unless stated otherwise. For reference purposes the resolution of grid D2 at specific control points is given in table 3.2. Details of grids used at higher Reynolds number are given in chapter 4.

	x	y	$\Delta\xi$	$\Delta\eta$
Stagnation point	0	0	1.5×10^{-3}	3×10^{-4}
Trailing edge	1	0	1.75×10^{-3}	4.2×10^{-4}
Exit boundary	6	0	3.1×10^{-2}	1×10^{-3}
Exit boundary	6	0.2	3.1×10^{-2}	3.75×10^{-3}
Exit boundary	6	1	3.1×10^{-2}	2×10^{-2}
Exit/free stream boundary	6	5.3	3.1×10^{-2}	1.95×10^{-1}

Table 3.2: Grid resolution at selected control points for grid D2.

3.3 Direct numerical simulations

Having determined an appropriate computational domain size, simulations were run at $Re_c = 10^4$, zero-degrees incidence, whilst varying the Mach number. Simulations at five Mach numbers were performed; $M = 0.2$, 0.3, 0.4, 0.6, 0.7 and 0.8, although where results are presented not all simulations may be shown for the sake of clarity. The simulations were progressed until transient effects were deemed to have passed, and statistical data capture was performed for a minimum of 40 non-dimensional time-units.

3.3.1 Time dependent behaviour

At $Re_c = 10^4$ an unsteady wake is observed at all Mach numbers; downstream of the airfoil trailing edge the wake becomes unstable and rolls up to form vortices, characteristic of a von-Kármán instability. Both the size and intensity (in terms of peak vorticity magnitude) of the wake vortices increases with Mach number, and the onset of vortex shedding moves upstream toward the trailing edge (figure 3.2). As a result of the wake unsteadiness, the airfoil experiences an oscillating lift-coefficient, with both amplitude and frequency varying with Mach number (figure 3.3, left). The magnitude of lift-coefficient oscillations increases with increasing Mach number, and the frequency decreases. Fourier transforms of the time dependent lift-coefficient are shown plotted against Strouhal number (figure 3.3, right), where the Strouhal number is defined as

$$St = \frac{f(2\delta^{*}{}_{\mathrm{te}})}{u}, \tag{3.1}$$

where f is the frequency of lift-coefficient oscillation, $\delta^{*}{}_{\mathrm{te}}$ is the displacement thickness at $x = 0.99$ (measured on one side of the airfoil) and u is the free-stream velocity. The Strouhal numbers associated with the dominant oscillatory mode collapse to $St = 0.2$ ($\pm13\%$) in all cases.

In comparison to the similar study by Bouhadji & Braza (2003), several differences may be noted. Firstly the amplitude of C_L oscillations is much lower in the

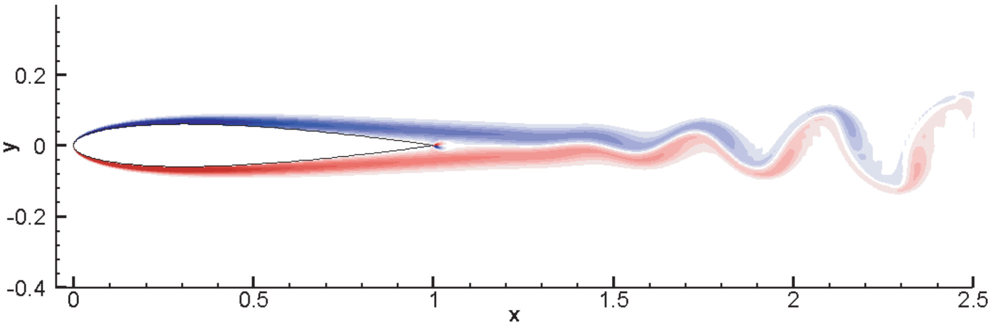

a) $M = 0.2$

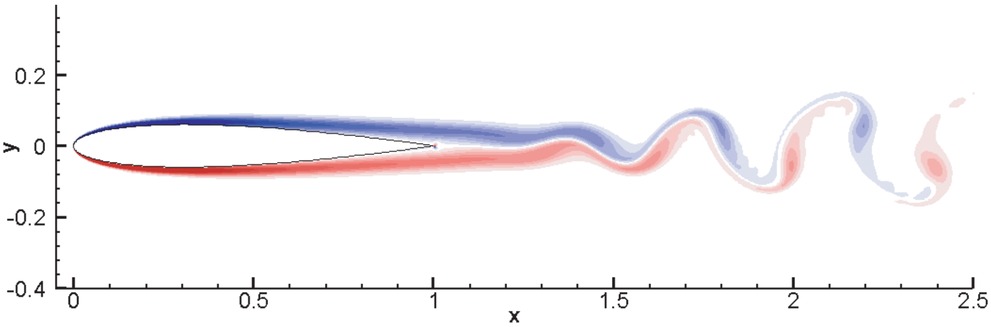

b) $M = 0.4$

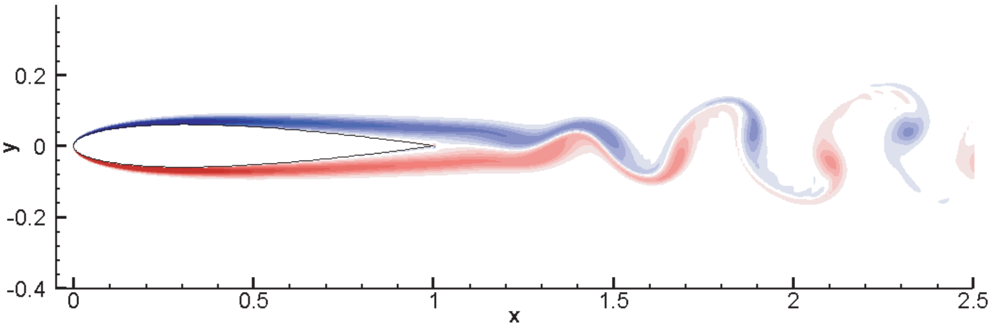

c) $M = 0.6$

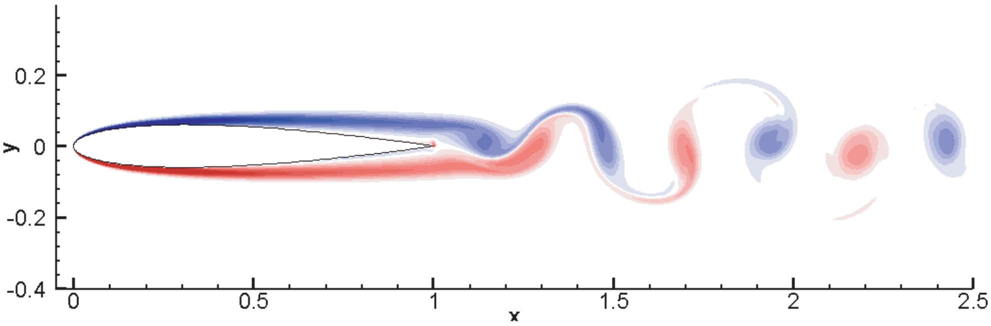

d) $M = 0.8$

Figure 3.2: Iso-contours of vorticity, using 20 levels over the range ±50, for the case $Re_c = 10^4$, $\alpha = 0^\circ$ at Mach numbers indicated.

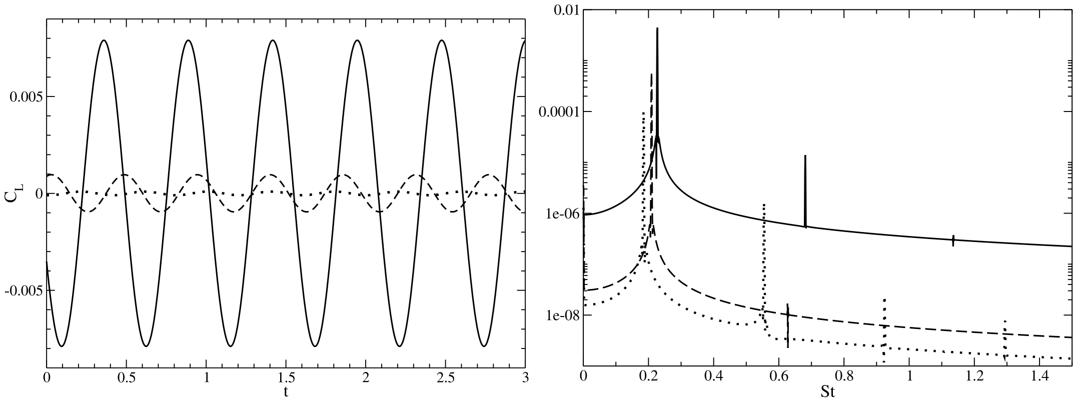

Figure 3.3: Time dependent C_L (left) and direct Fourier transform of time dependent C_L (right) at $Re_c = 10 \times 10^4$, showing Mach numbers 0.2 (···), 0.6 (– –) and 0.8 (—).

current study, for some Mach numbers appearing as much as four times lower. Secondly, Bouhadji & Braza report a secondary low frequency mode occurring in the Mach number range 0.75-0.85 which was not observed in the current study (but which was observed at higher Reynolds numbers; see section 4). Finally, Bouhadji & Braza report a steady, small non-zero (6×10^{-4}) lift-coefficient at $M = 0.2$ whereas the current study observed a lift-coefficient oscillating about zero with peak-to-peak amplitude approximately 1×10^{-4}. It is likely however that the differences observed are due to the much finer grids, especially in the wake, which were used in the current study. The discrepancies between the studies do however raise the question as to whether the vortex shedding observed at $M = 0.2$ is physical, or whether it is caused by an unphysical mechanism, such as a feedback loop caused by fluid structures striking the outflow boundary. This issue is addressed in section 3.4

The pressure drag coefficient (C_{DP}) increases with increasing Mach number (figure 3.4, right), whilst the skin-friction drag coefficientC_{DF} decreases slightly. Drag coefficients predicted by XFoil (Drela & Giles, 1987) vary by as much as 9.5% from the DNS results, although similar Mach number trends are predicted for both drag coefficients.

3.3.2 Time-averaged results

Time-averaged pressure-coefficient distributions (figure 3.5, left) indicate that the location of minimum C_P moves downstream with increasing Mach number. Also, the minimum C_P increases in magnitude with Mach number. When compared to results generated using XFoil (Drela & Giles, 1987) there appears to be a discrepancy regarding the location and magnitude of minimum C_P. XFoil does not appear to predict the movement downstream of the minimum C_P with

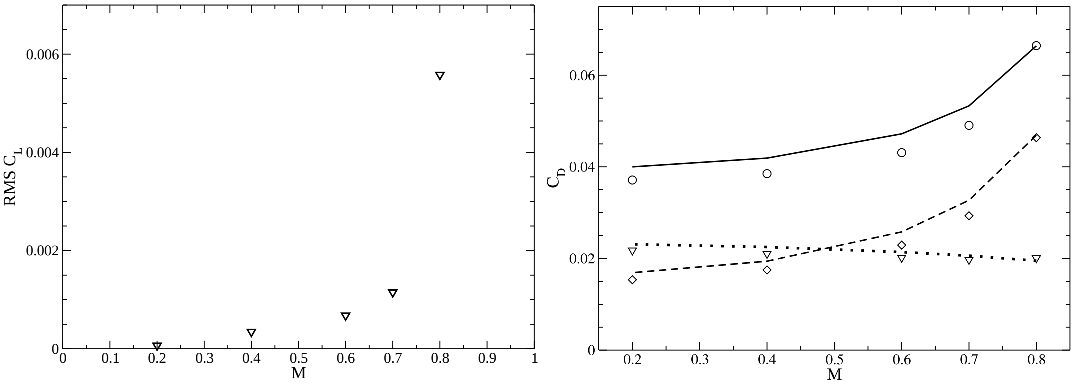

Figure 3.4: Variation of RMS lift-coefficient with Mach number (left), variation of time-averaged C_{DP} (◇), C_{Df} (▽) and total drag (○) with Mach number (right), with lines illustrating XFoil predictions.

increasing Mach number, and also predicts a minimum C_P that is overly large in magnitude.

Skin friction coefficient distributions (figure 3.5, right) indicate that at all Mach numbers the airfoil boundary layer stays attached until downstream of the point of maximum thickness. Towards the trailing edge the boundary layer separates and a region of recirculation is present; the separation point moves upstream with increasing Mach number. The region of recirculation extends downstream of the airfoil into the wake.

The momentum thickness distribution (figure 3.6, left) varies little with Mach number, however the displacement thickness (figure 3.6, right) downstream of separation clearly increases with Mach number. Similar trends are predicted by XFoil.

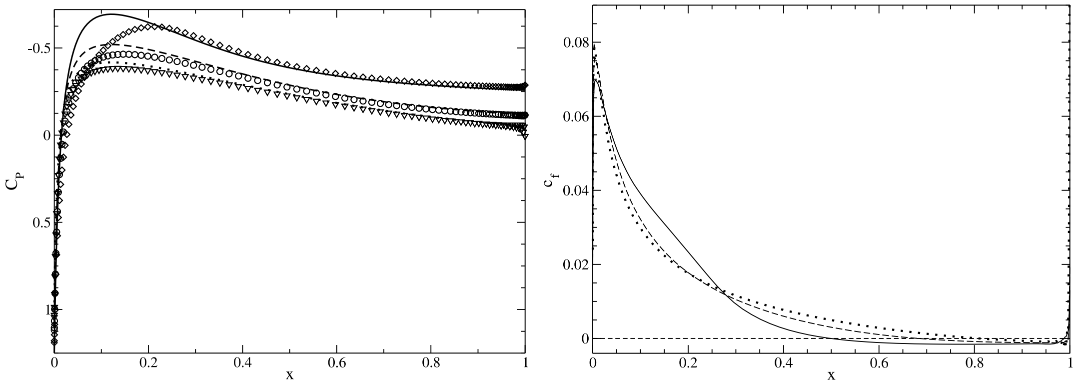

Figure 3.5: Time-averaged C_P at Mach numbers 0.2 (▽), 0.6 (○) and 0.8 (◇) with lines illustrating showing XFoil predictions (left), and time-averaged C_f (right) at Mach numbers 0.2 (···), 0.6 (– –) and 0.8 (—).

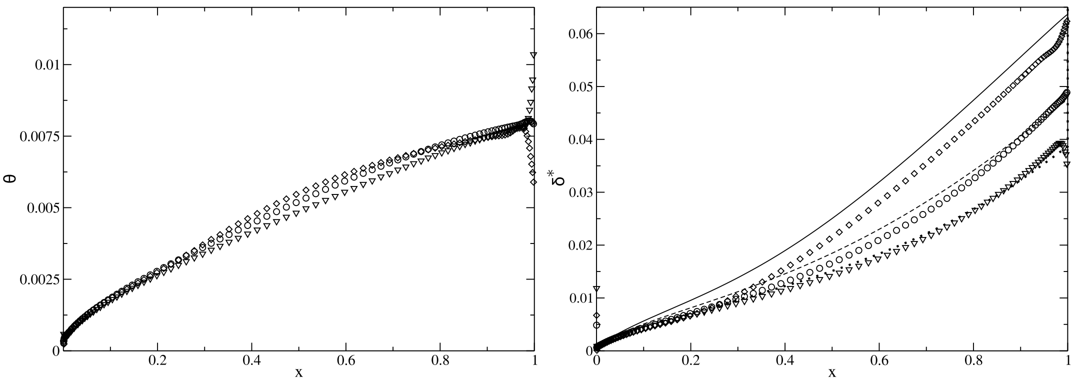

Figure 3.6: Time-averaged θ (left) and δ^* (right) distributions at Mach numbers 0.2 ($\triangledown$), 0.6 ($\circ$) and 0.8 ($\diamond$), with lines illustrating showing XFoil predictions.

3.4 An investigation of the vortex shedding behaviour at $M = 0.2$

Since vortex shedding was observed at $M = 0.2$ in the current study, but not in the study of Bouhadji & Braza (2003), it is pertinent to determine whether the vortex shedding is physical. In order to do this the development of wake unsteadiness is monitored from a simulation with a symmetry condition applied across the wake-cut, and then stability analysis of the airfoil wake is performed.

3.4.1 Onset of wake instability

Using grid D2 (defined in section 4.3.2), with wake length $W = 5$ airfoil chords, a simulation was run at Mach 0.2 with the additional boundary condition of $v = 0$ applied on the wake dividing line in order to obtain a symmetric solution. Upon attaining a steady solution, the boundary condition was removed and the simulation continued. Wake unsteadiness was then allowed to develop naturally and, by measuring time dependent pressure at several locations in the wake, the onset of the wake instability was investigated. Unfortunately a fully symmetric solution could not be achieved, and a steady lift-coefficient of magnitude approximately 1×10^{-6} was observed. The grid used was subsequently found to be asymmetric. The average difference between grid-point locations on opposite sides of the airfoil is 7×10^{-6} in the x direction and 1×10^{-6} in the y direction, the asymmetry presumably being incurred during the grid generation process. Despite the presence of a small non-zero lift-coefficient, the simulation appeared steady and near-symmetric, as shown by vorticity contours in figure 3.7. Upon removal of the $v = 0$ condition along the wake centre line the wake became unsteady, in contrast to the study of Bouhadji & Braza (2003) where a steady wake was observed.

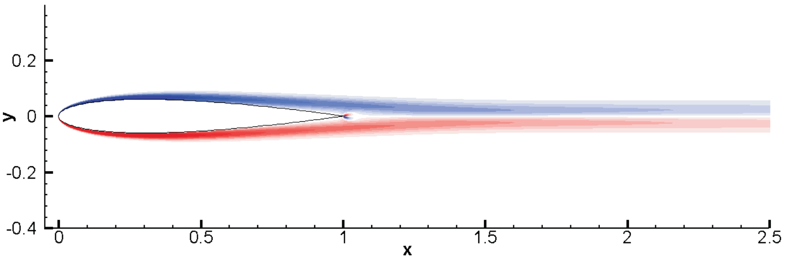

Figure 3.7: Iso-contours of vorticity for the case $Re_c = 10^4$, $M = 0.2$, $\alpha = 0°$, with $v = 0$ condition applied to the wake dividing line, using 20 levels over the range ±50.

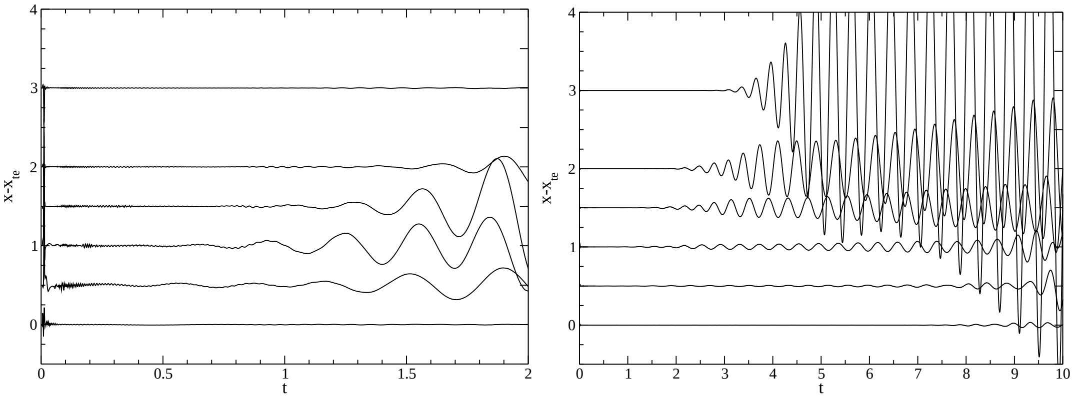

Figure 3.8: Derivative of time dependent pressure with respect to time, after the symmetry condition was removed at t=0. Distance of the measurement location from the trailing edge is given on the left hand x-axis. Left hand image illustrates the behaviour immediately after the symmetry condition was released, right hand image illustrates the quasi-linear behaviour over a longer period of time

The behaviour immediately after removing the symmetry condition is monitored by recording time-dependent pressure at a number of streamwise locations in the wake. Figure 3.8 illustrates the time-dependent behaviour of dp/dt with x-location, in the form of an x/t plot. Immediately after the symmetry condition is removed, pressure oscillations are observed to initiate and grow in amplitude at locations 0.5 and 1 chord downstream of the trailing edge (figure 3.8, left). The very sudden localised onset and growth of this oscillation suggests that the wake is absolutely unstable at some location in the region $0 - 1$ chords downstream of the trailing edge, since the oscillation appears to be growing temporally and does not appear to originate from an upstream location. After a short period of time pressure oscillations are observed at all points in the wake downstream of the trailing edge, and the amplitude of oscillation appears to increase with downstream distance from the trailing edge (figure 3.9, right). The fact that the amplitude of oscillation increases with downstream location suggests that the wake may also be convectively unstable. Over time the wake instability ultimately leads to roll-up and vortex shedding, at which point the pressure response increases dramatically in amplitude and becomes non-linear, illustrated in figure 3.9 for the measurement location 1 chord downstream of the trailing edge.

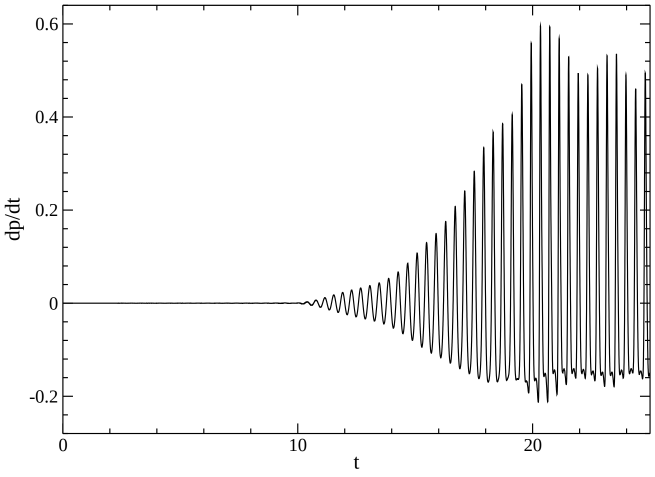

Figure 3.9: Derivative of time dependent pressure with respect to time at 1 chord downstream of the trailing edge.

The disturbance amplitude does not appear to follow a pure exponential envelope, as would be expected for linear disturbance growth (Hannemann & Oertel, 1989). However, if the wake unsteadiness was caused by a feedback loop initiated by unphysical reflections from the downstream exit boundary propagating to some point of receptivity in the wake, this would be likely to cause periodic behaviour in time dependent quantities. Fluctuations would be apparent with period corresponding to the time taken for a fluid structure to convect from the point of receptivity to the exit boundary, plus the time taken for a pressure wave to propagate from the exit boundary to the point of receptivity. There is no evidence for this kind of behaviour in the current simulation.

3.4.2 Cusp-map analysis of the airfoil wake

The time-averaged flowfield, instantaneous flowfield and the symmetrised flowfield extracted from the case at $Re_c = 10^4$, $M = 0.2$ and $\alpha = 0°$ (figure 3.10) have been analysed using the Orr-Sommerfeld solver in conjunction with the cusp-map method (see section 2.4.5). The complex α plane was swept with a minimum resolution of $\Delta\alpha_r = \Delta\alpha_i = 2$. The corresponding resolution in the complex ω plane is much higher in the vicinity of a branch-point, since $\frac{\partial\omega}{\partial\alpha} \approx 0$. Branch point singularities associated with zero group-velocity instability waves have been tracked, traversing the wake over the region 0.01-0.5 chords downstream of the airfoil trailing edge. Imaginary parts of the complex frequency associated with $c_g = 0$ are plotted in figure 3.11 (left). For all cases, at 0.01

chords downstream of the trailing edge the $c_g = 0$ wave is growing temporally, i.e. $\omega_i > 0$, hence the flow is absolutely unstable. The temporal growth rate decreases with increasing x, and at approximately 0.3 chords downstream of the trailing edge $\omega_i = 0$, hence the flow transitions from absolutely unstable to convectively unstable. As x increases to 0.5 chords downstream of the trailing edge ω_i decreases further. Results for the instantaneous and time-averaged flowfields appear similar, however the symmetrised flowfield exhibits a greater tendency toward absolute instability (i.e. ω_{i} is greater).

There is clear evidence then, of absolute instability in the near wake region for these flow parameters. What is surprising is that absolute instability can be observed not only in the time-averaged and symmetrised flow fields, but also in the instantaneous flowfield. This is surprising because, although the near-wake region appears similar over the region $0.01 - 0.5$ chords downstream of the airfoil trailing edge for all three cases (figure 3.10), by the definition of absolute instability one would expect exponential temporal growth of normal-mode perturbations in any region of absolute instability. This is not the case in the fully-developed simulation, where limit-cycle behaviour is observed. It is possible that whilst absolute instability may be observed in the instantaneous flowfield, exponential temporal disturbance growth does not occur due to the presence of nonparallel effects, i.e. the global undulation of the wake. Instead, the near-wake reaches a limit-cycle oscillatory behaviour. It should also be noted that the final stages of vortex roll-up occur significantly downstream of the transition from absolute to convective instability. This suggests that the final stages of vortex roll-up are caused by convective amplification of wake perturbations generated by a region of absolute instability.

Real parts of the complex frequency associated with $c_g = 0$ are plotted in figure 3.11 (right). A simple criterion for predicting the saturation frequency of wake shedding is Koch's criterion (Koch, 1985), which states that the final shedding frequency may be approximated as ω_r associated with the $c_g = 0$ wave at the location where transition from absolute to convective behavior occurs. The corresponding value of ω_r computed from linear stability analysis of the symmetrised wake is 16.6, corresponding to frequency $f = 2.64$. The frequency of vortex shedding in the fully developed case is $f = 2.52$, providing approximate agreement.

3.4.3 Direct numerical simulation with forcing terms

A simulation has been performed using forcing terms to maintain the initial condition, in order to determine the response of the symmetrised flowfield to

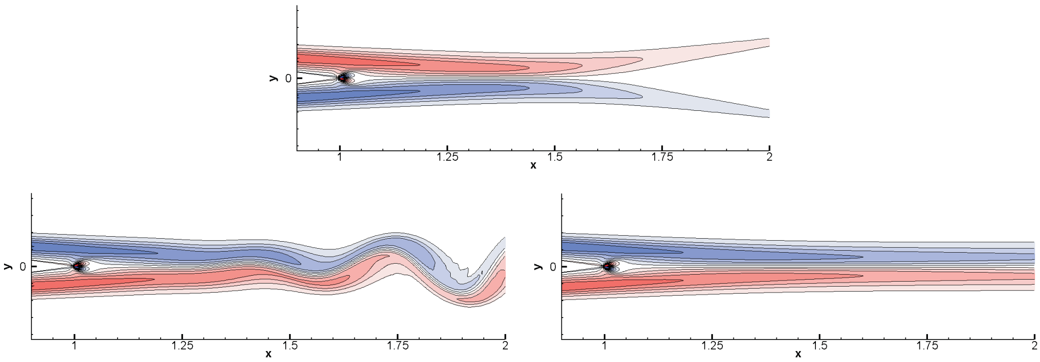

Figure 3.10: Iso-contours of vorticity using 20 levels over the range ±50 for the time-averaged flowfield (top), instantaneous flowfield (bottom-left) and symmetrised flowfield (bottom-right) of the $Re_c = 10^4$, $M = 0.2$, $\alpha = 0°$.

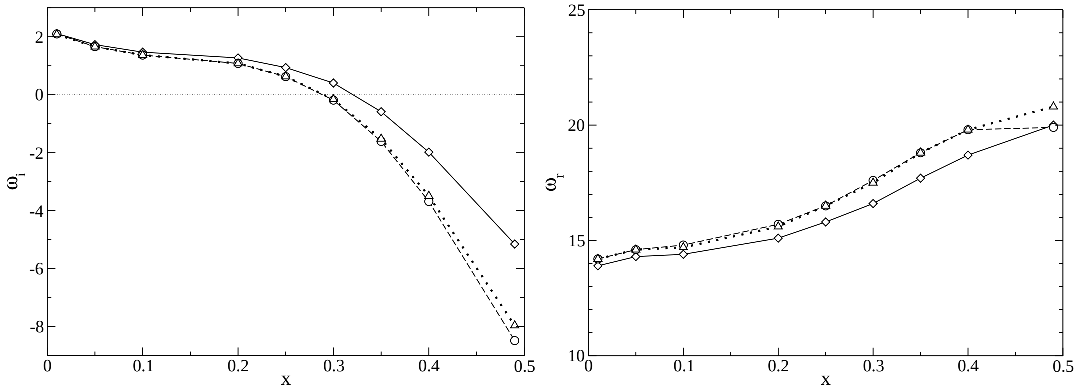

Figure 3.11: Variation with x of ω_i (left) and ω_r (right) associated with $c_g = 0$, for the case $Re_c = 10^4$, $M = 0.2$, $\alpha = 0°$, with x-axis showing distance downstream from the airfoil trailing edge, showing results for the time-averaged flowfield (○ – –○), instantaneous flowfield (△ · · · △) and the flowfield with symmetry condition applied (◇——◇).

low-amplitude perturbations. As well as confirming the linear stability analysis results, this will validate the use of numerical simulations with forcing terms as a tool to detect absolute instability.

The initial condition is specified as the symmetrised flowfield presented in 3.4.1. If the simulation were to be initialised in this fashion and progressed in time, the flowfield would relax to the vortex shedding observed in the original simulation. Instead, forcing terms are added to the governing equations, in order to maintain the initial condition as the simulation is progressed. Assuming there is no change to the flowfield, the initial condition will be maintained. The behaviour of small perturbations on the initial condition (i.e. the symmetrised flowfield) can then be determined. The process is performed as follows.

At initialisation, time $t = 0$, temporal derivatives of the conservative variables are calculated and stored. The simulation is then progressed in time as normal, except wherever a temporal derivative is computed, the temporal derivative at

$t = 0$ is subtracted, i.e.

$$\frac{dq}{dt} = \mathbf{RHS} - \frac{dq}{dt}_{t=0}. \tag{3.2}$$

Where boundary conditions are applied, additional temporal derivatives are computed that must be treated in the same fashion. The result is that, assuming there is no change or perturbation to the flowfield, the initial condition can be maintained as a reference state, upon which the behaviour of small perturbations can be investigated.

The initial condition is specified as the time-averaged flowfield of the two-dimensional simulation at $Re_c = 10^4$, $M = 0.2$, $\alpha = 0°$ with the symmetry condition applied in the wake, illustrated in figure 3.10 (bottom-right). A region of 3×3 grid-points about the location $(x, y) = (1.00, 0.05)$, corresponding to a location within the upper surface boundary layer at the trailing edge, is subject to an increment of 1×10^{-8} in u, v and ρ. This effectively introduces a disturbance with a sharp-edged spatial distribution, which will excite a range of frequencies at low amplitude. No further perturbations are introduced, and the response of the flow is monitored as the simulation is progressed. If the flow were only convectively unstable, the initial perturbation would be expected to convect downstream growing in amplitude, ultimately leaving the flow over the airfoil unperturbed. If the flow were absolutely unstable, the initial perturbation would be expected to grow exponentially in time at some location until saturation or the onset of some secondary behaviour, ultimately affecting the entire flow-field.

The response of the flowfield is monitored in two ways; by recording the time-dependent pressure at several x-locations within the wake, and by analysing contour plots of flowfield quantities. If post-processed quantities were plotted for the instantaneous flowfield, the perturbation and its subsequent response would not be visible. This is because variations in the mean flowfield are much larger in magnitude than those caused by the perturbation. In order to better visualise perturbations to the mean field, iso-contours of the perturbation z-vorticity rate are plotted, defined as $\omega'_z = \omega_{z t=t_1} - \omega_{z t=0}$, where $\omega_{z t=t_1}$ is the z-vorticity at time t_1 and $\omega_{z t=0}$ is the z-vorticity at time $t = 0$.

Figure 3.12 shows time series of dp/dt taken at several streamwise locations within the airfoil wake. Time $t = 0$ is the initialisation time, at which the perturbation was introduced. Signals are plotted at an arbitrary amplitude, however all signals were scaled by the same factor. Considering first the interval $0 < t < 2$ (figure 3.12, left), the pressure is observed almost immediately to begin to fluctuate at 0.5 chords downstream of the trailing edge. The amplitude of unsteadiness increases at 1 chord downstream of the trailing edge, however the onset of unsteadiness occurs at a later time. When plotted for the interval $0 < t < 16$ (figure 3.12, right) the pressure fluctuations are observed to increase in amplitude temporally, in an exponential fashion, at all locations downstream of the trailing edge. The amplitude of pressure fluctuations also increases with distance from the trailing edge. No unsteadiness is observed in the boundary layer directly at the trailing edge when plotted at these levels. The behaviour observed in figure 3.12 (left) appears strikingly similar to that observed in figure 3.9, where the onset of unsteadiness from the symmetrised wake was observed. Iso-contours of ω_z' (figure 3.13) reveal that these fluctuations are associated with a vorticity perturbation that is oscillatory in x and symmetric about the wake centre-line. The associated u-velocity perturbation would be antisymmetric about the wake centre-line.

This behaviour, in conjunction with the results of both section 3.4.1 and section 3.4.2, confirms that a region of absolute instability is present in the region $0 - 0.5$ chords downstream of the trailing edge. It appears that unsteadiness is generated in the region $0 - 0.5$ chords downstream of the trailing edge via absolute instability. Downstream of this location the perturbations are subsequently convectively amplified, ultimately leading to the vortex shedding behaviour observed. Furthermore, the method of performing forced Navier–Stokes simulations to determine the flowfield response to small perturbations has been proven capable of detecting absolute instability.

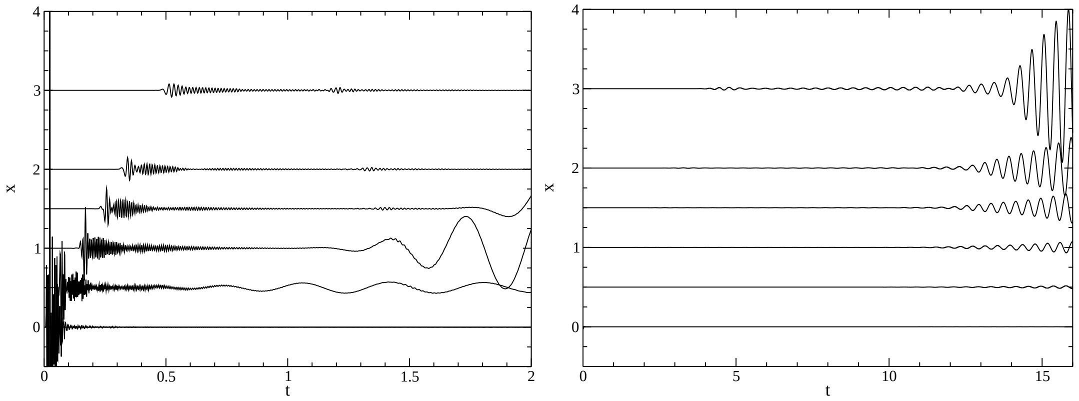

Figure 3.12: Time histories of $\frac{dp}{dt}$, with streamwise distance from the airfoil trailing edge indicated on the vertical axis, for time $0 < t < 2$ (left) and $0 < t < 16$ (right).

3.5 Summary

At $Re_c = 10^4$ the flow is dominated by vortex shedding from an unstable wake. An investigation into the effect of computational domain size suggests that a domain radius of 5.3 airfoil chords is sufficient to capture the potential flow

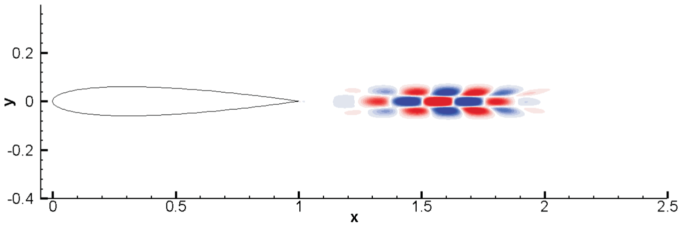

Figure 3.13: Iso-contours of ω_z' for the simulation with forcing terms at $M = 0.2$, using 20 levels over the range $\pm 2 \times 10^{-8}$.

about the airfoil. By forming a Strouhal number St, based on trailing edge displacement thickness, frequencies have been found to collapse.

The nature of the wake unsteadiness has been investigated via both simulation and stability analysis. Unsteadiness appears to develop naturally as the result of a combination of absolutely and convectively unstable regions in the airfoil wake; there is no evidence that boundary reflections are responsible for the unsteadiness observed. The numerical method has proven capable of capturing weakly unstable flows that may not be evident in simulations where artificial viscosity or damping is introduced. Both the cusp-map method and numerical simulations with forcing have proven to be able to detect regions of absolute instability.

Chapter 4

Two dimensional simulations at Reynolds number 50,000[1]

4.1 Introduction

Two-dimensional simulations have been performed of the flow around an airfoil at $Re_c = 5 \times 10^4$. At zero degrees incidence and low Mach number the flow is found to be qualitatively similar to that observed at $Re_c = 10^4$, however as the Mach number is increased a large-amplitude, low-frequency oscillation develops.

A grid study is performed at incidence $\alpha = 5°$ in order to ensure that the flow is fully resolved. When the grid resolution is considered in terms of wall units, using skin-friction predictions generated by XFoil (Drela & Giles, 1987), the final grid appears suitable for use with three-dimensional simulations with turbulence. A series of two-dimensional simulations at incidences over the range $\alpha = 3° - 8.5°$ are then performed, with grids generated on similar principles to that for the $\alpha = 5°$ case. The effect of incidence upon both the physics of the flow around the airfoil and the aerodynamic performance of the airfoil is studied.

4.2 Simulations at zero degrees incidence

4.2.1 Grid parameters

Two-dimensional simulations at incidence $\alpha = 0°$ were performed upon a grid generated by increasing the resolution of grid D2 specified in section 4.3.2, denoted grid G0. Important parameters for grid G0 are given in table 4.1. Simulations at zero degrees incidence were run at five Mach numbers in the range $M = 0.4 - 0.8$.

---

[1] See also Jones *et al.* (2006)

N_ξ	2001
N_ξ airfoil	541
N_ξ wake	741
N_η	430
N_{total}	305879
Wake length - W	5
Radius - R	5.3
Buffer length	9,465
Buffer points	31
Total domain length	12.2
Total domain height	10.6

Table 4.1: Grid parameters for grid G0.

4.2.2 Time dependent behaviour

At zero degrees incidence and $Re_c = 5 \times 10^4$ the lift-coefficient oscillates about zero at all Mach numbers in the range $0.4 \leq M \leq 0.8$. At $M = 0.4$, the lift-coefficient is initially subject to a large amplitude fluctuation (figure 4.1, left), presumably due to transient effects of the initialisation, that subsequently decays to zero leaving only a higher frequency mode present (figure 4.1 left, insert). In contrast to the $Re_c = 10^4$ cases, in the range $0.5 \leq M \leq 0.8$ a secondary low frequency, high amplitude mode is present (figure 4.1, right). Vorticity contours at $M = 0.4$ (figure 4.2) indicate that the higher frequency mode of oscillation is caused by the presence of an unsteady wake with vortex shedding in a similar fashion to the $Re_c = 10^4$ cases. When the shedding frequency is non-dimensionalised in the same manner as for the $Re_c = 10^4$ cases, the Strouhal number is found to collapse to a similar value of approximately $St = 0.22$. In contrast, the low frequency mode of oscillation is up to an order of magnitude larger in amplitude than oscillations associated with vortex shedding in the wake, and two orders of magnitude lower in frequency. Associated Strouhal numbers are in the range 0.004 - 0.008 based on the definition given in equation 3.1.

For all cases at zero-degrees incidence, upstream propagating pressure waves are generated at the airfoil trailing edge (figure 4.3). At $M = 0.4$ the trailing edge noise appears periodic and symmetric, whereas at $M = 0.8$ neither the trailing edge noise nor the vortex shedding in the wake are periodic. Acoustic scattering was also observed at $Re_c = 10^4$, albeit at very low amplitude. The increased amplitude at $Re_c = 5 \times 10^4$ can be attributed to closer proximity of the wake unsteadiness to the airfoil trailing edge.

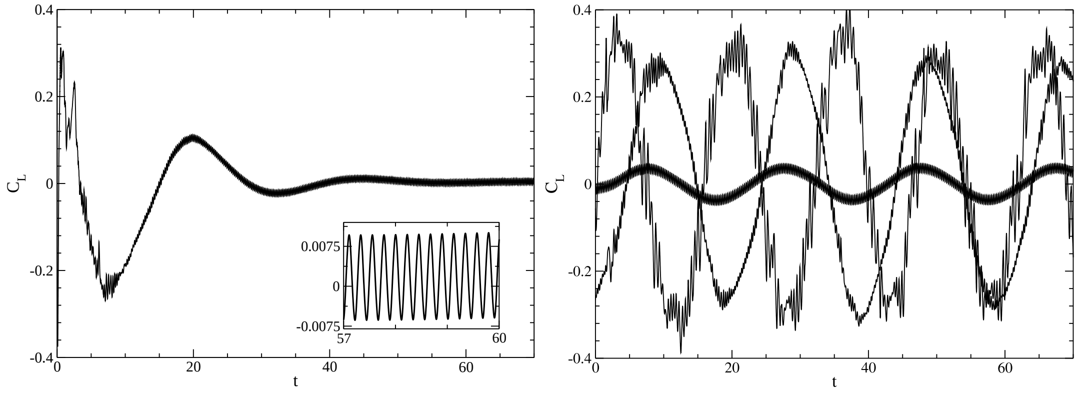

Figure 4.1: Time dependent C_L at $Re_c = 5 \times 10^4$, $\alpha = 0°$, showing the high frequency mode at $M = 0.4$ (left), and both high and low frequency response for $M = 0.5 - 0.8$ (right), where the Mach number increases with amplitude.

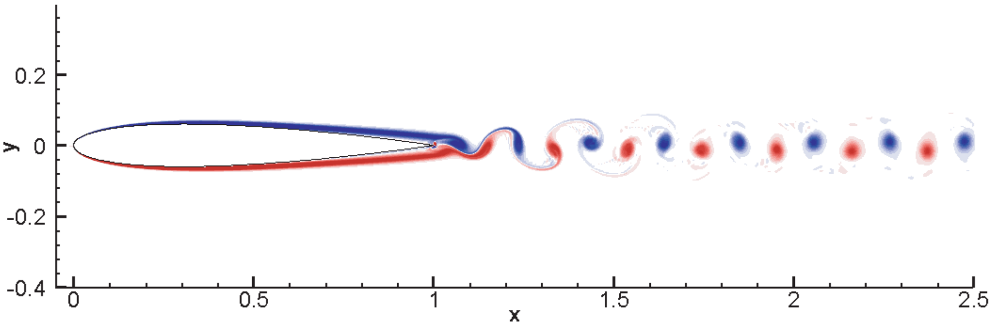

Figure 4.2: Iso-contours of z-vorticity using 20 levels over the range ±50, at $Re_c = 5 \times 10^4$, $M = 0.4$, $\alpha = 0°$.

4.2.3 Analysis of the low frequency (flapping) oscillation

Analysis of iso-contours of $|\nabla \rho|$ and u-velocity (figure 4.4) shows that the low frequency mode of oscillation is caused by asymmetric boundary layer separation, whereby the boundary layer over one airfoil surface appears stalled, whilst the boundary layer on the opposing surface is fully attached. The airfoil boundary layers periodically switch between stalled and unstalled states, and the behaviour is accompanied by local acceleration and deceleration of the flow. By cross referencing animated images with instantaneous images taken at known points of the low frequency cycle, a more detailed description is possible. Boundary layer behaviour and local velocity at key points of the low frequency cycle are shown in figure 4.4a-4.4d for the $M = 0.8$ case. Although some numerical oscillation is present due to the high intensity pressure waves, the strong separation at this Mach number makes the flapping easier to observe than at lower Mach numbers. A summary of behaviour throughout the cycle follows.

For the purposes of this study, the start of the low frequency cycle will be

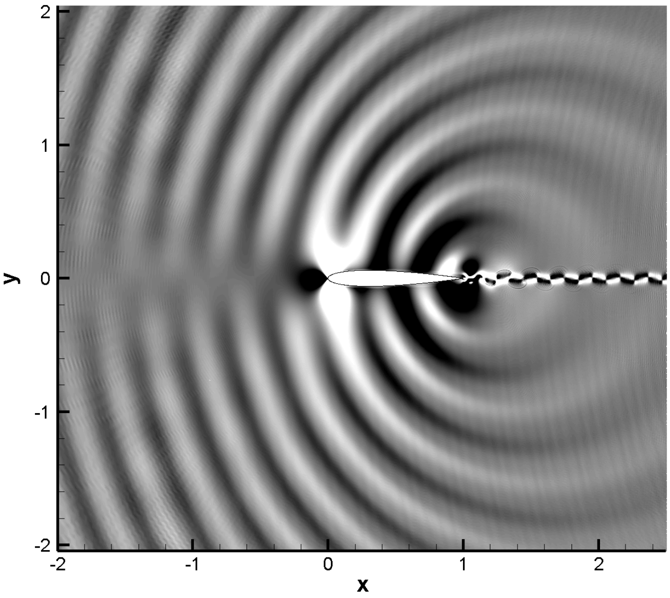

Figure 4.3: Iso-contours $\nabla.\mathbf{U}$ using 20 levels over the range ± 0.05, at $Re_c = 5 \times 10^4$, $M = 0.4$ and $\alpha = 0°$.

defined as the point where the lift-coefficient is at a maximum. At this point in the cycle, with phase angle defined as $\phi = 0°$, the velocity over the upper surface is at a maximum, and the boundary layer separates at a location close to the trailing edge. As the cycle progresses, the separation point slowly moves upstream. Meanwhile the boundary layer on the lower surface is separated but slowly reattaching. At around $\phi = 90°$ the upper boundary layer is fully separated. Vortical structures are formed within the boundary layer and convect downstream, generating upstream travelling pressure waves as they pass over the trailing edge. At this point the lower boundary layer is fully attached. The velocity over the upper surface is decreasing, and the velocity over the lower surface is increasing, thus $\phi = 90°$ marks a median (i.e. approximately zero) point in the lift-coefficient cycle, with the lift-coefficient decreasing. The structures formed in the upper boundary layer ultimately convect downstream, and no more structures are produced until the next cycle. After structures in the upper boundary layer have convected downstream, the upper boundary layer slowly begins to reattach. At $\phi = 180°$ the velocity over the lower surface is at a maximum, and the lower boundary layer slowly begins to separate, starting at the trailing edge in the same manner as for the upper surface. The lift-coefficient is now at a minimum. Behaviour is the same as at $\phi = 0°$, but mirrored across the airfoil chord. At around $\phi = 270°$ the lower boundary layer is fully separated. Structures form in the lower surface boundary layer and convect downstream, as they did for the upper boundary layer at $\phi = 90°$. The velocity over the lower surface decreases, and velocity over the upper surface increases. The lift-coefficient is at a median point on the cycle (approximately zero) and is increasing. The structures formed in the lower boundary layer ultimately convect downstream, and the separated lower boundary layer starts to slowly reattach. The upper boundary layer is fully attached. Essentially the behaviour is the same as at $\phi = 90°$, but mirrored across the airfoil chord. Acoustic waves are produced at the airfoil trailing edge at all stages of the flapping cycle. In particular, when the separated boundary layer becomes unstable and structures are generated, strong acoustic waves are observed propagating away from the opposing airfoil surface.

Variation of flapping frequency and RMS amplitude of lift-coefficient with Mach number, for cases at $Re_c = 5 \times 10^4$, $\alpha = 0°$, are shown in figure 4.5. The amplitude of the low frequency oscillation rises dramatically with Mach number after the initial onset at $M = 0.5$, suggesting that the mode only occurs above a critical Mach number, and the amplitude saturates for $M > 0.7$. The frequency of the oscillation increases with increasing Mach number, and hence cannot be collapsed by forming a Strouhal number based on some measure of boundary layer thickness, since both boundary layer thickness and the frequency of oscillation increase with Mach number.

In order to further explore the onset of the low frequency mode, several simulations were run across the range $Re_c = 10^4 - 5 \times 10^4$ and Mach number range 0.4-0.8 in steps of 10^4 for Reynolds number and 0.1 for Mach number. Figure 4.6 summarises the results of these simulations, illustrating that for a constant Reynolds number the low frequency oscillation only occurs above a certain Mach number, and vice versa. In the present study, the low frequency oscillation was only found at $Re_c = 2 \times 10^4$ and above, whereas Bouhadji & Braza (2003) reported similar behaviour at $Re_c = 10^4$. Although the onset of the low frequency mode is Mach number dependent, it appears to be distinct from transonic buffet, where the presence of an oscillating attached shockwave (Lee, 1990) leads to low frequency oscillation of the lift-coefficient. In contrast, the low frequency mode observed here is present at subsonic Mach numbers where no local supersonic flow is present. The observation of acoustic waves at the trailing edge suggests that an acoustic feedback mechanism may be present, however animations at $M = 0.6$ and 0.8 display a marked difference in upstream wave velocities but only minimal variation in the period of the low frequency cycle. This appears to discount a simple (feedback) model based on downstream convection of vortices followed upstream acoustic waves, which would predict an increase in period with increasing Mach number. Instead, it is suggested

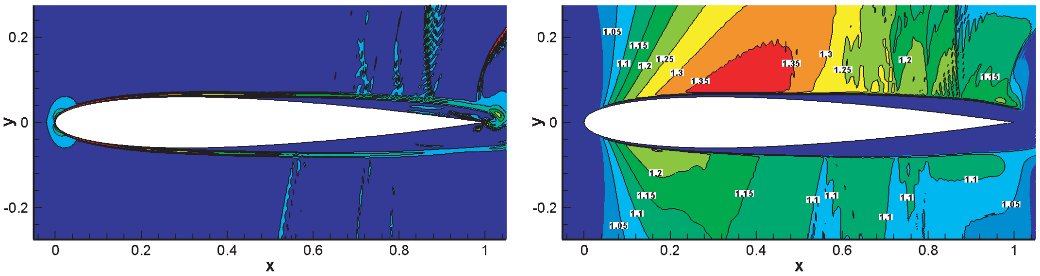

a) $\phi = 0$

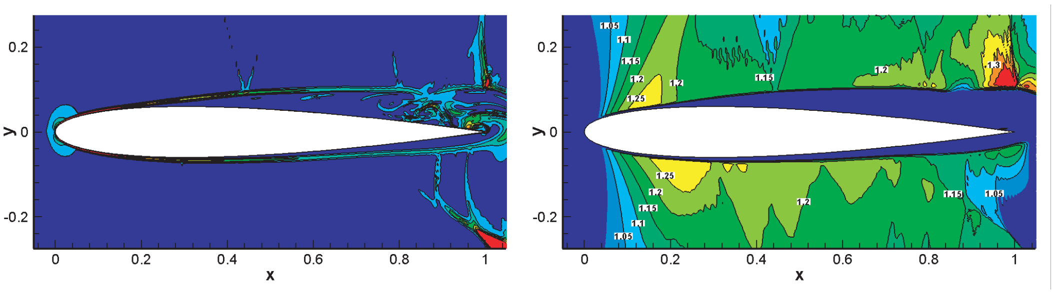

b) $\phi = \frac{\pi}{4}$

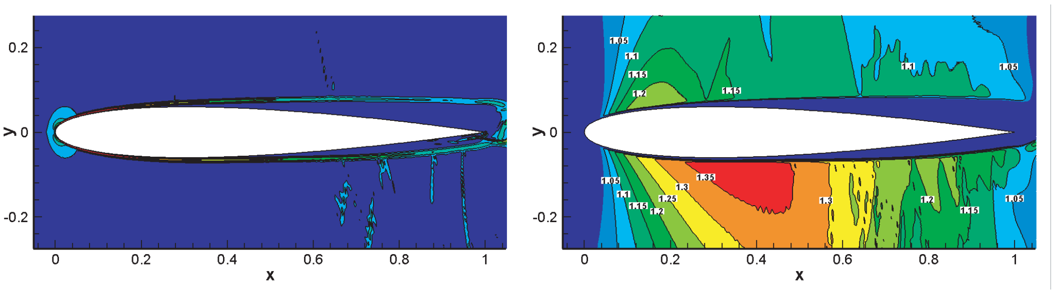

c) $\phi = \frac{\pi}{2}$

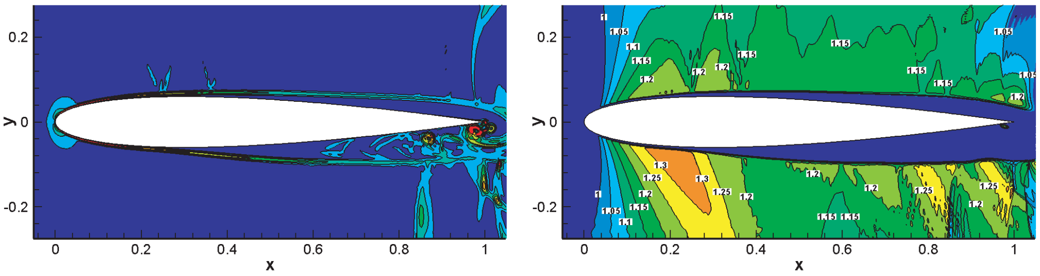

d) $\phi = \frac{3\pi}{4}$

Figure 4.4: Iso-contours of $|\nabla\rho|$ (left) using six levels in the range 3.5-20 and iso-contours of u-velocity (right) with levels marked, at $Re_c = 5 \times 10^4$, $M = 0.8$, $\alpha = 0°$. Four phases (ϕ) of the low-frequency oscillation are shown.

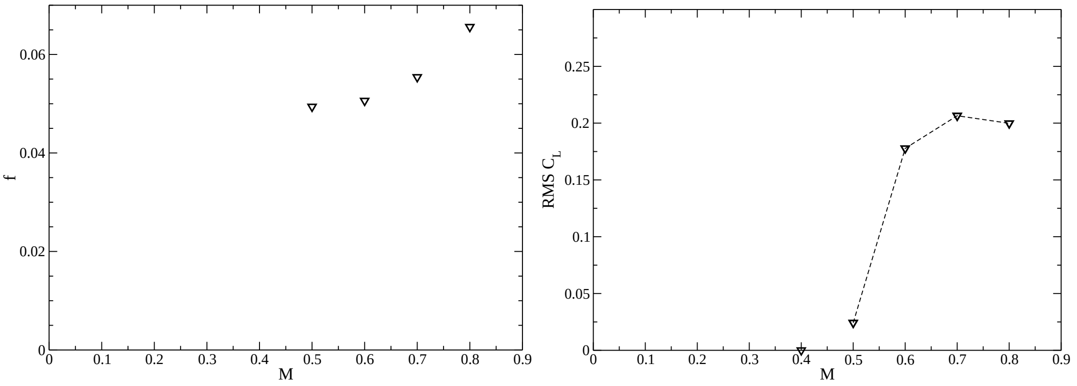

Figure 4.5: Frequency (left) and RMS (right) of C_L vs. Mach number at $Re_c = 5 \times 10^4$ and $\alpha = 0°$.

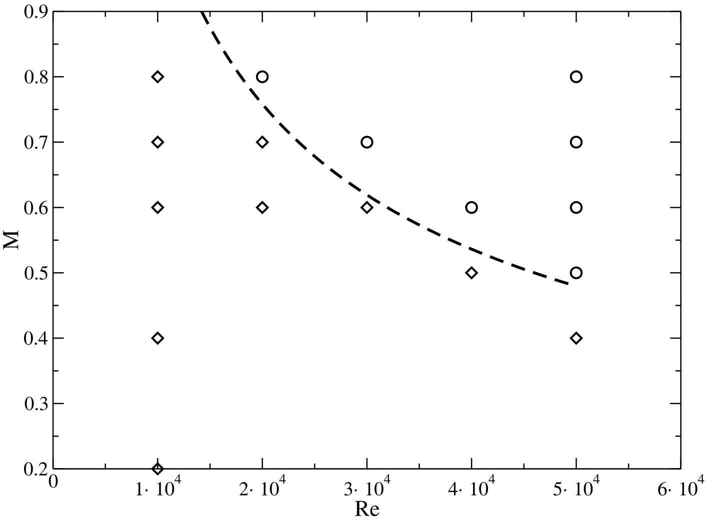

Figure 4.6: Occurrence of low frequency (flapping) mode with Reynolds number and Mach number. Points marked $\diamond$ indicate cases where flapping was not observed, points marked $\circ$ indicate cases where flapping was observed. The dashed line indicates a possible onset behaviour.

that a more complex viscous-acoustic mechanism is responsible for the observed behaviour.

4.3 Simulations at incidence

Preliminary studies of the flow around a NACA-0012 airfoil at $Re_c = 5 \times 10^4$ using XFoil (Drela & Giles, 1987) suggest that separated regions of flow are likely to occur over the upper airfoil surface. Simulations at these conditions represent an opportunity to capture numerically a laminar separation bubble on an airfoil at flight conditions similar to those of micro-air-vehicles. Although the goal is ultimately to perform three-dimensional simulations, two-dimensional simulations provide insight into mechanisms and behaviour which may persist or

Grid	G1	G2	G3
R	5.3	5.3	7.3
W	5	5	5
N_ξ	2001	2570	2570
N_η	440	440	692
N_{foil}	541	1066	1066
N_{wake}	1462	1506	1506

Table 4.2: Domain and grid dimensions for grid resolution investigation at $Re_c = 5 \times 10^4$, $\alpha = 5°$.

otherwise be relevant to the three-dimensional simulation case. It is also sensible to use a fully developed two-dimensional flowfield as the initial condition for a three-dimensional simulation, in order to reduce the time taken to achieve a statistically stationary state.

4.3.1 Grid resolution at $\alpha = 5°$

Resolution requirements for direct simulation of the flow around an airfoil at incidence are complex, since a variety of fluid phenomena are present and must be resolved. The iterative method of grid production (outlined in section 2.2.16) is particularly useful for the current case, since a priori grid requirements are not known for all regions. The iterative grid production process has been performed for the case at $Re_c = 5 \times 10^4$, $M = 0.4$, and $\alpha = 5°$, in two dimensions. Simulations were run on three grids in total, and sufficient data was recorded to compare the performance of each grid. The first grid, G1, was generated by estimating resolution requirements based on simulations at zero degrees incidence. Two further grids, denoted G2 and G3 were subsequently produced in order to improve the resolution of the simulation. Details of all grids are given in table 4.2.

Results from the two-dimensional simulation at $Re_c = 5 \times 10^4$, $M = 0.4$ and $\alpha = 5°$ are presented in full in section 4.4. Essentially, the upper airfoil boundary layer is observed to separate near the leading edge of the airfoil and the separated shear layer subsequently rolls-up to form vortices (figure 4.9c). The system of laminar separation, shear-layer roll-up and periodic vortex shedding gives rise to a characteristic $\overline{c_f}$ distribution and causes C_L to oscillate.

Time-averaged skin-friction and lift-coefficients are compared for grids G1-G3 in figure 4.7. When run using grid G1, C_L oscillates in an almost perfectly periodic fashion. The time-averaged c_f distribution exhibits separation, secondary separation (the small region of positive $\overline{c_f}$ within the larger separated region) and reattachment. Downstream of reattachment a wave-like $\overline{c_f}$ distribution is observed. This appears to be a characteristic feature of two-dimensional sepa-

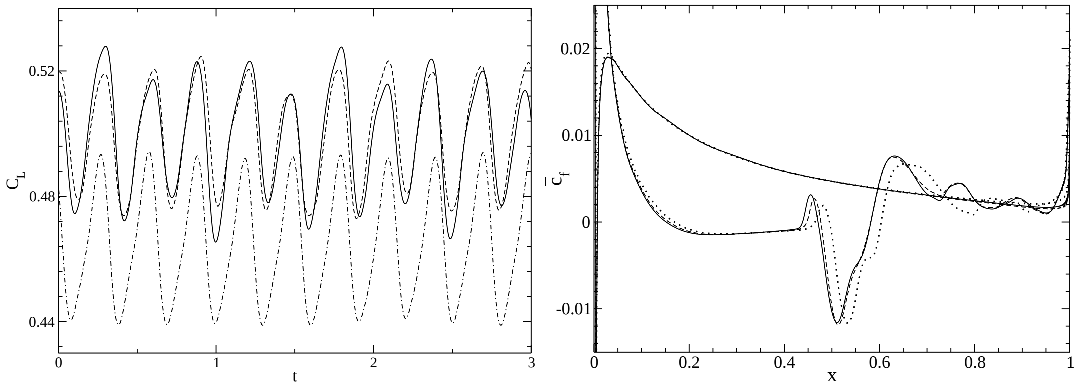

Figure 4.7: Time dependent C_L (left) and time-averaged c_f (right) for grids G1 ($\cdots$), G2 ($--$) and G3 (—).

ration bubbles with vortex shedding, and is discussed further in section 4.4.2.

Some evidence of numerical oscillation was observed for grid G1 when iso-contours of vorticity were plotted at sensitive levels, hence grid G2 was generated with an increased streamwise grid resolution over the airfoil surface. When the simulation was continued on grid G2, the mean lift-coefficient increased, and the time dependent behaviour became slightly less regular. Numerical oscillations could no longer be observed in hydrodynamic properties. The fundamental frequency of the vortex shedding remained unchanged, however the reattachment point, and hence by inference the vortex shedding location, moved upstream slightly. This alters the wave-like $\overline{c_f}$ distribution downstream of reattachment. Grid G3 was generated with increased wall-normal resolution and a larger domain radius compared to grid G2. Only small differences are observed in C_L and $\overline{c_f}$ between grids G2 and G3. The behaviour of $\overline{c_f}$ in the region of secondary separation changes very slightly, however elsewhere the $\overline{c_f}$ distributions are nearly identical. It appears that grid G2 adequately captures the vortex shedding behaviour observed in two-dimensions, with no evidence of under-resolution, however grid G3 will be more suited to three-dimensional simulations, since the increased wall normal resolution is more appropriate for resolving turbulence. Estimates of skin-friction using XFoil (Drela & Giles, 1987), with $Re_c = 5 \times 10^4$, $M = 0.$, and $\alpha = 5°$, suggest the maximum $\overline{c_f}$ in the turbulent region will be $\overline{c_f} = 5.25 \times 10^{-3}$ at $x = 0.6$. The resultant resolution in wall-units for this region for grid G3 would then be $x^+ = 2.6$, and the number of grid-points in the region $y^+ < 10$ would be 11, comparing favourably with the well resolved plane-channel flow in Sandham *et al.* (2002).

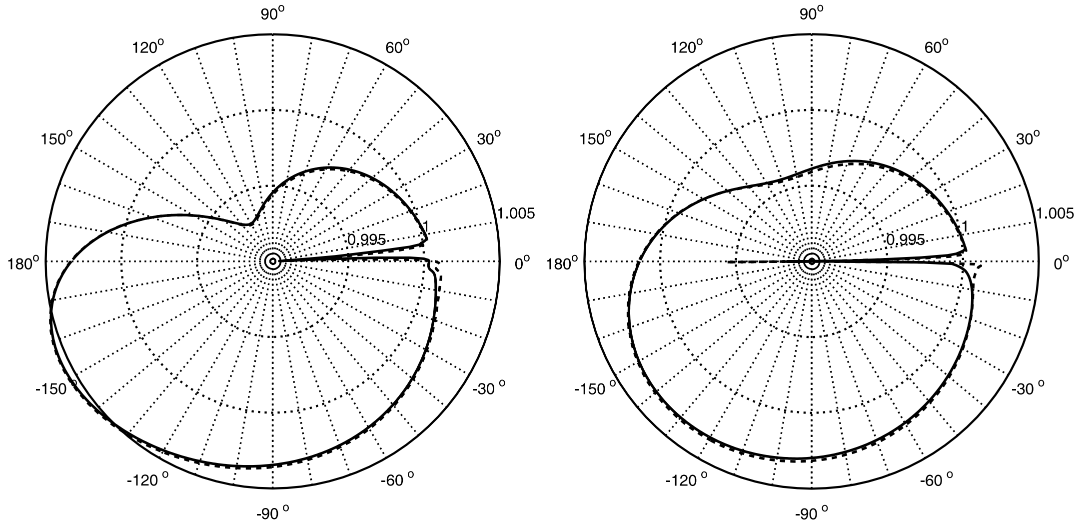

Figure 4.8: Azimuthal variation of p/p_∞ over the range 0.99 to 1.005, at two chords (left) and three chords (right) radius from the airfoil trailing edge, for grids G2 (−−) and G3 (—).

4.3.2 Domain size

The effect of domain size upon the potential flow about the airfoil may be investigated by considering simulations run using grids G2 and G3 (defined in section 4.3.1); grid G2 is of radius $R = 5.3$, whereas grid G3 is of radius $R = 7.3$. The azimuthal variation of p/p_∞, where p_∞ is the free-stream pressure, is plotted in figure 4.8 for both grids, at a radius of two chords (left) and three chords (right) from the airfoil trailing edge.

At around 0° there is a difference of approximately $p/p_\infty = 1.5\times10^{-3}$ between the two grids, presumably caused by differences in resolution in the η direction in the wake region, however this is the only significant difference observed. The azimuthal pressure distribution in the potential flow region appears remarkably similar for both cases, and at three chords radius the difference between grids in this region is significantly less than $p/p_\infty = 1\times10^{-3}$. If the radius of the domain were increased beyond seven chords, further changes would be even smaller in amplitude. It appears then that a domain radius of 5.3 airfoil chords adequately captures the potential flow about the airfoil, and hence a domain radius of 7.3 chords is more than adequate. The characteristics based boundary conditions appear sufficiently effective that a comparatively modest domain size is able to capture the potential flow.

In light of grid resolution and domain size studies, all two-dimensional simulations at $\alpha = 5°$ were performed on grid G3. For reference purposes important parameters for grid G3 are given in table 4.3, and grid resolution at specified control points is given in table 4.4. A series of grids at other non-zero inci-

N_ξ	2570
N_ξ airfoil	1066
N_ξ wake	753
N_η	692
N_{total}	1778440
Wake length - W	5
Radius - R	7.3
Buffer length	0.6
Buffer points	31
Total domain length	12.3
Total domain height	14.6

Table 4.3: Grid parameters for grid G3.

	x	y	$\Delta\xi$	$\Delta\eta$
Stagnation point	0	0	1×10^{-3}	2.5×10^{-4}
Trailing edge	1	0	1×10^{-3}	3.8×10^{-4}
Exit boundary	6	0	1.5×10^{-2}	1×10^{-3}
Exit boundary	6	0.2	1.5×10^{-2}	2×10^{-3}
Exit boundary	6	1	1.5×10^{-2}	8×10^{-3}
Exit/free stream boundary	6	1.5	3.1×10^{-2}	5×10^{-2}

Table 4.4: Grid resolution at selected control points for grid G3.

dences were generated based on the requirements for the $\alpha = 5°$ case, using similar numbers of grid points and similar resolution. These grids were used for two-dimensional simulations only, and will not be discussed in detail.

4.4 Two-dimensional simulations at incidence, for $Re_c = 5 \times 10^4$, $M = 0.4$

Having generated grids with the appropriate resolution, a series of two-dimensional simulations at incidence $\alpha = 3°, 5°, 7°$ and $8.5°$ were conducted. All simulations were run at $Re_c = 5 \times 10^4$, $M = 0.4$, with time-step $\Delta t = 1.4 \times 10^{-4}$, and statistics were taken over a minimum of 40 non-dimensional time-units after achieving a statistically stationary flow.

4.4.1 Time-dependent behaviour

Iso-contours of vorticity illustrate the flow behaviour in the vicinity of the airfoil for all cases, in figure 4.9. At $\alpha = 0°$ the flow over the airfoil is steady. The boundary layer separates over the aft section of the airfoil, and the wake rolls-up into von-Kármán-type vortex shedding immediately downstream of the trailing-edge. As the airfoil incidence is increased, the separation point on the upper airfoil surface moves upstream. By $\alpha = 3°$, vortex shedding from the separated shear layer over the upper surface is observed, as opposed to vortex shedding from an unsteady wake, and the same-sign vortex shedding from the separated shear layer occurs at approximately half the frequency of the antisymmetric wake shedding. Both the separation point and the onset of vortex-shedding continue to move further upstream with increasing incidence.

The time-dependent lift-coefficient oscillates due to the vortex shedding behaviour. For cases at $0^\circ \leq \alpha \leq 5^\circ$ the lift-coefficient oscillates in a periodic fashion, with a clear dominant frequency (figure 4.10). Above $\alpha = 5^\circ$, however, the time-dependent lift-coefficient oscillates in a more irregular fashion, with a more complex frequency content. Plotting the direct Fourier transform of the lift-coefficient for $\alpha = 3^\circ$ and $\alpha = 7^\circ$ confirms that this is the case (figure 4.11). The direct Fourier transform of the lift-coefficient at $\alpha = 3^\circ$ (figure 4.11, left) exhibits a clear peak, that of the dominant shedding frequency ($f = 2.27$), and several lower amplitude peaks associated with higher-harmonics. At $\alpha = 7^\circ$, however, the direct Fourier transform of the lift-coefficient exhibits a much more broadband spectrum (figure 4.11, right). Hence it appears that at some value of α in the range $5^\circ < \alpha < 6^\circ$ the vortex shedding behaviour transitions from being dominated by a single frequency, to a more broadband behaviour. Hoarau, Braza, Ventikos, Faghani & Tzabiras (2003*a*) observed a similar transition to a more complex shedding behaviour, and in the case of Hoarau *et al.* the increased complexity was due to the onset of a Kelvin-Helmholtz instability in the free-shear layer. Were a Kelvin-Helmholtz instability present one could reasonably expect to observe small scale vortices to be generated within the shear layer, as in the study of Hoarau *et al.*, however no such fundamental change in behaviour is observed here. In the current case the change in behaviour appears to be associated with increased complexity of the vortex dynamics present at higher incidence (for example, by a mechanism similar to the 'period doubling' also observed by Hoarau *et al.* (2003*a*)). The dominant vortex shedding frequency appears to increase almost linearly from $\alpha = 3^\circ$ to $\alpha = 5^\circ$ before broadband behaviour takes precedence at $\alpha > 6^\circ$ (figure 4.12, left). No real conclusions can be drawn on the dependency of f upon α however, since relatively few data points are available. The RMS lift-coefficient varies little over the range $\alpha = 4^\circ$ to $\alpha = 5^\circ$, but once broadband behaviour occurs at $\alpha = 6^\circ$ the RMS lift-coefficient increases dramatically (figure 4.12, right). The RMS lift-coefficient for cases above $\alpha = 5^\circ$ is approximately three times larger than at $\alpha = 5^\circ$ and below.

Acoustic waves are generated by acoustic scattering as vortices convect over the trailing edge (Ffowcs Williams & Hall, 1970), and the trailing edge noise undergoes a similar behavioral change to the vortex shedding for $\alpha > 5^\circ$. For

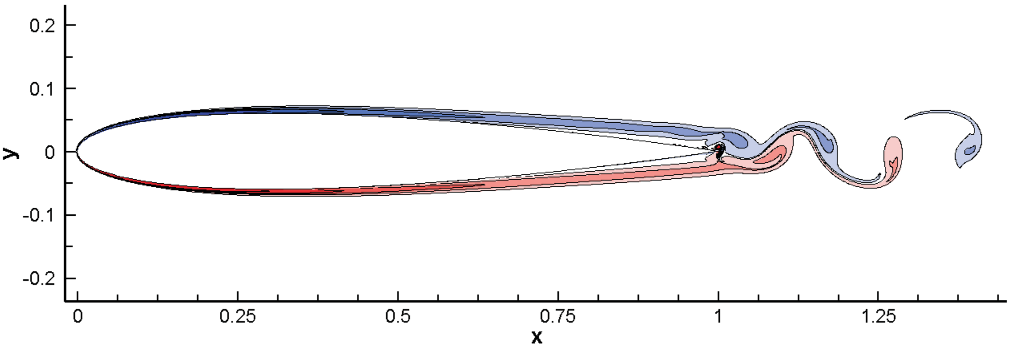

a) $\alpha = 0°$

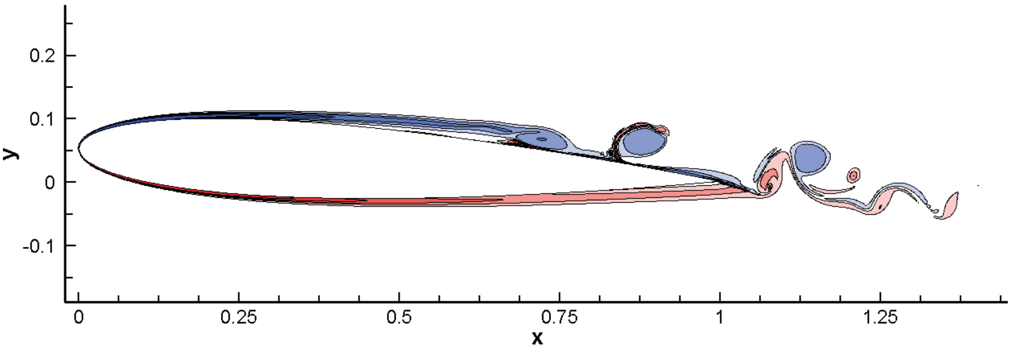

b) $\alpha = 3°$

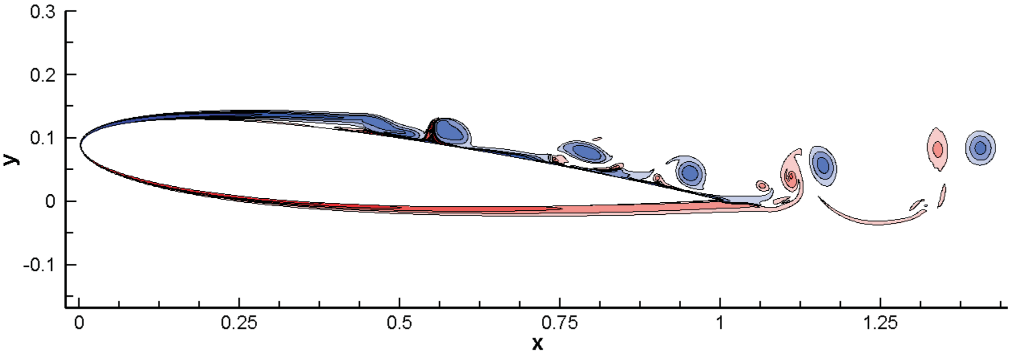

c) $\alpha = 5°$

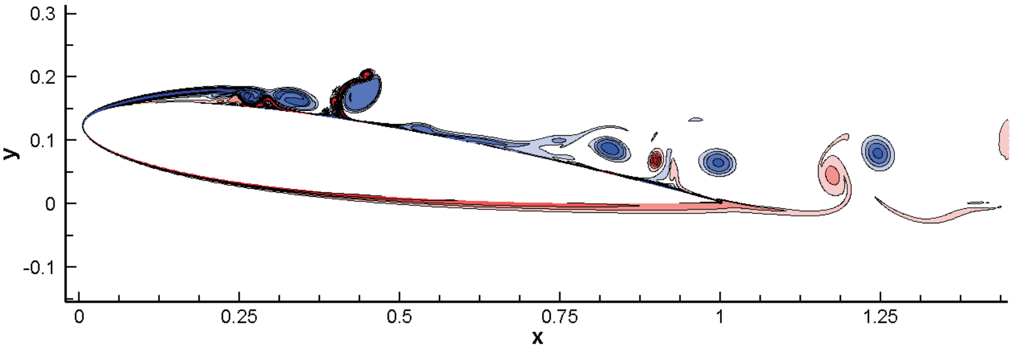

d) $\alpha = 7°$

Figure 4.9: Iso-contours of vorticity, using 20 levels over the range ±150, at $Re_c = 5 \times 10^4$, $M = 0.4$, displaying four angles of attack as labeled.

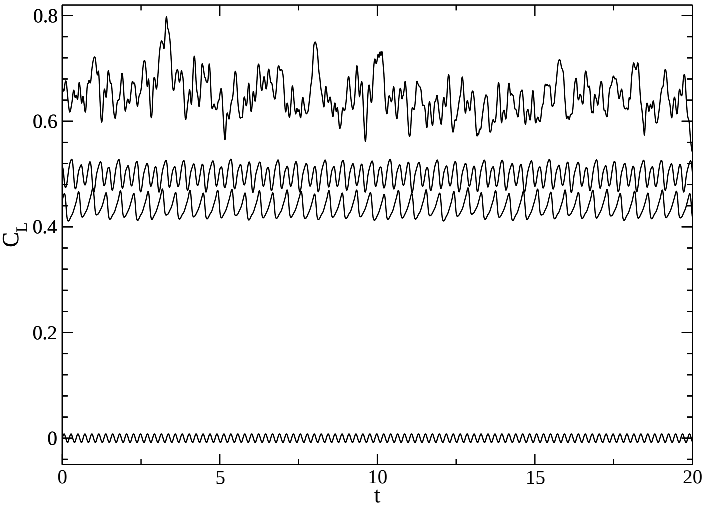

Figure 4.10: Time-dependent C_L for simulations at $Re_c = 5 \times 10^4$, $M = 0.4$, displaying incidence $\alpha = 7°$, $\alpha = 5°$, $\alpha = 3°$ and $\alpha = 0°$, moving from top-to-bottom.

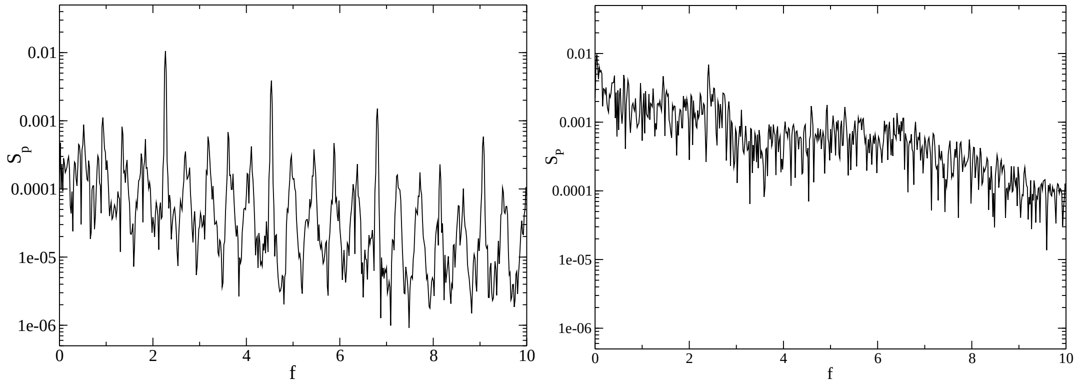

Figure 4.11: Direct Fourier transform of the time-dependent lift-coefficient at $Re_c = 5 \times 10^4$, $M = 0.4$, for incidence $\alpha = 3°$ (left) and $\alpha = 7°$ (right)

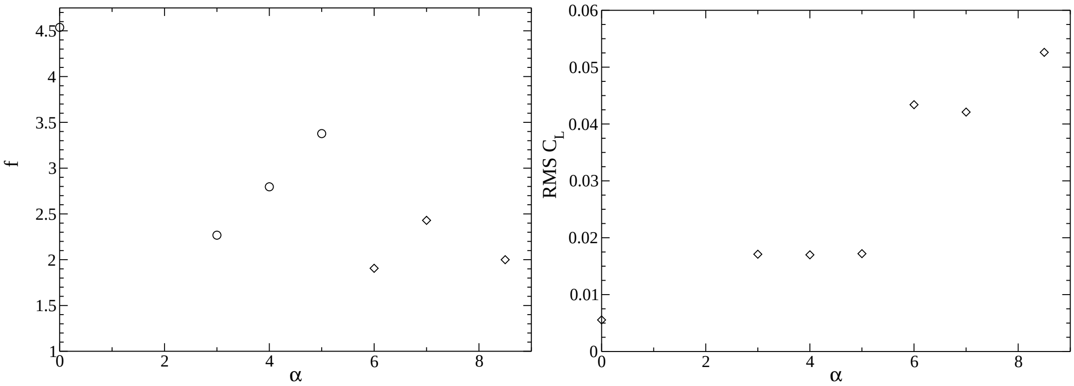

Figure 4.12: Variation with incidence of the dominant frequency observed in C_L (left), and variation of the RMS C_L with incidence (right), at $Re_c = 5 \times 10^4$, $M = 0.4$. Points marked ○ on the left hand image indicate cases with a clear dominant frequency, points marked ◇ indicate cases with a more broadband frequency composition.

$\alpha \leq 5^\circ$, where the vortex shedding is periodic, trailing edge noise is observed to be tonal in nature, whereas for $\alpha > 5^\circ$, where the vortex shedding is irregular, trailing edge noise is observed to be more broadband. This is illustrated by plotting iso-contours of $\nabla.\mathbf{U}$ for $\alpha = 5^\circ$ (figure 4.13, left) and for $\alpha = 7^\circ$ (figure 4.13, right). At $\alpha = 5^\circ$ the trailing edge noise appears symmetric and near-periodic. However, at $\alpha = 7^\circ$, the trailing edge noise appears asymmetric and non-periodic; the amplitude of acoustic waves is greater above the airfoil, and the frequency content appears more complex. There also appears to be more than one acoustic source present on the upper airfoil surface at $\alpha = 7^\circ$. Acoustic waves appear well-resolved to a radius of at least three airfoil chords from the trailing edge for these grids. Further acoustic analysis of simulations presented in this chapter is presented in Sandberg, Jones, Sandham & Joseph (2007)

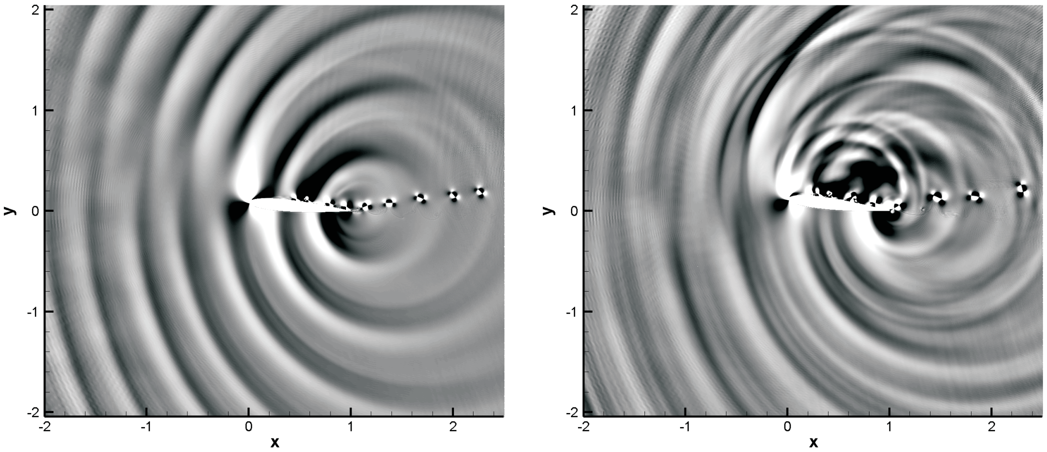

Figure 4.13: Iso-contours of $\nabla.\mathbf{U}$ over the range ± 0.1 for $\alpha = 5^\circ$ (left), and $\alpha = 7^\circ$ (right), at $Re_c = 5 \times 10^4$, $M = 0.4$.

4.4.2 Statistical analysis

The time-averaged lift-coefficient increases with incidence (figure 4.14, left), as expected. When plotting the available results it does not appear possible to link all data points by a straight line intersecting $(C_L, \alpha) = (0, 0)$. It is likely that the formation of a separation bubble at modest incidence increases the lift-coefficient more rapidly in the range $0^\circ < \alpha < 3^\circ$ than in the range $4^\circ < \alpha < 7^\circ$, where a separation bubble is present for all values of α. The time-averaged friction drag coefficient, C_{DF} (figure 4.14, right), varies little with incidence. The time-averaged pressure drag coefficient (C_{DP}), however, and hence the total drag-coefficient, increase modestly until $\alpha = 5^\circ$ and then more rapidly for $\alpha > 5^\circ$. This change in $dC_D/d\alpha$ appears to coincide with the behavioural change observed in vortex shedding, discussed in section 4.4.1.

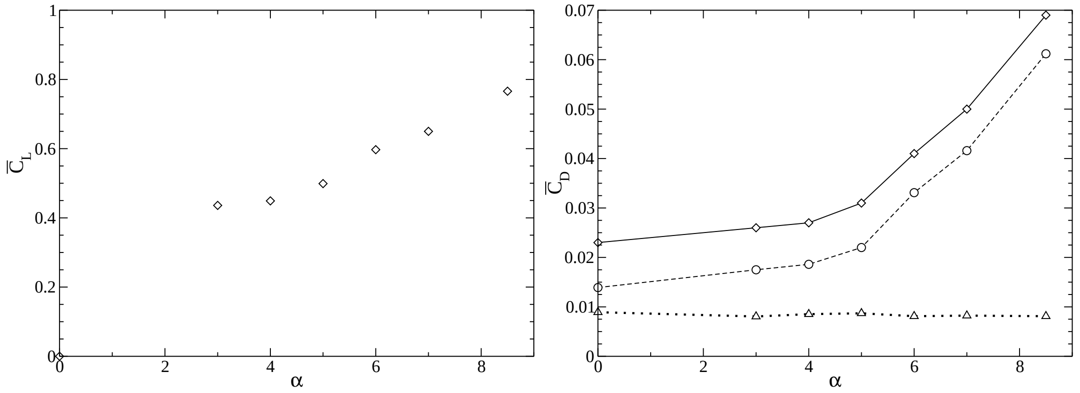

Figure 4.14: Variation of time-averaged lift-coefficient (left) and drag coefficients (right) with incidence at $Re_c = 5 \times 10^4$, $M = 0.4$. Right hand image shows skin-friction drag coefficient (△ · · · △), pressure drag coefficient (○ – –○), and total drag coefficient (◇—◇).

At $\alpha = 0°$ the time-averaged skin-friction is symmetric with both boundary layers separating over the aft section of the airfoil. For all cases at $\alpha \geq 3°$ the time-averaged skin-friction is characteristic of the presence of a separation bubble, with an extended region of negative $\overline{C_f}$ present on the upper airfoil surface. A region of positive $\overline{C_f}$ is observed within all separation bubbles, associated with the so-called secondary separation which occurs upstream of the reverse flow vortex, itself located just upstream of the reattachment point. The case at $\alpha = 5°$ exhibits a wave-like distribution of skin-friction coefficient over the upper airfoil surface, in the region $0.6 < x < 1$. The behaviour in this region does not change when statistics are taken over a longer period of time ($\Delta t = 60$), and similar wave-like behaviour may also be observed in other fluid properties, such as z-vorticity. Alam & Sandham (2000) observed similar behaviour for a two-dimensional separation bubble induced on a flat surface, which also exhibited vortex shedding. This suggests that this behaviour is a characteristic of two-dimensional separation bubbles with regular vortex shedding, and is not related to the presence of a trailing edge. It should be noted that the wavelength of the vortex shedding is of similar order of magnitude to that observed in the skin-friction distribution. Above $\alpha = 5°$ a wave-like pattern cannot be observed in flowfield properties, presumably because of the more complex frequency content of vortex shedding. Below $\alpha = 5°$ there is only a comparatively short distance between the reattachment point and airfoil trailing edge, hence the vortex shedding wavelength is too long to produce noticeable wave-like behaviour.

The movement of the separation and reattachment points with incidence, and the variation of the total separation bubble length, is plotted in figure 4.16. Both the separation point and reattachment point move upstream with increasing incidence. The reattachment point moves upstream at a greater rate

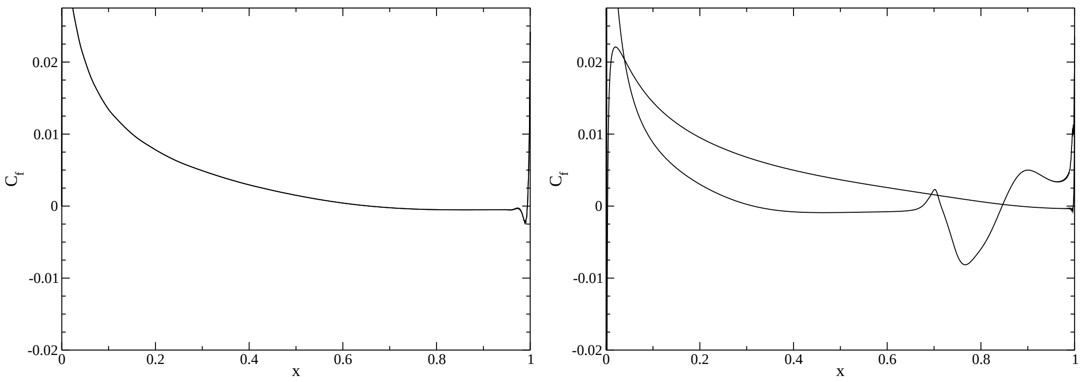

a) $\alpha = 0°$ b) $\alpha = 3°$

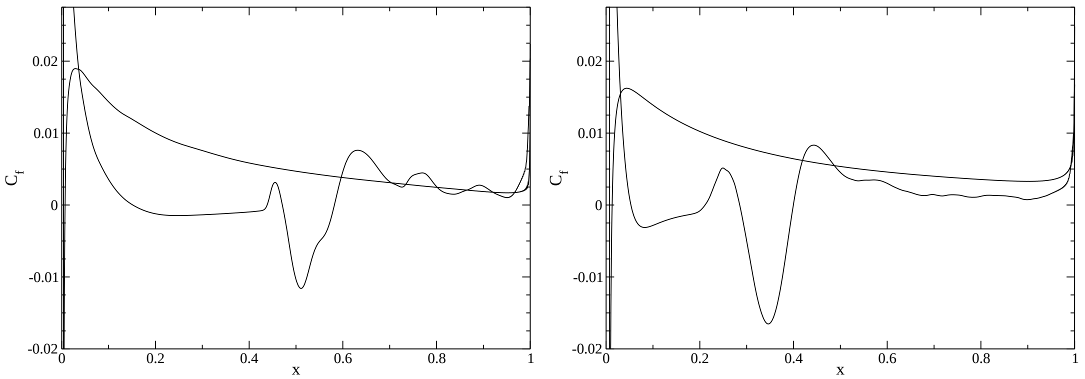

c) $\alpha = 5°$ d) $\alpha = 7°$

Figure 4.15: Time-averaged c_f distribution at $Re_c = 5 \times 10^4$, $M = 0.4$, for several angles of attack, as labeled.

than the separation point however, and hence the bubble length decreases with increasing incidence. Thus the two-dimensional case does not exhibit the characteristics of thin-airfoil stall, where the reattachment point moves downstream and the separation bubble increases in length with increasing incidence (McCullough & Gault, 1951). Characteristics of trailing-edge stall or leading-edge stall are not observed either, however this may be because the airfoil incidence is insufficient to observed such behaviour. Time-averaged pressure-coefficient distributions illustrate the length and magnitude of the pressure-plateau caused by the separation bubble (figure 4.17). As expected, the length and magnitude of the pressure-plateau increase with incidence. A local maxima can clearly be observed near the end of the pressure plateau for all separation bubbles. This is a two-dimensional phenomenon which has been observed in flat plate simulations (e.g. see Alam & Sandham, 2000; Pauley *et al.*, 1990), and is not expected to persist in cases with turbulence.

Time-averaged momentum and displacement thickness distributions are given

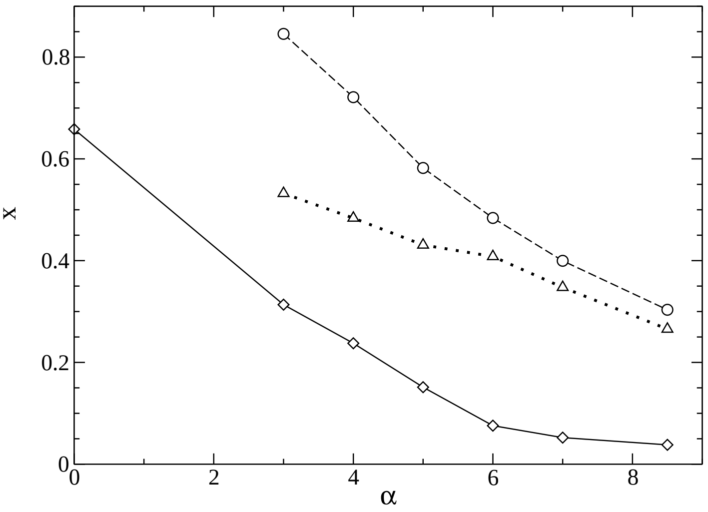

Figure 4.16: Variation of time-averaged separation point (◇—◇), reattachment point (○ − −○), and total bubble length (△ · · · △) with incidence, at $Re_c = 5 \times 10^4$, $M = 0.4$.

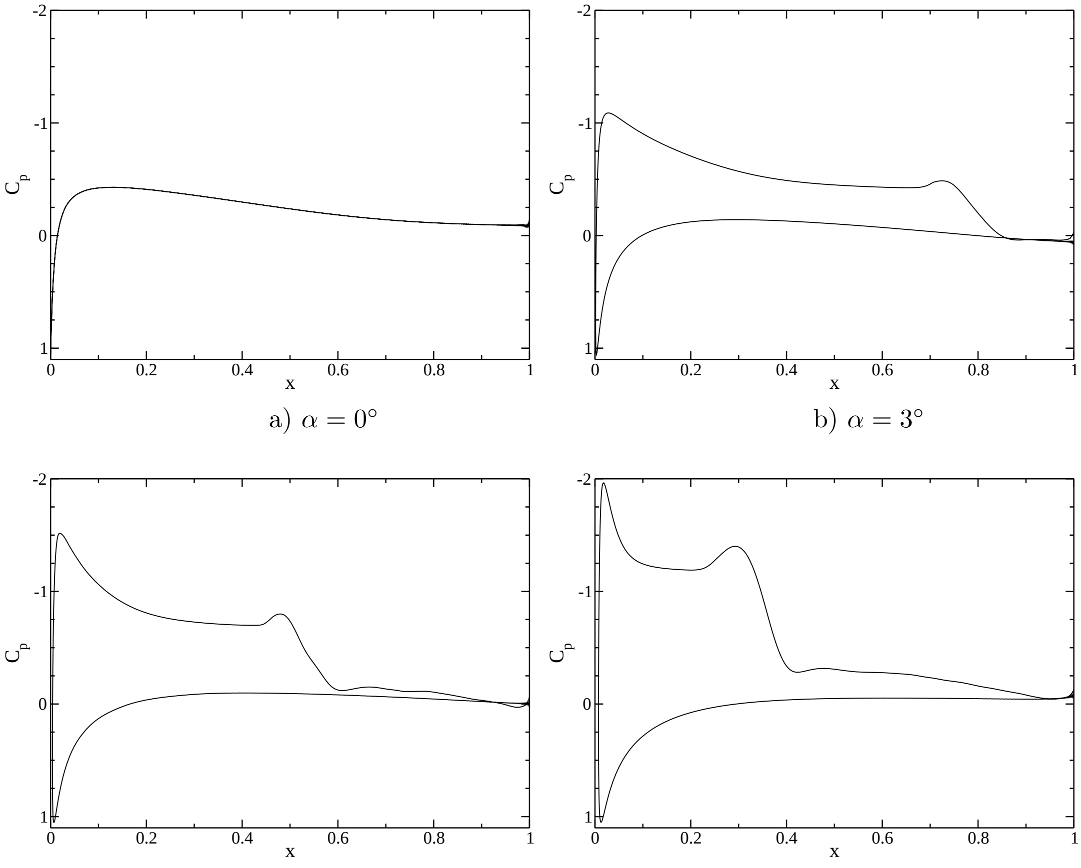

a) $\alpha = 0°$

b) $\alpha = 3°$

c) $\alpha = 5°$

d) $\alpha = 7°$

Figure 4.17: Time-averaged C_P distribution at $Re_c = 5 \times 10^4$, $M = 0.4$, displaying four angles of attack, as labeled.

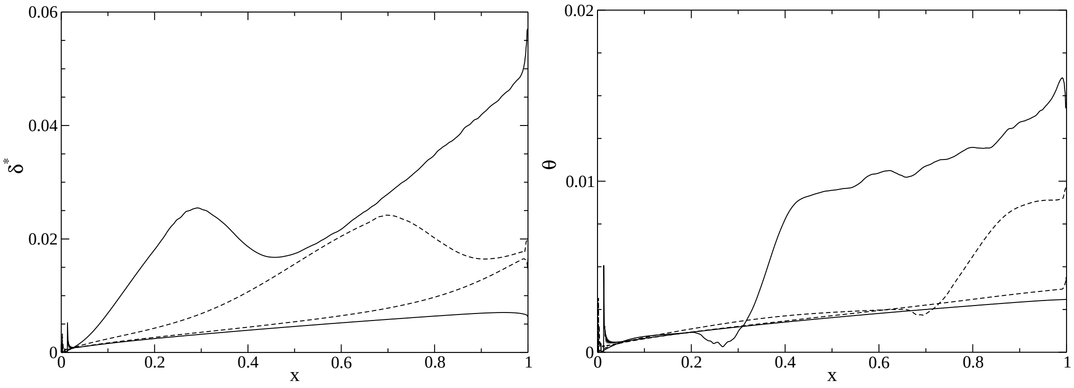

Figure 4.18: Displacement thickness distribution (left) and momentum thickness distribution (right) for the case at $\alpha = 3°$ (−−) and the case at $\alpha = 7°$ (—), at $Re_c = 5 \times 10^4$, $M = 0.4$.

in figure 4.18 for the case at $\alpha = 3°$ and at $\alpha = 7°$. Displacement thickness increases rapidly across the separated region, until reaching a local maxima. Upon reaching this local maxima, the displacement thickness decreases slightly before increasing steadily once more until the trailing edge is reached. Similar behaviour is observed for all the two-dimensional separation bubbles, however the growth rate of δ^* across the bubble increases with incidence. The momentum thickness increases only slowly, and does not vary significantly with incidence, across the separated region. At the onset of vortex shedding the momentum thickness rapidly increases by a factor of four or more over a comparatively short distance, before increasing steadily until the trailing edge is reached.

The variation with α of the percentage reverse-flow observed in the time-averaged flowfield, normalized by the local boundary layer edge velocity, is plotted in figure 4.19. The percentage reverse flow increases with incidence over the range $4° \leq \alpha \leq 7°$, and appears to saturate for $\alpha > 7°$. At $\alpha = 3°$ the percentage reverse flow is greater than at $\alpha = 4°$. The reason why is not clear, however for the case at $\alpha = 3°$ the separation occurs due to a combination of surface curvature and adverse pressure gradient, whereas for $\alpha \geq 5$ separation occurs solely under the influence of an adverse pressure gradient. This may potentially have an influence on the boundary layer characteristics in this region. For all cases at positive incidence, the percentage reverse flow present is greater than that found necessary to sustain local absolute instability (20%), as determined by Hammond & Redekopp (1998) and Rist & Maucher (2002) for analytic profiles.

4.5 Summary

At $Re_c = 5 \times 10^4$, $\alpha = 0°$ a low frequency oscillation was observed in conjunction with vortex shedding from an unstable wake. The low frequency (flapping)

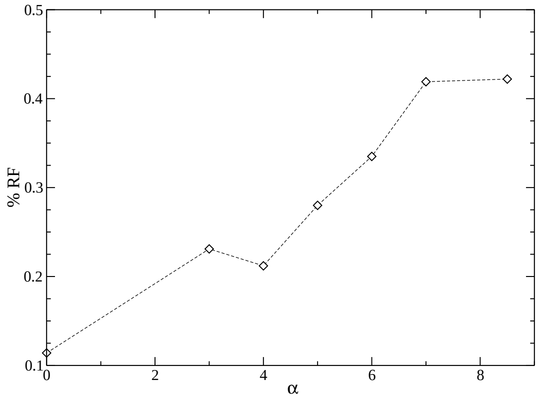

Figure 4.19: Variation of the maximum reverse flow observed in the time-averaged flowfield with α, at $Re_c = 5 \times 10^4$, $M = 0.4$.

oscillation was found to be associated with asymmetric boundary-layer stall periodically switching airfoil surfaces, accompanied by periodically alternating accelerating and decelerating flow. The onset of this low frequency mode has been determined over the range $Re_c = 10^4 - 5 \times 10^4$ and $M = 0.2 - 0.8$. The low frequency oscillation is distinct from transonic buffet, and the period appears unrelated to upstream acoustic wave velocities.

A grid resolution study was performed for the two-dimensional case at $Re_c = 5 \times 10^4$, $M = 0.4$ and $\alpha = 5°$. Further grids were then produced for several values of positive incidence, with similar resolution, and used to perform a series of two-dimensional simulations at incidence. Vortex shedding from an unsteady separation bubble was observed for all cases, and time-averaged skin-friction and pressure-coefficient distributions were characteristic of two-dimensional separation bubbles. The vortex shedding appears to undergo a change in behaviour when the airfoil incidence is increased above $\alpha = 5°$. For $\alpha \leq 5°$ the vortex shedding appears regular and near-periodic, and lift-coefficient spectra exhibit clear tones. For $\alpha > 5°$ the vortex shedding is irregular, and lift-coefficient spectra exhibits broadband behaviour. Both the RMS lift-coefficient and $dC_D/d\alpha$ also exhibit sudden changes at $\alpha = 5°$. The onset of this behavioural change does not appear to coincide with the occurrence of any fundamentally different physical behaviour, apart from the increased complexity of vortex dynamics present. Trailing edge noise was observed for all cases, and found to be dominated by the characteristics of the vortex shedding behaviour. Where the vortex shedding is periodic, trailing edge noise is observed to be tonal in nature. Where the vortex shedding is irregular, trailing edge noise is observed to be more broadband. Additionally, acoustic radiation appeared to be produced not only at the trailing edge, but also at a secondary source located above the airfoil.

Chapter 5

The effect of boundary layer forcing on three-dimensional separation bubble behaviour[1]

5.1 Introduction

In this chapter the simulation at $Re_c = 5 \times 10^4$, $M = 0.4$, $\alpha = 5°$ is extended into three-dimensions; the intention is to capture a separation bubble exhibiting laminar separation and turbulent reattachment on an airfoil at MAV flight conditions, and to investigate the effect of low-amplitude boundary layer disturbances upon bubble behaviour.

Initially, forcing is introduced in order to promote transition to turbulence. After obtaining sufficient data from this forced case, the explicitly added disturbances are removed and the simulation run further. Upon removal of disturbances, the turbulence is observed to self-sustain, with increased turbulence intensity in the reattachment region. A comparison of the forced and unforced cases shows that forcing may improve aerodynamic performance whilst requiring little energy input.

5.2 Extension to three dimensions

In chapter 4 section 4.3.1, grid G3 was found capable of resolving of resolving the turbulent boundary layer at $Re_c = 5 \times 10^4$, $M = 0.4$ and $\alpha = 5°$, based on $\overline{c_f}$ predictions from XFoil (Drela & Giles, 1987) and comparison to Sandham *et al.* (2002). The spanwise domain width was selected based upon criteria determined from simulations of the flow over a backward facing step (Terzi, 2004).

---

[1] See also Jones *et al.* (2007*a*,*b*)

Simulation	Δx^+	Δz^+	Δy^+	$N_\eta : y^+ < 10$
Case 3DF	3.36	6.49	1.0	9
Sandham *et al.* (2002)	15	7.5	-	10

Table 5.1: Grid resolution in wall units at the maximum $\overline{c_f}$ location for case 3DF.

A domain width of at least 4 times the step height (corresponding approximately to the reattachment length), is necessary to resolve fully the case of flow over a backwards facing step. Making an analogy with the maximum bubble height based on displacement thickness, δ^*, a domain width $L_z = 0.2$ was chosen, being 9.6 times the maximum bubble height of $\delta^* = 2.09 \times 10^{-2}$ and 7.2 times δ^* at the trailing edge. The number of spanwise grid-points was chosen to be 96, again based on the resolution requirements of turbulent plane channel flow and $\overline{c_f}$ predictions from XFoil.

During initial stages of three-dimensional simulations, flowfield properties were checked in order to confirm that all fluid structures appeared resolved. A final confirmation of adequate spatial and temporal resolution is provided by *a posteriori* statistical analysis of the DNS data. Grid resolution in wall-units, taken at the maximum turbulent $\overline{c_f}$ location observed over all simulations, was found to differ slightly from XFoil predictions, but was still found to be well resolved based on turbulent plane channel flow criteria. Resolution in wall units for case 3DF (defined in section 5.5), taken at $x = 0.612$ where the maximum $\overline{c_f}$ of 7.60×10^{-3} is observed, is given in table 5.1.

In order to confirm that turbulent behaviour is resolved over all time and length scales, power spectra of turbulence kinetic energy, defined as $K = \frac{1}{2}(\overline{u'u'} + \overline{v'v'} + \overline{w'w'})$, are computed. To incorporate a reasonable number of samples, spanwise spectra are integrated over the finite wall-normal distance $1 < y^+ < 50$ as well as time-averaged, using nine flowfields taken at intervals of $t = 0.7$. Figure 5.1 displays spanwise power spectra of K taken at three x-locations for case 3DF (left) and case 3DU (right, defined in section 5.5). A roll off of order 10^3 is observed with increasing wavenumber, comparable with the well-resolved turbulent boundary layer DNS performed by Spalart (1988) using a fully spectral method. Temporal power spectra of K at specific locations (figure 5.2) are computed using three segments and Hanning windowing (as detailed in section 2.3), and display a minimum roll-off of 10^6 with increasing frequency.

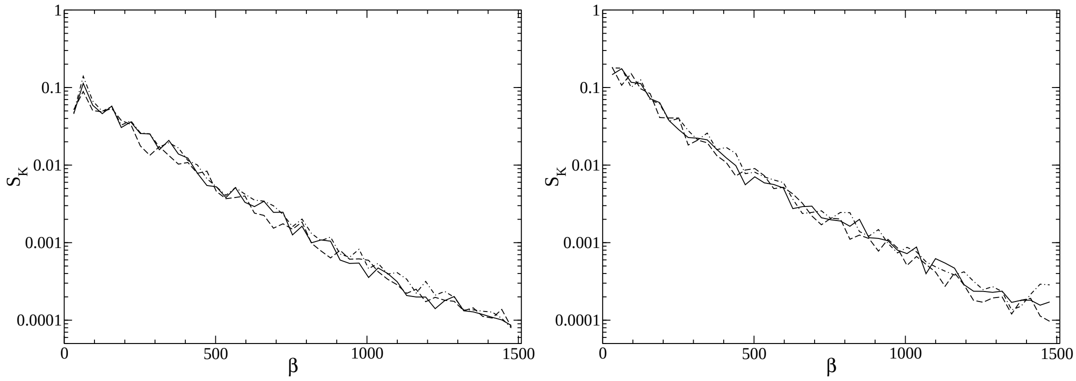

Figure 5.1: Spanwise power spectra of K, integrated over the range $1 < y^+ < 50$, taken for case 3DF (left) and case 3DU (right) at $x = 0.8$ $(-)$, $x = 0.9$ $(--)$, and $x = 1.0$ $(-\cdot)$.

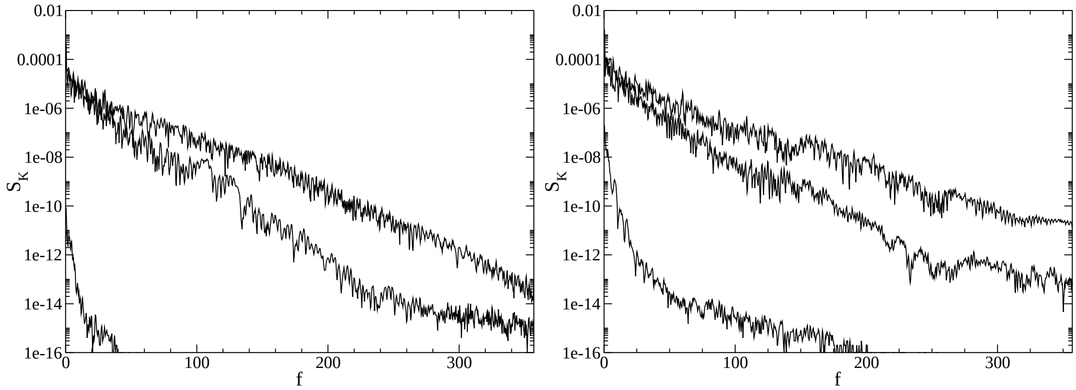

Figure 5.2: Temporal power spectra of K, taken at $x = 0.9$ at the airfoil mid-span for case 3DF (left), at $y^+ = 12.3$, $y^+ = 51$ and $y^+ = 313$ moving from top-to-bottom, for and case 3DU (right) taken at $y^+ = 54$, $y^+ = 13.2$ and $y^+ = 335$ moving from top-to-bottom.

5.3 The effect of compressibility

A compressible code is employed in order to capture the acoustic response of the airfoil. This means that at low Mach numbers, due to the increased velocity of acoustic waves, very small time-steps must be used in order to capture their propagation. This leads to dramatically increased computational cost at low Mach numbers, and is clearly undesirable. Conversely, it is also undesirable to perform these simulations at Mach numbers where compressibility effects are pronounced, since aircraft operating at low Reynolds numbers will operate at very low Mach numbers. Therefore a Mach number of 0.4 was selected as a compromise between computational requirements and the desire to minimise compressibility effects. The magnitude of compressibility effects present in the simulation can be quantified *a posteriori* by comparing plots of Favre averaged quantities, which include density weighting, to corresponding plots of Reynolds averaged quantities for the fully developed three-dimensional flow. A full discussion of Favre averaged quantities can be found in Huang *et al.* (1995).

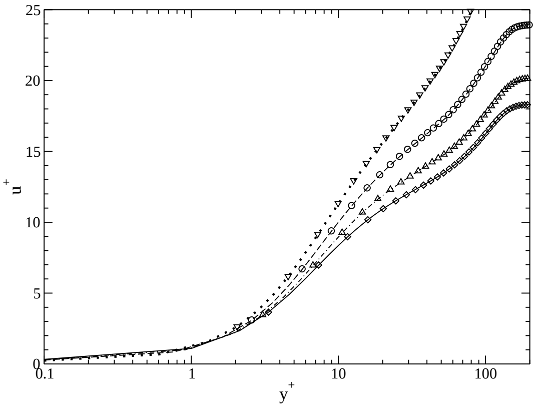

Figure 5.3: Comparison of time-averaged boundary layer profiles at $x = 0.7$ (—), $x = 0.8$ (−−), $x = 0.9$ (·−), $x = 0.99$ (···) with Favre-averaged boundary layer profiles at $x = 0.7$ (◇), $x = 0.8$ (△), $x = 0.9$ (○), $x = 0.7$ (▽) for case 3DF.

Essentially, $\overline{f}$ refers to the ensemble average of f, $\widetilde{f}$ refers to the Favre average of f, and

$$\widetilde{u_i} = \frac{\overline{\rho u_i}}{\overline{\rho}}, \tag{5.1}$$

$$u_i'' = u_i - \widetilde{u_i}, \tag{5.2}$$

$$\widetilde{u_i'' u_j''} = \overline{u_i' u_j'} - \overline{u_i''}\,\overline{u_j''} + \frac{\overline{\rho' u_i' u_j'}}{\overline{\rho}}. \tag{5.3}$$

Comparing Reynolds and Favre averaged boundary layer profiles (figure 5.3) and stresses (figure 5.4) for simulation 3DF (defined in section 5.5) clearly illustrates that Reynolds averaged statistics are almost identical to Favre averaged statistics for the current case. This suggests that compressibility effects are small, and that plotting Reynolds averaged statistics, i.e. with no density weighting, is sufficient. Additionally, linear stability analysis using an incompressible solver will incur minimal error due to compressibility effects.

5.4 Volume forcing

Volume forcing is applied to the x and y momentum equations in the three-dimensional simulation using the method outlined in section 2.2.10. The goal is to introduce three-dimensional disturbances that are amplified in the free-shear layer and subsequently break down to turbulence. Forcing is centred on the location $x = 0.1$, $y = 0.129$, corresponding to a point within the boundary layer of the time-averaged solution, and is periodic in both time and span. The forcing is varied smoothly from a maximum at the centre of the forcing location to zero at radius 5×10^{-3} from the forcing location. Frequencies were chosen based

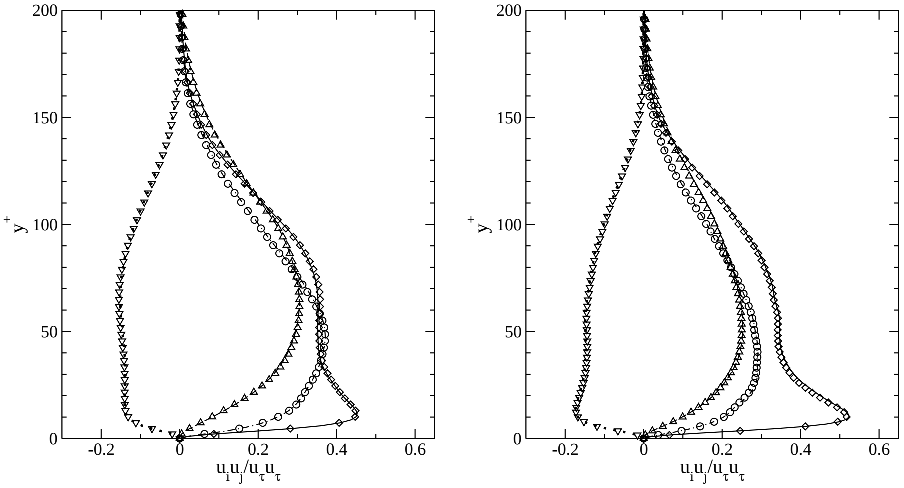

Figure 5.4: Comparison of Reynolds stresses with Favre-averaged stresses for case 3DF at $x = 0.7$ (left) and $x = 0.9$ (right), showing $\overline{u'u'}$ (—), $\overline{v'v'}$ (−−), $\overline{w'w'}$ (·−), $\overline{u'v'}$ (···), $\widetilde{u''u''}$ (◇), $\widetilde{v''v''}$ (△), $\widetilde{w''w''}$ (○), $\widetilde{u''v''}$ (▽).

ω	β
48.76	31.42
53.60	94.24
53.60	125.66

Table 5.2: Forcing parameters used for case 3DF.

on linear stability analysis of the time-averaged flowfield extracted from the two-dimensional simulation (presented in section 7), selecting the most unstable modes observed. Forcing was applied at several spanwise wavenumbers, with the total amplitude 0.1% of the freestream velocity. Details of forcing parameters are given in table 5.2, where $\omega = 2\pi f$, with f the frequency, and β the spanwise wavenumber.

5.5 DNS of forced and unforced laminar separation bubbles

Results from three DNS will be discussed, all run at $Re_c = 5 \times 10^4$, $M = 0.4$ and $\alpha = 5°$, with time-step $\Delta t = 1 \times 10^{-4}$, defined as follows:

Case 2D: The precursory two-dimensional simulation that was run in order to provide a suitable initial condition for the subsequent three-dimensional simulation, presented in section 4.3.

Case 3DF: The two-dimensional flowfield was extruded in the z-direction. Three-dimensionality was then introduced by explicitly adding disturbances via volume forcing, the goal being to excite unstable oblique modes which would subsequently be amplified within the separated shear layer, leading to transition to turbulence.

Case 3DU: After an appropriate amount of statistical data was captured from case 3DF, the simulation was progressed further in time with the explicitly added forcing removed. The dependency of bubble behaviour on the addition of disturbances could then be investigated.

5.5.1 Time dependent behaviour

In two-dimensions, the time dependent lift coefficient (C_L) exhibits periodic oscillatory behaviour with frequency $f = 3.37$ and $(C_L)_{RMS} = 0.0172$. As outlined in section 4.3.1, the cause of this behaviour can be attributed to periodic vortex shedding from the separated shear-layer present on the upper airfoil surface (figure 4.9c, section 4.3.1). This behaviour appears qualitatively similar to that observed by Marxen *et al.* (2003) and Pauley *et al.* (1990) in flat plate simulations, and results in the observed periodic oscillation in C_L and C_D.

Figure 5.5 shows a time-history of C_L and C_D starting at time $t = 0$, the start of case 3DF and the point at which forcing was introduced. The time dependent C_L initially displays oscillatory behaviour associated with two-dimensional vortex shedding. This oscillatory behaviour ceases by time $t = 2$, whereupon C_L increases significantly. At this stage in the flow development, time series of pressure taken within the separated shear layer (figure 5.6, $x = 0.4$) clearly exhibit periodic oscillation, associated with the strongly amplified instability waves induced by the forcing. Downstream of the vortex shedding location, at $x = 0.8$, the pressure signal is seemingly random, characteristic of turbulent fluctuations passing the measurement location. Instantaneous iso-contours of vorticity taken at the mid-span (figure 5.7, top) illustrate that the separated shear layer undergoes transition to turbulence, and that a developing turbulent boundary layer is now present over the aft section of the airfoil. Iso-surfaces of the secondary invariant of the velocity gradient tensor, Q, illustrate structures present in the transition region (figure 5.8, left). Structures within the boundary layer are observed to break down to smaller scales, however no large-scale Λ-vortices are observed here. After a transient lasting until approximately $t = 6.3$, case 3DF settles to a stationary flow and statistics were taken for $6.3 < t < 14$. Figure 5.5 illustrates the data capture period for both 3D simulations.

Case 3DF was then run further in time but with the forcing removed, and the resultant simulation denoted 3DU. Upon removing the forcing, the turbulent behaviour can be monitored by observing pressure fluctuations within the boundary layer (figure 5.6). It can be seen that downstream of the separation bubble, at $x = 0.8$, the pressure fluctuations do not decrease. In fact,

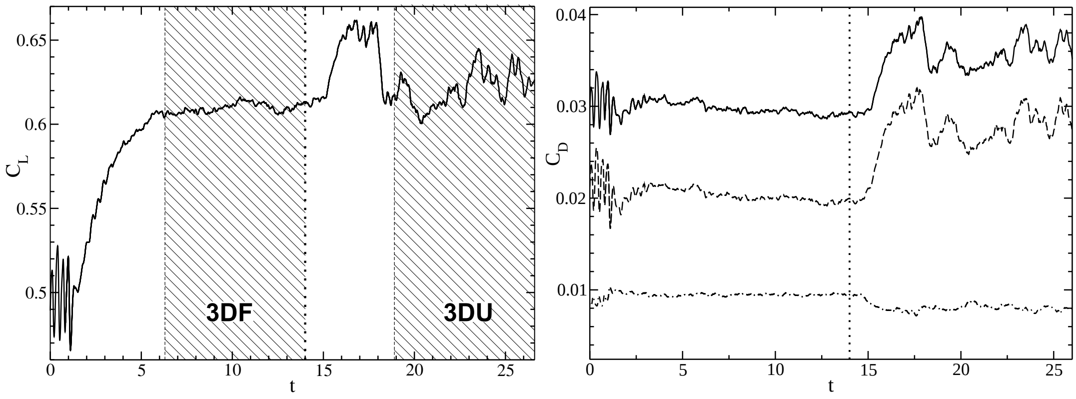

Figure 5.5: Left figure shows time dependent lift-coefficient, the dotted line indicates the time at which forcing was removed ($t = 14$) and hatched areas indicate periods over which statistical data capture was undertaken. Right figure shows time dependent skin friction drag coefficient (−−), pressure drag coefficient (·−), and total drag coefficient (—).

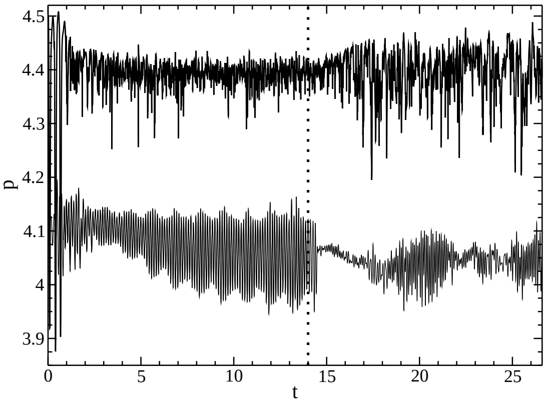

Figure 5.6: Time dependent pressure within the boundary layer at $x = 0.4$ (lower curve) and $x = 0.8$ (upper curve). The dotted line indicates the time at which forcing was removed.

the maximum amplitude of pressure fluctuations increases slightly. Oscillations are still observed within the separated shear layer at $x = 0.4$, however the signal is lower in amplitude, more intermittent, and no longer dominated by the forcing frequencies as observed in case 3DF. Statistics for case 3DU were taken for $18.9 < t < 26.6$. At the end of this period of time turbulent fluctuations have still not decreased in amplitude, and the transition to turbulence appears to self-sustain. Instantaneous iso-contours of vorticity taken at the mid-span (figure 5.7, bottom) suggest that the height of the separated shear layer has increased. Iso-surfaces of Q illustrate structures present in the transition region (figure 5.8, right). In contrast to the forced case, much larger structures may be observed, with clear spanwise orientation. These structures persist downstream of the transition region of case 3DF, until they break down into turbulence that still has a strong spanwise coherence. Animations of flowfield properties suggest that the transition process is highly erratic for case 3DU; for example, large

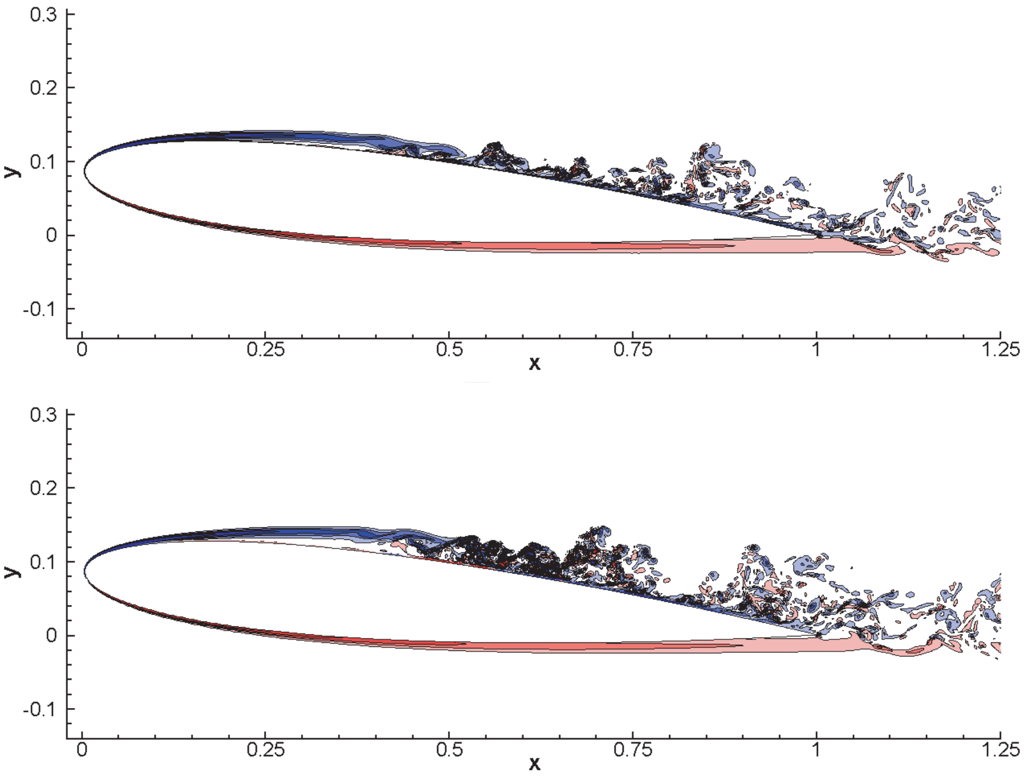

Figure 5.7: Iso contours of vorticity using 10 levels over the range ±200 for case 3DF at $t = 14$ (top) and case 3DU at $t = 23.8$ (bottom), taken at mid-span.

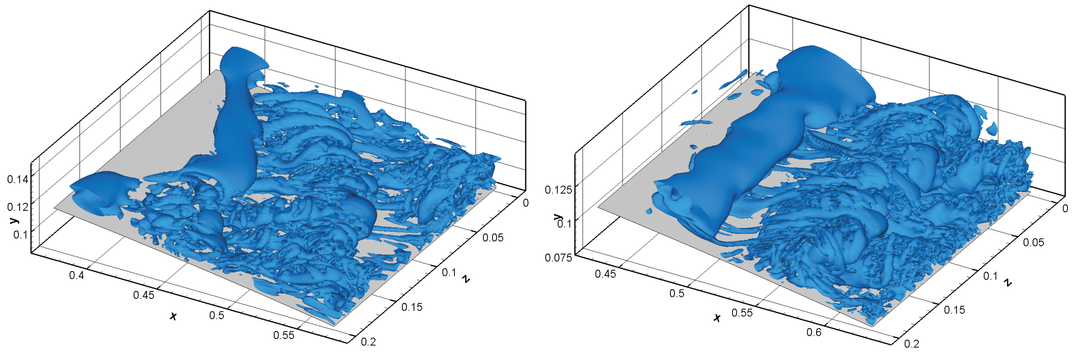

Figure 5.8: Iso-surfaces of the second invariant of the velocity gradient tensor at $Q = 500$, for case 3DF at $t = 14$ (left) and case 3DU at $t = 23.1$ (right).

scale fluctuations reminiscent of two-dimensional vortex shedding are observed to occur occasionally, which rapidly break down to turbulence.

5.5.2 Statistical analysis

Time dependent lift and drag coefficients are given in figure 5.5, with the associated time-averaged values in table 5.3. It can be seen that whilst removal of forcing leads to a slight increase in C_L and a very slight decrease in friction drag

Case	C_L	C_D	C_{DF}	C_{DP}
2D	0.499	0.0307	0.0087	0.0220
3DF	0.615	0.0294	0.0095	0.0199
3DU	0.621	0.0358	0.0081	0.0278

Table 5.3: Time-averaged lift and drag coefficients for all cases.

(C_{DF}), pressure drag (C_{DP}) is subject to a significant increase. The net effect is to decrease the lift-to-drag ratio from 21.1 to 17.2, hence it appears that the presence of forcing significantly improves the aerodynamic performance of the airfoil while requiring little energy input. By way of comparison, the synthetic jets employed by You & Moin (2006) at $Re_c \approx 9 \times 10^6$ operate with peak velocity of the order $2u_\infty$.

The displacement thickness across the separated region of case 3DF (figure 5.9, left) appears similar to that of the two-dimensional case in the region $0 < x < 0.35$. It appears that transition to turbulence has decreased the bubble length without significantly modifying the displacement thickness in the laminar region. In contrast, the displacement thickness over the separated region of the unforced case appears markedly different to that of either the two-dimensional case or case 3DF; δ^* increases much more rapidly with increasing x and reaches a greater peak value at the rear of the bubble. The momentum thickness distribution (figure 5.9, right) appears similar over the separated region for all three cases. Given that the momentum thickness stays the same in this region, whilst displacement thickness rises, this indicates that the separated shear layer in case 3DU has effectively increased in wall-normal distance from the airfoil. In the turbulent region, both δ^* and θ are larger in magnitude for case 3DU than for case 3DF. By the airfoil trailing edge δ^* and θ appear to be growing at a similar rate in both three-dimensional cases.

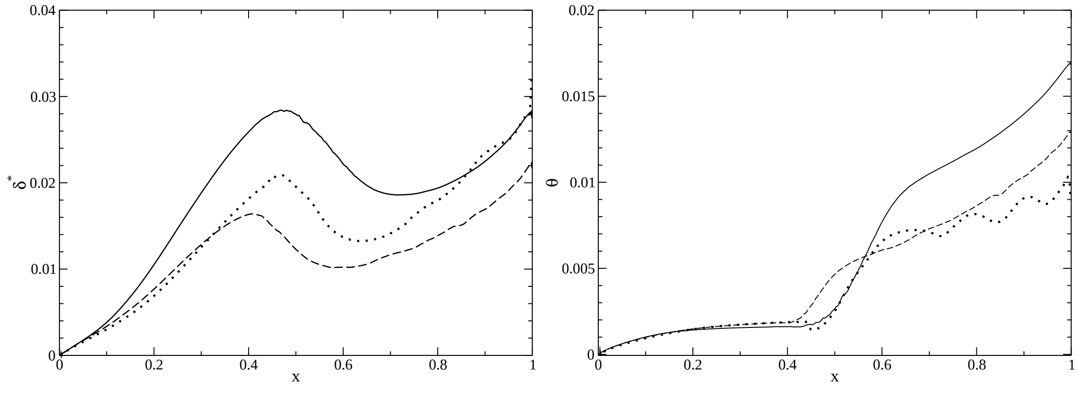

Figure 5.9: Time-averaged displacement thickness distribution (left) and time-averaged momentum thickness distribution (right), for the two-dimensional case (···), case 3DF (——) and case 3DU (− − −).

Dividing the distance from the separation point to the transition location (defined as the location at which the turbulent kinetic energy, K, is a maximum), denoted L_{lam}, by the momentum thickness at separation, θ_{sep}, gives a non-dimensional measure of bubble length. Plotting this parameter versus $Re_{\theta_{sep}}$ allows a general comparison of the bubbles formed to those of existing studies (figure 5.10). The first observation that can be made is that the separation bubbles studied here are formed at a comparatively low Reynolds number compared to those of Gaster (1966), formed on a flat plate. The second observation is that the bubbles appear 'long'. All of the bubbles observed by Gaster below $Re_{\theta_{sep}} = 250$, which are those that are closest in size and $Re_{\theta_{sep}}$ to the current study, were deemed to have burst. However, Weibust, Bertelrud & Ridder (1987) performed a study of separation bubbles formed on an airfoil at $Re_c = 0.9 - 2.2 \times 10^5$. The bubbles observed by Weibust *et al.* were all below $Re_{\theta_{sep}} = 200$ and appear similar in length to Gaster's 'burst' bubbles. The bubbles observed by Weibust *et al.* appear to be the most similar in nature to those observed in the current study. In fact, the proximity of the two studies is perhaps surprising given that the chordwise Reynolds numbers differ by a factor of 20. Hence although the bubbles observed here would be classically termed 'long' or 'burst', they appear of realistic dimension when compared to the study of Weibust *et al.*. The separation bubble studied by Spalart & Strelets (2000) appears of similar length and Reynolds number to the burst bubbles observed by Gaster, whereas the separation bubbles studied by Alam & Sandham appear quite 'short', shorter in fact than any of Gaster's bubbles.

Time-averaged pressure coefficient (C_p) distributions are plotted in figure 5.11, left. In all cases a pronounced pressure plateau is visible on the upper airfoil surface, illustrating the presence of a separation bubble. Comparing cases 3DF and 3DU, it can be seen that the length of the pressure plateau has increased significantly in the unforced case, whereas downstream of the bubble the C_p distributions are similar. The slight C_L increase observed in case 3DU is due to the increased length of the pressure plateau. The increase in C_{DP} for case 3DU can also be attributed to the increase in length of the pressure plateau, since pressure recovery is delayed downstream of the point of maximum airfoil thickness, in conjunction with the reduced suction peak observed near the leading edge.

Time-averaged skin friction coefficient ($\overline{c_f}$) distributions (figure 5.11, right) give a quantitative measure of bubble length (table 5.4). Comparing the two-dimensional simulation to case 3DF it can be seen that the bubble length has decreased in the forced three-dimensional case. Due to transition to turbulence

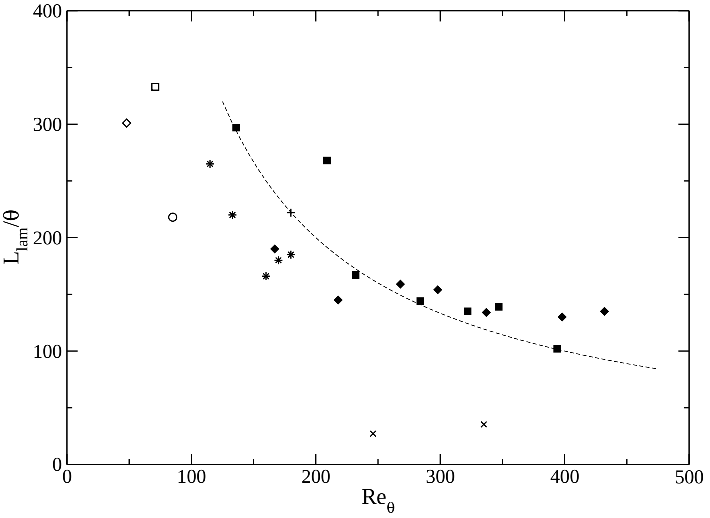

Figure 5.10: L_{lam}/θ_{sep} versus Re_{lam} showing Gaster (1966) series I (◆) and series II (■), Alam & Sandham (2000) (×), Spalart & Strelets (2000) (+), Weibust *et al.* (1987) ($*$), case 3DF (○), 3DU (□) and 3D7, defined in chapter 6, (◇). Dotted line shows empirical trend $L_{lam}/\theta_{sep} = 4 \times 10^4/Re_{\theta_{sep}}$ (Horton, 1969).

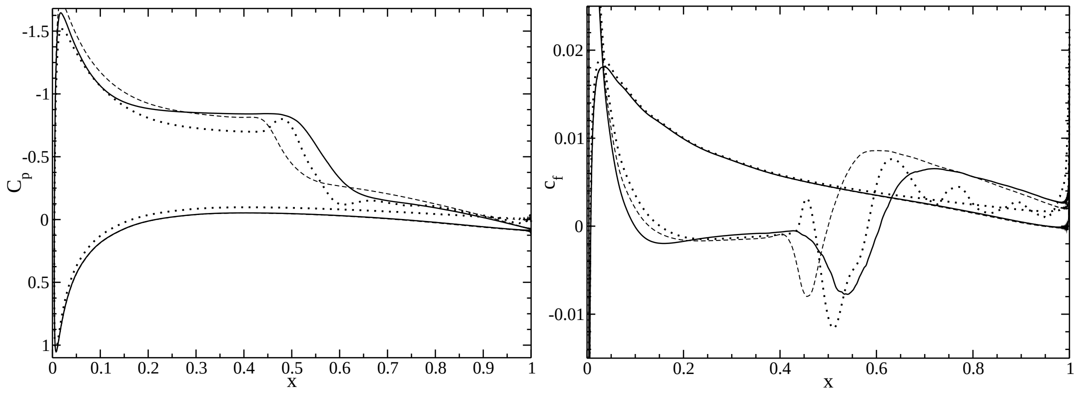

Figure 5.11: Time-averaged distributions of C_p (left) and c_f (right) for the two-dimensional case ($\cdots$), case 3DF (−−) and case 3DU (—).

and hence increased wall normal mixing, the reattachment point has moved upstream from $x = 0.582$ to $x = 0.504$. The separation point has also moved upstream slightly in the forced three-dimensional case. Comparing the three-dimensional cases, it can be seen that removing the forcing has increased the bubble length significantly. The reattachment point has moved from $x = 0.504$ in case 3DF to $x = 0.607$ in case 3DU. The $\overline{c_f}$ peak downstream of transition decreases upon removal of forcing, resulting in the slight decrease in C_{DF} observed in case 3DU.

The time-dependent nature of separation can be investigated by computing probability density functions (PDFs) of c_f. Ordinarily PDFs are constructed using a fixed number of 'bins' over a constant c_f range. In the present study, time-dependent c_f behaviour was observed to vary dramatically with x-wise location,

Case	x_{sep}	x_{reatt}
2D	0.151	0.582
3DF	0.133	0.504
3DU	0.099	0.607

Table 5.4: Time-averaged separation and reattachment points for all cases.

making this approach unsatisfactory. Instead, for each x-location the PDF was constructed using 30 bins equally spaced over three standard-deviations about the mean c_f. PDF bounds are thus given by the equation

$$\widetilde{c_f}(x,i) = \overline{c}_f(x) - 3S(x) + \frac{i-1}{29}6S(x), \quad \text{for} \quad i = 1, 30, \tag{5.4}$$

where $S(x)$ is the standard deviation of c_f at location x. Using different upper and lower bounds for each x-wise location means that the area under the PDF varies with x. To avoid this, the normalised PDF (i.e. N/N_{total}, where N is the number of samples in a given bin and N_{total} is the total number of samples across all bins) is divided by the standard deviation, $S(x)$. This ensures the area under the PDF is constant.

Iso-contours of c_f PDFs for a finite x-wise region on the upper airfoil surface are plotted for each case. Figure 5.12 shows iso-contours of c_f PDFs for the two-dimensional case (top), case 3DF (bottom-left) and case 3DU (bottom-right). The upper and lower PDF boundaries represent c_f at three standard-deviations from the mean, hence where the PDF is very narrow c_f varies only little with time, whereas where the PDF is wide c_f varies strongly. Upstream of transition c_f displays little temporal variation in either case 3DF or case 3DU, confirming that in this region the flow is effectively steady. Similarly, the two-dimensional simulation exhibits little temporal variation upstream of the onset of vortex shedding. Downstream of transition there is considerable variation in c_f for all cases, as illustrated in figure 5.12 by the comparatively large width of the PDF distributions compared to $\overline{c}_f$. Although all cases exhibit large temporal variation of c_f over the aft section of the airfoil, the two-dimensional and three-dimensional PDF distributions appear fundamentally different in this region. The three-dimensional PDF distributions appear smooth and symmetric about the mean c_f, whereas the two-dimensional PDF exhibits greater temporal variation overall and in certain locations has more than one maximum. For all cases, downstream of transition (or onset of vortex shedding in the two-dimensional case) there is no location where c_f is positive for 100% of the time, or negative for 100% of the time. That is to say, even where the time-averaged c_f suggests the boundary layer is attached, there will be some degree of reverse flow observed in the

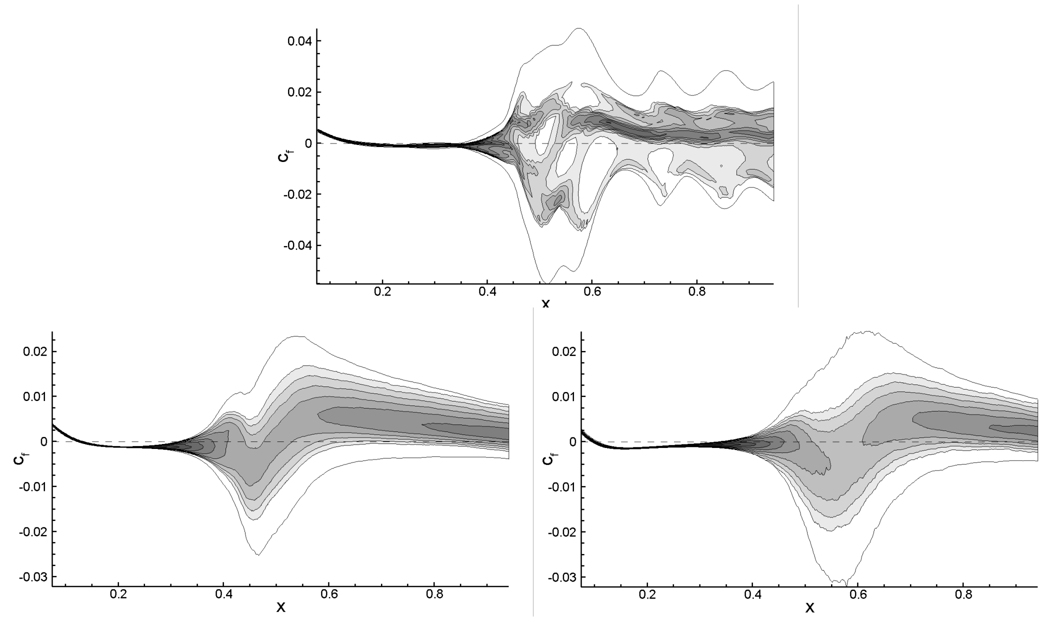

Figure 5.12: Iso-contours of the normalised c_f PDF, $n/(S(x)n_t)$, for the two-dimensional case (top), case 3DF (bottom-left) and case 3DU (bottom-right), using 12 levels exponentially distributed over the range 2 to 1000.

instantaneous flowfield, and vice versa for separated boundary layer regions. Plotting PDFs at the mean reattachment point (figure 5.13, left), i.e. where $\overline{c}_f = 0$, illustrates the different distributions of the c_f fluctuations. For both three-dimensional cases the time dependent c_f varies strongly over the range ± 0.02 at this location, and for the two-dimensional case the variation is even greater. To put this into context, the maximum time-averaged c_f observed in the attached turbulent boundary layer in any case was 7.6×10^{-3} (figure 5.11). Hence at the reattachment point, where the time-averaged c_f is zero, the instantaneous c_f reaches more than double the maximum $\overline{c}_f$ observed after reattachment.

Downstream of transition (e.g. figure 5.13, right) the shape of the PDF distribution appears similar for both case 3DF and case 3DU; a symmetric distribution about the mean c_f. The PDF distribution for the two-dimensional case is markedly different at this location however, consisting of a skewed distribution exhibiting two peaks at positive c_f, and a plateau extending to another peak at $c_f = -0.02$. For the three-dimensional cases the c_f PDF downstream of transition can be approximated by two parameters, $\overline{c}_f(x)$ and $S(x)$, with minimal loss of information. The two-dimensional simulation appears to exhibit fundamentally different behaviour however, and cannot be modelled in this fashion.

Spanwise coherence can be determined by computing two-point spanwise correlations of surface pressure, defined as

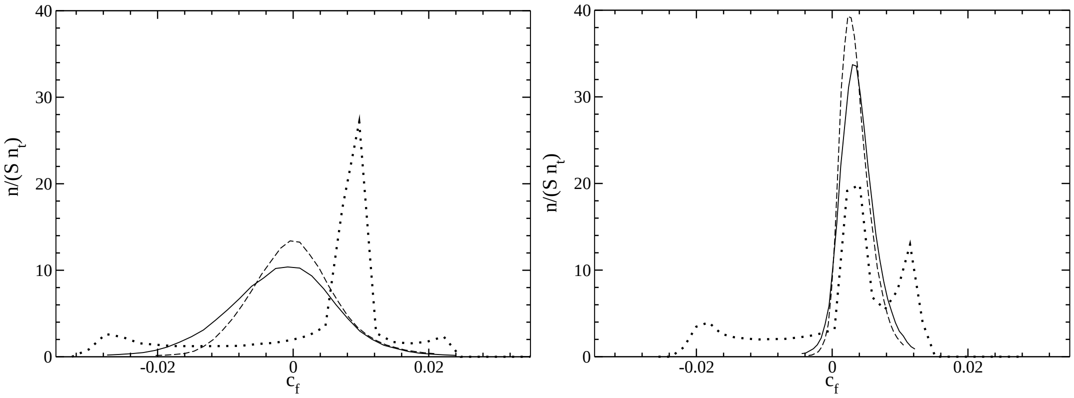

Figure 5.13: Probability density functions of c_f taken at reattachment (left), and at $x = 0.85$ (right) for the two-dimensional case ($\cdots$), case 3DF (−−) and case 3DU (—).

$$C_{z_1 z_2} = \frac{S_{z_1 z_2}}{\sigma_{z_1} \sigma_{z_2}}, \tag{5.5}$$

where $S_{z_1 z_2}$ is the covariance of surface pressure for z_1 and z_2, and σ_{z_n} is the standard deviation of surface pressure at z_n. Two-point spanwise correlations of surface pressure taken at several x-locations for case 3DF are displayed in figure 5.14 (left). For $x \leq 0.2$, $C_{z_1 z_2}$ is close to 1 across the entire span, hence there is strong positive spanwise correlation. The strong spanwise correlation suggests that boundary layer fluctuations are primarily two-dimensional in this region. By $x = 0.4$ there is strong negative correlation, with $C_{z_1 z_2} \approx -0.75$. For case 3DF the spanwise wavenumber $\beta = 2\pi/L_z$ was forced at double the amplitude of higher wavenumber modes. The strong negative correlation observed at $x = 0.4$ can be attributed to the strong amplification within the separated shear layer of perturbations with wavenumber $\beta = 2\pi/L_z$ introduced by the volume forcing. Downstream of $x = 0.4$, $C_{z_1 z_2}$ decreases in amplitude until by $x = 0.7$ there is minimal correlation. This would appear to justify the spanwise domain width of $z = 0.2$ as being sufficiently large.

Case 3DU (figure 5.14, right) exhibits very different behaviour. For $x < 0.3$ the surface pressure appears perfectly correlated. In the region $0.3 \leq x \leq 0.5$ surface pressure becomes slightly less correlated, however unlike case 3DF no negative correlation is observed. This appears to confirm that the negative correlation observed in case 3DF is caused by forcing the boundary layer. Downstream of transition surface pressure becomes less correlated, but $C_{z_1 z_2}$ only decreases to around 0.3. Thus case 3DF exhibits significant correlation in surface pressure downstream of transition. However, referring to instantaneous plots of Q (figure 5.8), in case 3DU large structures are observed with strong spanwise coherence that are not observed in case 3DF. The non-zero correlation observed

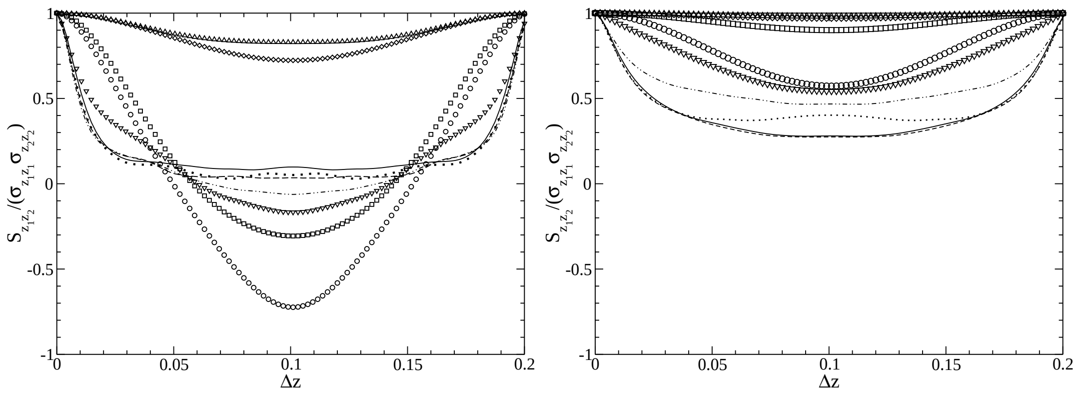

Figure 5.14: Two-point spanwise correlations of surface pressure for case 3DF (left) and case 3DU (right), at x-locations 0.1 (◇), 0.2 (△), 0.3 (□), 0.4 (○), 0.5 (▽), 0.6 (− · ·), 0.7 (· · ·), 0.8 (− −), and 0.9 (—).

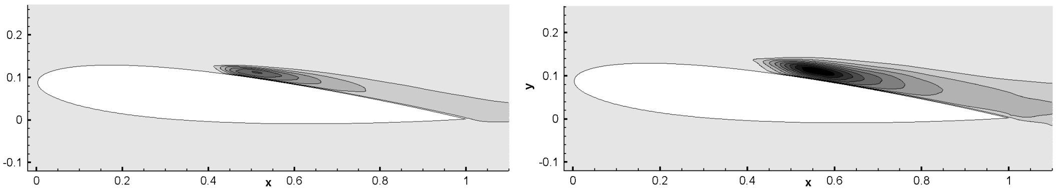

Figure 5.15: Iso contours of K for case 3DF (left) and 3DU (right), using 20 levels over the range 0 to 0.11.

in downstream of transition for case 3DU serves to confirm quantitatively that the turbulence downstream of reattachment retains significant spanwise coherence all the way to the trailing edge.

Iso contours of turbulent kinetic energy, K, are plotted in figure 5.15, and the variation of the maximum K in the wall normal direction with x-location is plotted in figure 5.16. Upon removal of forcing a significant increase in peak K is observed (increasing from 0.074 to 0.124), thus it appears the transition process in the unforced case is more energetic than in the forced case. In case 3DU the peak K occurs upstream of the time-averaged reattachment point, whereas in case 3DF the peak K occurs in the direct vicinity of reattachment, which may explain why the peak $\overline{c_f}$ is lower in case 3DU (figure 5.11). At all locations downstream of transition K is greater in magnitude for case 3DU than for case 3DF by approximately 50%, hence the intensity of turbulent fluctuations downstream of transition appears significantly greater for case 3DU.

Boundary layer profiles for the laminar region of case 3DF and case 3DU, normalised by the displacement thickness and edge-velocity (defined as the maximum $u(\eta)$ occurring at the corresponding x-location), are plotted in figure 5.17. Visual inspection suggests that the amount of shear in boundary layer profiles from case 3DU is greater than that of case 3DF. The amount of shear can be

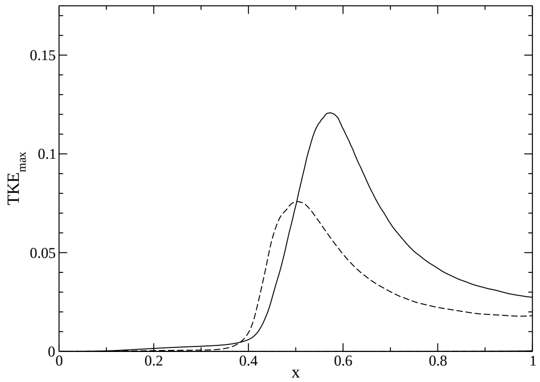

Figure 5.16: Variation of the y-maximum turbulent-kinetic energy, K, with x-location for case 3DF (−−)and 3DU (—).

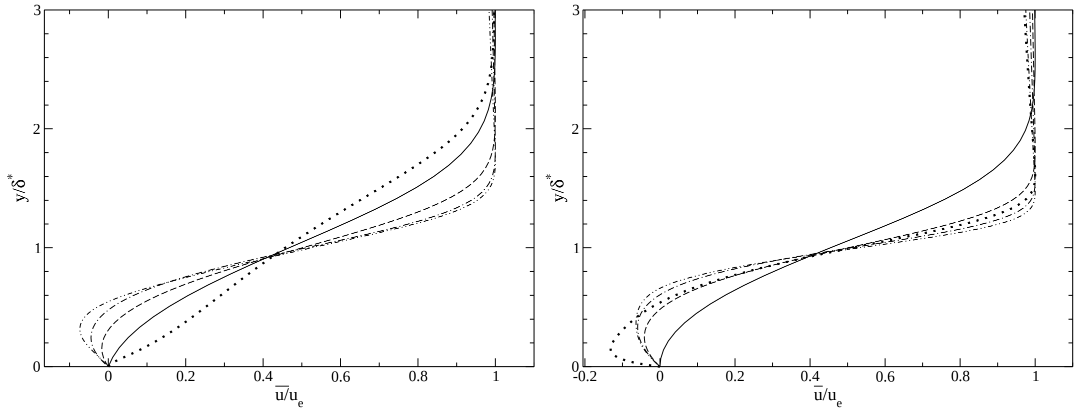

Figure 5.17: Time-averaged boundary layer profiles taken at selected x-locations within regions of laminar flow, from case 3DF (left) and case 3DU (right), showing $x = 0.1$ (——), $x = 0.2$ (−−), $x = 0.3$ (−), $x = 0.4$ (− · ·) and $x = 0.5$ (· · ·).

quantified by considering the maximum du/dy observed, which for case 3DF is 1.38 (at $x \approx 0.4$), compared to 2.20 (again at $x \approx 0.4$) for case 3DU. Rist & Maucher (2002) suggest that the shear-layer strength is a critical parameter for the onset of absolute instability. This suggests that case 3DU should exhibit increased tendency toward absolute instability, as well as increased convective instability growth rates. This is confirmed by the linear stability analysis performed in chapter 7.

Boundary layer profiles extracted from the turbulent regions of case 3DF and case 3DU are plotted in figure 5.18, using wall-scaling. It is apparent that at no point in either simulation does the boundary layer appear to be approaching log-law behaviour. This is not surprising, since previous studies (e.g. Alam & Sandham, 2000) suggest that relaxation to log-law behaviour takes of the order of seven bubble lengths to occur. In the current study the flow reaches the trailing edge less than two bubble lengths after reattachment, and the turbulent boundary layer is formed under an adverse pressure gradient.

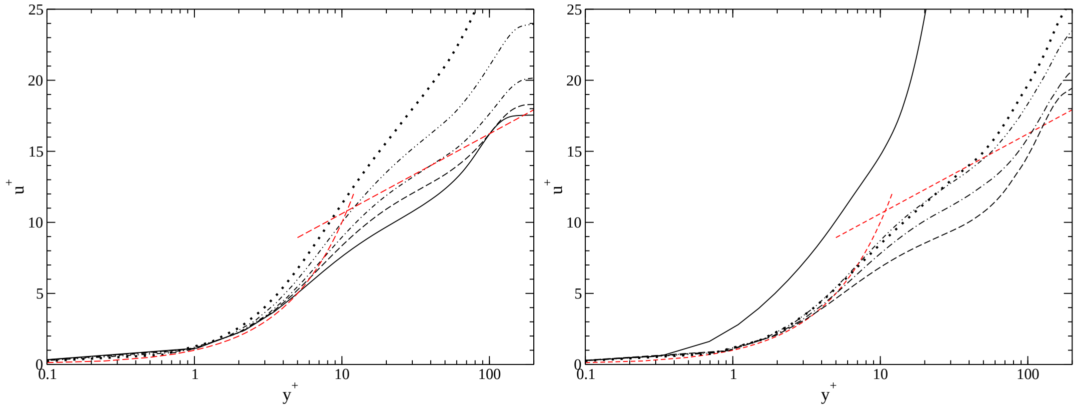

Figure 5.18: Time-averaged boundary layer profiles taken at selected x-locations within regions of turbulent flow, from case 3DF (left) and case 3DU (right), showing $x = 0.6$ (——), $x = 0.7$ (−−), $x = 0.8$ (· − ·), $x = 0.9$ (− · ·) and $x = 0.99$ (· · ·). Red lines show $u^+ = y^+$ and $u^+ = 1/0.41\log(y^+) + 5$.

Reynolds stress profiles, plotted in wall-scaling for locations within the turbulent region, are given for case 3DF in figure 5.19 and for case 3DU in figure 5.20. The Reynolds stress profiles for case 3DF appear qualitatively similar over the range $0.7 \leq x \leq 0.99$; $\overline{u'u'}$ exhibits a clear peak near the wall, at $y^+ = 10$, and a broad 'bulge' in the region $30 < y^+ < 90$. Alam & Sandham (2000) provide K budgets at three locations for a separation bubble induced on a flat plate; near the reverse flow vortex all significant non-zero terms were located within the free-shear layer, whereas far downstream of the bubble all activity was located near the wall. At an intermediate location one bubble-length downstream of reattachment however, the budget displayed characteristics of both a newly forming turbulent boundary layer (for $y^+ < 20$) and a free-shear layer (for $y^+ => 60$). The $\overline{u'u'}$ profiles for case 3DF suggest that the turbulent boundary layer is at this intermediate stage; the near wall-peak is reminiscent of a turbulent channel or boundary layer flow (e.g Kim *et al.*, 1987; Spalart, 1988) and the plateau for $30 < y^+ < 90$ appears associated with the mixing-layer type behaviour observed by Alam & Sandham.

Case 3DU exhibits slightly different behaviour (figure 5.20). The first observation is that the Reynolds stress profiles are less smooth for case 3DU. Statistical data was taken for the same period of time as for case 3DF, hence it appears that the turbulent region exhibits more erratic or intermittent behaviour for case 3DU. Secondly, both axes had to be re-scaled since both the magnitude of Reynolds stresses and the wall-normal distance over which the turbulent behaviour occurs is greater. The skin-friction in the range $0.7 \leq x \leq 0.99$ is similar for cases 3DF and 3DU, hence differences in the magnitude of Reynolds stresses will still be observed if wall-scaling is not employed. Unlike case 3DF, for which a well-defined peak and plateau were observed, for case 3DU two clear peaks are observed in $\overline{u'u'}$. The peak nearest the wall for case 3DU is broader and less distinct than that of case 3DF, occurring in the range $10 < y^+ < 40$, and does not appear to resemble that of a turbulent boundary layer so closely. For case 3DF, $\overline{u'u'}$ was observed to be significantly larger at the near-wall peak than at any other location. In contrast, for case 3DU the outer peak is of a similar amplitude to the inner peak, suggesting that turbulent fluctuations associated with mixing-layer type behaviour are stronger here. It is also noticeable that in contrast to turbulent boundary layers or channel flow, $\overline{v'v'}$ and $\overline{w'w'}$ appear of similar amplitude to $\overline{u'u'}$ for case 3DU. This would also suggest that the dominant turbulent behaviour is relatively unaffected by the presence of the airfoil surface. Indeed, mixing layer flow exhibits peak $\overline{v'v'}$ and $\overline{w'w'}$ values that are closer in amplitude to $\overline{u'u'}$ than for turbulent boundary layers or channel flow (Rogers & Moser, 1994). These differences are likely to be related to the occurrence of large-scale events, appearing partially reminiscent of two-dimensional vortex shedding events, that appear to be active in case 3DU but are not observed for case 3DF.

5.6 Summary

DNS were conducted of a laminar separation bubble on a NACA-0012 airfoil at five degrees incidence. The three-dimensional separation bubble was found to be highly dependent on the presence of forcing. Compared to the unforced case, the inclusion of forcing increases the lift-to-drag ratio by approximately 23% and significantly reduces the intensity of turbulent/unsteady fluctuations over the airfoil. In particular, the addition of forcing appears to reduce the intensity of turbulent fluctuations away from the wall. Fluid structures downstream of transition are found to exhibit increased spanwise coherency in the unforced case. Forcing in a similar fashion could therefore potentially be used as a control mechanism for improving low Reynolds number airfoil performance. Both of the three-dimensional separation bubbles exhibited large temporal variation of skin-friction. At no point downstream of transition was the flow either fully attached or fully separated, suggesting that the concept of a reattachment ‘point’ is misleading. Comparison of skin-friction PDFs illustrates that time-dependent behaviour of the two-dimensional separation bubble is fundamentally different to that of the three-dimensional bubbles.

It is important to note that upon removal of forcing, although the bubble properties change significantly, the bubble does not revert to two-dimensional behaviour. If the bubble were purely convectively unstable, one would expect turbulent fluctuations to convect downstream and ultimately leave the flow over the airfoil in an unperturbed state. This is clearly not the case, and some other local or global instability mechanism must be present in order for the turbulence to self-sustain. This issue will be studied in more detail in chapter 8.

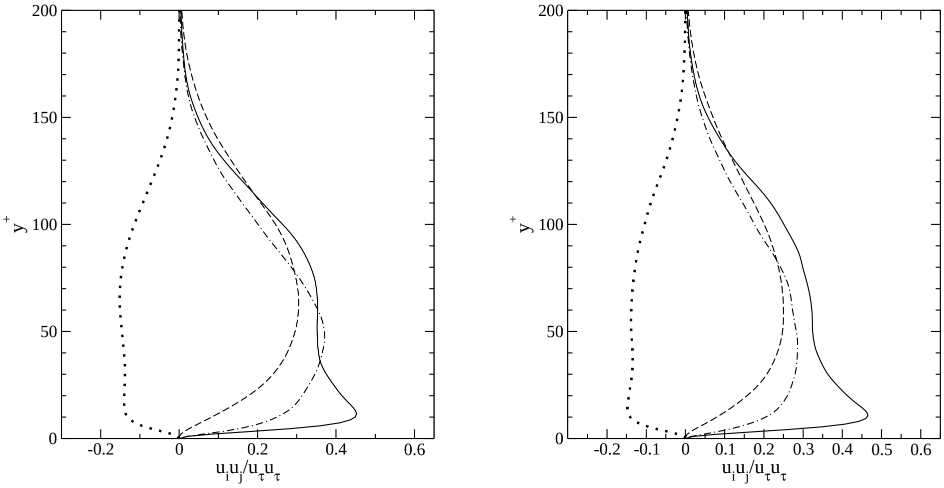

a) $x = 0.7$

b) $x = 0.8$

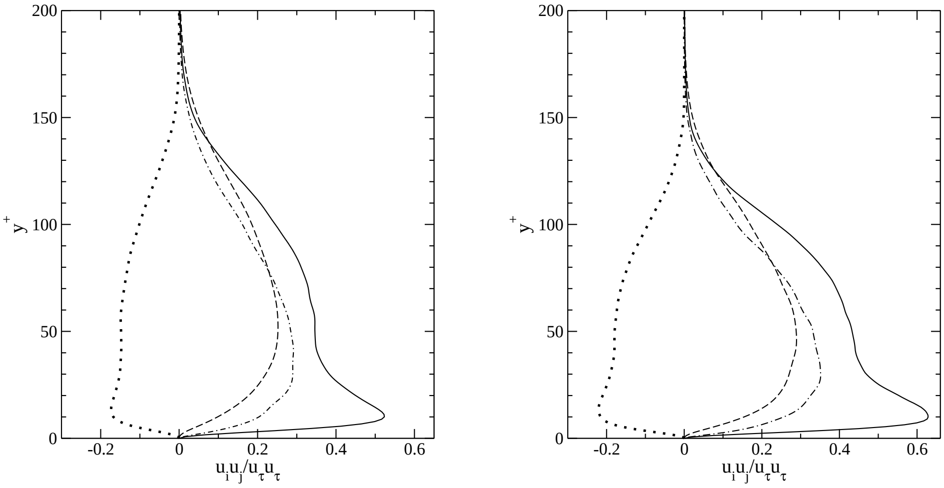

c) $x = 0.9$

d) $x = 0.99$

Figure 5.19: Reynolds-stresses for case 3DF, showing $\overline{u'u'}$ (—), $\overline{v'v'}$ (−−), $\overline{w'w'}$ (− ·) and $\overline{u'v'}$ (···), taken at x-locations indicated on the upper airfoil surface.

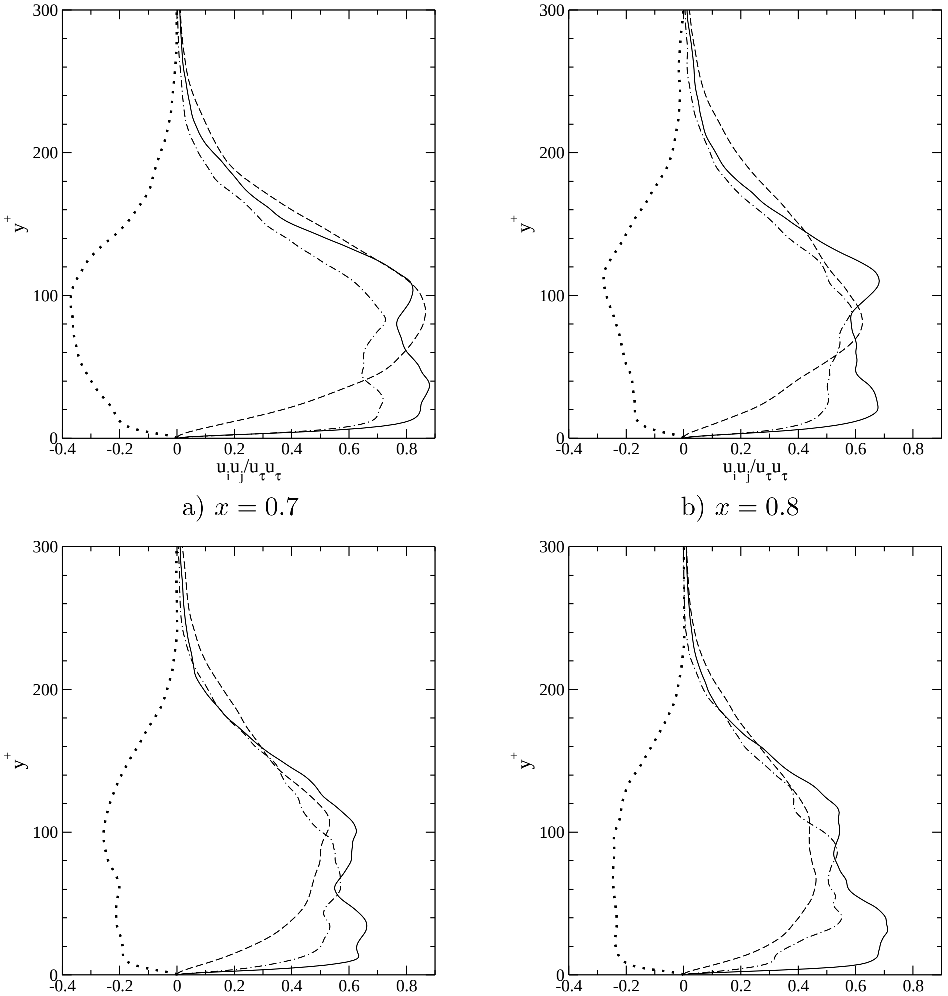

a) $x = 0.7$

b) $x = 0.8$

c) $x = 0.9$

d) $x = 0.99$

Figure 5.20: Reynolds-stresses for case 3DU, showing $\overline{u'u'}$ (—), $\overline{v'v'}$ (−−), $\overline{w'w'}$ (− ·) and $\overline{u'v'}$ (···), taken at x-locations indicated on the upper airfoil surface.

Chapter 6

The effect of incidence on separation bubble behaviour

6.1 Introduction

When an airfoil is subject to a change of incidence, the pressure distribution and the structure of the boundary layer will change in a coupled fashion. Where a laminar separation bubble is present, the system becomes more complex; the separation and reattachment points will translate, the boundary layer stability characteristics will alter and hence transition to turbulence will occur at a different streamwise location. The effect of increasing incidence on separation bubble behaviour is therefore complex.

Flat plate simulations have been proven able to reproduce experimental data by using suitable viscous-inviscid interaction based boundary schemes (Maucher *et al.*, 2000), however non-dimensional parameters (e.g. inlet δ^*) and the pressure distribution must be specified *a priori* and cannot vary significantly during the simulation. The velocity distribution in the potential flow region must be known beforehand and will be dependent not only on the airfoil geometry and incidence, but also the boundary layer properties, which will in turn depend upon transitional behaviour. Furthermore, any time-dependent behaviour related to changes in circulation about the airfoil will not be captured.

In this chapter the effect of incidence on separation bubble behaviour will be investigated by performing a further three-dimensional simulation at incidence $\alpha = 7°$, and comparing results to those observed at $\alpha = 5°$.

6.2 Simulation parameters

Similar methodology is employed for the simulation at $\alpha = 7°$, as for the three dimensional simulations at $\alpha = 5°$ presented in chapter 5. The computational domain is of the same dimensions, and the grid is generated with similar resolution and numbers of grid-points. The initial condition is generated in the same way, i.e. by running a precursory two-dimensional simulation and extruding the flowfield in the z-direction, however three-dimensionality is introduced in a different manner. The simulation is run at $Re_c = 5 \times 10^4$, $M = 0.4$, with time-step $\Delta t = 1.4 \times 10^{-4}$; selected results from the precursory two-dimensional simulation were given in chapter 4, section 4.4. The simulation is analogous to case 3DU, where no explicitly added forcing was present, except the airfoil incidence is $\alpha = 7°$. For the sake of conciseness the simulation will be referred to as simulation 3D7 henceforth. Where comparisons are made to results at $\alpha = 5°$, case 3DU is being referred to unless explicitly stated otherwise.

6.3 Grid properties

The grid used for simulation 3D7, denoted grid G7, was generated based on experience producing grids for the three-dimensional simulations at incidence $\alpha = 5°$ presented in chapter 5. Similar numbers of grid points and similar resolution were employed, although the precise distribution of grid-points over the airfoil surface has been modified to suit the differences in the flow at $\alpha = 7°$. In particular, the resolution is increased slightly in the region where transition is expected ($0.2 < x < 0.4$). Preliminary studies using XFoil Drela & Giles (1987) suggest that the time-averaged skin-friction in the turbulent region at $\alpha = 7°$ will not increase over that at $\alpha = 5°$, hence the grid-resolution will not need to be increased in this region in order to achieve the same resolution in wall-units. Grid parameters are given in tables 6.1, and the grid resolution at specified control points is the same as that of grid G3, given in table 4.4 section 4.3.1.

As for simulations at $\alpha = 5°$, during the initial stages of the 3D simulation flowfield properties were checked in order to confirm that all fluid structures appeared resolved and a final confirmation of adequate spatial and temporal resolution is provided by *a posteriori* statistical analysis of the DNS data. The maximum $\overline{c_f}$ observed was approximately the same as that of case 3DU, and hence the resolution in wall-units is approximately the same (section 5, table 5.1), and compares favourably with that of well-resolved plane-channel flow (Sandham *et al.*, 2002).

N_ξ	2587
N_ξ airfoil	1507
N_ξ wake	753
N_η	692
N_{total}	1790204
Wake length - W	5
Radius - R	5.3
Buffer length	0.6
Buffer points	31
Total domain length	12.2
Total domain height	10.6

Table 6.1: Grid parameters for grid G7.

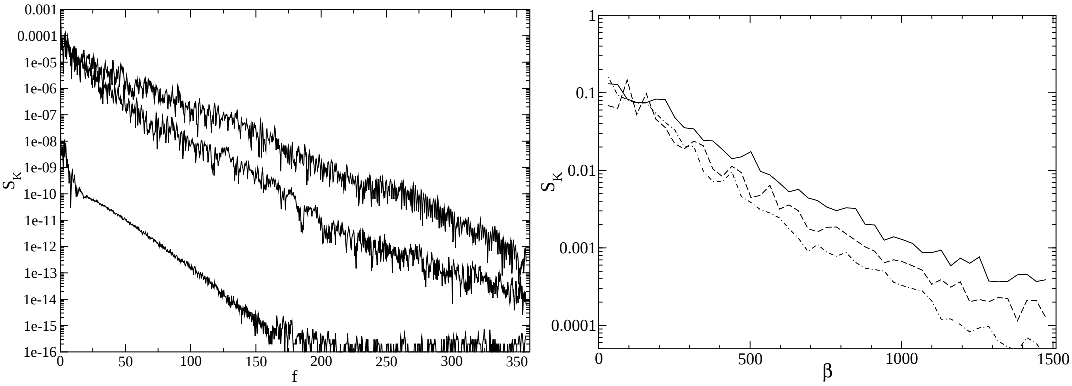

Figure 6.1: Temporal power spectra of K (left), taken at $x = 0.9$ at the airfoil mid-span for case 3D7 at $y^+ = 8.6$, $y^+ = 101$ and $y^+ = 238$ moving from top-to-bottom, and spanwise power spectra of K (right), integrated over the range $1 < y^+ < 50$, taken for the case at $\alpha = 7°$ at $x = 0.8$ (–), $x = 0.9$ (––), and $x = 1.0$ (– ·).

In order to confirm that turbulent behaviour is resolved over all time and length scales, power spectra of turbulence kinetic energy, K, are computed in the same manner specified in chapter 5, section 5.2. Figure 6.1 (left) displays spanwise power spectra of K taken at three x-locations. A decreased magnitude of roll-off is observed compared to cases at $\alpha = 5°$, however the spectra still compare reasonably well with Spalart (1988). Temporal power spectra of K at specific locations (figure 6.1, right) are computed using three segments and Hanning windowing (as detailed in section 2.3), and display a minimum roll-off of 10^6 with increasing frequency.

6.4 Simulation initialisation

The flowfield from the two-dimensional simulation at $\alpha = 7°$ presented in chapter 4 is extruded in the z-direction and used as the initial condition. No explicitly added time-periodic forcing is introduced, instead a narrow strip of w-

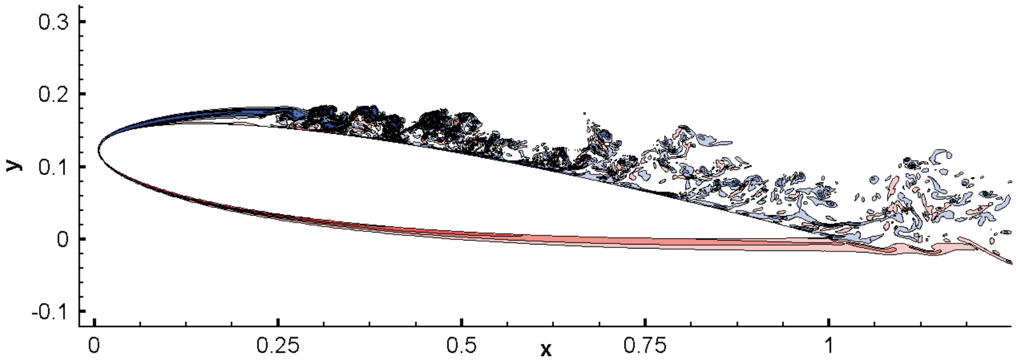

Figure 6.2: Iso-contours of spanwise vorticity for case 3D7, using 20 levels over the range ±200.

velocity perturbations in the form of white-noise is added at $t = 0$, at $(x, y) = (0.05, 0.153)$, and no further perturbations are added. Perturbations are added over an area of 3×3 grid-points in ξ and η, and span the entire domain. The simulation is progressed in time and behaviour is monitored by point readings of w-velocity. In this manner, should the simulation be stable to the initial perturbation, the simulation can be halted.

6.5 Time-dependent behaviour

Upon progressing the simulation the upper surface boundary layer is observed to be unstable to the initial perturbation, undergoing transition to turbulence within approximately two and a half non-dimensional time-units, and the transition process is observed to self-sustain as at $\alpha = 5°$. The structure of the flow field, including turbulent behaviour, is clearly illustrated by plotting iso-contours of vorticity (figure 6.2). Qualitative observations are that the bubble appears shorter, and the turbulent boundary layer thicker, than for case 3DU. Upon transition to turbulence, large amplitude, high frequency fluctuations in lift-coefficient associated with the irregular vortex shedding cease and the lift-coefficient increases (figure 6.3, left). The drag coefficients remain approximately the same (figure 6.3, right), although again the large amplitude, high frequency fluctuations cease. The simulation is progressed until $t \approx 16$, and statistical data is captured over the final 7.7 time-units, as for cases 3DF and 3DU.

Pressure is monitored at specific locations within the airfoil boundary layer, however point-pressure readings are unavailable for the first 2.8 time units, since during this time w-velocity was monitored instead (discussed in chapter 8, section 8.5). At $x = 0.6$ the pressure signal is appears random, and is characteristic of the passage of turbulent flow. At $x = 0.2$, within the separated shear layer,

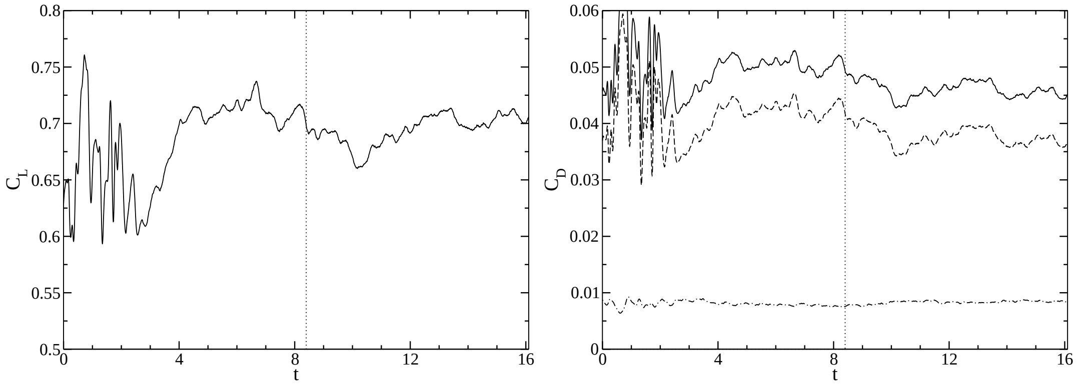

Figure 6.3: Time-dependent lift-coefficient (left) and time-dependent drag coefficients (right) for case 3D7. The shaded area indicates the period for which statistics were taken, right hand image shows skin-friction drag (—·), pressure-drag (– –) and total drag (—).

pressure oscillates but with a seemingly more narrow frequency content.

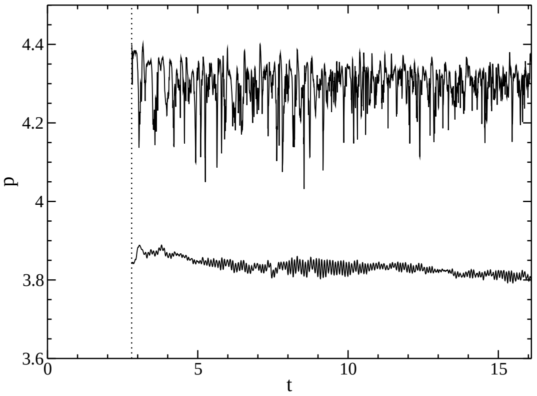

Figure 6.4: Time dependent pressure within the boundary layer at $x = 0.2$ (lower curve) and $x = 0.6$ (upper curve) for case 3D7.

Fluid structures present in the transition region are illustrated by plotting iso-surfaces of the second invariant of the velocity gradient tensor, Q (figure 6.5). Large structures are observed to break down very rapidly to small scale turbulence. The large structures do not appear to be orientated in the spanwise direction as for case 3DU. Interestingly, at $t = 10.5$ the largest structure present appears oblique in nature, being aligned approximately $\phi = 14^\circ$ to the z-axis. Caution should be exercised before assuming this behaviour is always present however, since if the same quantity is plotted at time $t = 11.2$ (figure 6.5, right), the behaviour is not clearly observed. Upon breakdown to turbulence a variety structure scales are visible, however the behaviour appears highly disordered and no regularly occurring coherent structures are observed, e.g. Λ-vortices.

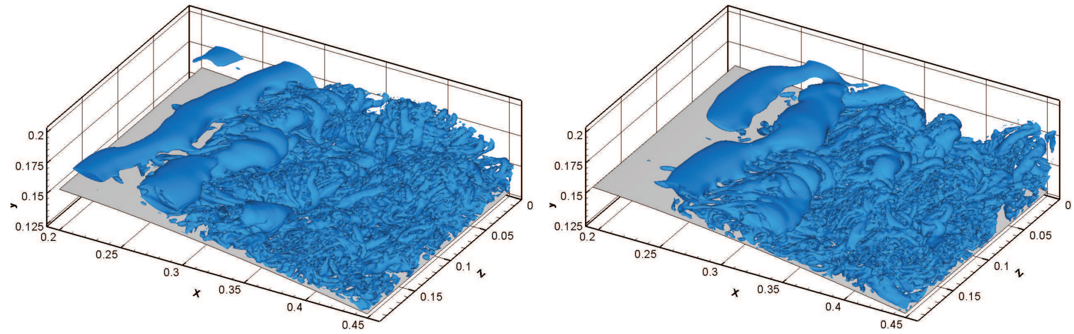

Figure 6.5: Iso-surfaces of $Q = 500$ for case 3D7, taken in the transition region at time $t = 10.5$ (left) and $t = 11.2$ (right).

Case	C_L	C_D	C_{DF}	C_{DP}
2D	0.648	0.0498	0.0082	0.0416
3D7	0.694	0.0461	0.0083	0.0377
3DU	0.621	0.0358	0.0081	0.0278

Table 6.2: Time-averaged lift and drag coefficients for cases 3DU, 3D7, and the two-dimensional simulation at $\alpha = 7°$.

6.6 Statistical analysis

The time-averaged lift and drag-coefficients for case 3D7 and 3DU are given in table 6.2. The increased incidence over case 3DU results in increased lift-coefficient and pressure drag-coefficient, and a reduction in the lift-to-drag ratio. The time-averaged skin-friction coefficient and pressure-coefficient distributions are plotted in figure 6.6. The time-averaged skin-friction coefficient distribution illustrates that increasing the incidence has decreased the length of the separation bubble. The separation point has moved upstream from 0.099 to $x = 0.0489$, and the reattachment point has moved upstream from 0.607 to 0.390, hence the total bubble length has decreased from 0.508 to 0.341. Accordingly, the time-averaged pressure coefficient distribution exhibits a shorter pressure plateau associated with the separation bubble, which also possesses greater pressure magnitude than for case 3DU. The negative skin-friction peak just before reattachment is greater in magnitude than for case 3DU, suggesting that the reverse-flow vortex is stronger in magnitude. The maximum reverse flow observed in the time-averaged flowfield is 17.9%, significantly greater than that observed at 5° (15.2%) which would appear to confirm that this is the case. Visual inspection suggests that the skin-friction and pressure coefficient distributions exhibit very slight local maxima at the rear of the separation bubble, reminiscent of those observed for the two-dimensional simulation, at $x = 0.275$ for skin-friction, and $x = 0.3$ for pressure.

Case	x_{sep}	x_{reatt}
2D	0.053	0.402
3D7	0.049	0.390
3DU	0.099	0.607

Table 6.3: Time-averaged separation and reattachment points for cases 3DU, 3D7, and the two-dimensional simulation at $\alpha = 7°$.

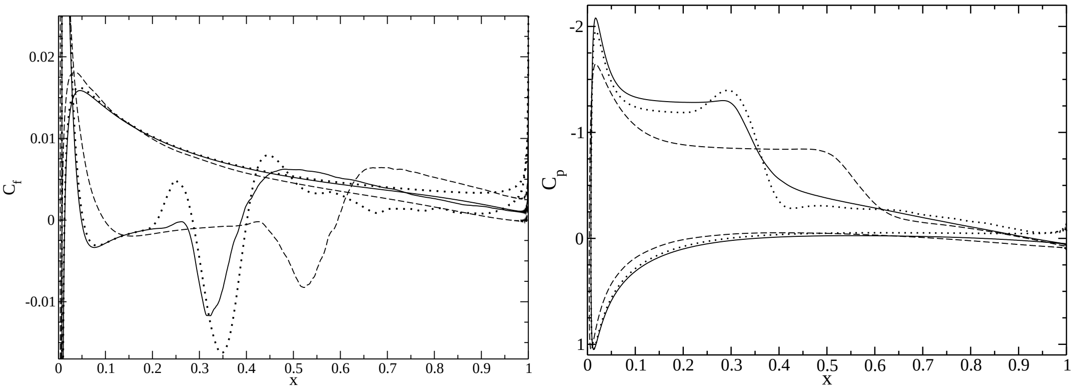

Figure 6.6: Time-averaged skin-friction coefficient distribution (left) and pressure coefficient distribution (right) for cases 3DU (−−), 3D7 (—), and the two-dimensional simulation at $\alpha = 7°$ ($\cdots$).

The time-averaged displacement thickness grows more rapidly with increasing x-location at $\alpha = 7°$ than at $\alpha = 5°$ due to the stronger adverse pressure gradient. This is true both for the laminar separated region, and for the turbulent boundary layer. The peak displacement thickness before transition and reattachment is larger at $\alpha = 5°$ however. Momentum thickness across the separated shear-layer varies minimally from case to case. Upon transition the momentum thickness increases rapidly and at an approximately similar rate with increasing x for both case 3DU and case 3D7. The shape factor $H = \delta^*/\theta$ increases more rapidly over in the turbulent boundary layer for case 3D7 than for case 3DU, as a result of the stronger adverse pressure gradient. This would imply a greater tendency toward separation in this region.

Probability density functions of skin-friction were computed using the same method as in 5, section 5.5.2, and are plotted in figure 6.8 for both the two and three-dimensional cases at $\alpha = 7°$. The PDFs appear qualitatively similar to those at $\alpha = 5°$, consisting of a smooth symmetric distribution about the mean skin-friction. Again, the skin-friction is most unsteady in the transition region at the rear of the separation bubble. The skin-friction PDF at reattachment (figure 6.8, left) again shows that comparatively large non-zero values of skin-friction regularly occur here, even though the time averaged skin-friction is zero; the time-averaged skin-friction coefficient varies over the range $\pm 2 \times 10^{-2}$, compared to a peak value of 6.2×10^{-3} in the turbulent region. Both the size and shape of

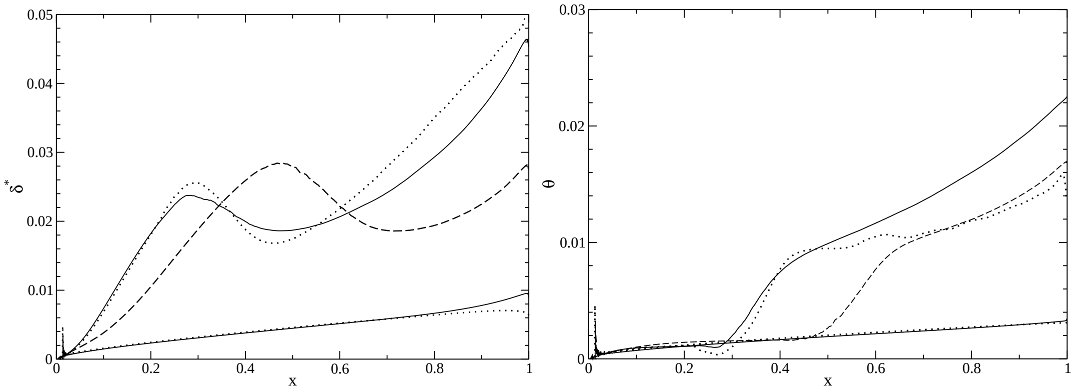

Figure 6.7: Time-averaged displacement-thickness distribution (left) and momentum-thickness distribution (right) for cases 3DU (−−), 3D7 (—), and the two-dimensional simulation at $\alpha = 7°$ ($\cdots$).

the skin-friction PDF at this location appear remarkably similar to case 3DU. At $x = 0.85$, (figure 6.8, left) the skin-friction PDF is significantly narrower for $\alpha = 7°$ than for $\alpha = 5°$, indicating that the time-dependent behaviour is more steady. The time-averaged skin-friction (figure 6.6) is lower at this location for $\alpha = 7°$, hence the skin-friction is negative at this location for a greater percentage of time. Although the flow is attached in the mean, the stronger adverse pressure gradient increases the probability that instantaneous separation will occur when compared to the equivalent case at $\alpha = 5°$.

The skin-friction PDF of the two-dimensional simulation at $\alpha = 7°$ appears different to that at $\alpha = 5°$. The PDF at $\alpha = 5°$ contained several regions where there appeared to be two PDF maxima at a given x-location, and the PDF exhibited a wave-like pattern similar to that observed in time-averaged skin-friction distributions. At $\alpha = 7°$ there appear to be two maxima at $x \approx 0.35$, however downstream of the onset of vortex shedding there appears to be only one maxima present at any given x-location, and no wave-like patterns are present. The differences between the two-dimensional cases can probably be attributed to the different vortex shedding behaviour observed; at $\alpha = 5°$ the vortex shedding was regular and periodic, whereas at $\alpha = 7°$ the vortex shedding occurred at a range of frequencies. Comparing the two-dimensional skin-friction PDF at reattachment and at $x = 0.65$ to that of the three-dimensional simulation reveals that although only one maximum is present for the two-dimensional case, the PDF is fundamentally different in that it is significantly skewed at both locations. Interestingly, the skin-friction PDF of the two-dimensional case indicates that the separated shear-layer is much more unsteady than for the three-dimensional simulation, as illustrated by the increased thickness in the region $0.1 \geq x \geq 0.2$ (figure 6.8, top). It seems likely that the large-scale vortex shedding motion exerts greater influence on the laminar region than the smaller scale unsteadiness present when vortex shedding is suppressed by transition to turbulence. A similar tendency to increased unsteadiness can be observed at $\alpha = 5°$, however the increase is only very slight at that incidence.

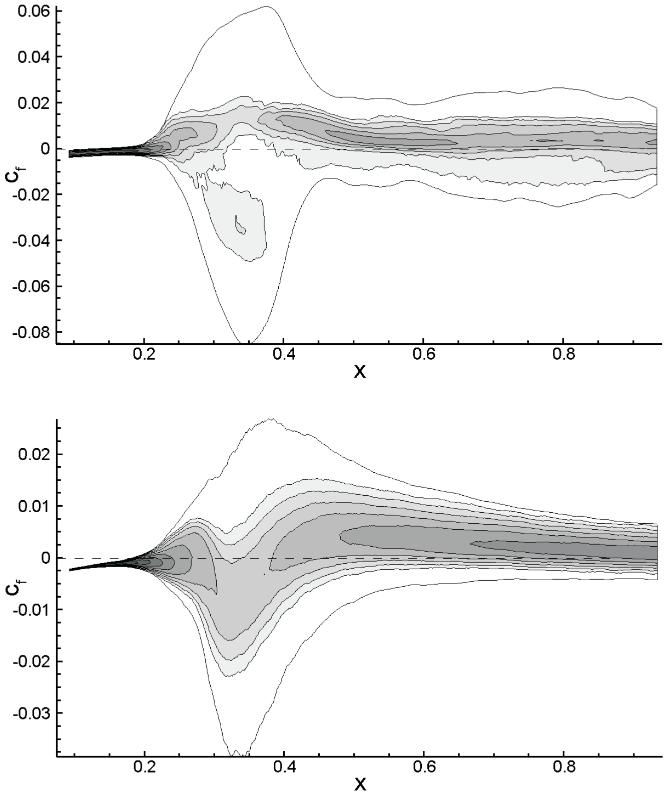

Figure 6.8: Iso-contours of the normalised c_f PDF, $n/(S(x)n_t)$, both the two-dimensional (top) and three-dimensional (bottom) case at $\alpha = 7°$, using 12 levels exponentially distributed over the range 2 to 1000.

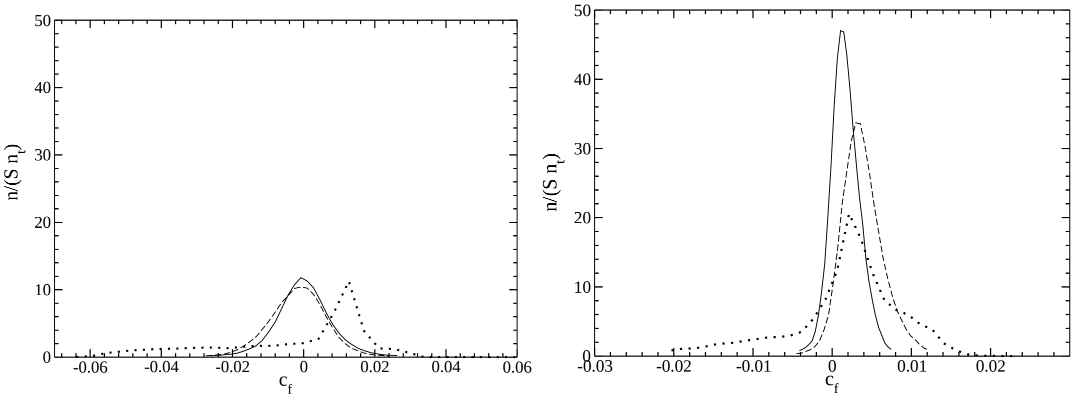

Figure 6.9: Probability density functions of c_f taken at reattachment (left), and at $x = 0.85$ (right) for cases 3DU (−−), 3D7 (—), and the two-dimensional simulation at $\alpha = 7°$ ($\cdots$).

Two-point spanwise correlations of surface pressure are computed as described in chapter 5, section 5.5.2, and are plotted in figure 6.10. At $x = 0.1$ there is strong spanwise correlation, suggesting that boundary layer fluctuations are primarily two-dimensional in this region. At $x = 0.2$ less correlation is observed, which is expected since three-dimensional perturbations are expected to be amplified over the extent of the separated shear layer. At $x = 0.3$, however, there is significant negative spanwise correlation. Negative correlation was observed throughout the separated region for case 3DF, and was attributed to the presence of forcing with spanwise wavenumber equal to the domain width, however no forcing was introduced for $\alpha = 7°$. By $x = 0.4$ the flow exhibits near zero spanwise-correlation, indicating that the flow is fully three-dimensional and that the domain is sufficiently wide such that the turbulence is not constrained in the z-direction. Downstream of $x = 0.4$ the spanwise correlation increases with increasing x-location.

The two unexpected features of the spanwise correlation are the negative correlation observed at $x = 0.3$, and the tendency for the flow to become more correlated with increasing x-location in the region $0.4 < x < 1$. The presence of negative correlation in the transition region perhaps suggests that in the early stages of transition some form of disturbance mode is present with spanwise wavelength $\lambda = L_z$. Three-dimensional plots of Q (figure 6.5) illustrate behaviour that, should it occur regularly, may explain the anti-correlation. Figure 6.5a displays oblique structures orientated at approximately 14° to the z-axis. Since these structures are periodic in the z-direction, at a given x-location the flow at $z = 0$ will be out of phase with the flow at the mid-span. Therefore, if this behaviour occurs for an appreciable percentage of time, the phase difference will result in anti-correlation. The nature of boundary layer fluctuations in the transition region was investigated by computing Fourier transforms of the time-dependent surface pressure. Plotting the real coefficient for specific frequencies revealed that in addition to predominantly two-dimensional boundary layer disturbances, oblique modes are indeed also present. This is illustrated in figure 6.11. Given three frequencies that differ only slightly, three distinct perturbation forms are observed; an oblique mode with positive phase angle, an oblique mode with negative phase angle and a mode with zero phase angle. The occurrence of this behaviour is expected, since weakly oblique modes are only marginally more stable than two-dimensional fluctuations (Dovgal, Kozlov & Michalke, 1994). The finite spanwise domain width, in conjunction with the presence of oblique modes appears responsible for the negative correlation observed.

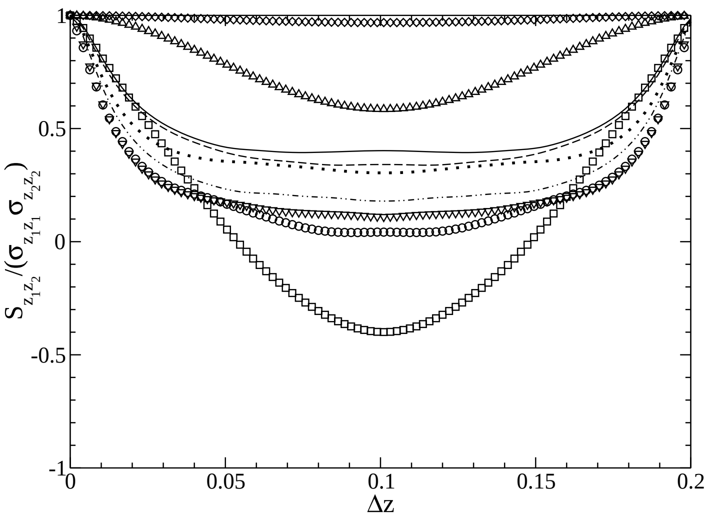

Figure 6.10: Two-point spanwise correlations of surface pressure for the case at $\alpha = 7°$, at x-locations 0.1 (◇), 0.2 (△), 0.3 (□), 0.4 (○), 0.5 (▽), 0.6 (− · ·), 0.7 (· · ·), 0.8 (−−), and 0.9 (—).

The increased correlation with x-location in the region $0.4 < x < 1$ may interpreted two ways. It could be conceived that the increase in correlation is in fact physical and that the turbulence is exhibiting increased spanwise coherence as for case 3DU. The absence of large scale structures exhibiting spanwise coherence, as observed for case 3DU (chapter 5), would not tend to support this argument however. The second interpretation would be that the spanwise domain width is affecting the physics of the flow. The boundary layer is increasing in thickness in this region due to the adverse pressure gradient present. This means that the largest length scale associated with the turbulent boundary layer is also increasing, hence it is possible that the computational domain begins to constrain the turbulence in the z-direction in this region. At the trailing edge the displacement thickness is $\delta^* = 0.05$, and hence the domain width is equal to $4\delta^*$. It should be noted however that compared to simulations presented in chapter 5, the ratio of spanwise domain width to separation bubble length has in fact increased.

The time-averaged turbulent kinetic energy, K, is plotted in figure 6.12, and the variation of y-maximum K with x-location is plotted in figure 6.13. The peak K occurs at $x = 0.33$, just downstream of the vortex shedding location in the two-dimensional simulation. The peak K observed is significantly greater in amplitude than for case 3DU, however downstream of transition K decreases more rapidly than for case 3DU. The decay rate of K decreases with increasing x-location, and K appears to almost, but not quite, reach $dK/dx = 0$ at $x = 1$.

Boundary layer profiles for the laminar region of case 3D7, normalised by

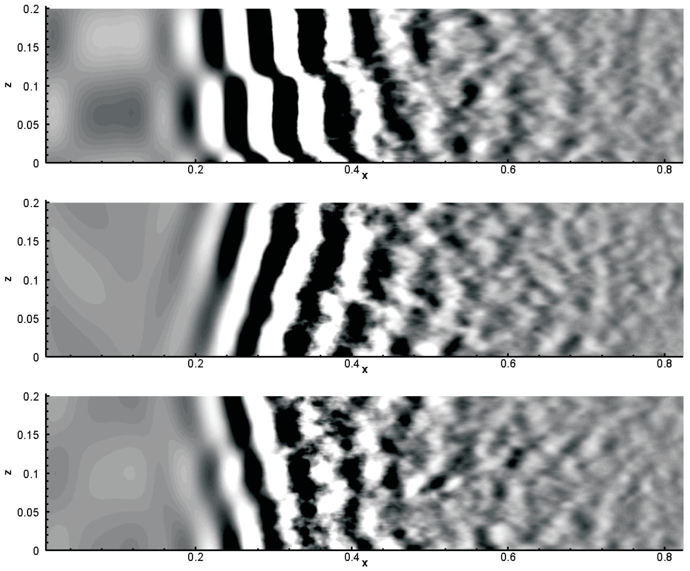

Figure 6.11: Iso-contours of the real-coefficient of the Fourier transformed surface pressure at frequencies $f = 11.04$ (top), $f = 11.17$ (middle) and $f = 11.29$ (bottom), showing the range $\pm 5 \times 10^{-3}$.

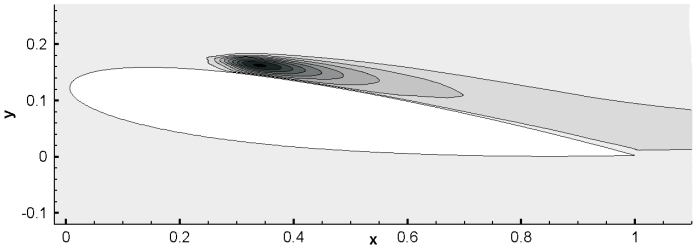

Figure 6.12: Iso-contours of turbulence kinetic energy, K, for case 3D7, using 20 levels over the range 0 to 0.16.

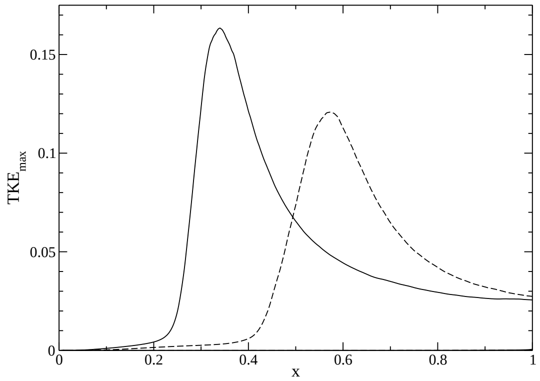

Figure 6.13: Variation of the y-maximum turbulent-kinetic energy, K, with x-location for case 3DU (−−)and 3D7 (—).

the displacement thickness and edge-velocity, are plotted in figure 6.14 (left). A measure of the shear-layer strength is given by the maximum du/dy observed, which for case 3D7 is 2.32 (at $x \approx 0.25$), compared to 2.20 (at $x \approx 0.4$) for

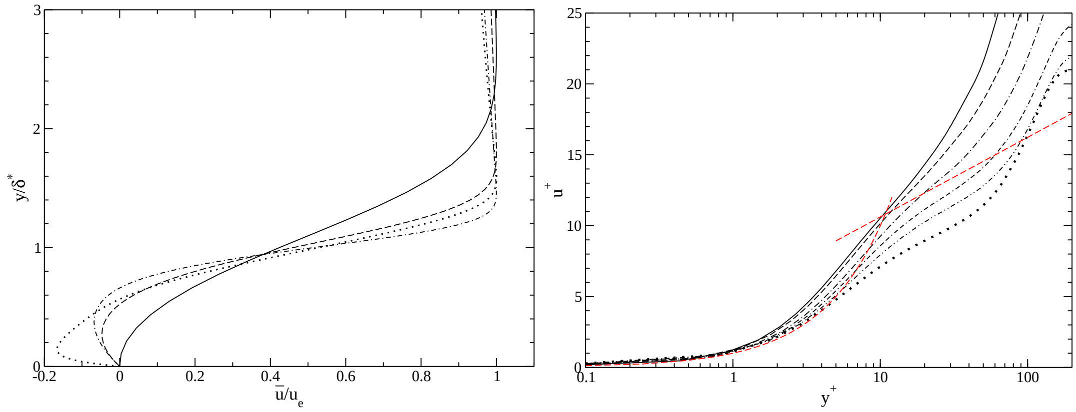

Figure 6.14: Time-averaged boundary layer profiles taken at selected x-locations within regions of laminar flow, non-dimensionalised with displacement thickness (left) showing $x = 0.05$ (——-), $x = 0.1$ ($--$), $x = 0.2$ ($-\cdot$) and $x = 0.3$ ($\cdots$), and at selected x-locations within regions of turbulent flow, scaled in wall-units (right) showing $x = 0.5$ (——-), $x = 0.6$ ($--$), $x = 0.7$ ($-\cdot$), $x = 0.8$ ($--\cdot$), $x = 0.9$ ($-\cdot\cdot$) and $x = 0.99$ ($\cdots$) for case 3D7. Red lines show $u^+ = y^+$ and $u^+ = 1/0.41 \log(y^+) + 5$.

case 3DU. This suggests that the laminar region will be slightly more unstable, and exhibit a slight increase in tendency toward absolute instability (Rist & Maucher, 2002). The effect of increasing incidence from $\alpha = 5°$ to $\alpha = 7°$ upon shear layer strength appears modest compared to the effect of adding boundary layer disturbances however (chapter 5). As for case 3DF, velocity profiles in the vicinity of the maximum reverse flow location exhibit decreased shear-layer strength when compared to profiles located just upstream. Boundary layer profiles extracted from the turbulent regions of case 3D7 are plotted in figure 6.14 (right), using turbulent scaling. As for simulations at $\alpha = 5°$, at no point does the boundary layer appear to be approaching log-law behaviour.

Reynolds stresses are plotted using wall-scaling in figure 6.15 at locations within the turbulent region for case 3D7. For case 3DU two peaks were observed in $\overline{u'u'}$; one near the wall, at $x^+ \approx 20$, and one at $y^+ \approx 100$. For case 3D7 $\overline{u'u'}$ appears greatest at $y^+ \approx 70$ at all locations, and the near-wall peak appears hard to discern. In any event, $\overline{u'u'}$ is noticeably lower in the vicinity of the wall than at $y^+ \approx 70$. It appears that at this incidence turbulent fluctuations associated with mixing-layer type behaviour are stronger than near-wall fluctuations associated with a developing turbulent boundary layer, more so than for case 3DU.

6.7 Summary

The effect of incidence upon separation bubble behaviour was investigated by performing a direct numerical simulation of the flow around a NACA-0012 airfoil at seven degrees incidence in three-dimensions, thus complementing the simulations performed at five degrees presented in chapter 5. A low-amplitude perturbation was introduced at initialisation, in order to introduce three-dimensionality, and no further disturbances were added. The upper surface boundary layer was observed to be unstable to the initial perturbation, undergoing transition to turbulence, and the transition process was observed to self-sustain as at $\alpha = 5°$. Although the transition process appears more energetic at $\alpha = 7°$, the turbulent fluctuations appeared to decrease in intensity more rapidly in the streamwise direction than at $\alpha = 5°$. Reynolds stress profiles taken in the turbulent region suggest that near-wall fluctuations are weaker in amplitude than fluctuations away from the wall. Oblique instability waves were observed in the transition region, which led to negative correlation of surface pressure in this region.

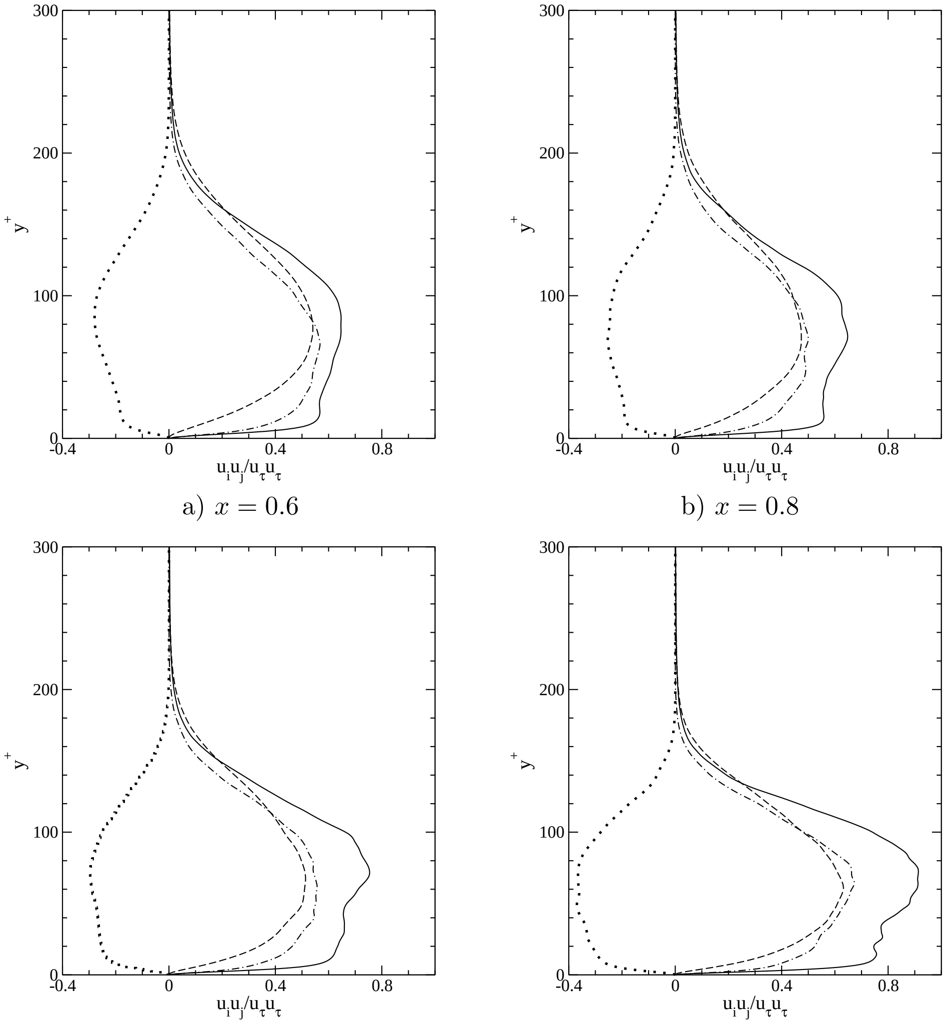

a) $x = 0.6$ b) $x = 0.8$

c) $x = 0.9$ d) $x = 0.99$

Figure 6.15: Reynolds-stresses for case 3D7, showing $\overline{u'u'}$ (—), $\overline{v'v'}$ (– –), $\overline{w'w'}$ (– ·) and $\overline{u'v'}$ (· · ·), taken at x-locations indicated on the upper airfoil surface.

Chapter 7

Stability analysis of the time-averaged flowfields

7.1 Introduction

Having performed simulations of both forced and unforced separation bubbles at 5° incidence in chapter 5, and of an unforced separation bubble at 7° incidence in chapter 6, the time-averaged flowfields extracted from these simulations can be investigated in terms of their stability characteristics. The goal of this chapter is to determine the stability characteristics of the separation bubbles, and to determine whether any regions of absolute instability are present that may explain the self-sustaining turbulence observed at both 5° and 7°. In order to achieve this, a combination of linear stability analysis and forced Navier–Stokes simulations is employed.

7.2 Linear stability analysis

Linear stability analysis of the time-averaged flowfield is comparatively inexpensive and can be used to investigate both absolute and convective instability behaviour. The assumption of parallel flow is made in deriving the Orr–Sommerfeld equation (the governing equation of the linear stability analysis performed here, see section 2.4), however despite this it is commonplace to perform linear stability analysis on nonparallel flows, including separation bubbles. Results from such studies have been found to agree well with both numerical simulation (Bestek, Gruber & Fasel, 1989) and experimental data (Lang, Rist & Wagner, 2004).

Performing convective stability analysis allows recovery of the so-called 'N-factor', the maximum amplification ratio of instability waves across the separation bubble. This parameter is critical to the e^N transition prediction model, as used in XFoil (Drela & Giles, 1987), and gives an indication of the sensitivity of the bubble to background turbulence levels. The frequency of the most unstable disturbance waves may also be determined, which not only aids in selecting forcing frequencies to promote transition to turbulence (as in section 5.4), but may potentially be relevant to the frequency content of acoustic radiation at the airfoil trailing edge (McAlpine *et al.*, 1999). It has long been conjectured as to whether regions of local absolute stability exist within separation bubbles, hence it is of interest to determine whether any regions of absolute instability are present, and whether absolute instability plays any role in the self-sustaining transition to turbulence observed at both 5° and 7°.

7.2.1 Convective stability characteristics

The convective stability characteristics of the three-dimensional separation bubbles presented in chapters 5 and 6, and the equivalent two-dimensional bubbles, have been investigated by solving the spatial Orr–Sommerfeld problem (chapter 2, section 2.4) for velocity profiles extracted from the time-averaged flowfield, starting at a location near the airfoil leading-edge and traversing to beyond the reattachment point in each case. At each x-location a range of real disturbance frequencies was specified, for which the code returns the associated complex wavenumber (α), the imaginary part of which corresponds to the spatial growth rate of the instability wave. Assuming an initial disturbance amplitude of 1 at $x = 0.05$, disturbances are then integrated spatially across the bubble using an Euler method, to determine an 'N-factor' for each disturbance frequency, i.e. $\ln(A/A_0)$, where A_0 is the initial disturbance amplitude and A is the disturbance amplitude at some point of interest.

Results are summarised in figure 7.1 for cases at five degrees incidence noting that, although only eight frequencies are plotted, calculations were performed for sixteen frequencies in total, over the same range. Only half of the data is plotted for the sake of clarity. Images on the left display the variation of spatial growth rate, -α_{i}, with x for all frequencies and hence indicate how the stability of travelling waves varies. Images on the right display how the N-factor of instability waves varies with x and frequency.

The maximum spatial growth rate of instability waves computed for case 3DF and the two-dimensional case are similar at -$\alpha_i \approx 32$, however for case 3DU the maximum spatial growth rate is significantly larger at $-\alpha_{\mathrm{i}} \approx 40$, immediately suggesting that the separated region in case 3DU is more unstable than either the two-dimensional case or case 3DF. The frequency of the instability wave with the largest spatial growth rate appears to vary from case to case. For the

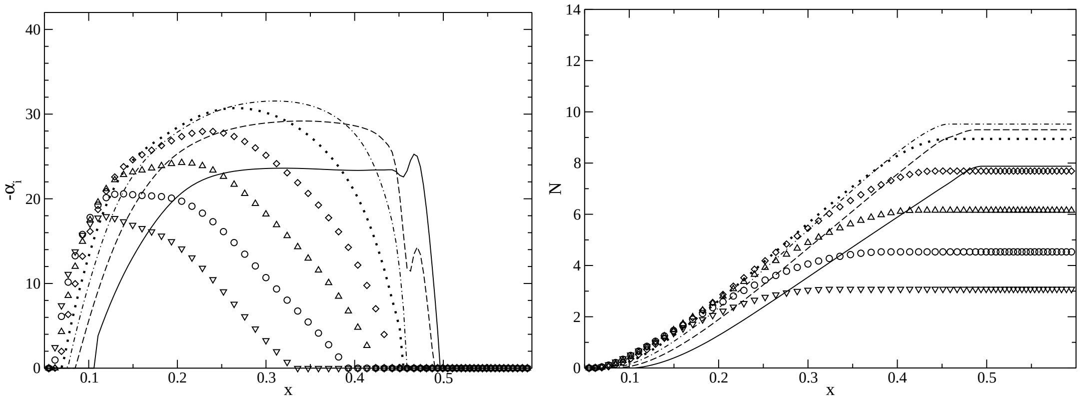

a) The two-dimensional case at $\alpha = 5^\circ$

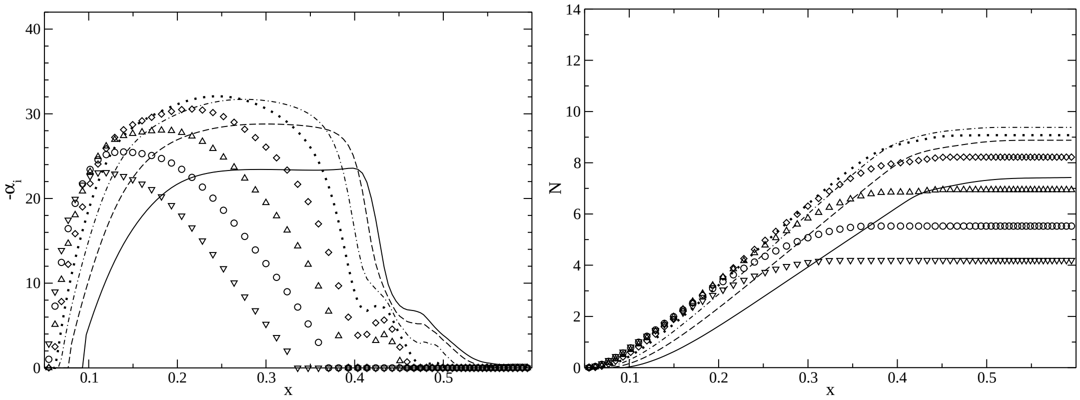

b) Case 3DF

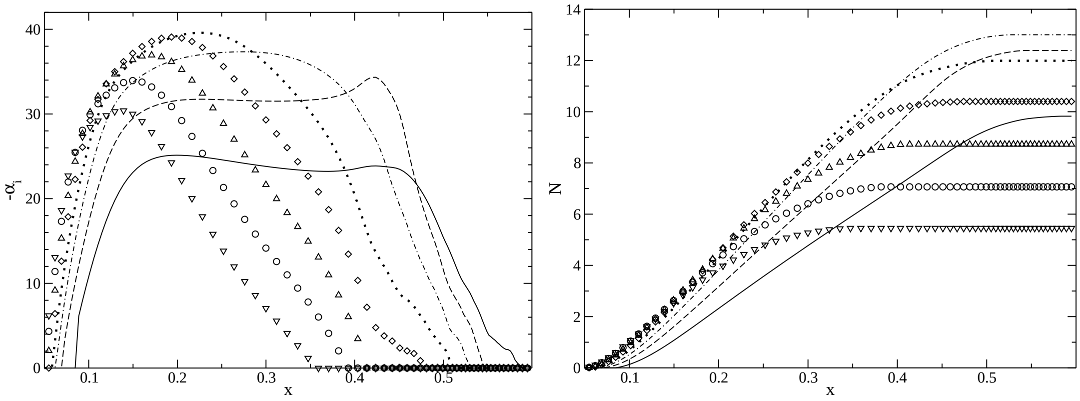

c) Case 3DU

Figure 7.1: Variation of spatial growth rate with x (left), and variation of N-factor with x (right) for the two-dimensional simulation, case 3DF and case 3DU, at frequencies $f = 4.24$ (—), $f = 6.37$ (– –), $f = 8.49$ (–·), $f = 10.61$ (···), $f = 12.73$ ($\diamond$), $f = 14.85$ ($\triangle$), $f = 16.98$ ($\circ$), and $f = 19.10$ ($\triangledown$).

two-dimensional case the peak growth rate occurs for frequency $f = 8.49$. For cases 3DF and 3DU the peak growth rate occurs for frequency $f = 10.61$. For all frequencies computed $\alpha_{\rm i}$ is either zero or very small amplitude for all frequencies at $x = 0.05$. This implies that N-factor across the bubble and the frequency of the most amplified instability wave would not change if the starting point of the stability analysis was moved further upstream. The neutral point as regards convective instability appears to be $x \approx 0.06$ for all cases.

Despite variations in the frequency of the instability wave with the maximum $\alpha_{\rm i}$, the frequency of the instability wave with the highest N-factor (i.e. the most amplified instability wave across the bubble) is approximately $f = 8.49$ ($\omega = 53.3$) for all cases. This justifies the selection of similar forcing frequencies ($f = 7.76$ and 5.53, or $\omega = 48.76$ and 53.6) for the simulation presented in section 5. It can be seen that whilst case 3DF and the two-dimensional case exhibit similar maximum N-factors of around 9.5, for case 3DU the maximum N-factor is much larger at around 13. It appears then, that whilst case 3DF and the two-dimensional case are comparatively similar in terms of convective instability growth rates, case 3DU is significantly more unstable. Upon removing the forcing, the stability characteristics of case 3DU actually deviate further from both the two-dimensional simulation and case 3DF. It should be noted that the frequency of the greatest N-factor disturbance wave for the two-dimensional case at $\alpha = 5°$ ($f = 8.49$) is much higher than that of the vortex shedding which occurs at $f = 3.37$. This suggests that the vortex shedding behaviour is not caused by convective amplification of instability waves, in contrast with Pauley *et al.* (1990) who, for a separation bubble induced on a flat plate, found the frequency of the most-amplified instability wave to agree with that of the vortex shedding present. It should be noted that, for all cases, the N-factors observed are too small to amplify round-off error ($\sim 1 \times 10^{-16}$) to non-linear amplitudes ($\sim 1 \times 10^{-2}$). This appears to discount amplification of round-off error as a possible route to transition to turbulence.

Amplification rates and N-factors for simulations at seven degrees incidence are plotted in figure 7.2. Again, images on the left display the variation of spatial growth rate, -$\alpha_{\rm i}$, with x-location whilst images on the right display how the N-factor of instability waves varies with x-location. It is apparent that at $\alpha = 7°$ the maximum convective growth rate of instability waves is significantly greater than at $\alpha = 5°$ (-$\alpha_{\rm i} \approx 60$, as opposed to -$\alpha_{\rm i} \approx 40$), and that higher frequency disturbances are more unstable than at $\alpha = 5°$. The most unstable disturbance frequency is $f = 19.10$ and the disturbance frequency with the largest N-factor is $f = 12.73$, compared to $f = 10.61$ and $f = 8.49$ respectively for case 3DU. The increased growth rates may be attributed to the increased velocity gradient within the separated shear layer at $\alpha = 7°$. The manner in which convective stability characteristics change between the two-dimensional simulation and case 3D7 appears qualitatively similar to that observed at $\alpha = 5°$; the three-dimensional simulation exhibits increased instability growth rates and an increased N-factor over the separated region. For both cases at $\alpha = 7°$ the neutral point appears to be located at $x \approx 0.04$.

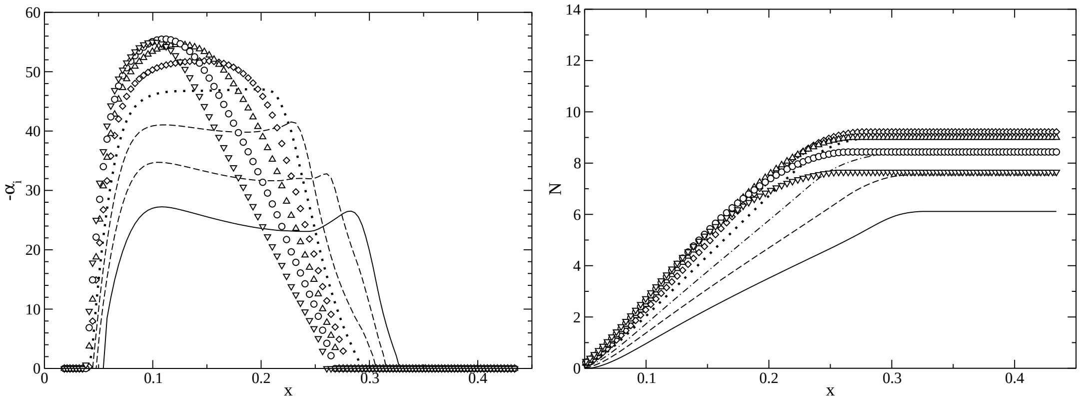

a) The two-dimensional case at $\alpha = 7°$

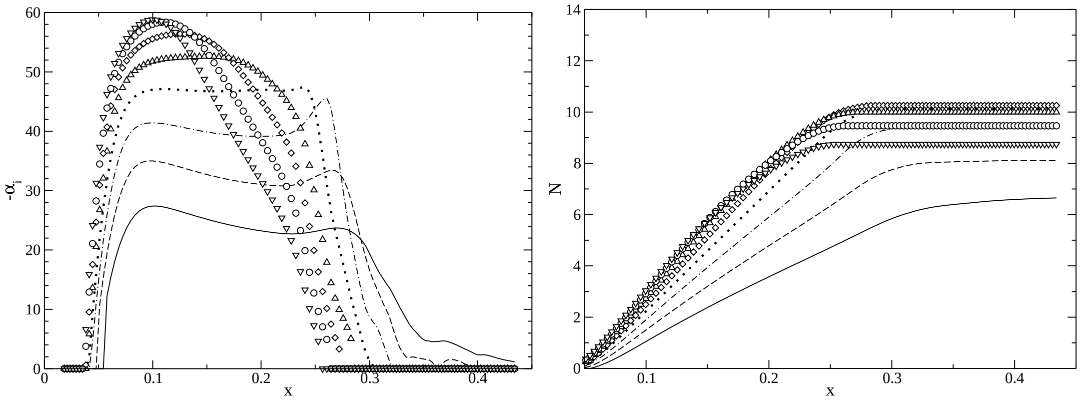

b) Case 3D7

Figure 7.2: Variation of spatial growth rate with x (left), and variation of N-factor with x (right) for case 3D7 and the corresponding two-dimensional simulation, at frequencies $f = 4.24$ (—), $f = 6.37$ (– –), $f = 8.49$ (–·), $f = 10.61$ (· · ·), $f = 12.73$ (◇), $f = 14.85$ (△), $f = 16.98$ (○), and $f = 19.10$ (▽).

7.2.2 Cusp-map analysis

The time and span-averaged flowfields of cases 3DF, 3DU and 3D7, as well as the time-average of the corresponding two-dimensional simulations, have been analysed using the Orr-Sommerfeld solver in conjunction with the cusp-map method (chapter 2, section 2.4.5) in order to determine whether any regions of local absolute instability are present. For each case the complex α plane was swept with a resolution of $\Delta\alpha_r = \Delta\alpha_i = 1$. The corresponding resolution in the complex ω plane is much higher in the vicinity of a branch-point, since $\partial\omega/\partial\alpha \approx 0$. Branch point singularities associated with zero group-velocity instability waves were then tracked, traversing the upper airfoil surface from $x = 0.1$ until it was no longer possible to locate any branch-point within the complex ω plane. Imaginary parts of the complex frequency associated with $c_g = 0$ are plotted in figure 7.3 for cases 3DF and 3DU, and in figure 7.4 for case 3D7. In all cases, as the $c_g = 0$ instability wave is tracked downstream, ω_i increases with x, until a maximum value is reached toward the rear of the separation bubble. After reaching this maximum value, ω_i decays with further increase in x. For all cases, at all locations analysed, ω_i associated with the singularity is negative, hence there is no evidence that absolute instability is present. Interestingly however, the location at which the strongest tendency towards absolute instability is observed (i.e. when the $c_g = 0$ wave is least damped) appears not to be the location at which the reverse flow is strongest. For case 3DF the maximum ω_i is observed at $x = 0.413$, for case 3DF at $x = 0.425$ and for case 3D7 at $x = 0.263$. For all cases the location of maximum ω_i is significantly upstream of the maximum reverse flow location, but does however correspond (approximately) to the region at which the maximum shear-layer strength was observed (chapter 5, section 5.5.2 and chapter 6, section 6.6).

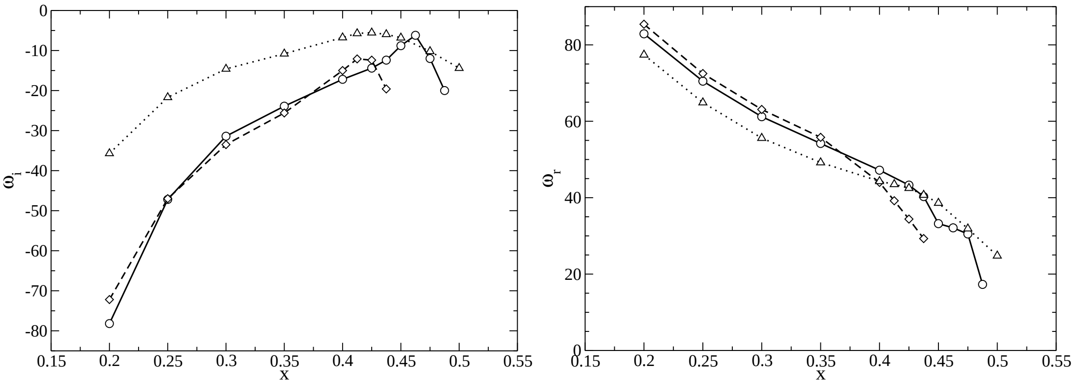

Figure 7.3: Variation with x of ω_i (left) and ω_r (right) associated with $c_g = 0$, for the two-dimensional case at $\alpha = 5°$ (○—○), case 3DF (◇ – –◇) and case 3DU (△ ··· △).

For each simulation, a branch point could not be located downstream of a certain x-location, unique to that case. Downstream of this location, the Orr-Sommerfeld solver returned trivial solutions for regions of the complex α sweep. Contours of u', defined as $u' = u - \overline{u}$, illustrate that for all cases the flowfield is

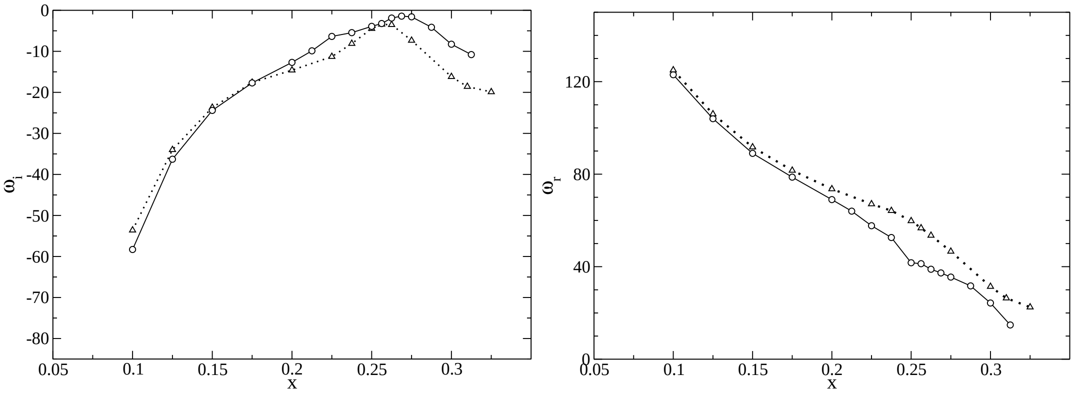

Figure 7.4: Variation with x of $\omega_{\rm i}$ (left) and $\omega_{\rm r}$ (right) associated with $c_g = 0$, for the two-dimensional case at $\alpha = 7°$ (○—○), and case 3D7 (△ ··· △).

already highly unsteady at the x-position at which the solver fails (figure 7.5). Depending on the case, u' and v' lie in the range 0.3-0.7 at the point where the solver fails. The time-averaged velocity profiles in this region will therefore be the average of a series of very different velocity profiles produced under unsteady flow conditions, and hence will not necessarily be solutions to the Navier–Stokes equations. This is not a problem in itself for the Orr–Sommerfeld solver; given a velocity profile the solver should return all unstable modes, it is not affected by whether the velocity profile is a solution of the Navier–Stokes or otherwise. A problem does occur however if unexpected or unphysical behaviour exists in the time-averaged velocity profile which causes the cusp-map method to fail.

By way of example, we shall consider the time-averaged velocity profile extracted at $x = 0.53$ (where the cusp-map method fails) from the two-dimensional simulation at $\alpha = 5°$, illustrated in (figure 7.6, left). The velocity profile exhibits near constant $d\overline{u}/dy$ over a finite region, which results in $d^2\overline{u}/dy^2$ crossing the y-axis twice in quick succession at $y \approx 0.008$ (figure 7.6, right). Behaviour such as this may cause difficulties in performing the cusp-map method in this region; if the velocity profile exhibits multiple inflection points in close proximity it may be difficult to track individual eigenvalues numerically. The lack of smoothness observed in $d^2\overline{u}/dy^2$(figure 7.6, right) illustrates that although a smooth velocity profile can be recovered by summing unsteady velocity profiles, the second derivative is much more sensitive and a very large number of samples must be taken to achiever near analytic smoothness. Figure 7.6 was produced by sampling every 10 iterations for a total of 4×10^5 iterations. This constitutes 40 non-dimensional time-steps ($\Delta t = 1 \times 10^{-4}$ was used for this case) or 134 vortex shedding cycles. Despite this large number of samples and long capture period, the second derivative is still not smooth. This problem may be surmounted by fitting analytic curves to the simulation data, however the motivation for this analysis is to determine whether absolute instability profiles occur for 'real' velocity profiles. Ultimately, the cusp-map analysis in this case is deemed to fail because of limitations of the numerical method in solving for velocity profiles that are time-averages of unsteady flow. It should be noted that in any case the assumption of small amplitude linear perturbations on a steady baseflow is violated under these conditions. The location of maximum reverse flow could therefore not be analysed for any of the simulations, however the magnitude of reverse flow observed in each simulation does allow qualitative discussion.

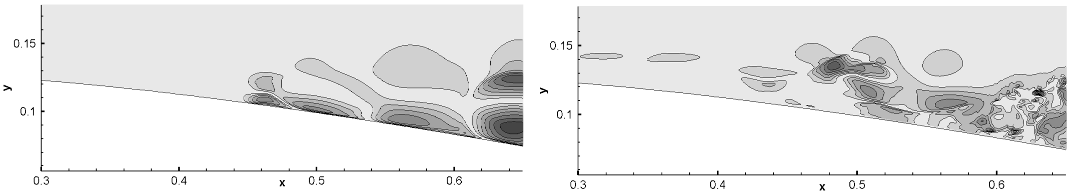

Figure 7.5: Iso-contours of $|u'|$ for the two-dimensional simulation, taken at an arbitrary time within the vortex shedding cycle (left), and for case 3DU taken at time $t = 26.6$ (right), using ten levels over the range 0-1.

When normalised by the local boundary layer edge velocity, case 3DF exhibits a maximum reverse flow magnitude of 12.3%. This is less than the critical value of 17% determined necessary to sustain absolute instability by Alam & Sandham (2000), for the associated Re_{δ^*} of 1050. Case 3DU exhibits an increased maximum reverse flow of 15.2%. This is only slightly less than the critical value of 16.5% for $Re_{\delta^*} = 1350$, determined by Alam & Sandham. However, Hammond & Redekopp (1998) determined a higher critical value of 20% for Falkner-Skan type boundary layers and Rist & Maucher (2002) determined that, even in the case of 20% reverse flow, the wall normal distance and intensity of

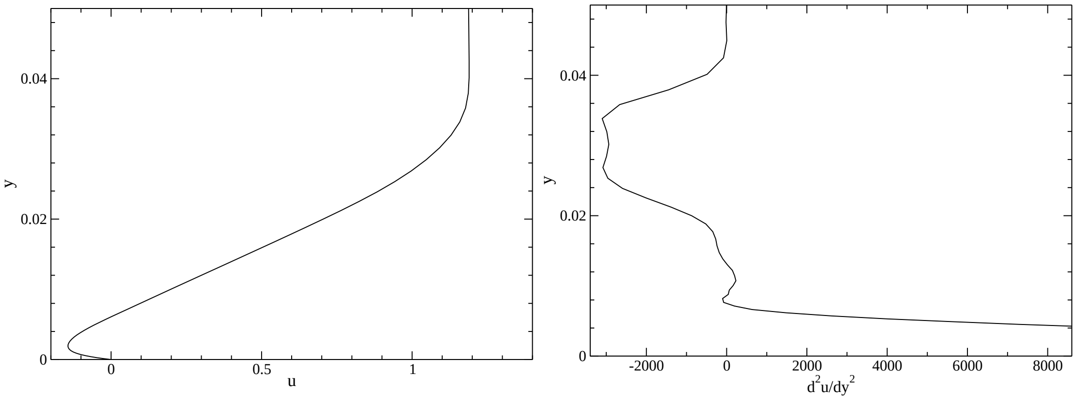

Figure 7.6: Time-averaged velocity profile (left) and second derivative of the time-averaged velocity profile (right), taken at $x = 0.53$ for the two-dimensional case at $\alpha = 5°$.

the shear layer had to exceed a certain threshold before absolute instability could be observed. The fact that $d\omega_i/dx < 0$ at the point where the cusp-map method fails suggests that absolute instability would be unlikely to be observed by linear stability analysis if the cusp-map could be continued further downstream. The two-dimensional simulation exhibited the largest magnitude reverse flow of all cases, 22.2%. This is certainly above threshold values observed by Alam & Sandham (2000) and Hammond & Redekopp (1998) however, as for case 3DU, the results of Rist & Maucher (2002) suggest that caution should be exercised before labelling the flow as absolutely unstable. On the one hand, it could be conjectured that the vortex shedding observed is the result of absolute instability, however it may be more useful to consider the shedding to be caused by a global instability mode (Theofilis, 2003), resulting in highly unsteady flow for which linear stability analysis is not valid.

The maximum reverse flow present at $\alpha = 7°$, equal to 29.5% in two dimensions and 17.9% in three-dimensions, is in both cases greater than threshold values given by Alam & Sandham, and for the two-dimensional case greater than that given by Hammond & Redekopp and Rist & Maucher. In contrast to the simulations at $\alpha = 5°$, the cusp-map could be performed up to and slightly beyond the location of maximum reverse flow for case 3D7. However, as at $\alpha = 5°$ no evidence of absolute instability was observed when performing the cusp-map analysis, although the two-dimensional simulation exhibited very marginal behaviour in that ω_i very nearly crossed the x-axis. It should however be noted that Hammond & Redekopp determined that an extended region of absolute instability would be necessary before the global dynamics were affected.

7.3 Direct numerical simulations with forcing terms

No evidence of local-absolute instability was observed in section 7.2.2 when a cusp-map analysis was performed on time-averaged flowfields of separation bubbles at $\alpha = 5°$ and $\alpha = 7°$ extracted from both two and three-dimensional simulations. In order to determine whether nonparallel effects or limitations of the numerical method have prevented the detection of absolute instability, simulations have been performed using forcing terms to maintain the initial condition, in order to investigate the behaviour of small perturbations on a given baseflow, using the method described in chapter 3 section 3.4.3. Such simulations are subject to less restrictive assumptions than linear stability analysis, and hence may be used to both confirm the results of linear stability analysis, as well as to check for behaviour not predictable by linear stability analysis. When forced

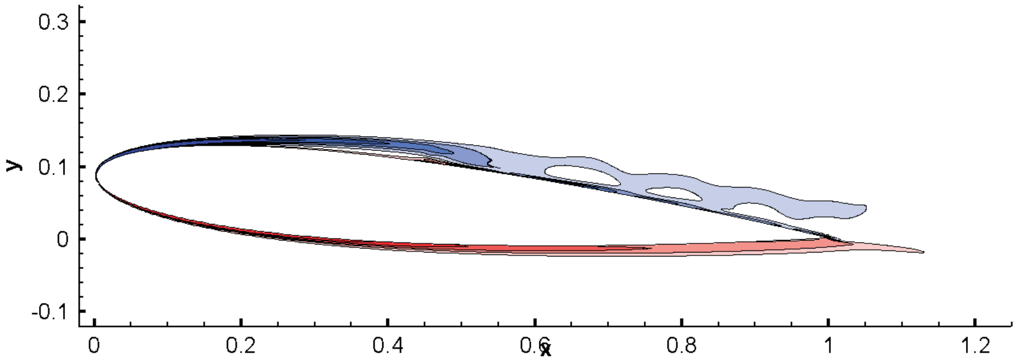

Figure 7.7: Iso-contours of vorticity using ten levels over the range ±150 plotted for the time-averaged flowfield of the two-dimensional case at $\alpha = 5°$.

Navier–Stokes simulations were performed on the time-averaged flowfield of the two-dimensional simulation at $\alpha = 5°$, instability via an acoustic feedback loop was observed. This simulation will be presented first, before other simulations are discussed within the context of this finding.

7.3.1 An acoustic feedback instability of the flow around an airfoil

The two-dimensional simulation at $\alpha = 5°$ will be considered, before discussing other simulations. The initial condition is specified as the time-averaged flowfield of the two-dimensional simulation, illustrated in figure 7.7. A region of 3×3 grid-points about the location $(x, y) = (0.25, 0.136)$, corresponding to a location within the separated shear layer, is subject to an increment of 1×10^{-8} in u, v and ρ. This effectively introduces a disturbance with a sharp-edged spatial distribution, which will excite a range of frequencies at low amplitude. No further perturbations are introduced, and the response of the flow is monitored as the simulation is progressed. If the flow were only convectively unstable, the initial perturbation would be expected to convect downstream growing in amplitude, ultimately leaving the flow over the airfoil unperturbed. If the flow were absolutely unstable, the initial perturbation would be expected to grow exponentially in time at some location until saturation or the onset of some secondary behaviour, ultimately affecting the flow-field over the entire airfoil surface.

As in chapter 3 section 3.4.3, the response of the flowfield is monitored in two ways; by recording time dependent pressure at a variety of x-locations within the boundary layer, and analysing contour plots of perturbation quantities. In this case we define the perturbation dilatation as $\nabla.\mathbf{U}' = \nabla.\mathbf{U}_{t_1} - \nabla.\mathbf{U}_{t=0}$, where $\nabla.\mathbf{U}_{t_1}$ is the dilatation rate at time t_1 and $\nabla.\mathbf{U}_{t=0}$ is the dilatation rate at time $t = 0$.

Figure 7.8 shows time series of dp/dt taken at several streamwise locations within the upper surface boundary layer. Time $t = 0$ is the initialisation time, at which the perturbation was introduced. Signals are plotted at an arbitrary amplitude, however it should be noted that signals represented by dashed lines are plotted at levels 50 times more sensitive than those represented by solid lines, due to the difference in amplitude of hydrodynamic and acoustic waves. The x-location of each signal is indicated on the vertical axis, hence upstream travelling disturbances will move downwards with increasing t and downstream travelling waves will move upwards with increasing t. The response to the perturbation is as follows:

i) The initial response to the perturbation can be observed by considering the time interval $0 < t < 1$; the perturbation induces a single wavepacket which convects downstream towards the trailing edge. It should be noted that at no point does the wavepacket appear to trigger exponential temporal growth at a fixed x-location that would indicate the onset of absolute instability (e.g. as observed by Hannemann & Oertel, 1989).

ii) In the interval $1 < t < 2$ the original wave has convected over the airfoil trailing edge and no more downstream travelling waves are observed. However the first six probes indicate that an upstream travelling pressure wave is present, albeit at much lower amplitude.

iii) In the interval $2 < t < 3$, after the upstream travelling pressure wave has reached the leading edge of the airfoil, a further downstream travelling wave is observed. By $t = 3$ this pressure wave has reached the airfoil trailing edge, and a new upstream travelling pressure wave is subsequently observed.

This pattern of downstream travelling wave followed by upstream travelling wave continues and, crucially, both upstream and downstream travelling disturbances grow in amplitude at all x-locations. The cause of this behaviour is illustrated by plotting contours of $\nabla.\mathbf{U}'$. At $t = 0.49$ (figure 7.9a) the wavepacket generated by the initial disturbance is visible as a multi lobed structure. By $t = 0.98$ (figure 7.9b) the wavepacket has convected downstream over the trailing edge, whereupon scattering of the disturbances produces upstream travelling acoustic waves (Ffowcs Williams & Hall, 1970). The acoustic waves are more clearly visible at $t = 1.47$ (figure 7.9c). By $t = 2.45$ (figure 7.9d) another wavepacket is observed. This second wavepacket has reached the trailing edge of the airfoil by $t = 2.94$ (figure 7.9e), generating more upstream travelling acoustic waves which are clearly observed at $t = 3.43$ (figure 7.9f). Another wavepacket is generated at $t = 4.41$ (figure 7.9g), and the process continues as the amplitude of both downstream-travelling hydrodynamic structures and

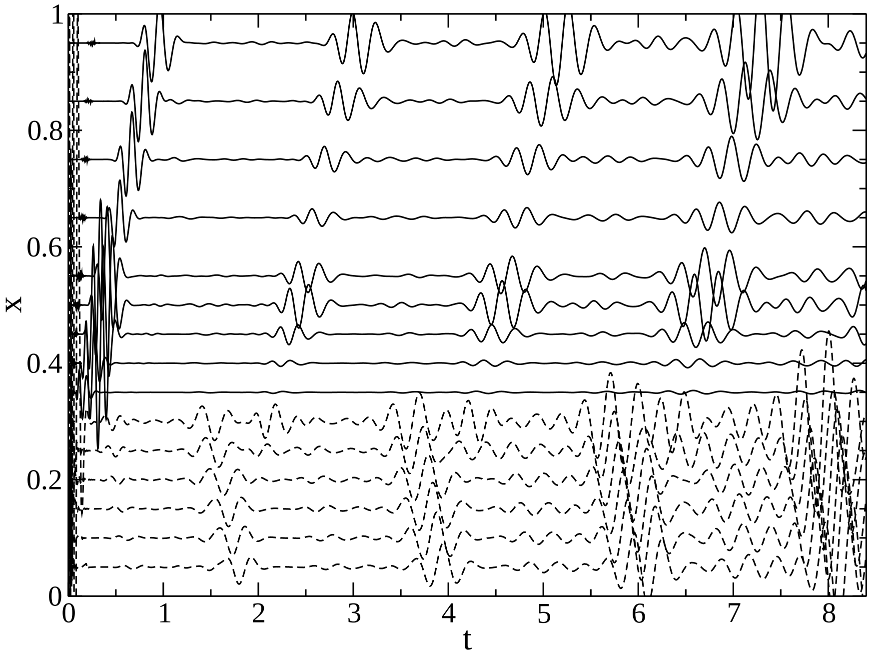

Figure 7.8: Time histories of dp/dt, with streamwise location indicated on the vertical axis, for two-dimensional case at $\alpha = 5°$. Solid lines have been multiplied by 2.5×10^5 and dashed lines by 1.25×10^7.

upstream travelling acoustic waves increases.

From the time-series, it appears that the downstream travelling wavepacket induced by the initial perturbation generates upstream travelling acoustic waves when it convects over the trailing edge. These upstream travelling acoustic waves then reach some location of receptivity, probably the airfoil leading edge, and generate another downstream travelling wavepacket. The process repeats with increasing amplitude at all x-locations and hence represents an instability of the flow, via a combination of convective instability of hydrodynamic disturbances and an acoustic feedback loop. The growth rate of the feedback loop is observed to be exponential when longer time series of pressure signals are plotted (figure 7.10, left), with growth rate $e^{0.25t}$. When absolute values are plotted on a logarithmic scale (figure 7.10, right) it can be seen that initially the disturbance amplitude decays in time, before growing exponentially.

A schematic of the feedback loop is illustrated in figure 7.11, with the four processes involved labelled A to D. During stage A, hydrodynamic disturbances are amplified as they convect downstream. Upon reaching the airfoil trailing edge, at stage B, upstream travelling pressure waves are generated via acoustic scattering. The pressure waves generated at the trailing edge propagate upstream during stage C . When the pressure waves reach the vicinity of the leading edge, at stage D, further downstream convecting disturbances are gener-

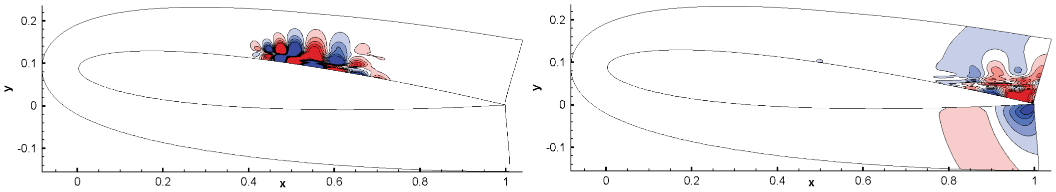

a) $t = 0.49$ b) $t = 0.98$

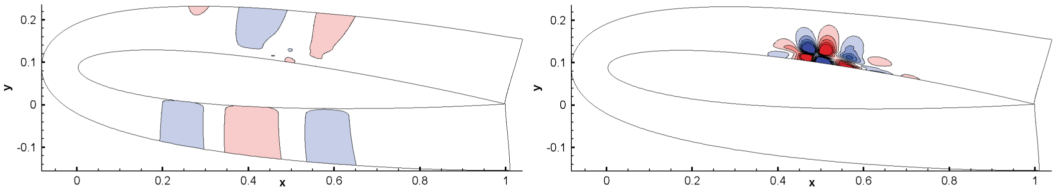

c) $t = 1.47$ d) $t = 2.45$

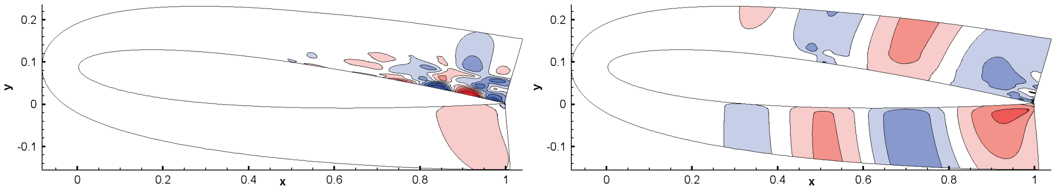

e) $t = 2.94$ f) $t = 3.43$

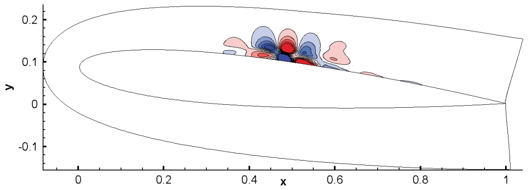

g) $t = 4.41$

Figure 7.9: Iso-contours of perturbation $\nabla \mathbf{U}'$ (defined in section 7.3)for the two-dimensional case at $\alpha = 5^\circ$ taken at times indicated, using 10 levels over the range $\pm 10^{-8}$

.

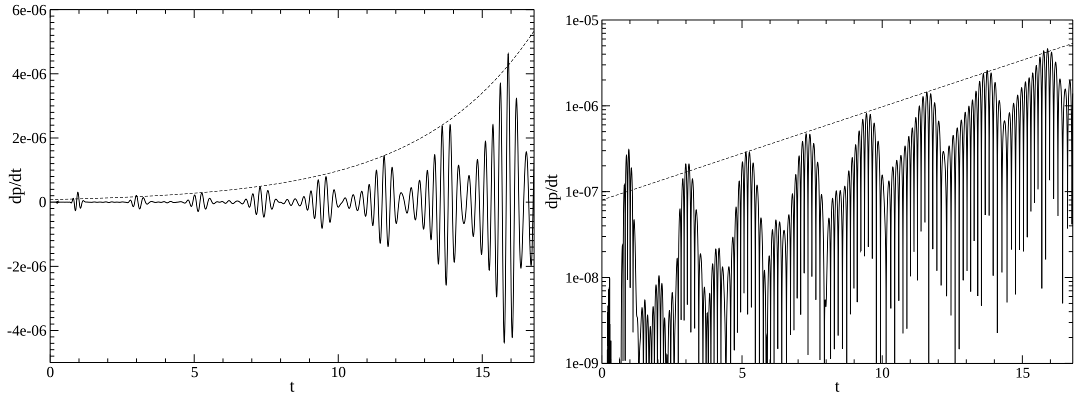

Figure 7.10: Time dependent $\frac{dp}{dt}$ taken at $x = 0.95$ for the two-dimensional case at $\alpha = 5°$, showing exponential disturbance growth at a rate of $e^{0.25t}$ (left), and the equivalent absolute values plotted on a logarithmic scale (right).

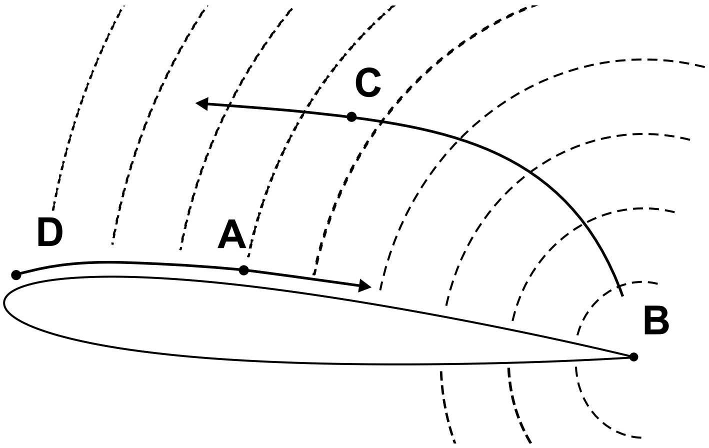

Figure 7.11: Stylised schematic for the acoustic feedback loop.

ated within the boundary layer and the cycle repeats. In order for the feedback loop to be unstable, the net gain of processes A to D must be greater than 1. Process A represents the only point at which amplification takes place within the loop, hence it appears likely that strong growth of hydrodynamic instabilities is necessary to offset the losses incurred at all other stages of the cycle. The mechanism is analogous to Rossiter modes observed in cavity flows (Rossiter, 1964), although in the current case it should be noted that the period of the feedback loop is distinct from, and much longer than, the period of the repeating hydrodynamic/acoustic disturbance.

In order to make sure that no temporal disturbance growth is present that is independent of the acoustic feedback loop, a further simulation was run. The time-averaged flowfield from the two-dimensional simulation at $\alpha = 5°$ was again used as the initial condition, and the simulation was perturbed in exactly the same way, but this time a weak buffer was applied (of the form detailed in chap-

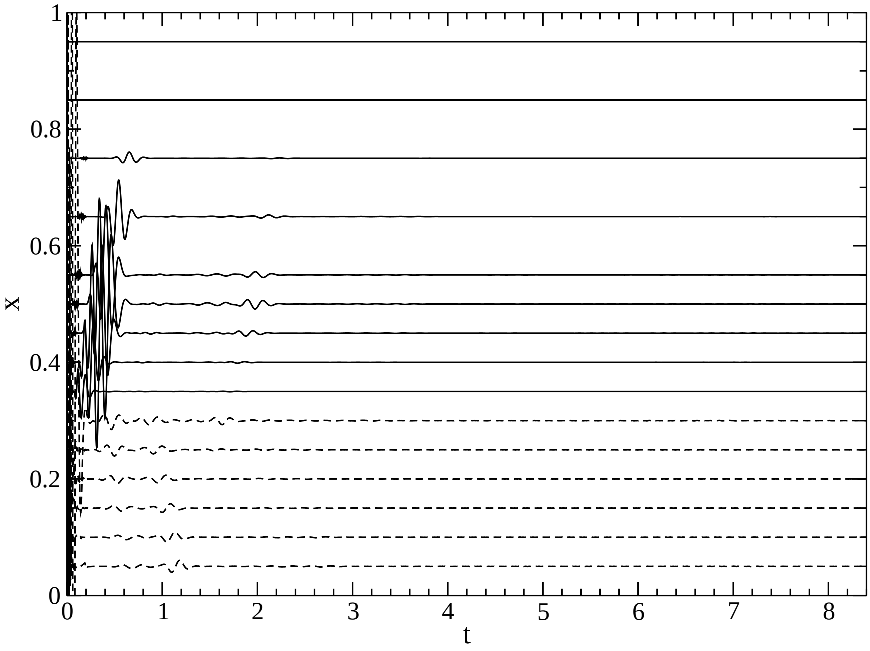

Figure 7.12: Time histories of dp/dt, with streamwise location indicated on the vertical axis, for the two-dimensional case at $\alpha = 5°$. A buffer was applied to damp trailing edge noise, ramping from zero to full effectiveness over the range $0.65 < x < 1$. Solid lines have been multiplied by 2.5×10^5 and dashed lines by 1.25×10^7.

ter 2, section 2.2.7), ramping from zero to 0.05 over the range $0.65 < x < 1$. The onset of the buffer is downstream of the bubble, hence any region of absolute instability present within the bubble should be unaffected whilst upstream travelling waves originating at the trailing edge will be damped. Figure 7.12 shows time series of dp/dt taken at several streamwise locations within the upper surface boundary layer. Upon progressing the simulation the initial response to the perturbation was the same; i.e. a downstream convecting wavepacket was observed. Upon reaching the buffer onset the wavepacket decayed, and only minimal evidence of upstream travelling acoustic waves was observed. The acoustic feedback loop was prohibited from developing, and no disturbance growth was observed at any other location within the simulation. This appears to validate the linear stability analysis performed in section 7.2.2; it appears that no region of absolute instability is present within the separation bubble, even when a non-parallel baseflow is taken into account.

7.3.2 Frequency content

Perturbation frequencies observed in the simulation with no buffer applied can be compared to the linear stability theory predictions of section 7.2.1 in order to confirm that both methods yield similar results. Since statistics are not

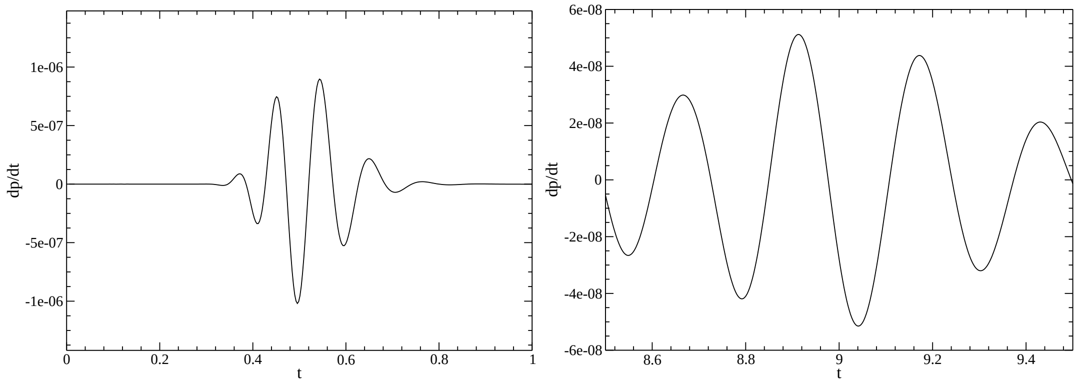

Figure 7.13: Time dependent $\frac{dp}{dt}$ taken at $x = 0.4$ for the two-dimensional case at $\alpha = 5°$, showing the initial response to the perturbation introduced at $t = 0$ (left), and the response after several feedback loop cycles (right).

available for the forced simulation, analysis is limited to inspection of individual wavepackets. The frequency content of the first wavepacket observed, i.e. that produced by the initial perturbation, was found to differ from that of wavepackets observed after one or more feedback-loop cycles. At $x = 0.4$, the initial wavepacket is observed to possess $f \approx 10.8$ ($\omega \approx 67.9$). This agrees reasonably well with linear stability analysis, which predicts that the instability wave with the maximum N-factor will be at $f \approx 9.6$. After three feedback-loop cycles however, the wavepacket at $x = 0.4$ is observed to possess $f \approx 4.0$ ($\omega \approx 25.1$). A similar drop in frequency is observed at $x = 0.95$; the initial wavepacket possesses $f \approx 6.9$ ($\omega \approx 43.4$), but after three feedback-loop cycles the wavepacket possesses $f \approx 4.0$ ($\omega \approx 25.1$). The initial response to the perturbation agrees reasonably well with linear stability theory in terms of the most amplified frequency, however it appears that the most unstable frequency of the acoustic-feedback loop is lower than that of the most convectively amplified instability wave over the upper airfoil surface. This may explain the apparent decay in amplitude of pressure fluctuations between the first and second wavepackets (figure 7.10, right). A significant proportion of the energy of the first wavepacket will be contained within frequencies which are not amplified efficiently by the feedback loop. Energy contained within these frequencies, and hence the total energy of the wavepacket, will decay initially, before the frequencies most efficiently amplified by the feedback loop grow sufficiently to recoup the energy loss.

7.3.3 Receptivity process

Boundary layer receptivity is required to occur for the acoustic feedback loop to be present, however boundary layer receptivity is in general not as well understood as boundary layer stability. It is known that regions of pronounced

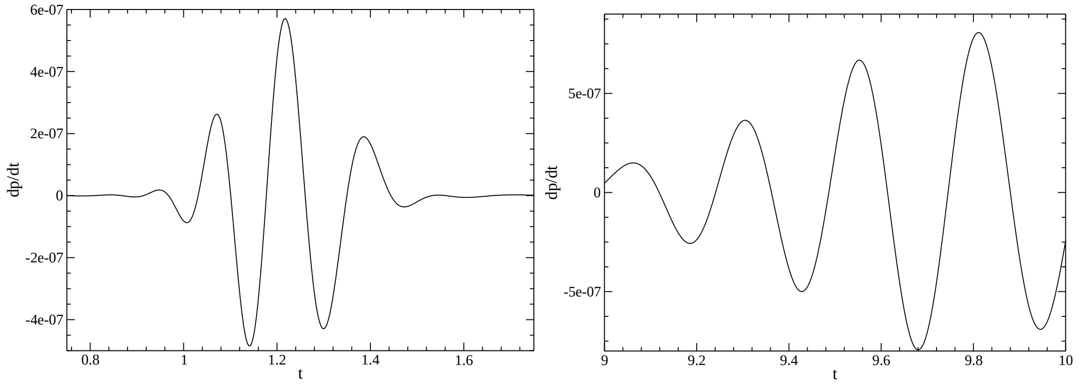

Figure 7.14: Time dependent $\frac{dp}{dt}$ taken at $x = 0.95$ for the two-dimensional case at $\alpha = 5°$, showing the initial response to the perturbation introduced at $t = 0$ (left), and the response after four feedback loop cycles (right).

streamwise variation in boundary layer flow are receptive to free-stream disturbances, including in particular finite radius leading edges (Saric, Reed & Kerschen, 2002), and the variation of the efficiency of the receptivity process with frequency has been quantified numerically for modified super-ellipses (Wanderley & Corke, 2001). However, such data is difficult to relate to the current study, where the airfoil leading edge differs in aspect ratio significantly and aerodynamic loading is present. The response of the time-averaged flowfield of airfoil flow to a free-stream (acoustic) disturbance, as opposed to a hydrodynamic disturbance, is therefore investigated by running a further simulation. The aim is to estimate, very approximately, at what frequencies the receptivity process occurs.

The time-averaged flowfield of the two-dimensional case at $\alpha = 5°$ is specified as the initial condition, and the flowfield is perturbed in the same way as previous simulations except at a location $(x, y) = (2, 1)$, i.e. downstream of the airfoil trailing edge. This will generate an acoustic pulse in the potential flow region, and the airfoil leading edge will experience an upstream travelling acoustic wavepacket as would be expected due to the presence of trailing edge noise. Running the simulation and forming an x/t-plot illustrates the response of the flow to the perturbation (figure 7.15). The upstream-travelling acoustic wavepacket generated by the initial pulse can be observed in the interval $0.8 < t < 1.6$, as a very high-frequency pulse. Upon reaching the vicinity of the leading edge, a downstream travelling hydrodynamic disturbance is generated, and the acoustic feedback instability commences. In the current case, we are interested in the first hydrodynamic disturbance generated by the receptivity of the leading edge region to the freestream (acoustic) disturbance. Effectively it is desired to know, when subject to a free-stream disturbance containing energy over a range of fre-

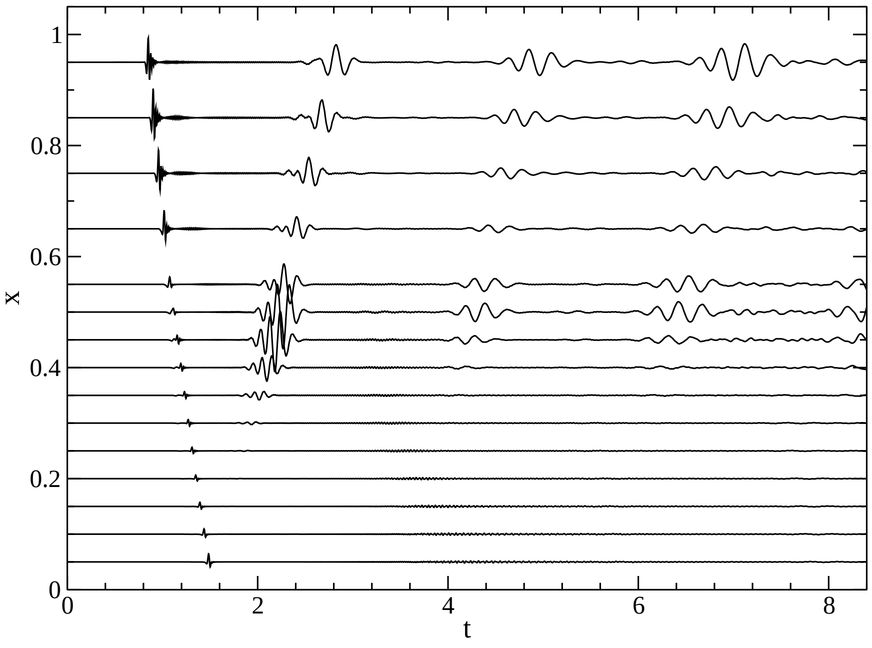

Figure 7.15: Time histories of dp/dt, with streamwise location indicated on the vertical axis, for two-dimensional case at $\alpha = 5°$ subject to an acoustic perturbation originating downstream of the airfoil. Lines have been multiplied by 1×10^5.

quencies, what is the resultant (self-selected) frequency of the hydrodynamic disturbance following boundary layer receptivity.

At $x = 0.5$, the first hydrodynamic pulse is at frequency $f \approx 9.5$ (figure 7.16, left). Upstream of this location the hydrodynamic pulse appears to be higher in frequency, e.g. $f \approx 11$ at $x = 0.3$ (figure 7.16, right), however the signal is less clear. Although this is based upon measurement of single wavepackets, and although the initial acoustic pulse will not possess uniform energy across all frequencies, this remains a useful result. Although it cannot be stated that $f = 9.5$ or $f = 11$ is the frequency at which boundary layer receptivity occurs most efficiently, it appears that leading-edge receptivity occurs at frequencies similar to, or slightly greater than, convective amplification for the current case. It should be noted however that considering a wavepacket at a modest distance from the receptivity location means that the stability characteristics of the boundary layer will influence the frequency of the wavepacket. Unfortunately it is not possible to determine the frequency of the hydrodynamic wavepacket directly in the vicinity of receptivity using the current technique.

From this simple analysis it appears that the combined receptivity and convective amplification process appears to select frequencies of the order $f \approx 9.5 - 11$. From linear stability analysis the most convectively amplified frequency is expected to be $f = 8.49$ (section 7.2), however the preferred frequency of the acoustic feedback loop appears to be considerably lower, at $f \approx 4$. This

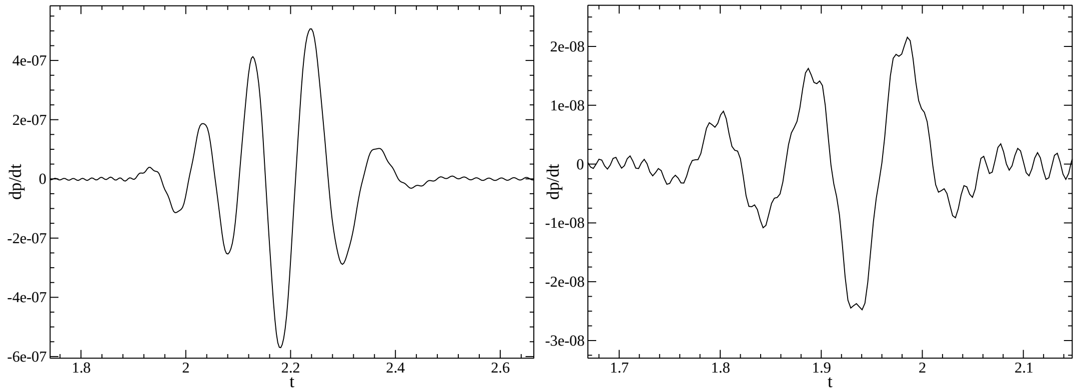

Figure 7.16: Time dependent $\frac{dp}{dt}$ for the two-dimensional case at $\alpha = 5°$ subject to an acoustic pulse downstream of the airfoil, showing the first hydrodynamic wavepacket observed at $x = 0.5$ (left) and $x = 0.3$ (right).

suggests that the preferred frequency of the acoustic scattering process is much lower than that of either the boundary layer receptivity or convective amplification of boundary layer instabilities, and that acoustic scattering at the airfoil trailing edge plays a critical role in the frequency selection of the feedback loop.

7.3.4 Stability characteristics of two-dimensional simulations at incidence

Having observed the feedback loop at $\alpha = 5°$ and $M = 0.4$, additional simulations were conducted using the same procedure, and both the incidence and Mach number were varied to see if the feedback loop persisted for other two-dimensional flows. A brief summary of results is presented in table 7.1. All relevant x/t-plots are included at the end of the chapter.

At 3° incidence the feedback loop is observed to be present, but stable (figure 7.21). Hydrodynamic disturbances were generated by upstream travelling acoustic waves, as in figure 7.8, however the amplitude decreased from one cycle to the next. At 5°, 7° and 8.5° incidence (figures 7.87.23 and 7.22 respectively), the feedback loop was present and unstable in each case. Linear stability analysis suggests that the amplification rate of the most unstable wave over the separated region does not vary significantly with incidence. For cases at incidence $3° < \alpha < 7°$ the amplification factor varied over the range $e^{9.2} - e^{9.6}$. The reason the feedback loop is unstable at $\alpha \geq 5°$ but not at $\alpha = 3°$ appears to be because simulations at $\alpha \geq 5°$ exhibited stronger disturbance amplification over the aft section of the airfoil, due to the stronger adverse pressure gradient present. Cases at $\alpha = 7°$ and $\alpha = 8.5°$ exhibit similar behaviour to that at $\alpha = 5°$; the initial higher-frequency wavepacket appears to decay at first, before pressure fluctuations assume a lower frequency and exponential growth is ob-

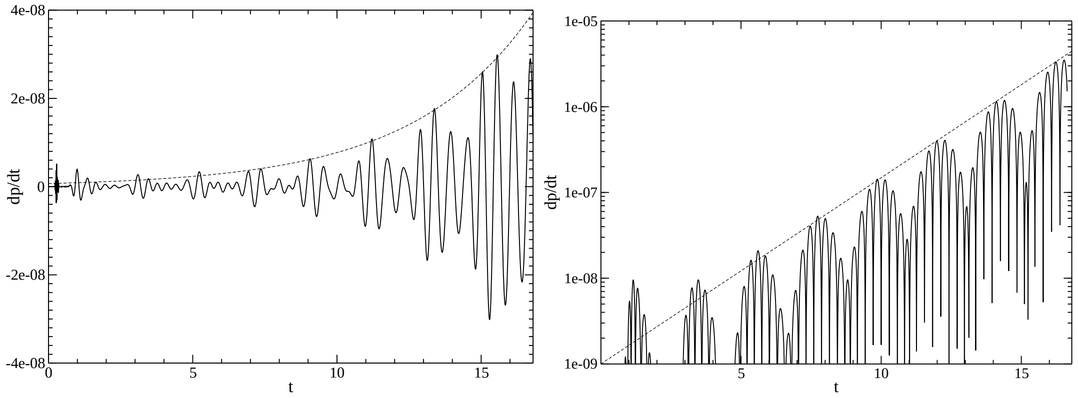

Figure 7.17: Time dependent $\frac{dp}{dt}$ taken at $x = 0.95$ for the two-dimensional case at $\alpha = 8.5°$, showing exponential disturbance growth at a rate of $\mathrm{e}^{0.5t}$ (left), and the equivalent absolute values plotted on a logarithmic scale (right).

α (degrees)	M	Feedback loop stability
3	0.4	Stable
5	0.4	Unstable
7	0.4	Unstable
8.5	0.4	Unstable
5	0.3	Stable

Table 7.1: Stability of the feedback loop for two-dimensional simulations for different angles of incidence, α, and Mach number.

Case	Growth rate	Feedback loop f	Dominant shedding f	f for largest N-factor
$\alpha = 5°$	0.25	4	3.37	8.45
$\alpha = 7°$	0.24	1.9	2.43	12.73
$\alpha = 8.5°$	0.5	1.7	2.00	-
3DU	0.21	3.3	-	8.49

Table 7.2: Growth rate and apparent preferred-frequency of the acoustic feedback instability for unstable cases.

served (illustrated in figure 7.17 for $\alpha = 8.5°$). Growth rates for cases where an unstable feedback-loop was observed are given in table 7.2.

The case at $\alpha = 8.5°$ exhibits clearly defined upstream and downstream travelling waves, as at $\alpha = 5°$, and the growth rate of the feedback loop appears to be greater than at $\alpha = 5°$. Pressure signals for the case at $\alpha = 7°$ are less clear however. Upstream and downstream travelling waves appear to be present, but the pressure signals at all x-locations exhibit constant unsteadiness, with none of the 'quiet' regions that so clearly define the individual wavepackets at $\alpha = 5°$ and $\alpha = 8.5°$. In order to make sure that no temporal disturbance growth is present that is independent of the acoustic feedback loop, a further simulation was run. The time-averaged flowfield from the two-dimensional simulation at $\alpha = 7°$ was again used as the initial condition, but this time a weak buffer was applied, ramping from zero to 0.05 over the range $0.45 < x < 1$, as for the simulation at $\alpha = 5°$ in section 7.3.1, to damp acoustic scattering at the trailing edge. A fluctuating pressure signal is observed in the vicinity of $x = 0.3$, which is lower in amplitude and higher in frequency than that associated with the acoustic feedback loop, and the signal appears possess neutral stability (figure 7.24). The cusp-map analysis performed in section 7.2.2 suggests that this case is only marginally absolutely stable. It is feasible then that this is a manifestation of a very weak absolute instability. Certainly the behaviour is unrelated to the acoustic feedback loop. A similar but more pronounced behaviour is observed for the equivalent three-dimensional simulation in section 7.3.5 and the behaviour is discussed in more detail.

In order to determine the influence of compressibility, the case at 5° incidence was repeated whilst reducing the Mach number to $M = 0.3$ (figure 7.25). A marginally stable feedback loop was observed, suggesting that the feedback loop would become unstable with a modest increase in M. The effectiveness of the acoustic scattering at the trailing edge reduces with Mach number, however the reason the feedback loop at $M = 0.3$ is stable appears in this case to be due to changes in the structure of the boundary layer over the aft section of the airfoil. Comparison of the two cases reveals that, despite the change in Mach number, the amplitude of acoustic waves generated is similar in both cases.

One would perhaps intuitively associate the presence of a feedback loop with some form of global frequency selection, e.g. of the vortex shedding behaviour, however periodic vortex shedding is observed in two-dimensions for $\alpha \leq 5°$, whereas an unstable acoustic feedback loop is only observed for $\alpha \geq 5°$. Above $\alpha = 5°$ a more broadband response occurs. Thus the only case exhibiting both vortex shedding in a clearly periodic fashion and an acoustic feedback loop in the time-average is the case at $\alpha = 5°$. However, for all two-dimensional cases there was a clear tonal contribution to the lift coefficient and pressure readings in the wake, even for simulations exhibiting a more broadband response (e.g. $f \approx 2$, figure 4.11, section 4.4). In all cases this tonal contribution lies in the range $1.5 < f < 4$, which is considerably lower than the most convectively amplified frequencies observed in section 7.2.1 (table 7.2).

It is feasible then, that the acoustic feedback loop may act as a frequency selection mechanism where periodic vortex shedding occurs, and may be responsible for selecting the dominant tonal content of more broadband vortex shedding behaviour. Where this occurs, the preferred frequency would be dependent on several factors. The efficiency of acoustic scattering at the trailing edge decreases with increasing frequency (see also chapter 9, section 9.5.2). On the other hand, the convective amplification rate of boundary layer disturbances is greatest at a relatively higher frequency, and decreases at low frequencies. If we define the frequency dependent amplification ratio of boundary layer disturbances across the boundary layer as $N(f)$, and some measure of acoustic scattering efficiency at the trailing edge as $T(f)$, presumably the preferred frequency would be the value of f for which $N(f)T(f)$ is greatest. However, this hypothesis ignores the receptivity mechanism occurring in the vicinity of the leading edge. The receptivity process is not well defined, and itself may influence the frequency selection process. At present then, it appears likely that the presence of an acoustic feedback loop such as this will act to select global frequencies or tones in airfoil flows with vortex shedding, however the frequency selection criteria appears complex.

7.3.5 The stability characteristics of three-dimensional simulations at incidence

Having performed forced simulations of a variety of time-averaged two-dimensional flowfields, the process was repeated for the time-averaged flowfields of cases 3DF, 3DU and 3D7, perturbing the simulations in the same manner as for the equivalent two-dimensional simulations. Case 3DF was found to be stable; no acoustic feedback loop was observed (figure 7.26). Case 3D7 was marginally stable, but exhibited a secondary behaviour that will be discussed later in this section (figure 7.28). Case 3DU however, was found to be unstable (figure 7.27). The differences in stability can be attributed to differences in N-factors across the separation bubbles; $N = 9.5$ for case 3DU, $N = 10.3$ for case 3D7, and $N = 13$ for case 3DU. Clearly a large N-factor is essential parameter defining the onset of the feedback loop. It also appears that a larger N-factor is necessary to sustain the feedback loop for three-dimensional simulations than for two-dimensional simulations. The fact that the feedback loop has been found present for the time-averaged flowfield of a three-dimensional simulation raises the question as to whether such behaviour will be observed in the fully developed time-dependent case. This is investigated in chapter 9, section 9.3.

For case 3D7 a secondary behaviour was observed, similar to that exhibited by the two-dimensional simulation at $\alpha = 7°$; a fluctuating pressure signal is observed in the vicinity of $x = 0.3$, that is lower in amplitude and higher in frequency than that associated with the acoustic feedback loop (figure 7.28). For case 3D7 the signal appears more prominent than in two-dimensions, with a marginally positive growth rate. When a simulation is performed with a simple buffer applied downstream of $x = 0.45$ the behavior persists figure (figure

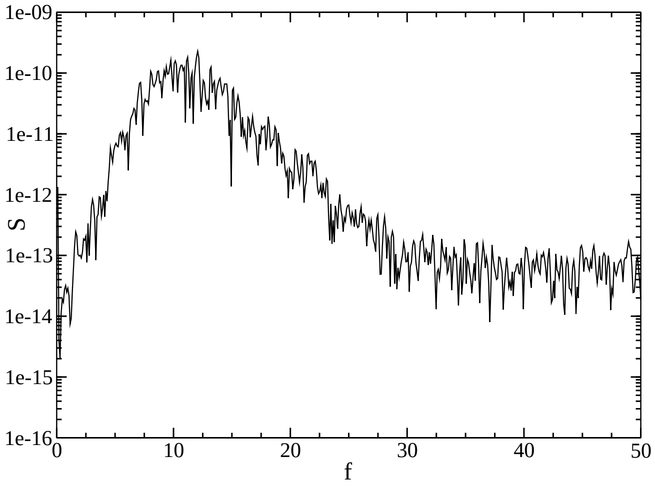

Figure 7.18: Direct Fourier transform of the pressure signal at $x = 0.3$ for case 3D7, computed for the time interval $4 < t < 12$.

7.29), and performing a direct Fourier transform of the time-series for the period $4 < t < 12$ suggests that the frequency of this perturbation is centered about $f = 10$ (figure 7.18). The fluid dynamics associated with this behavior are illustrated by plotting iso-contours of perturbation ω_z (figure 7.19); animations of perturbation ω_z suggest that disturbance waves are being generated at some location within the bubble, and are recirculating within the bubble. Hence the bubble is acting as an 'oscillator', and thus the behaviour represents a very weak form of absolute instability. No such behaviour was predicted by the cusp-map analysis performed in section 7.2.2. This may be because the behaviour is only weakly unstable; although errors due to nonparallel effects are likely to be small, a small error could potentially result in predicting a marginally stable flow instead of a marginally unstable flow. The least damped $c_g = 0$ wave as predicted by linear stability theory was observed at $x = 0.26$ for case 3D7, and the associated real frequency of this wave was $f = 9$ ($\omega = 56.7$), agreeing reasonably well with the dominant frequency of $f = 10$. This represents circumstantial evidence that this behaviour is caused by a global instability.

7.4 Summary

Linear stability analysis of the time-averaged flowfields extracted from cases 3DF, 3DU and 3D7, as well as the corresponding two-dimensional simulations, has been performed. The convective stability characteristics of the two-dimensional case at $\alpha = 5°$ and case 3DF appear similar in that the N-factor across the separation bubble does not change significantly between cases. Case 3DU however exhibits a much larger N-factor; upon removal of forcing the bubble appears

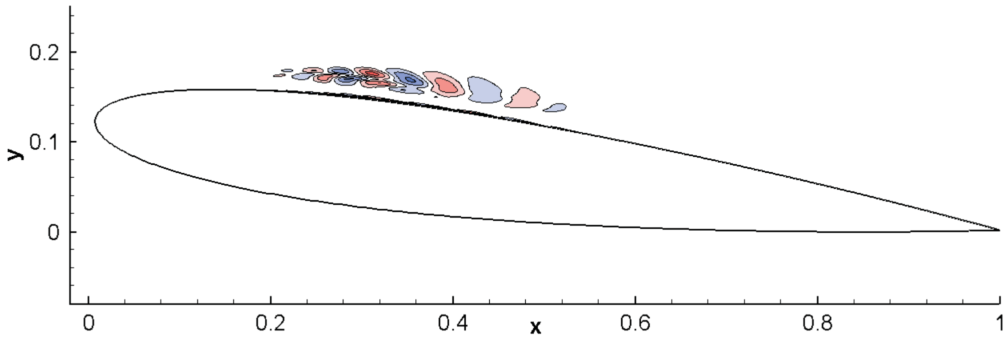

Figure 7.19: Iso-contours of perturbation vorticity for case 3D7 at $t = 8.4$, showing 10 levels over the range $\pm 2 \times 10^{-8}$.

to become more unstable than either the two-dimensional case or the forced 3D case. When the airfoil incidence is increased to $\alpha = 7^\circ$ the frequency of the most amplified instability wave increases, however the N-factor for case 3D7 actually reduces compared to that of case 3DU. The frequency of the most amplified instability wave has been identified for all cases, and appears significantly higher than that of the vortex shedding behaviour observed in two-dimensions.

No evidence of local absolute instability was observed for any of the cases investigated when a cusp-map analysis was performed. This was confirmed for simulations at $\alpha = 5^\circ$ by performing forced Navier–Stokes simulations, however at $\alpha = 7^\circ$ a very weakly unstable mode was observed that the cusp-map method did not predict. Forced Navier–Stokes simulations determined that for two dimensional cases in the range $5^\circ \leq \alpha \leq 8.5$ the time-averaged flowfield is unstable due to an acoustic feedback instability, in which instability waves convecting over the trailing edge of the airfoil generate acoustic waves that propagate upstream to some location of receptivity, and generate further instability waves within the boundary layer. As the cycle repeats, the amplitude of both hydrodynamic instabilities and acoustic waves increases. The resultant behavior may be defined as globally unstable, although no local absolute instability is present. It is suggested that an acoustic feedback loop of this type may act as a frequency selection mechanism for the vortex shedding observed in two-dimensions. At higher Reynolds numbers, the feedback loop may potentially be responsible for the generation of discrete tones of sound radiation in a similar fashion to behaviour observed by McAlpine *et al.* (1999), although their mechanism was limited to separated flow in the trailing edge region. The lack of a clear absolute instability of the time-averaged flow suggests that another mechanism is needed to explain the self-sustained turbulence observed for simulations 3DU and 3D7 in chapters 5 and 6. This is the subject of the next chapter.

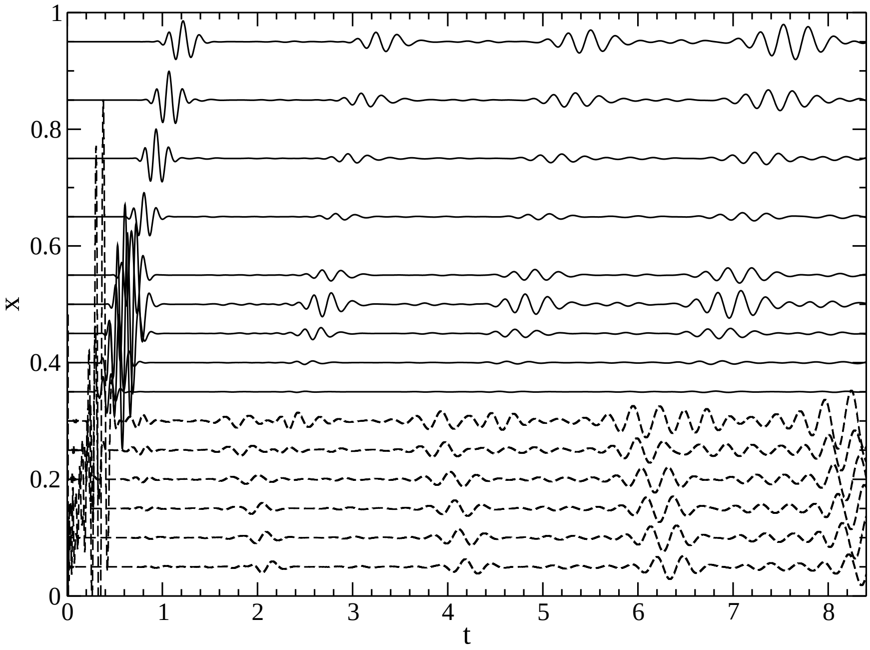

Figure 7.20: Time histories of dp/dt, with streamwise location indicated on the vertical axis, for the two-dimensional case at $Re_c = 5 \times 10^4$, $M = 0.4$, $\alpha = 5°$. A region of 1×1 grid-points was perturbed at $(x, y) = (0.05, 0.119)$. Solid lines have been multiplied by 2.5×10^5 and dashed lines by 1.25×10^7.

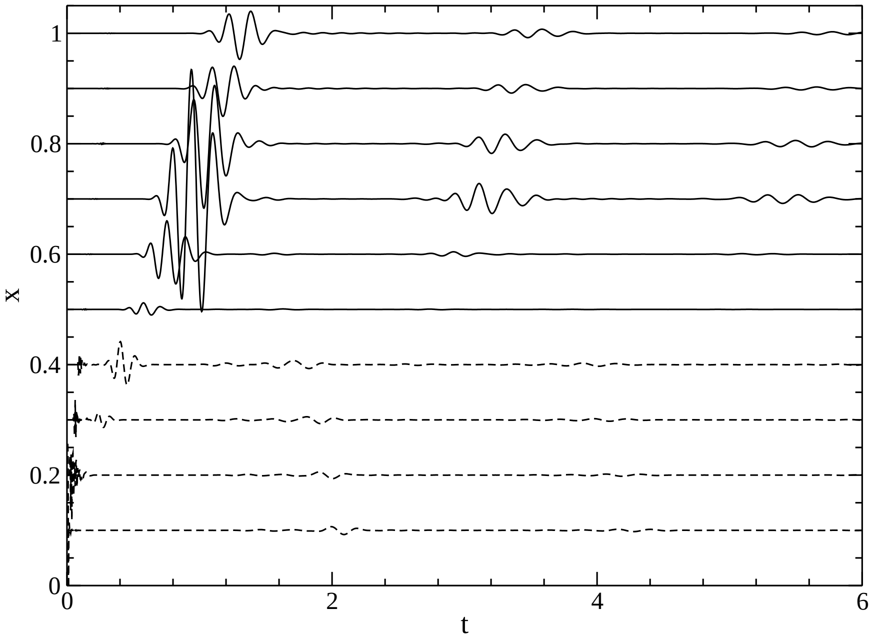

Figure 7.21: Time histories of dp/dt, with streamwise location indicated on the vertical axis, for the two-dimensional case at $Re_c = 5 \times 10^4$, $M = 0.4$, $\alpha = 3°$. A region of 3×3 grid-points was perturbed at $(x, y) = (0.3, 0.1)$. Solid lines have been multiplied by 2.5×10^5 and dashed lines by 1.25×10^7.

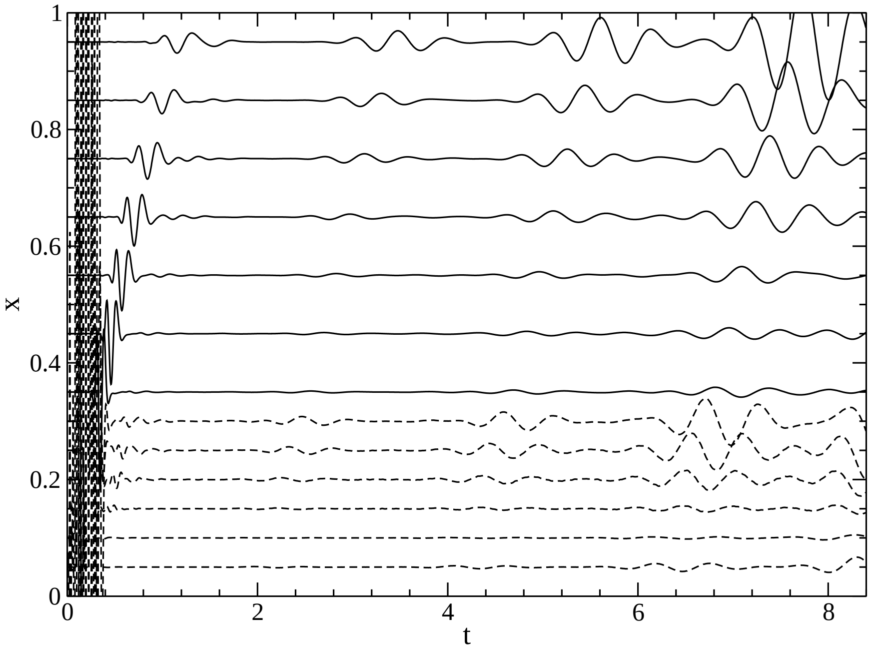

Figure 7.22: Time histories of dp/dt, with streamwise location indicated on the vertical axis, for the two-dimensional case at $Re_c = 5 \times 10^4$, $M = 0.4$, $\alpha = 8.5°$. A region of 3×3 grid-points was perturbed at $(x, y) = (0.025, 0.209)$. Solid lines have been multiplied by 2.5×10^5 and dashed lines by 1.25×10^7.

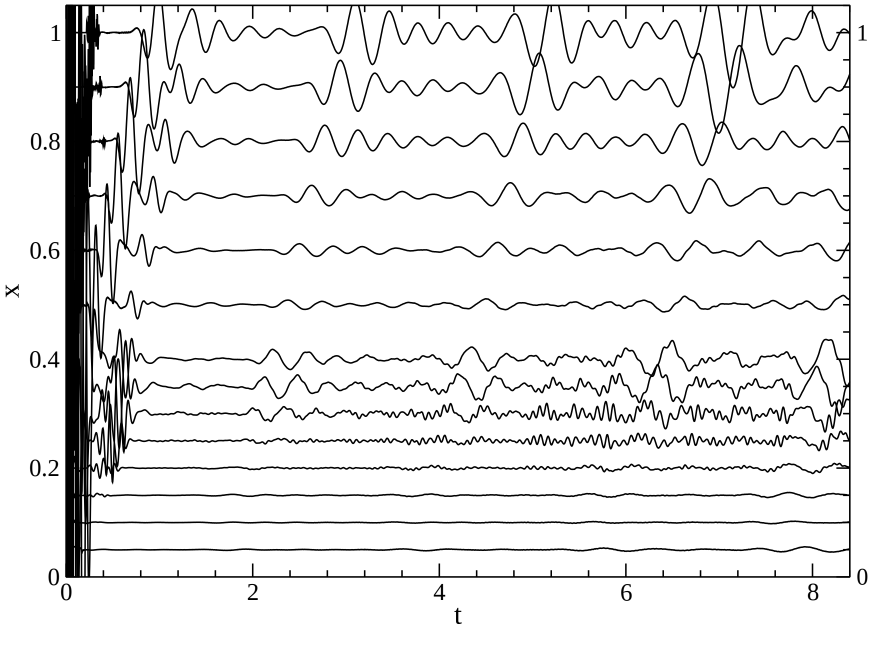

Figure 7.23: Time histories of dp/dt, with streamwise location indicated on the vertical axis, for the two-dimensional case at $Re_c = 5 \times 10^4$, $M = 0.4$, $\alpha = 7°$. A region of 3×3 grid-points was perturbed at $(x, y) = (0.2, 0.175)$.Solid lines have been multiplied by 2.5×10^7.

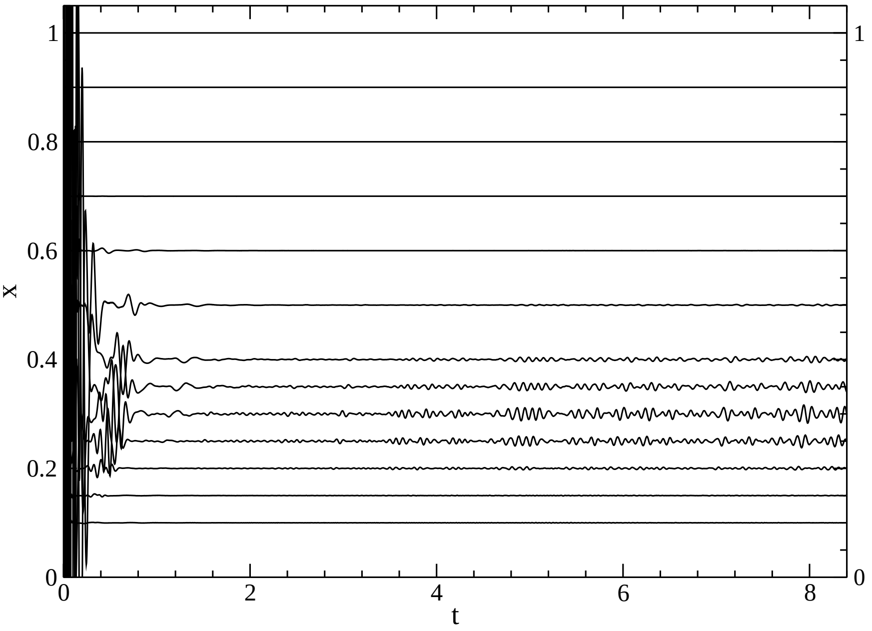

Figure 7.24: Time histories of dp/dt, with streamwise location indicated on the vertical axis, for the two-dimensional case at $Re_c = 5 \times 10^4$, $M = 0.4$, $\alpha = 7°$. A region of 3×3 grid-points was perturbed at $(x, y) = (0.2, 0.175)$, and a buffer was applied for $x > 0.45$. Solid lines have been multiplied by 2.5×10^7.

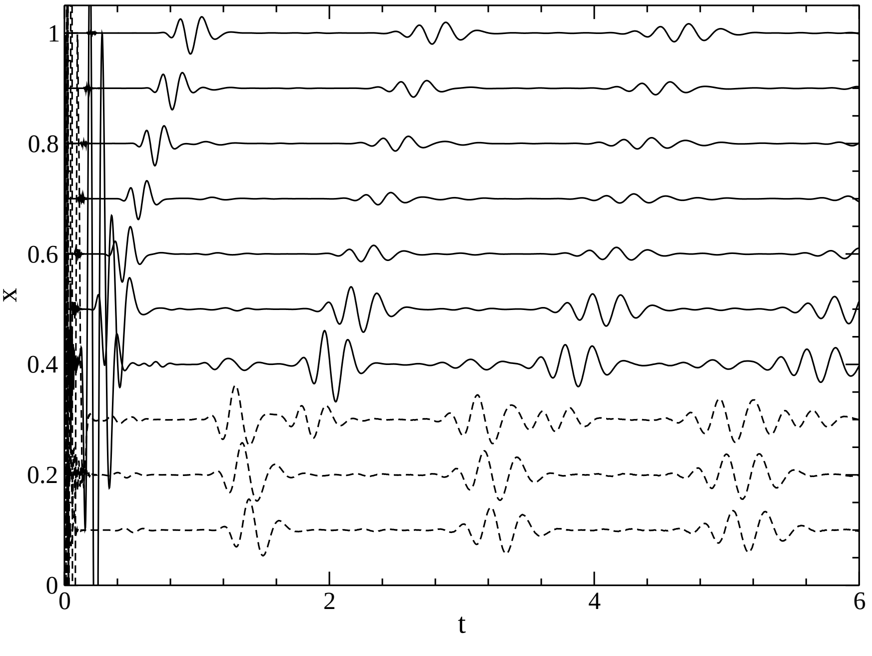

Figure 7.25: Time histories of dp/dt, with streamwise location indicated on the vertical axis, for the two-dimensional case at $Re_c = 5 \times 10^4$, $M = 0.3$, $\alpha = 5°$. A region of 3×3 grid-points was perturbed at $(x, y) = (0.25, 0.136)$. Solid lines have been multiplied by 2.5×10^5 and dashed lines by 1.25×10^7.

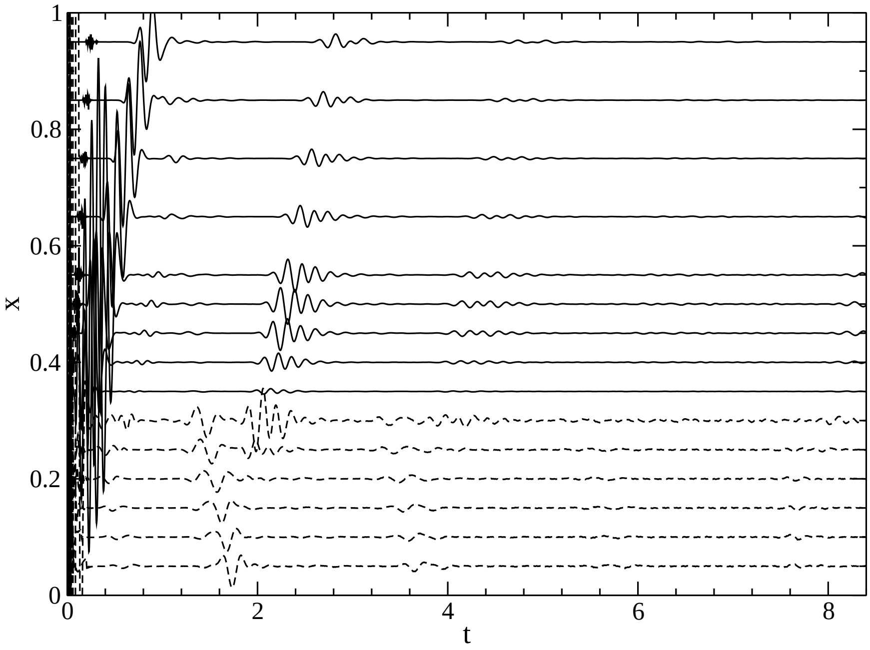

Figure 7.26: Time histories of dp/dt, with streamwise location indicated on the vertical axis, for the time-average of case 3DF ($Re_c = 5 \times 10^4$, $M = 0.4$, $\alpha = 5°$). A region of 3×3 grid-points was perturbed at $(x, y) = (0.25, 0.136)$. Solid lines have been multiplied by 1×10^6 and dashed lines by 4×10^7.

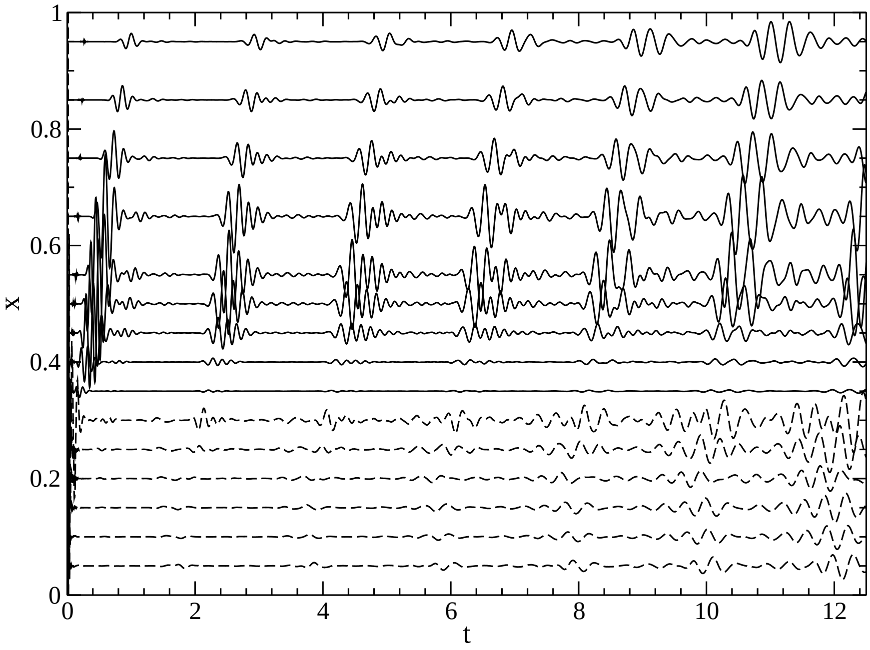

Figure 7.27: Time histories of dp/dt, with streamwise location indicated on the vertical axis, for the time-average of case 3DU ($Re_c = 5 \times 10^4$, $M = 0.4$, $\alpha = 5°$). A region of 3×3 grid-points was perturbed at $(x, y) = (0.25, 0.136)$. Solid lines have been multiplied by 1×10^6 and dashed lines by 4×10^7.

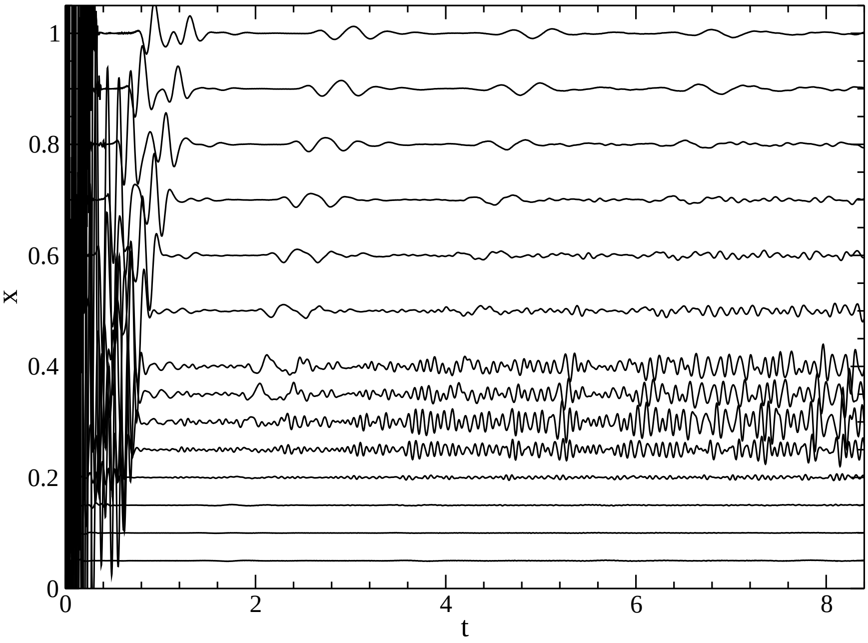

Figure 7.28: Time histories of dp/dt, with streamwise location indicated on the vertical axis, for the three-dimensional case at $Re_c = 5\times10^4$, $M = 0.4$, $\alpha = 7°$. A region of 3×3 grid-points was perturbed at $(x, y) = (0.2, 0.175)$. Lines have been multiplied by 2.5×10^7.

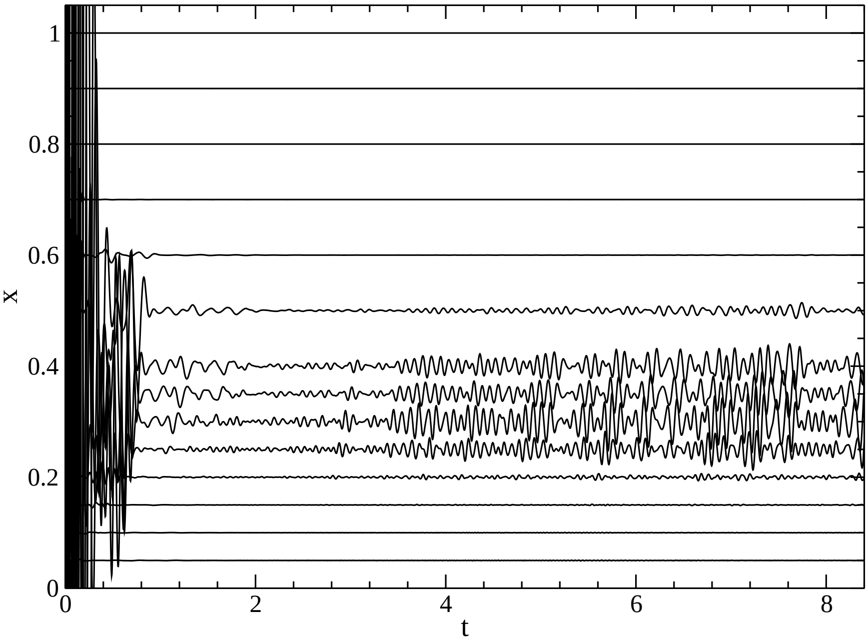

Figure 7.29: Time histories ofdp/dt, with streamwise location indicated on the vertical axis, for the three-dimensional case at $Re_c = 5\times10^4$, $M = 0.4$, $\alpha = 7°$. A region of 3×3 grid-points was perturbed at $(x, y) = (0.2, 0.175)$, and a buffer was applied for $x > 0.45$. Lines have been multiplied by 2.5×10^7.

Chapter 8

A mechanism for self-sustaining turbulence[1]

The persistence of turbulence upon removal of forcing, observed in chapters 5 and 6, suggests that some mechanism other than convective disturbance growth is present. Stability characteristics of the time-averaged flowfield have been investigated in chapter 7. The time-averaged flowfield of case 3DU was found to be unstable via an acoustic feedback loop, however it could not be determined whether such behaviour occurs in the fully developed flow. Although the time-averaged flowfield of case 3D7 was found to exhibit a very weak temporal instability, the growth rate was close to zero. In this chapter an alternative instability of the unsteady two-dimensional vortex shedding flow to three-dimensional perturbations is investigated.

8.1 Numerical method

A three-dimensional simulation is initialised in the same manner as case 3DF. Grid G3 (defined in section 4.3.1) is used, specifying a small number of spanwise points ($N_z = 16$) over the same spanwise domain width ($L_z = 0.2$). No time periodic forcing is added, but w-perturbations are superposed onto the initial condition in the form of white noise. The w-perturbations are 1×10^{-8} in amplitude, and only the boundary layer over the upper surface of the airfoil is seeded in this fashion. The simulation is progressed from this initial condition and no further disturbances are added. The stability characteristics of the unsteady two-dimensional separation bubble with vortex shedding may then be determined. The perturbations will either convect downstream ultimately leaving the flow over the airfoil unperturbed, or the perturbations will grow temporally

---

[1] See also Jones *et al.* (2007*b*)

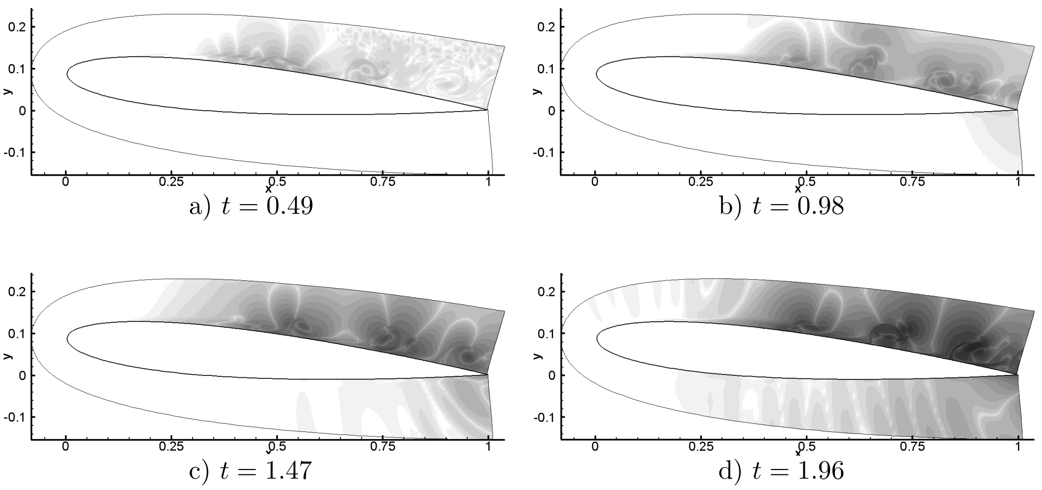

a) $t = 0.49$ b) $t = 0.98$

c) $t = 1.47$ d) $t = 1.96$

Figure 8.1: Iso contours of $|w|$ velocity in the vicinity of the airfoil, using 20 contours exponentially distributed over the range 10^{-10} to 10^{-2}, showing development with time after initialisation.

as in absolute instability. Effectively the method may be considered equivalent to a Floquet analysis, however the current method differs in that the baseflow is not perfectly periodic in time.

8.2 Time dependent behaviour

The resultant behaviour is illustrated by plotting absolute values of w-velocity in the vicinity of the airfoil at intervals of $t = 0.49$ (figure 8.1). It can be seen that the initial disturbances do not convect downstream leaving the source unperturbed, but grow in amplitude temporally until nonlinear magnitudes are reached. The w-perturbations grow in amplitude within individual vortices as they convect downstream. Additionally, in the vicinity of the vortex shedding location the perturbations exhibit growth in amplitude without convecting downstream. Temporal growth occurs immediately upon initialisation, and hence the onset is far too rapid to be explained by an acoustic feedback mechanism involving the trailing edge. The N-factor across the separated region has been computed via linear stability analysis to be $N = 9.5$. This precludes amplification of round of error as a route to transition, since a much larger N-factor would be required to amplify round-off error ($\sim 10^{-16}$) to non-linear amplitudes.

Having observed rapid temporal perturbation growth for the case with two-dimensional vortex shedding at five degrees incidence, the simulation was repeated at other angles of attack.The simulations all exhibited two-dimensional vortex shedding. Absolute values of w-velocity taken in the vicinity of the onset of vortex shedding are plotted in figure 8.2. Although erratic, due to variations during the shedding cycle, the amplitude of w-velocity perturbations appears to grow exponentially with time, and the temporal growth rate increases with incidence.

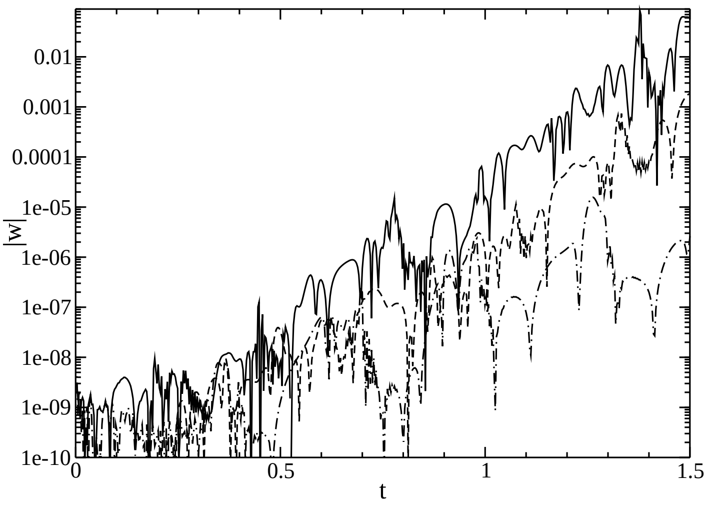

Figure 8.2: Time series of absolute w-velocity taken in the vicinity of vortex shedding at 5° (− ·), 7° (−−) and 8.5° (—)incidence.

8.3 Spatial onset

In order to isolate the spatial onset of the instability, a simulation was run using a different initial disturbance input, and an increased number of w-probes. Instead of seeding the entire upper airfoil boundary with white noise, a narrow 'strip' of white noise is used, centred at $(x, y) = (0.25, 0.136)$, and spanning the width of the domain. The evolution of the initial disturbance may then be tracked both spatially and temporally. Figure 8.3 shows an x/t plot of disturbance growth for this case. Due to the large growth rates present the probe readings were multiplied by $e^{-\sigma t}$, where $\sigma = 4$ is the temporal growth rate observed in the vicinity of vortex shedding, in order to better visualise the data. Therefore, where a probe signal appears constant in amplitude in figure 8.3, it is in fact growing at the rate of e^{4t}. The response to the perturbation varies with the x-location, as follows:

i) For $x \leq 0.2$ no perturbations are observed using this scaling.

ii) For $0.3 \leq x \leq 0.45$ the initial pulse generates a wavepacket in the boundary layer, which convects downstream. After $t = 0.3$ no further disturbances are visible for $x \leq 0.4$ using this scaling.

iii) For $0.5 \leq x \leq 0.55$ the initial wavepacket is observed to trigger disturbances that are lower in frequency than the initial disturbance, and are subsequently observed to grow exponentially in time.

iv) For $x \geq 0.6$ it is difficult to detect whether the initial wavepacket is present or not. Periodic disturbances are observed to occur, with a frequency the same as that of the vortex shedding ($f = 3.37$). The amplitude of disturbances at any fixed x-location appears to grow at the approximate rate e^{4t}, and the amplitude of disturbances also appears to increase with increasing x-wise location.

Rapid, sustained temporal disturbance growth first occurs in the region $0.5 \leq x \leq 0.55$, suggesting that some form of instability is sustained in the vicinity of the vortex shedding region. The temporal growth rate of perturbations appears approximately constant at all locations ($\sigma \approx 4$), however the increase in amplitude of perturbations with x-wise location for $x \geq 0.6$ suggests that the flow is also convectively unstable. The rapid onset of sustained temporal disturbance growth, and the absence of intermittent behaviour over long time-scales, suggest that this behaviour cannot be explained by an acoustic feedback loop similar to that observed in section 7.3.

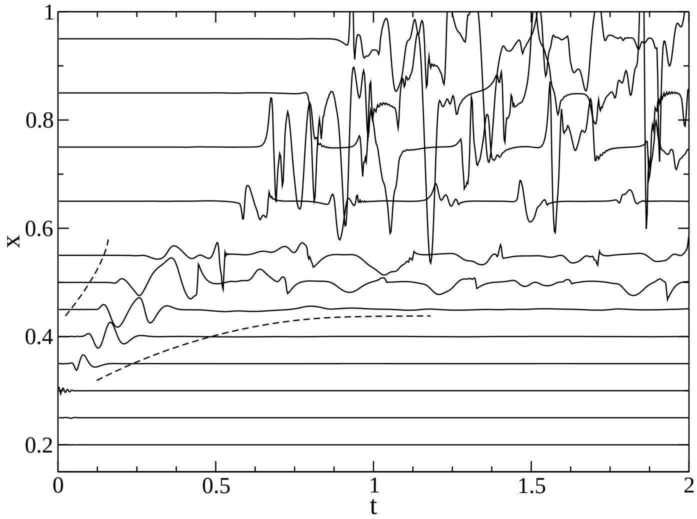

Figure 8.3: Time series of w scaled by multiplying with e^{-4t}, taken at several locations within the boundary layer, the dashed line indicates the wave-packet envelope.

8.4 Instability mechanism

The preceding section has identified a region instability in the vicinity of the vortex shedding location. Because the instability is subject to exponential growth, plots of perturbation quantities such as streamwise vorticity, ω_x, or w-velocity, for example, will vary markedly in amplitude depending on the time at which they are taken. To surmount this problem, the quantity ω_x^* is instead plotted, defined as

$$\omega_x^* = \omega_x A_0 e^{-\sigma t}, \tag{8.1}$$

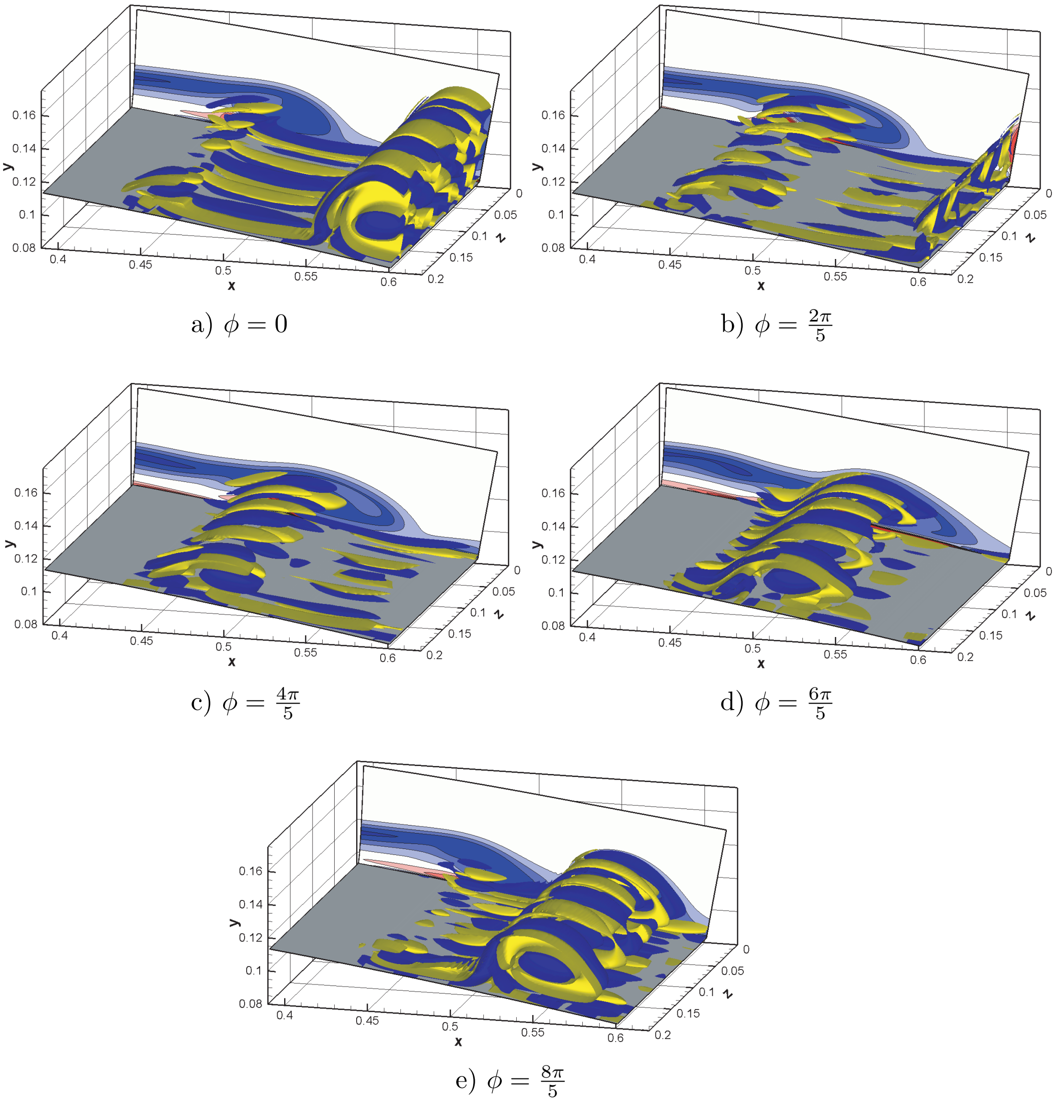

a) $\phi = 0$

b) $\phi = \frac{2\pi}{5}$

c) $\phi = \frac{4\pi}{5}$

d) $\phi = \frac{6\pi}{5}$

e) $\phi = \frac{8\pi}{5}$

Figure 8.4: Iso-surfaces of ω_x^* taken at five phases of the vortex shedding cycle. The far xy-plane displays iso-contours of ω_z, using ten levels over the range ±150.

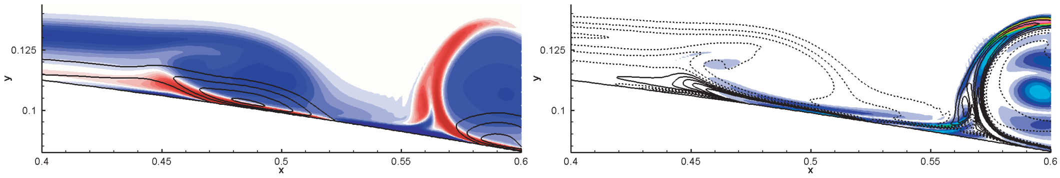

a) $\phi = 0$

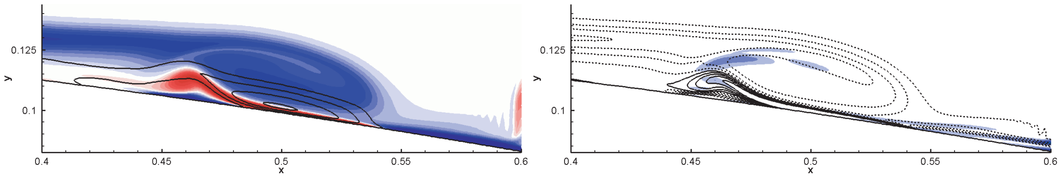

b) $\phi = \frac{2\pi}{5}$

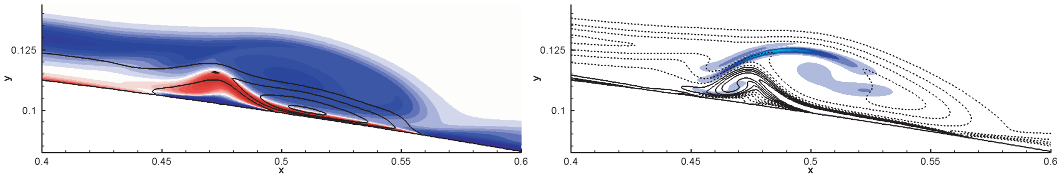

c) $\phi = \frac{4\pi}{5}$

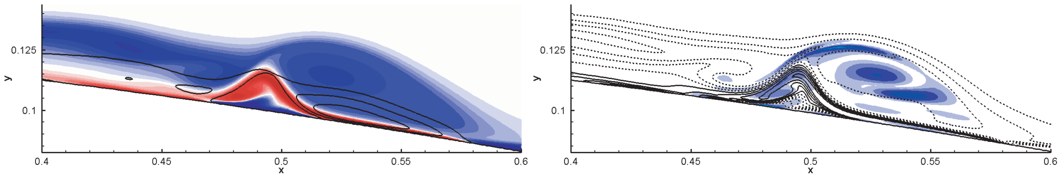

d) $\phi = \frac{6\pi}{5}$

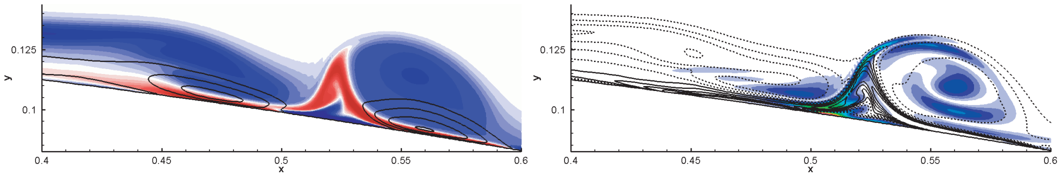

e) $\phi = \frac{8\pi}{5}$

Figure 8.5: The left-hand image shows iso-contours of ω_z, using 20 contours over the range ±150, with lines of constant u-velocity superposed using 4 levels over the range $-0.7 < u < 0$. The right-hand image shows iso-contours of ω_x^* using 20 levels over the range $5 - 100$ with lines of constant ω_z superposed using 10 levels over the range ±150. From top to bottom, five phases within the vortex shedding cycle are shown.

where A_0 is a constant chosen as 1×10^{-8} and $\sigma = 4$ is the exponential disturbance growth rate at $x = 0.5$. Plotting iso surfaces of ω_x^* in the vicinity of vortex shedding at five phases, ϕ, of the shedding cycle (figure 8.4) reveals spanwise-periodic structures that are associated with the instability. Depending on the phase of the vortex cycle, the structures appear both within and also wrapped around the spanwise vortices. Although only one shedding cycle is illustrated, the behaviour of the instability appears qualitatively similar from one cycle to the next.

The production and behaviour of ω_x is illustrated more clearly in figure 8.5, again for five phases within the shedding cycle. Images on the left of figure 8.5 illustrate the two-dimensional vortex shedding upon which the three-dimensional perturbations are growing, as well as regions of upstream fluid flow. Images on the right illustrate the spanwise root-mean-square (RMS) of ω_x^*, and hence indicate the magnitude of three-dimensional perturbations. Over the course of the shedding cycle a vortex is generated at the rear of the separation bubble before being released downstream. As the vortex begins to convect downstream, the magnitude of ω_x increases within the vortex core at a rate faster than the overall instability growth rate, as indicated by the increase in ω_x^* from figure 8.5a to 8.5e. This confirms the findings of section 8.3, that vortices convecting downstream are subject to convective perturbation growth. A second region of ω_x^* growth is observed during the shedding cycle, just upstream of the developing vortex, in the so called ‘braid’ region of high strain rate between successive vortices. At $\phi = \frac{4\pi}{5}$ a growing perturbation is clearly observed; it is orientated parallel to the x-axis and is the region exhibiting the largest magnitude of ω_x. As the developing vortex is shed and begins to convect downstream, the structure increases in length and vorticity magnitude and is wrapped around the vortex, forming an S-shape visible at $\phi = \frac{8\pi}{5}$ just upstream of the downstream travelling vortex. Again, ω_x increases at a rate faster than the overall instability growth rate. These regions of pronounced perturbation growth appear to closely match regions of instability growth identified in mixing layers and bluff body wakes; namely the vortex cores and the braid region between vortices (Williamson, 1996). The current case appears perhaps to hold a stronger analogy to shear-layer flow, however the mechanisms responsible for instability growth in braid regions and vortex cores are more extensively discussed in the literature for bluff body wakes. In the context of bluff body wakes, short wavelength perturbations within vortex cores are commonly attributed to elliptic instability, whereas two forms of instability growth have been observed within the braid region, denoted mode-A and mode-B. A brief summary of each mode follows, necessary to categorise observations of the current case.

Elliptic instability is the name given to the instability of two-dimensional elliptical streamlines to three-dimensional perturbations, for which a review is given in Kerswell (2002). The physical mechanism of instability is vortex stretching, and the instability manifests itself as a spanwise periodic deformation of the vortex core. Leweke & Williamson (1998*b*) suggest that the spanwise wavelength of the most amplified instability mode is of the order $\lambda = 3D$, where D is the diameter of the region of elliptical flow, comparing favourably with the results of Leweke & Williamson (1998*a*). Floquet analysis by Barkley & Henderson (1996) suggests a spanwise wavelength of $\lambda = 4D$ at onset. The presence of elliptic streamlines in the current case (figure 8.6) suggests that elliptic instability is likely to occur.

Instability growth within the braid region between vortices has been observed experimentally, both for bluff body wakes Williamson (1992) and free shear layers (Corcos & Lin, 1984; Bernal & Roshko, 1986). In bluff body wakes, two distinct instabilities have been observed in the braid region, denoted mode-A and mode-B (Williamson, 1996). Both forms of instability occur as spanwise periodic, streamwise 'tubes' of vorticity, formed in the braid region and extending between neighbouring two-dimensional vortices, that appear qualitatively similar to the structures observed in figure 8.4. Mode-A instability is associated with spanwise wavelength approximately the same as that of elliptic instability, i.e. 3 to $4D$, and occurs in conjunction with deformation of the vortex core, whereas mode-B is associated with spanwise wavelength approximately $\lambda = D$ and occurs with no deformation of the vortex core (Williamson, 1996). In the light of these differences it has been suggested that mode-A is caused by elliptic instability (Thompson, Leweke & Williamson, 2001), and that mode-B is in fact a manifestation of the instability of two-dimensional hyperbolic streamlines, analogous to that of elliptic instability (Leweke & Williamson, 1998*b*), denoted hyperbolic instability. For bluff body wakes mode-A is first observed at $Re_d > 190$, where Re_d is the Reynolds number based on cylinder diameter, and mode B is first observed at $Re_d > 240$.

Having identified similar regions of instability growth to those observed in bluff body vortex shedding, the spanwise wavelength of three-dimensional perturbations can be compared. The diameter, D, of vortices in the current case is approximately 0.05. The corresponding spanwise wavelengths for elliptic and mode-A instability are therefore expected to be in the range $0.15 < \lambda < 0.2$, and the corresponding wavelength for mode-B instability is expected to be of the order $\lambda = 0.05$. In figure 8.4 the most prominent structures present in the braid regions are streaks of ω_x, which possess a spanwise wavelength of on average $\lambda = 0.05$. This wavelength appears to correspond to that expected for mode-B instability, and is too small to be associated with either elliptic or mode-A instability. The spatial distribution of Floquet modes associated with mode-B instability in the study of Barkley & Henderson (1996) appears to closely match regions outside vortex cores where growth is observed in the current case, hence the streamwise vortices produced in braid regions appear similar in nature to mode-B instability observed in bluff body wakes. Plotting streamlines at $\phi = \frac{4\pi}{5}$ (figure 8.6) illustrates the presence of hyperbolic flow in the braid region upstream of each developing vortex. In order to detect any elliptic instability, perturbations within the vortex cores must be analysed. It is difficult to observe the vortex cores in three-dimensional plots, since they are masked by the ω_x structures wrapped around the vortices. Instead, iso-contours of ω_x^* are plotted for an $x - z$ plane through the vortex core at $\phi = \frac{8\pi}{5}$ in figure 8.7. The vortex core exhibits pronounced perturbations with the same spanwise wavelength as observed outside the vortex core, i.e. 0.05. However, in contrast to perturbations outside the core which are uniform in amplitude across the span, ω_x^* is much larger in magnitude over the range $0.16 < z < 0.2$ ($\omega_x^* \approx 100$) than at $0.05 < z =< 0.1$ ($\omega_x^* \approx 50$). Contours of perturbation z-vorticity taken at mid-span for $\phi = \frac{8\pi}{5}$, formed by subtracting the span-averaged z-vorticity from the instantaneous z-vorticity, are illustrated in figure 8.8. The structure within the vortex core appears similar to the localised perturbation solutions presented by Waleffe (1990) for unbounded elliptical flow, and is orientated along the axis of strain associated with the vortex deformation. The vortex core therefore appears perturbed at two distinct spanwise wavelengths with similar amplitude, $\lambda_1 \approx 0.05$ and $\lambda_2 \approx 0.2$. The first wavelength corresponds to that exhibited by ω_x structures outside the vortex core, i.e. mode-B instability, however the second wavelength is significantly larger and is comparable to wavelengths associated with elliptic instability. The structure of the perturbation within the vortex core appears similar to that associated with elliptic instability.

Evidence suggests then, that the production of ω_x occurs due to a combination of instabilities within the vortex cores and braid regions, appearing similar to elliptic and mode-B instabilities respectively, as observed in bluff body wakes (Williamson, 1996). It seems that the combination of elliptic and mode-A/B instabilities has not been considered in terms of its absolute or convective nature for bluff body wakes. In the current case, although the instability mechanism differs from the classical definition of absolute instability for disturbances on parallel baseflows, at a given x-location exponential temporal growth occurs. Hence

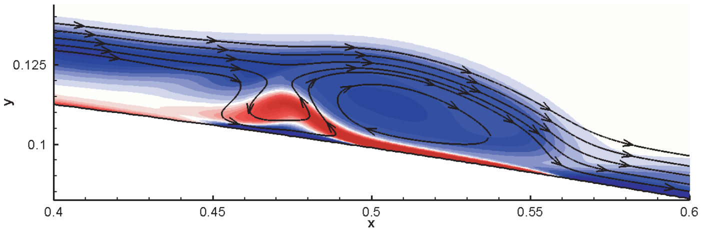

Figure 8.6: Iso-contours of ω_z taken at $\phi = \frac{4\pi}{5}$, using 20 levels over the range ±150, with streamlines superposed illustrating both the presence of both hyperbolic streamlines upstream of a developing vortex and elliptic streamlines within the vortex itself.

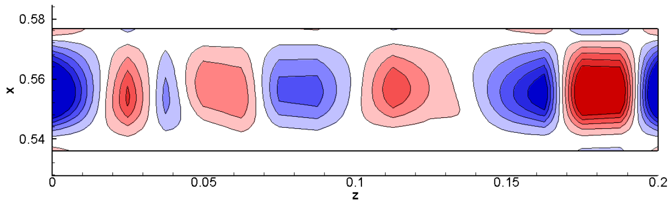

Figure 8.7: Iso-contours of ω_x taken across the centre of the vortex at $\phi = \frac{8\pi}{5}$, using 10 levels over the range ±100.

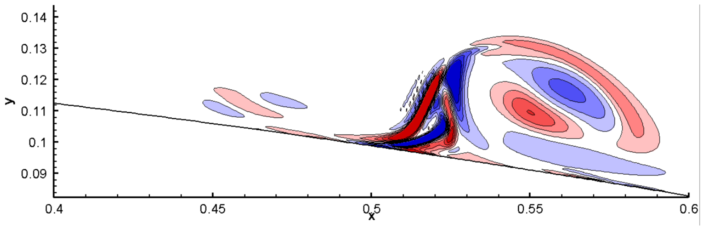

Figure 8.8: Iso-contours of perturbation z-vorticity at $t = 1.96$ after initialisation, corresponding to $\phi = \frac{8\pi}{5}$, using ten levels over the range $\pm 5 \times 10^{-3}$.

the term absolute instability is still useful to describe the behaviour present. Effectively the mechanism acts as an ‘oscillator’ as opposed to an ‘amplifier’.

The absolute nature of this instability can be explained by referring back to figure 8.5. At $\phi = \frac{8\pi}{5}$, in the region of hyperbolic flow upstream of the vortex a comparatively long S-shaped perturbation with large ω_x magnitude is observed, attributed to the presence of mode-B instability. This perturbation extends into a region of strong upstream fluid flow ($u \approx -0.7$) as illustrated in figure 8.5e, left. Hence ω_x perturbations present in the braid region, amplified in the vicinity of hyperbolic flow, are convected upstream with comparatively large velocity and, critically, into the braid region associated with the next developing vortex. This can be clearly seen in figures 8.5a-8.5c. The long thin ω_x perturbation near to the airfoil surface in the region $0.45 < x < 0.55$ in figure 8.5a, that is a remnant of the previous shedding cycle, convects into a region of hyperbolic flow and generates the streamwise orientated structure clearly visible in figure 8.5c. This behaviour is also illustrated in three dimensions in figure 8.4. Clearly the absolute mechanism is driven by instability growth within the braid region of vortices. Instability growth within vortex cores, whilst exhibiting similar temporal growth rate, appears to exhibit little upstream influence.

A schematic for the absolute instability mechanism is given in figure 8.9. Perturbations are amplified in braid regions, forming streamwise vortices, and extend into regions of high magnitude reverse flow. These streamwise vortices are convected upstream and into the braid region of the next developing spanwise vortex. The process then repeats with increasing amplitude. The absolute nature of the instability is sustained due to the existence of local regions of reverse flow for which the velocity magnitude greatly exceeds that of the time-average, in conjunction with large instability growth rates observed in hyperbolic regions of fluid flow. This instability mechanism is clearly not predictable via linear stability analysis of the time-averaged flowfield. Case 3DF may thus be described as exhibiting transition driven by convective instability and case 3DU by absolute instability of two-dimensional vortex shedding, by a combination instabilities similar to elliptic and mode-B instability observed in bluff body wakes. There is clear evidence that the secondary absolute instability of a forced separation bubble observed by Maucher *et al.* (1998) is driven by the same mechanism; the behaviour observed by Maucher *et al.* appears similar in many respects, including similar transitional structures. The instability mechanism may also be responsible for the rapid breakdown to turbulence observed by Spalart & Strelets (2000) in the absence of added disturbances. Laminar reattachment is not possible for the current case, due to the presence of this absolute instability.

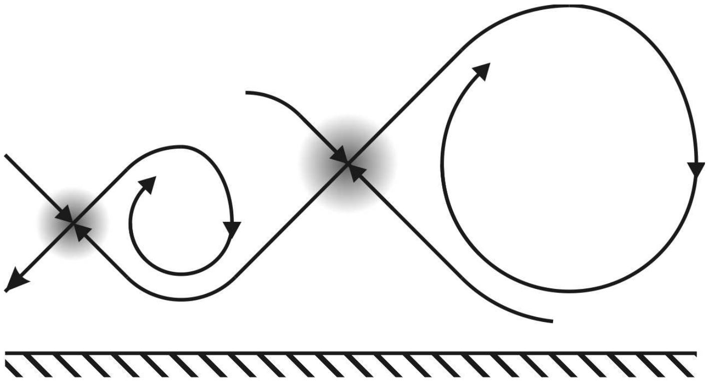

Figure 8.9: Schematic of the manner in which fluid exiting the braid region developed behind one vortex, subject to mode-B instability growth, enters the braid region associated with the subsequent vortex. Hyperbolic regions of fluid flow, where mode-B instability is observed to occur, are shaded.

8.5 Confirmation at $\alpha = 7°$

Having proposed an instability mechanism that appears responsible for the self-sustaining turbulence, it is useful to confirm the presence of this mechanism for a well-resolved simulation. The three-dimensional simulation at $\alpha = 7°$, presented in chapter 6, was performed with *a priori* knowledge of the instability mechanism proposed in this chapter, and hence was initialised in a manner allowing investigation of the transition process. Details of the initialisation process are given in section 6.4. Essentially the laminar vortex shedding flow was subject to a three-dimensional perturbation near the leading edge at the start of the simulation, and the subsequent was behaviour monitored.

When the simulation is progressed in time, the upper surface boundary layer appears unstable to the initial perturbation, and behaves in a similar fashion to that presented in section 8.2; perturbations grow in amplitude exponentially until non-linear amplitudes are reached. Figure 8.10 shows an x/t plot of w-velocity disturbance growth for this case, plotted in a similar fashion to that in section 8.3. Due to the large growth rates the probe readings were multiplied by $e^{-\sigma t}$, where $\sigma = 11$ is the temporal growth rate observed in the vicinity of vortex shedding, in order to better visualise the data. Therefore, where a probe signal appears constant in amplitude in figure 8.10, it is in fact growing at the rate of e^{11t}. The behaviour appears qualitatively similar to that observed at $\alpha = 5°$. During the period $0 < t < 0.4$, a wavepacket induced by the initial perturbation is observed to convect downstream. When the wavepacket reaches $x = 0.3$, sustained temporal disturbance growth is observed in the region $0.3 < x < 0.35$, corresponding to the region at which vortex shedding takes place. Plotting iso-surfaces of ω_x in the vortex shedding region (figure 8.11) illustrates the presence of spanwise periodic disturbances that appear similar to those identified in section 8.4, at $\alpha = 5°$. The spanwise wavelength appears to be $\lambda = 0.67$, slightly larger than that observed at $\alpha = 5°$.

It appears that the secondary absolute-instability of the vortex shedding behaviour to three-dimensional perturbations is also observed at $\alpha = 7°$, hence the presence of the instability mechanism has been confirmed for a well-resolved simulation. Since the simulation is well resolved in the z-direction (in contrast to the simulation at $\alpha = 5°$ in this chapter), it can be progressed further in time upon reaching nonlinear disturbance amplitudes. This is performed in chapter 6. Upon doing so transition to turbulence is observed, which confirms that the instability mechanism represents a route to transition, and the transition process is again observed to self-sustain.

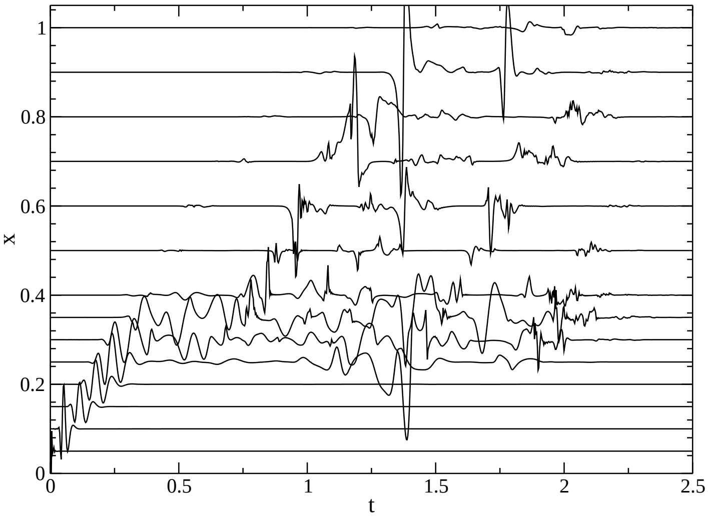

Figure 8.10: Time series of w-velocity scaled by multiplying with e^{-11t}, taken at several locations within the boundary layer, for case 3D7.

8.6 Summary

A series of three-dimensional simulations, resolving the linear response to three-dimensional perturbations, suggest that the two-dimensional vortex shedding behaviour is absolutely unstable to three-dimensional perturbations. The instability is associated with the production of streamwise vortices located in the braid regions between successive spanwise vortices, with spanwise wavenumber comparable to that of mode-B instability as observed in bluff body wakes. A mechanism by which the instability can self sustain is proposed, dependent on strong local reverse flow and large instability growth rates in braid regions. The temporal growth rate of the instability increases with airfoil incidence, presum-

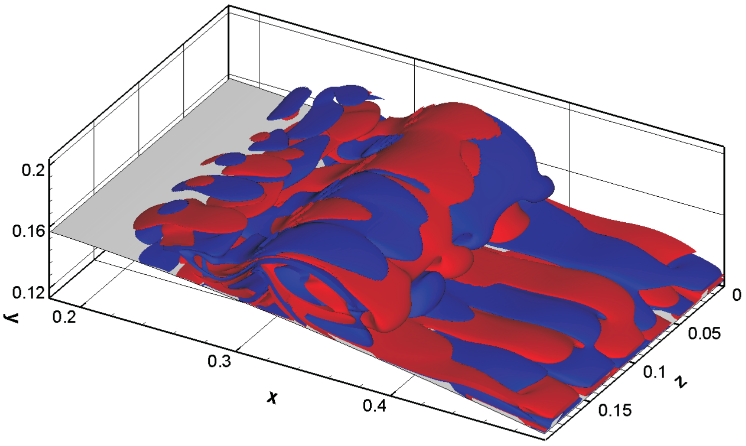

Figure 8.11: Iso-surfaces of streamwise vorticity for case 3D7 at $t = 0.7$, showing surfaces at $\pm 1 \times 10^{-5}$.

ably due to the larger magnitude of reverse flow present in the two-dimensional separation bubble. This instability mechanism is unrelated to the acoustic feedback instability observed in section 7.3.

It appears therefore, that in the absence of convectively driven transition within the shear layer, transition will take place by absolute instability of the two-dimensional vortex shedding in a manner not predicted by classical linear stability analysis of the time-averaged flowfield. This has important implications for the modelling of laminar separation bubbles, suggesting that if freestream turbulence levels drop below a certain value, the time-averaged transition and reattachment locations will be fixed and not vary with further decreases in freestream turbulence levels.

Chapter 9

Acoustic and spectral analysis of separation bubbles on airfoils at incidence

9.1 Introduction

Historically, much of the effort in reducing aircraft noise has been focused on that produced by the engines. Continued reductions in engine noise now mean that the contribution of airframe noise, including that produced by turbulent flow over lifting surfaces, is now becoming important. Solving the compressible Navier–Stokes equations allows both the hydrodynamic field and the acoustic response of the airfoil to be studied, and can potentially provide insight to mechanisms of sound generation.

For the current case of the flow over an airfoil with a separation bubble, the dominant acoustic source is expected to be acoustic scattering at the airfoil trailing edge. Turbulent fluctuations in free-space are inefficient radiators of noise in low speed flows, since the radiated acoustic intensity scales as M^8, (Lighthill, 1952) however when turbulent fluctuations pass a sharp edge, the acoustic radiation scales as M^5 (Ffowcs Williams & Hall, 1970). Hence at low Mach numbers (e.g. during take-off and landing) trailing edge noise will contribute significant amount to the total noise generated by an aircraft.

In this chapter the acoustic response of the three airfoil flows presented in chapters 5 and 6 will be compared in terms of their frequency-dependent behaviour.

9.2 General observations

Acoustic waves present in the three-dimensional simulations may readily be observed by plotting iso-contours of the divergence of velocity, $\nabla.\mathbf{U}$. The divergence of velocity is plotted for all three-dimensional simulations in figure 9.1. In comparison to the two-dimensional simulation at $\alpha = 5°$, cases 3DF and 3DU exhibit a more broadband frequency content, with more high-frequencies present. The acoustic response appears to be somewhat asymmetric, in that acoustic waves above the airfoil appear to possess more high-frequency content than those below the airfoil, as well as being slightly larger in amplitude. The amplitude of the acoustic radiation appears larger for case 3DU than for case 3DF, and the asymmetry appears more pronounced. Case 3D7 appears similar in nature to the three-dimensional simulations at $\alpha = 5°$, with a similar asymmetry in noise amplitude and frequency content. The amplitude of the acoustic radiation appears greater than for case 3DU, and the asymmetry appears more noticeable still. Acoustic waves appear resolved for at least three chords radius from the airfoil trailing edge.

At this point it should be noted that the acoustic field of case 3DF is of lesser quality than that of cases 3DU and 3D7. Case 3DF was initialised with a two-dimensional baseflow, and hence at the start of the simulation trailing edge noise produced by the two-dimensional vortex shedding flow was present in the domain (figure 9.2). When this transient acoustic radiation reached the freestream boundary, reflections were produced that propagated back into the domain, ultimately contaminating the near-airfoil region. The problem appears to have been exacerbated because the two-dimensional radiation is much greater in amplitude than three-dimensional radiation. By the time the forcing was removed, and case 3DU progressed, the contamination appears to have reduced significantly. Case 3D7 was performed using a simple buffer at the free-stream boundary in order to avoid this problem (as described in chapter 2, section 2.2.7), and hence the acoustic data from case 3D7 is the highest quality of all the three-dimensional simulations.

A simple measure of the amplitude of acoustic radiation generated by the airfoil flow is $\overline{p'p'}$. Iso-contours of $\overline{p'p'}$ for all three-dimensional simulations are plotted in figure 9.3. The most striking observation is that pressure fluctuations in the potential flow region appear significantly lower in amplitude for case 3DF than for cases 3DU and 3D7. This suggests that the addition of forcing has reduced the amplitude of acoustic waves generated by the flow around the airfoil. Low-frequency unsteadiness associated with the hydrodynamic field will also cause pressure fluctuations however, hence the frequency specific behaviour

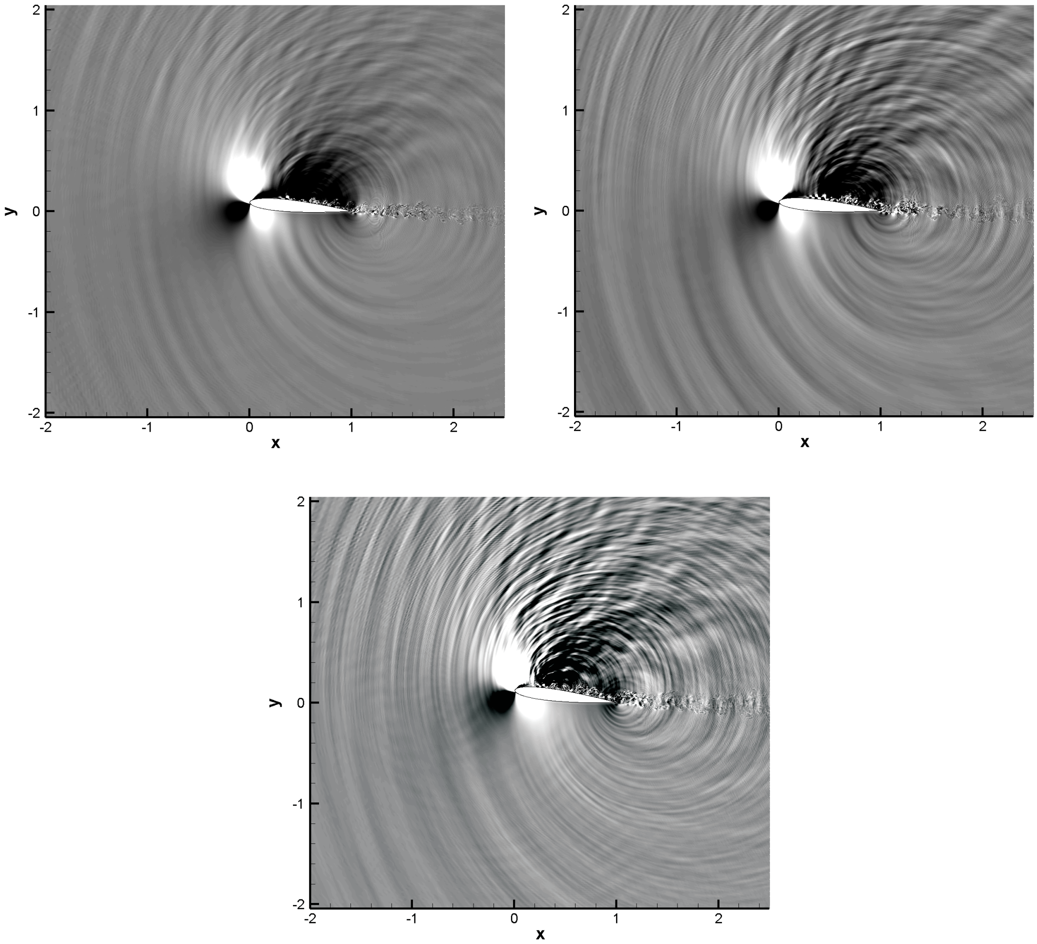

Figure 9.1: Instantaneous iso-contours of $\nabla.\mathbf{U}$ over the range $\pm 5 \times 10^{-2}$ for case 3DF (top-left) case 3DU (top-right), and case 3D7 (bottom).

should be considered before making too bold a conclusion. Iso-contours of $\overline{p'p'}$ for case 3D7 appear to be a similar order of magnitude to those of case 3DU.

The azimuthal variation of $\overline{p'p'}$ at three differing radii from the airfoil trailing edge is plotted in figure 9.4 for case 3DU and case 3D7. Case 3DF is omitted as transient effects, outlined above, corrupted the directivity plot. Two large lobes, one above and one below the airfoil, are observed for both cases. At three airfoil chords from the trailing edge case 3D7 exhibits a greater amplitude of $\overline{p'p'}$ than case 3DU, and the directivity appears to have changed slightly. Radiation below the airfoil exhibits a more pronounced upstream directivity, at 140°, and radiation above the airfoil exhibits more pronounced directivity at 100°.

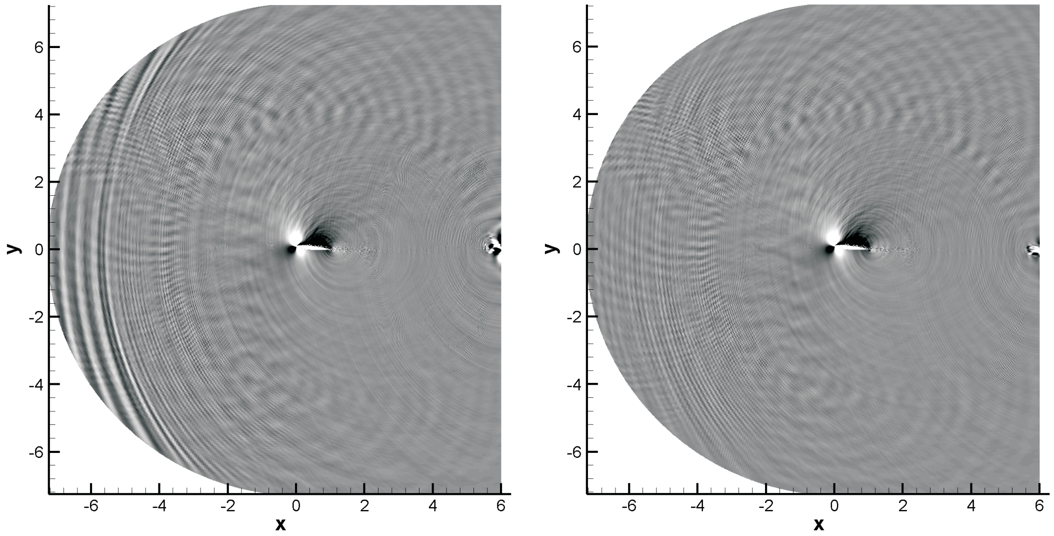

Figure 9.2: $\nabla.\mathbf{U}$ over the range $\pm 5 \times 10^{-2}$ for case 3DF at time $t = 5.6$ (left), and $t = 7.1$ (right), showing the effect of residual two-dimensional pressure waves.

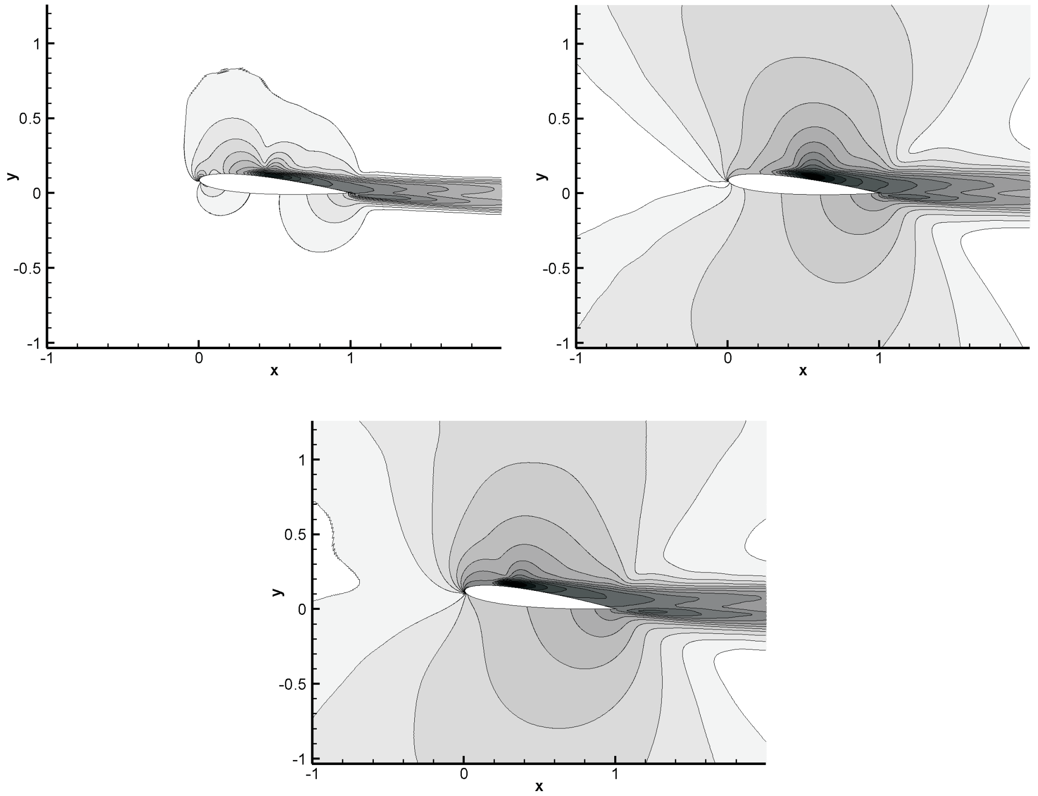

Figure 9.3: Iso-contours of $\overline{p'p'}$ for case 3DF (top-left), case 3DU (top-right) and case 3D7 (bottom), using 15 exponentially distributed levels over the range 5×10^{-7} to 1×10^{-2}.

9.3 Point pressure spectra

Pressure power-spectra were computed at several locations within the upper surface boundary layer and potential flow region for all the three-dimensional

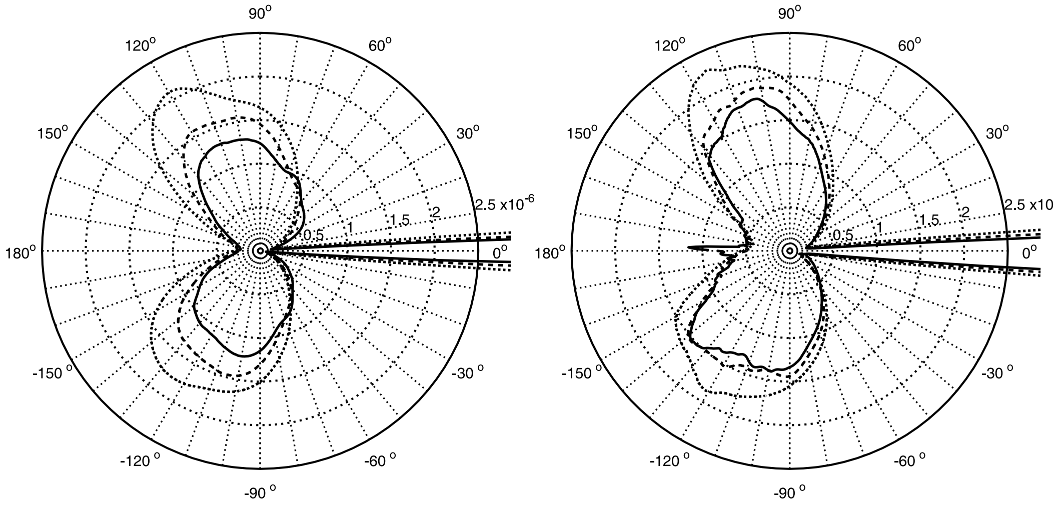

Figure 9.4: Azimuthal variation of $\overline{p'p'}$ at one $(\cdots)$, two $(--)$ and three $(—)$ chords radius from the airfoil trailing edge, for case 3DU (left) and case 3D7 (right)

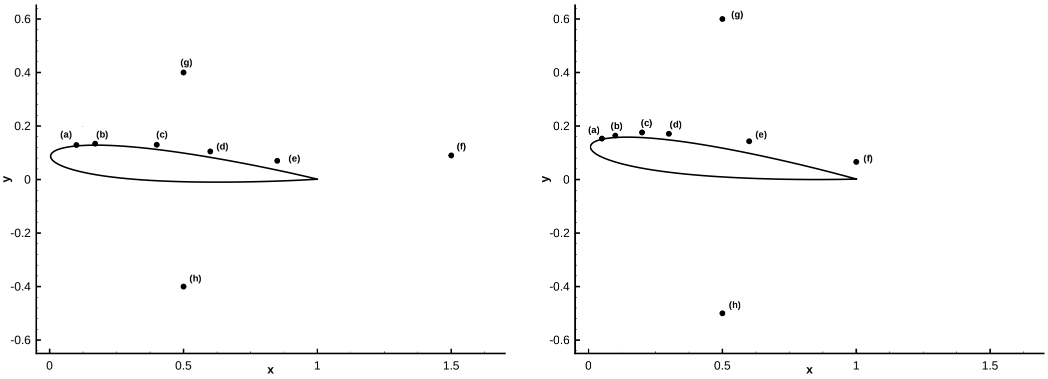

Figure 9.5: Illustration of point pressure probe locations for cases 3DF and 3DU (left), and case 3D7 (right).

cases, to allow comparison of frequency-dependent behaviour. Spectra were computed over an interval of 7.7 time units, using three overlapping segments with Hanning windowing applied (as detailed in section 2.3). For reference, figure 9.5 illustrates point pressure probe locations for cases 3DF, 3DU and 3D7, while table 9.1 gives a qualitative description of the fluid behaviour at each location. Specific x/y-locations are given under the relevant figure.

Pressure power-spectra computed at six locations for case 3DF are plotted in figure 9.6 Case 3DF was subject to explicitly added forcing at frequencies $f = 7.76$ and $f = 8.53$ in order to promote transition. The effect of the forcing can be observed in the laminar region (figures 9.6a-9.6c) as a double-peak at the forcing frequencies. The effect of the forcing can be seen most clearly at $x = 0.4$ (figure 9.6c), by which time the explicitly added disturbances have been

Probe	Description
a)	Upper surface boundary layer
b)	Upper surface separated shear-layer
c)	Upper surface separated shear-layer
d)	Vortex shedding onset (in two-dimensions)
e)	Upper surface turbulent boundary
f)	Airfoil near-wake
g)	Upper potential flow
h)	Lower potential flow

Table 9.1: Description of point pressure-probe locations.

amplified significantly via convective instability, and cause a broad peak in the power-spectra with amplitude of the order $\sim 10^{-2}$. The peak associated with the forcing frequencies clearly persists downstream of transition, at $x = 0.6$, (figure 9.6d) and is just visible at $x = 0.85$, (figure 9.6e). The effect of forcing does not persist into the wake however, (e.g. $x = 1.5$, figure 9.6f), and is not observed for either of the probes in the potential flow region (figures 9.6g-9.6f). Pressure power-spectra taken in the potential flow region illustrate clear differences between acoustic noise present above and below the airfoil (figure 9.6g-9.6f). The amplitude of pressure fluctuations is similar in the range $0 < f < 10$, but for $f > 15$ the amplitude of pressure fluctuations observed in the potential flow above the airfoil is significantly greater than that observed below the airfoil.

In addition to the explicitly added forcing, additional tones are present at $x = 0.1$ (figure 9.6a) and $x = 0.17$ (figure 9.6b). The fundamental tone appears to be at frequency $f = 11.2$, and at least three higher harmonics are observed at $x = 0.1$. This additional tone is larger in amplitude than the forcing at $x = 0.1$, however the amplitude has decreased by $x = 0.17$ and the tone cannot be observed downstream of transition, unlike the explicitly added forcing. That a tone of this frequency should be present at all is surprising, since no frequencies were introduced that can explain its presence. Subharmonics and higher harmonics of the forcing frequencies may reasonably expected to occur (Dovgal *et al.*, 1994), as would the difference and sum of the forcing frequencies (e.g. $f_1 + f_2$ and $f_2 - f_1$), however this would not explain the occurrence of a tone at $f = 11.2$. When pressure power-spectra are plotted for the two-dimensional simulation at $\alpha = 5°$, no tone is observed at $f = 11.2$ (figure 9.7, left).

No explicitly added disturbances were present for case 3DU, and hence the peaks observed in the laminar region for case 3DF at $f \approx 8$ are not present for case 3DU (figures 9.8a-9.8c). The additional tone observed at $f = 11.2$ for case 3DF persists however, and can clearly be observed at $x = 0.1$ (figure

9.8a), $x = 0.17$ (figure 9.8b), and $x = 0.4$ (figure 9.8b). The amplitude of this additional tone is larger than for case 3DF at all x-locations. If we were to assume the peak in the spectra is caused by an instability wave, the increase in amplitude over case 3DF is likely to be because case 3DU exhibits larger convective growth rates across the bubble than case 3DU (see section 7.2.1). The presence of the additional tone for both cases confirms that its presence is unrelated to the explicitly added forcing. Spectra at $x = 0.6$ and $x = 0.85$ are broadly similar in amplitude to those for case 3DF, although case 3DU exhibits increased amplitude at low frequencies. At $x = 1.5$ case 3DU exhibits power-spectra approximately two orders of magnitude larger in amplitude than case 3DF over the range $0.13 < f < 50$, despite similar spectra at $x = 0.85$. Assuming the pressure fluctuations at $x = 0.6$ and $x = 0.85$ are primarily caused by the passage of turbulent structures, it would appear that turbulence in the boundary layer of case 3DF is decaying more rapidly than that of case 3DU. The probe located in the upper potential flow exhibits slightly greater amplitude than that of case 3DF across all frequencies plotted. For the probe in the lower potential flow an even larger increase in amplitude is observed for case 3DU. Similar differences in behaviour between the upper and lower potential-flow probes are observed for case 3DU as for case 3DF; again the upper probe exhibits greater amplitude at higher frequencies.

In chapter 7, section 7.3.5 an acoustic/hydrodynamic feedback loop was observed for the time-averaged flowfield of case 3DU. The fact that the feedback loop has been found present for the time-averaged flowfield of a three-dimensional simulation raises the question as to whether such behaviour will be observed in the fully developed time-dependent case. Given that the effect of explicitly adding forcing at $f \approx 8$ can still be observed at $x = 0.85$ in pressure spectra within the boundary layer for case 3DF (figure 9.6e), it seems feasible that a tonal contribution to the turbulent fluctuations, and hence also to the acoustic response, could occur if an acoustic feedback loop is present. It could be argued that pressure spectra at $x = 0.6$ and $x = 0.85$ exhibit a local maxima at $f \approx 4$ for case 3DU (figures 9.8d and 9.8e), which would be of similar order to that expected for the feedback loop, however the maxima is not distinct, and no such maxima is observed for pressure spectra taken in the potential flow region. There is therefore no strong evidence of acoustic-feedback-related phenomena for case 3DU, however the possibility that such a mechanism may generate a tonal response in turbulent airfoil flows cannot be ruled out. If pressure spectra could be obtained for much longer time series the low frequency behaviour of case 3DU could be investigated with more confidence.

The topology of the flow around the airfoil at $\alpha = 7°$ is different to that at $\alpha = 5°$, hence direct comparisons of spectra taken at individual x-locations are less meaningful, so probes have been placed in locations where similar fluid phenomena is occurring as for the probes in cases 3DU and 3DF. Again, no explicitly added disturbances were present for case 3D7, however an additional tone is still observed in the laminar region (figures 9.9a-9.9c), along with higher harmonics. Surprisingly the tone is at the same frequency as for cases 3DF and 3DU, and again the additional tone is not observed for the equivalent two-dimensional simulation (figure 9.7, right). The tone persists until the transition region ($x = 0.3$, figure 9.9d), but is not present in any other spectra. Spectra at $x = 0.6$ (figure 9.9e) appear remarkably similar to those taken at $x = 0.85$ for cases 3DF and 3DU, where boundary layer properties are similar (e.g. c_f, δ^*). The same asymmetry between upper and lower sides of the airfoil is observed for probes in the potential flow, with the upper probe exhibiting greater amplitude at for higher frequencies.

9.4 Surface pressure spectra

Surface pressure spectra are computed in order to describe the frequency content of fluctuations present in the airfoil boundary layer. Spectra are computed for all points on the airfoil surface before being span-averaged. No windowing or segmenting is performed, since span averaging already improves the quality of the spectra. Iso-contours of the pressure-spectra modulus are then plotted against S, where S is the airfoil surface coordinate, defining the leading edge as $S = 0$. By plotting S instead of x-location the leading-edge region can be observed more clearly. Surface pressure spectra are plotted in this fashion for case 3DF, 3DU and 3D7 in figures 9.10, 9.11 and 9.12 respectively.

Surface pressure spectra from case 3DF clearly illustrate the presence of the explicitly added forcing at $f = 7.76$ and $f = 8.53$ on the upper airfoil surface. The forcing at $f = 7.76$, $\beta = 2\pi/L_z$ appears to be more strongly amplified than that at $f = 8.53$, which was forced at $\beta = 6\pi/L_z$ and $\beta = 8\pi/L_z$. The higher harmonic $f = 15.52$ can be observed, and a ‘ladder’ structure of tones appears present around the two primary forcing frequencies; additional tones appear with frequency spacing the difference of the two explicitly added forcing frequencies, i.e. $\Delta f = 8.53 - 7.76$. Upstream of transition the only significant fluctuations appear to be either low frequency in nature in the region $0. \leq x \leq 0.3$ or fluctuations at the forcing frequencies. Little other unsteadiness is present. In the vicinity of transition, $x = 0.45$, the modulus of all frequencies increases

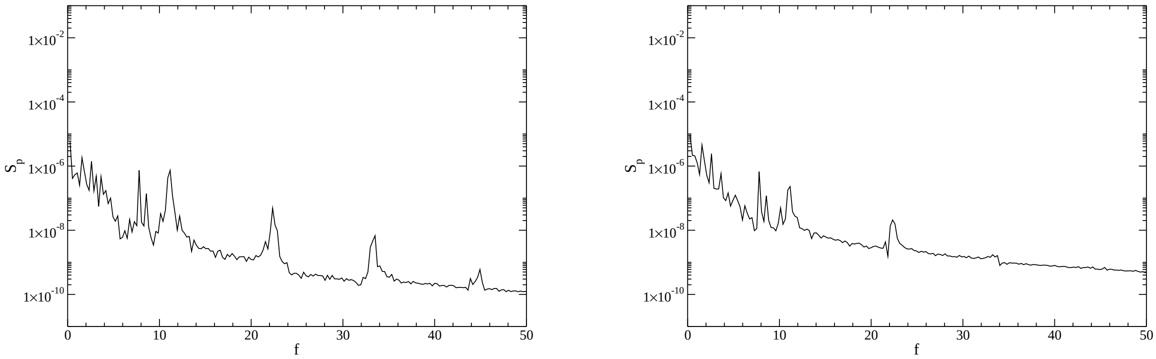

a) $x = 0.1$, $y = 0.129$ b) $x = 0.17$, $y = 0.134$

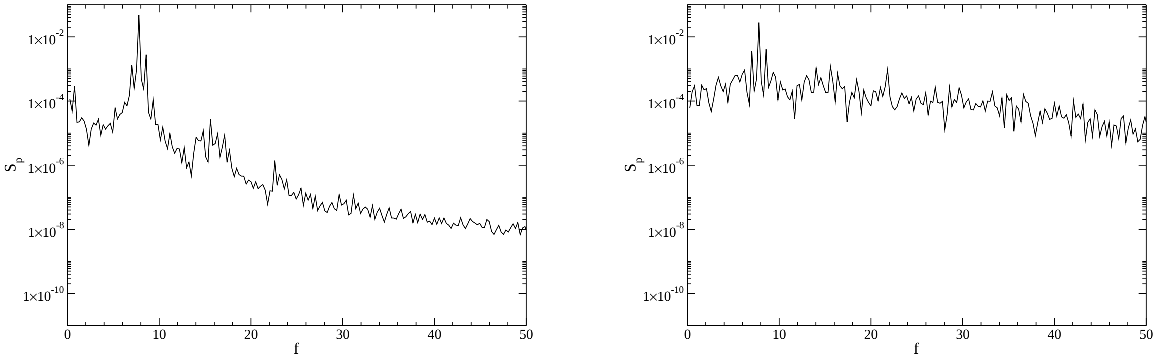

c) $x = 0.4$, $y = 0.130$ d) $x = 0.6$, $y = 0.105$

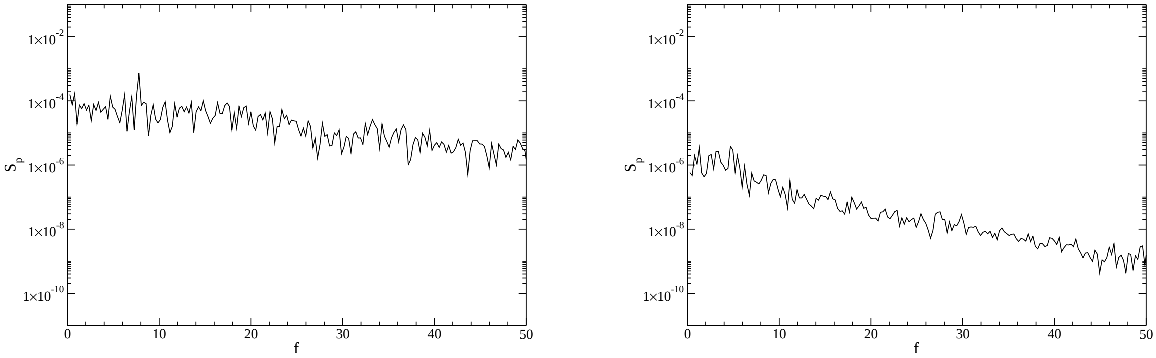

e) $x = 0.85$, $y = 0.070$ f) $x = 1.5$, $y = 0.090$

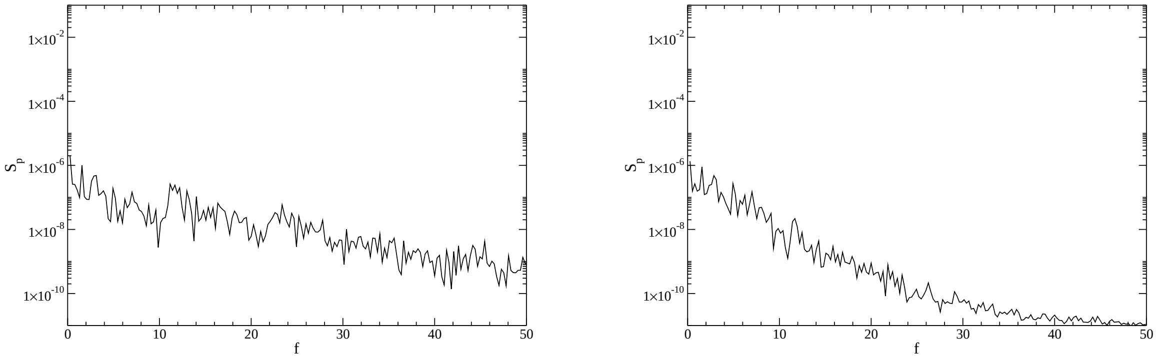

g) $x = 0.5$, $y = 0.400$ h) $x = 0.5$, $y = -0.400$

Figure 9.6: Temporal pressure spectra for case 3DF, taken at x-locations indicated.

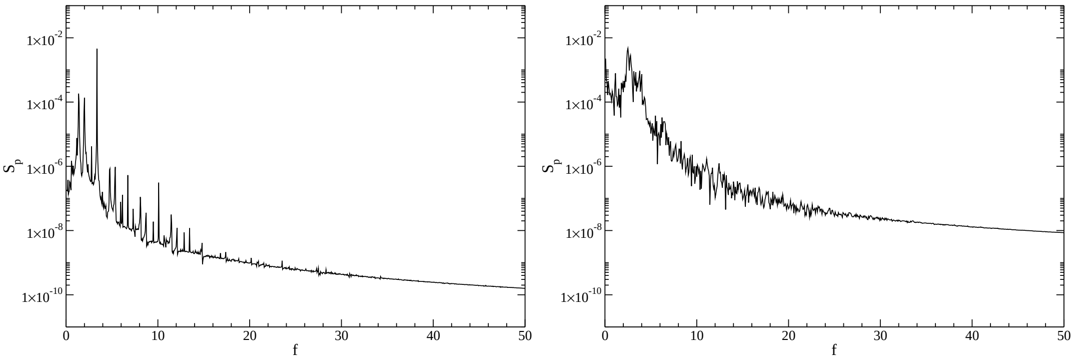

Figure 9.7: Temporal pressure spectra for the two-dimensional case at $\alpha = 5°$, taken at $x = 0.17$, $y = 0.134$ (left), and for the two-dimensional case at $\alpha = 7°$, taken at $x = 0.15$, $y = 0.17$ (right).

dramatically. Downstream of transition the amplitude of fluctuations decreases with increasing x-location, with the amplitude of high frequency fluctuations decreasing more rapidly than that of the low frequencies. The additional tone at $f = 11.2$ is also visible in surface spectra, and appears largest in amplitude at $x \approx 0.1$. The tone appears small in amplitude in comparison to the forcing frequencies.

On the lower airfoil surface the behaviour is markedly different. There appear to be very few fluctuations at mid to high frequencies. Pressure fluctuations are observed at low frequencies however, and appear to increase in amplitude both with proximity to the airfoil trailing edge and with decreasing frequency. The lower surface boundary layer is subject to a favourable pressure gradient until around the mid-chord, and hence no instability wave growth is expected in this region. It appears that the pressure fluctuations on the lower airfoil surface are caused by the passage of acoustic waves generated at the trailing edge, and hence for case 3DF trailing edge-noise appears to be significant primarily for $f < 10$.

As expected, case 3DU (figure 9.11) exhibits no clear tones in the transition region. Although local maxima may be observed in the transition region, they are not significantly larger in amplitude than at other similar frequencies. Compared to case 3DF, frequencies in the range $1 < f < 8$ appear significantly larger in amplitude in the transition region. The amplitude of fluctuations in the range $1 < f < 4$ over the separated region is also greater than for case 3DF, suggesting that the entire bubble is more unsteady, as well as the transition process being more energetic. The additional tone is observed to be present, at greater amplitude than for case 3DF, and reveals itself to consist of two closely spaced peaks, at $f = 10.9$ and $f = 11.3$. Although the amplitude of the tone is significant, it does not reach levels similar to those observed during transition at lower frequencies, and hence is unlikely to play a primary role in instigating

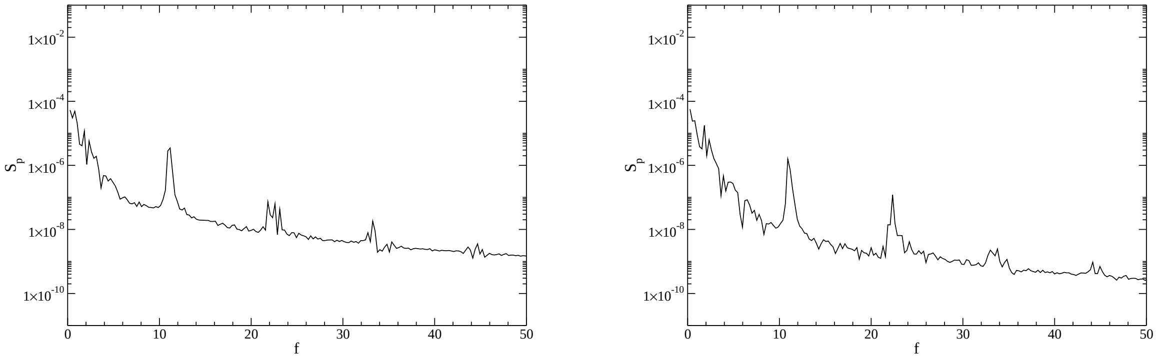

a) $x = 0.1$, $y = 0.129$ b) $x = 0.17$, $y = 0.134$

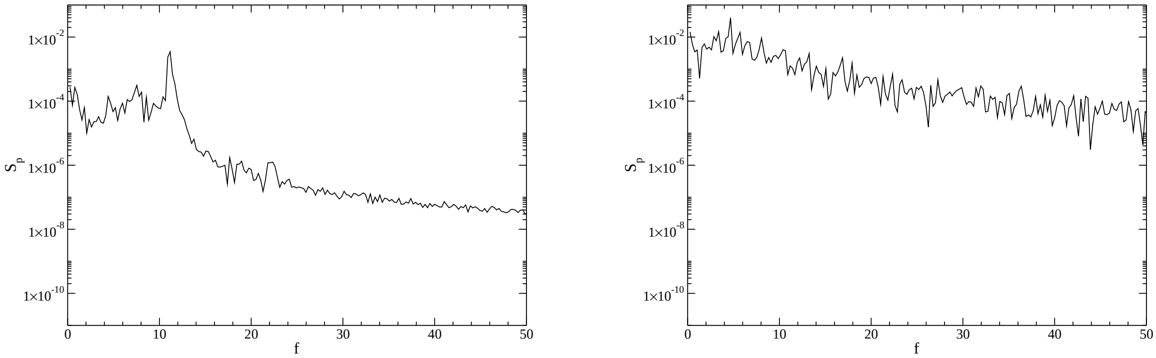

c) $x = 0.4$, $y = 0.130$ d) $x = 0.6$, $y = 0.105$

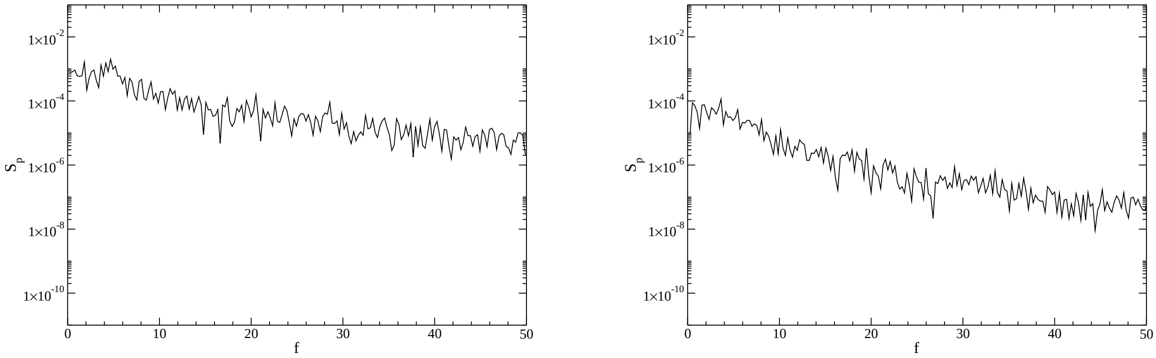

e) $x = 0.85$, $y = 0.070$ f) $x = 1.5$, $y = 0.090$

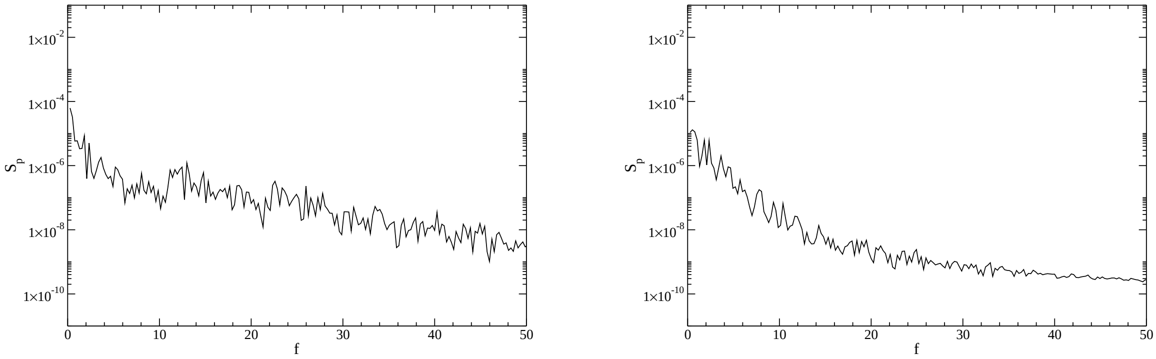

g) $x = 0.5$, $y = 0.400$ h) $x = 0.5$, $y = -0.400$

Figure 9.8: Temporal pressure spectra for case 3DU, taken at x-locations indicated.

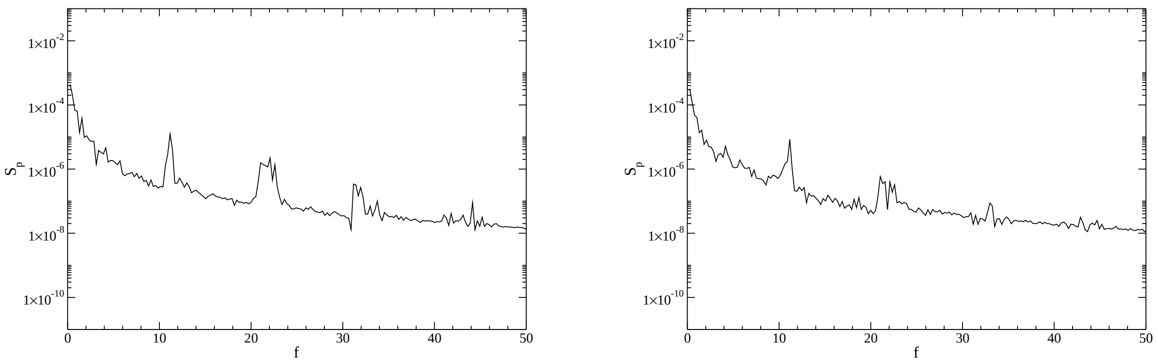

a) $x = 0.05$, $y = 0.153$ b) $x = 0.1$, $y = 0.164$

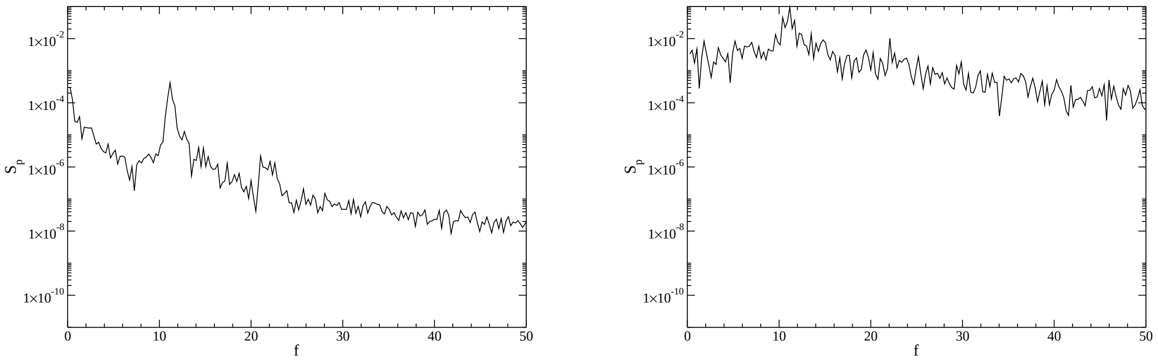

c) $x = 0.2$, $y = 0.176$ d) $x = 0.3$, $y = 0.171$

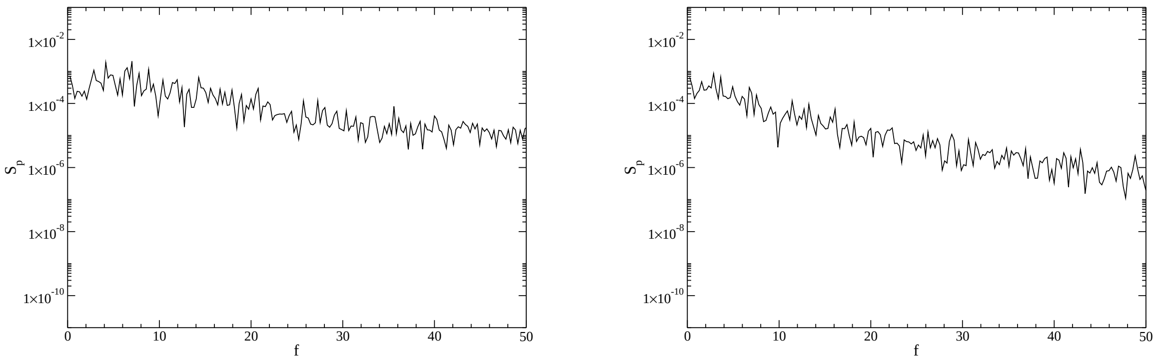

e) $x = 0.6$, $y = 0.143$ f) $x = 1.0$, $y = 0.066$

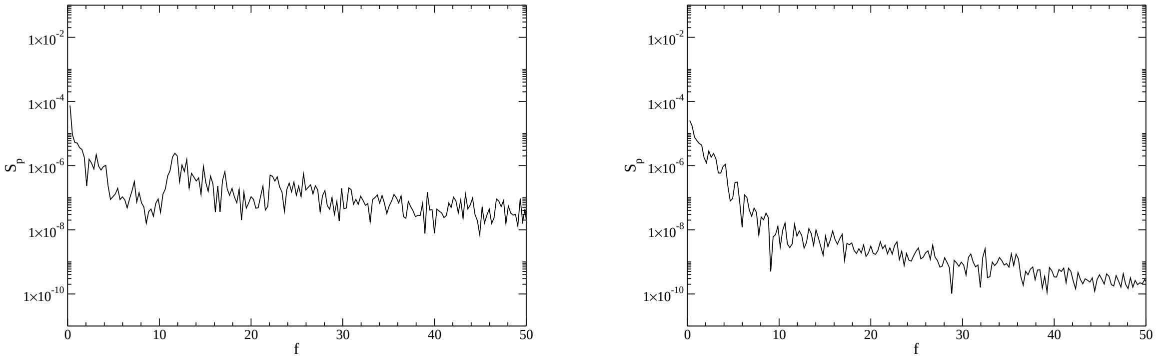

g) $x = 0.5$, $y = 0.600$ h) $x = 0.5$, $y = -0.500$

Figure 9.9: Temporal pressure spectra for case 3D7, taken at x-locations indicated.

transition. As for case 3DF, the acoustic scattering appears to be significant primarily for $1 < f < 10$, based on the amplitude of pressure fluctuations on the lower airfoil surface, however the amplitude of fluctuations on the lower airfoil surface is much greater for case 3DU. This would appear to be due to the increased amplitude of fluctuations in the range $1 < f < 8$ over the upper airfoil surface, and the closer proximity of the transition location to the trailing edge.

Case 3D7 also exhibits a clear maximum at the frequency of the additional tone, $f = 11.2$ (figure 9.12). The additional tone appears to take the form of a single peak, and is the largest amplitude fluctuation present. The spectral behaviour of the additional tone appears qualitatively similar to that of the explicitly added forcing of case 3DF; almost as if a single-frequency instability wave has been introduced and is strongly convectively amplified. The additional tone reaches peak amplitude at $x \approx 0.3$. The laminar region shows increased amplitude of fluctuations at all frequencies compared to the cases at $\alpha = 5°$. Pressure spectra on the lower airfoil surface again show that trailing-edge scattering is most effective for $f < 10$. Visual inspection suggests that the amplitude of spectra on the lower surface is of a similar order of magnitude to that of case 3DU.

For cases 3DF and 3DU, and to a very limited extent for case 3D7, unusual behaviour can be observed near the leading edge on the upper airfoil surface. Most noticeably for case 3DF, there appears to be a local maxima in the spectra occurring across a range of frequencies, located directly in the vicinity of the leading edge but biased slightly toward the upper airfoil surface. Acoustic scattering is known to occur at the leading edge of airfoils (Roger & Moreau, 2005), however due to the finite leading-edge radius one would expect it to be predominant only for even lower frequencies than trailing edge noise. Certainly, Roger & Moreau (2005) suggest that leading-edge back-scattering will be significant only for $kc < 10$, where k is the acoustic wavenumber and c the airfoil chord. For case 3DF the speed of sound in the vicinity of the leading edge is ~ 1.1, suggesting that leading-edge scattering will be significant for $f < 1.75$. The local maxima appears at significantly higher frequencies than 1.75, hence is unlikely to be caused by leading-edge scattering, based on the criteria of Roger & Moreau.

A further possibility is that the local maxima represents a location of boundary layer receptivity to free-stream (acoustic) disturbances. The receptivity process was observed numerically in section 7.3.1, and found to be a critical stage in the observed acoustic feedback instability. Where boundary layer receptivity does occur, the resultant hydrodynamic disturbances will either decay or amplify dependent on the local boundary layer stability characteristics. Linear stability analysis (section 7.2) suggests that boundary layer disturbances will not convectively amplify until $x > 0.05$, hence boundary layer receptivity and subsequent decay of the hydrodynamic disturbances may potentially be responsible for the maxima observed at airfoil the leading edge. Certainly, boundary layer receptivity is expected to occur over a range of frequencies (Wanderley & Corke, 2001), and in section 7.3.1 was observed to take place for frequencies as low as $f = 1.7$ and as high as $f = 11$. It is therefore felt that leading-edge receptivity is a more likely explanation for the presence of the local maxima than leading-edge back-scattering.

9.5 Free-stream pressure spectra

In order to study the frequency dependent-behaviour of the acoustic response of the airfoil, temporal pressure spectra were computed for the potential flow region for every fourth point in both the ξ and η directions, at the airfoil mid-span. The spectra are presented in two ways. First, the real coefficient of the Fourier transformed pressure field is plotted for specific frequencies. This clearly illustrates the directivity of acoustic radiation at specific frequencies. Secondly, the modulus of the spectra is averaged over finite frequency ranges and plotted. This illustrates more general trends of frequency dependent behaviour.

9.5.1 Real coefficient of the Fourier transformed pressure field

The real coefficient of the direct Fourier transform of pressure is plotted at four frequencies for each three-dimensional simulation. Plotting the real coefficient illustrates clearly the directivity and origin of pressure fluctuations. The frequencies were chosen for their possible physical significance. Frequency $f = 3.37$ corresponds to the frequency of the naturally occurring vortex shedding at $\alpha = 5°$, frequency $f = 7.76$ corresponds to the dominant forcing frequency of case 3DF, frequency $f = 11.2$ corresponds to the additional tone observed in point pressure spectra (section 9.3) and surface pressure spectra (section 9.4), and frequency $f = 15$ is an arbitrarily selected higher frequency.

The real part of the Fourier transformed pressure field is plotted for case 3DF, case 3DU and case 3D7 in figures 9.13, 9.14 and 9.15 respectively. The behaviour of individual frequencies varies strongly both with frequency and from case-to-case. For cases 3DF and 3D7, the real coefficient at frequency $f = 3.37$ appears indicative of trailing edge noise. The real-coefficient takes the form of periodic waves originating at the airfoil trailing edge, with primarily upstream

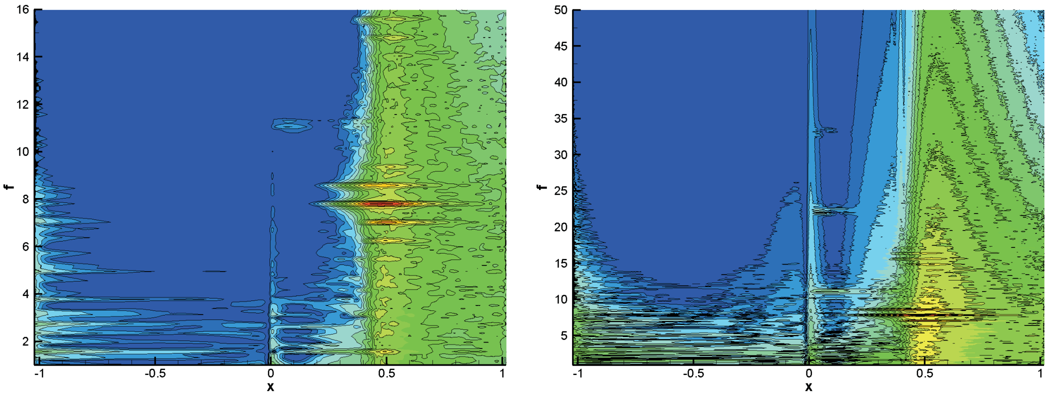

Figure 9.10: Modulus of the span-averaged Fourier transform of surface pressure for case 3DF showing frequencies $1 < f < 16$ (left), plotted using 15 levels exponentially distributed over the range $1 \times 10^{-4} - 4 \times 10^{-2}$, and frequencies $1 < f < 50$ (right), plotted using levels similarly distributed over the range $1 \times 10^{-5} - 4 \times 10^{-2}$.

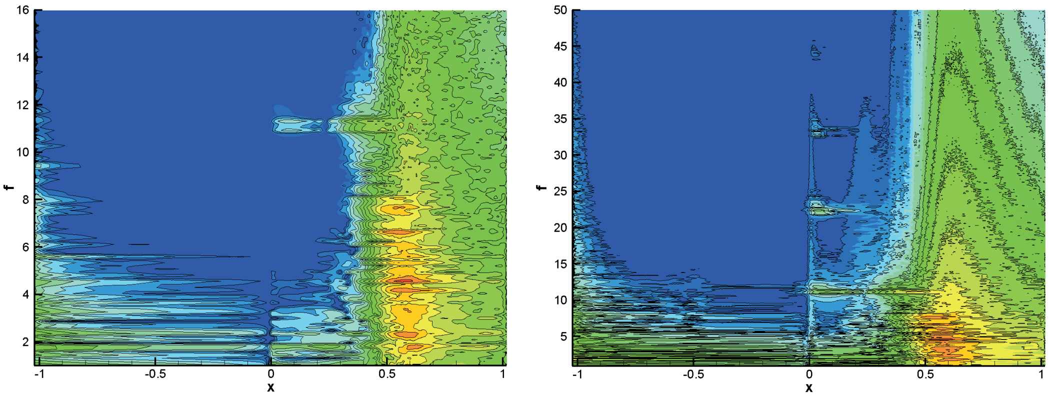

Figure 9.11: Modulus of the span-averaged Fourier transform of surface pressure for case 3DF showing frequencies $1 < f < 16$ (left), plotted using 15 levels exponentially distributed over the range $1 \times 10^{-4} - 4 \times 10^{-2}$, and frequencies $1 < f < 50$ (right), plotted using levels similarly distributed over the range $1 \times 10^{-5} - 4 \times 10^{-2}$.

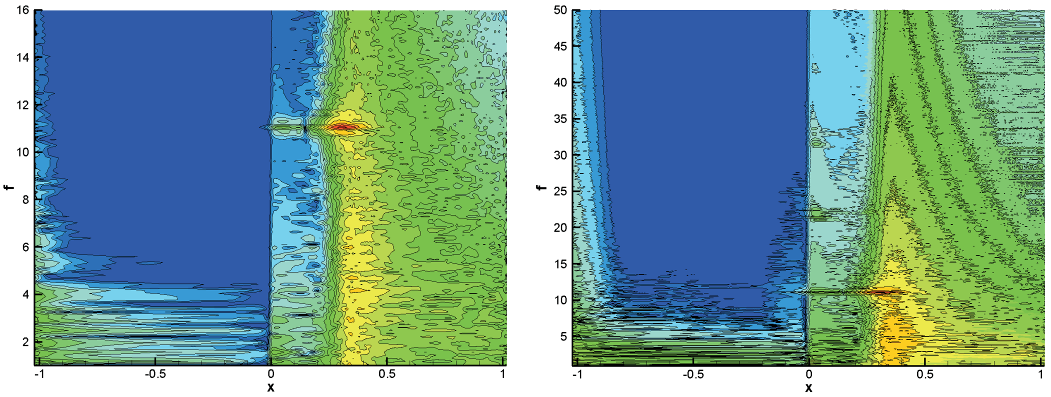

Figure 9.12: Modulus of the span-averaged Fourier transform of surface pressure for case 3DF showing frequencies $1 < f < 16$ (left), plotted using 15 levels exponentially distributed over the range $1 \times 10^{-4} - 4 \times 10^{-2}$, and frequencies $1 < f < 50$ (right), plotted using levels similarly distributed over the range $1 \times 10^{-5} - 4 \times 10^{-2}$.

directivity. Iso-contours of the real coefficient for case 3D7 in particular appear visually similar to the trailing edge noise observed in two-dimensions, at $\alpha = 5^\circ$ (section 4.4.1), with similar out-of-phase behaviour above and below the airfoil. Pressure-field spectra for case 3DF are of lesser quality, however qualitatively similar behaviour can still be observed. For case 3DU there is still evidence of trailing edge noise, but the real-coefficient appears asymmetric, as though the acoustic radiation over the upper airfoil surface is stronger.

Frequency $f = 7.76$ exhibits different behaviour depending on the airfoil incidence. At $\alpha = 5^\circ$ (i.e for cases 3DF and 3DU) trailing-edge noise appears to be the dominant acoustic source, although there is a slight kink in wave fronts above the airfoil for case 3DF, and an upstream pointing lobe of higher amplitude at $x \approx 0.5$ for case 3DU. At $\alpha = 7^\circ$ there is almost no trailing-edge noise present. Instead, the acoustic radiation appears to originate from a second acoustic source. This secondary source appears to be located on the upper airfoil surface, at around $x = 0.4$, and possesses clear upstream directivity. The presence of forcing at $f = 7.76$ cannot be detected by visual inspection of case 3DF, hence the forcing appears ‘quiet’ in comparison to naturally occurring acoustic events.

Frequency $f = 11.2$ corresponds to the additional tone observed in point pressure spectra (section 9.3), and surface pressure spectra (section 9.4). The real coefficient at this frequency exhibits unexpected behaviour; the real coefficient is large above and close to the airfoil, but does not seem to be representative of pressure waves propagating into the freestream. Taking the Fourier transformed pressure field, performing an inverse transform for the single frequency $f = 11.2$ and animating the real part of the fluctuating pressure signal allows the direction of wave propagation to be determined. The pressure field for case 3DU at $f = 11.2$ is plotted in figure 9.16 for three phases, $\phi = 0$, $\phi = \pi/2$ and $\phi = 3\pi/2$, however the resultant behaviour is most clearly illustrated in animations. In light of animated data it is apparent that the pressure fluctuations at $f = 11.2$ take the form of upstream travelling waves that rapidly decay in amplitude upstream of the airfoil leading edge. Measuring as close to the airfoil surface as possible, the disturbance wavelength appears to lie in the range $0.2 - 0.29$, which corresponds to a propagation velocity in the range $2.24 < c < 3.25$. Conversely, above the airfoil the streamwise velocity varies over the range $1.1 < u < 1.5$, and given a Mach number $M = 0.4$ this would suggest upstream wave propagation velocities in the range $1 < c < 2.1$. Furthermore, trailing edge noise is apparent below the airfoil at low amplitudes in figure 9.16, and the wavelength of the trailing edge noise below the airfoil appears significantly smaller than that of the pressure waves above the airfoil, despite the fact that the freestream velocity is lower below the airfoil hence the wavelength should be longer. Effectively the radiation above the airfoil possesses a wavelength longer than that expected for pressure waves propagating upstream at the speed of sound at $f = 11.2$. It should be noted that the structures observed are very large in comparison to the grid spacing, and hence do not appear to be grid-dependent. In light of this unusual behaviour, the additional tone observed at $f = 11.2$ is discussed in more detail in section 9.6.

At frequency $f = 15$, for all cases, the dominant source of acoustic radiation does not appear to be the airfoil trailing edge, but at some location on the upper airfoil surface. The apparent source of acoustic radiation appears to be located slightly further upstream for case 3D7 than for cases 3DF and 3DU, and the wave-front pattern suggests that the transition/reattachment region is generating acoustic radiation. The directivity of acoustic waves is primarily upstream, although for case 3D7 and, to a lesser extent, case 3DU there is evidence of radiation with downstream directivity. The production of acoustic radiation in the transition/reattachment region appears to be an entirely separate phenomenon to that of acoustic scattering at the trailing edge, and hence would not be predicted by classical trailing-edge theory (Amiet, 1976).

It appears that for the airfoil flow investigated here, there two main sources of acoustic radiation present. Acoustic waves are generated both by scattering at the airfoil trailing edge, and also in the transition/reattachment region. The trailing edge noise appears to possess primarily upstream directivity, and appears approximately symmetric in both amplitude and directivity. Acoustic waves generated in the transition region appear to possess both upstream and downstream directivity and, being produced solely on the upper airfoil surface, the directivity is highly asymmetric. At $f = 11.2$ unusual behaviour is observed in time-dependent pressure above the airfoil. Upstream travelling pressure waves are present, with wavelength longer than that expected for acoustic waves travelling at the speed of sound, that decay rapidly upstream of the airfoil trailing edge.

9.5.2 Frequency-averaged modulus of the Fourier transformed pressure field

In section 9.5.1 the real coefficient of the Fourier transformed pressure field was plotted for four individual frequencies, revealing the directivity and apparent origin of acoustic waves in each case. Having identified what appear to be the dominant sources of acoustic radiation, general trends of the frequency depen-

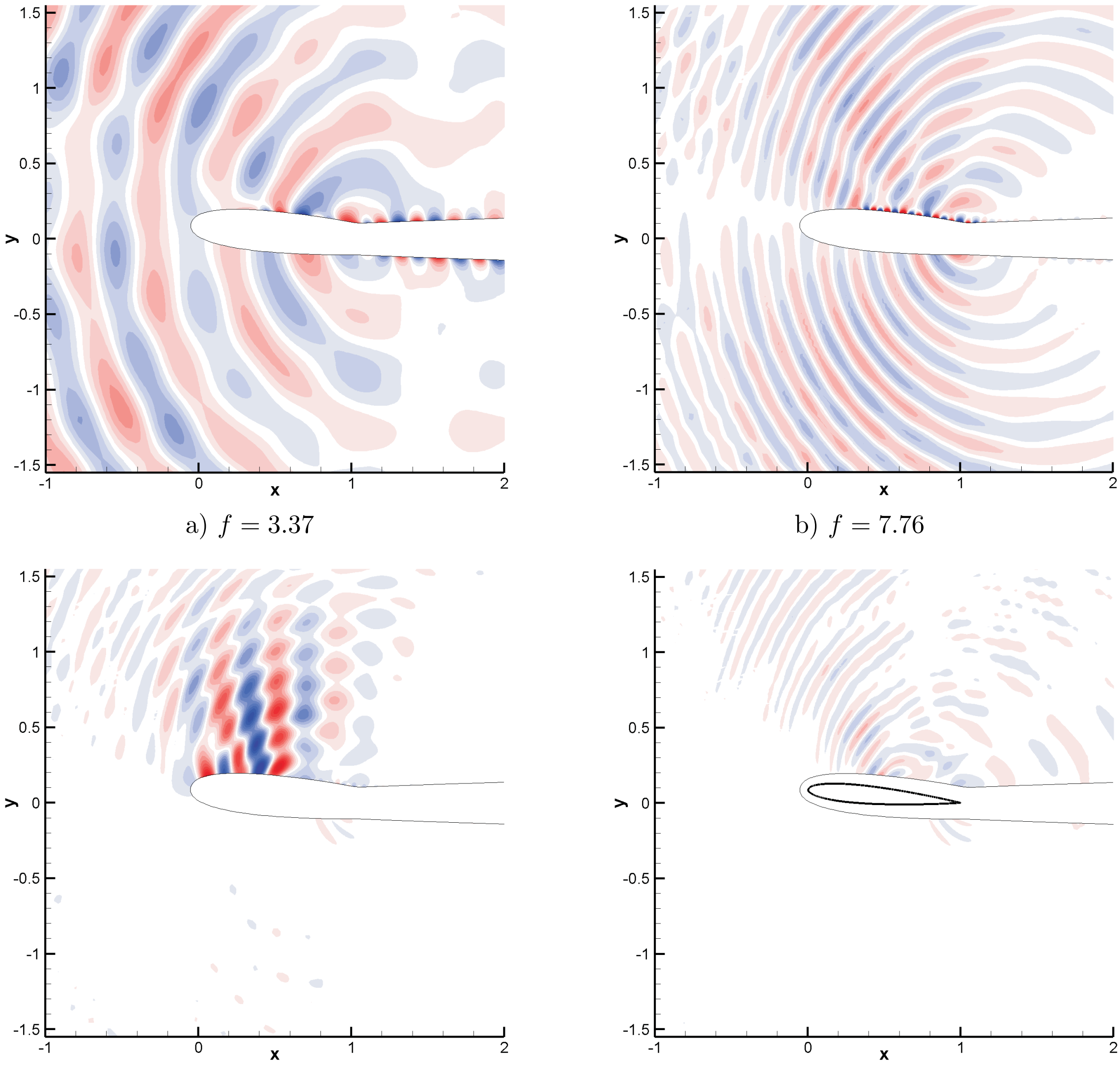

a) $f = 3.37$ b) $f = 7.76$

c) $f = 11.2$ d) $f = 15$

Figure 9.13: Iso-contours of the real part of S_p for case 3DF, plotted over the range $\pm 3 \times 10^{-4}$, for frequencies indicated.

dent acoustic behaviour will now be studied. In order to do this, the frequency-averaged modulus of the Fourier transformed pressure field is plotted for four frequency intervals; $1 \leq f \leq 4$, $4 \leq f \leq 9$, $9 \leq f \leq 12$ and $12 \leq f \leq 16$, for all three-dimensional simulations. The frequency averaged modulus is formed by summing the modulus over all available frequencies then dividing by the number of frequencies, e.g.

$$\overline{S_p}(f) = \Sigma_{n=1}^{n=N} \frac{S_p(f)}{N}, \tag{9.1}$$

where N is the total number of frequencies averaged, hence the amplitude of each frequency range may be compared directly.

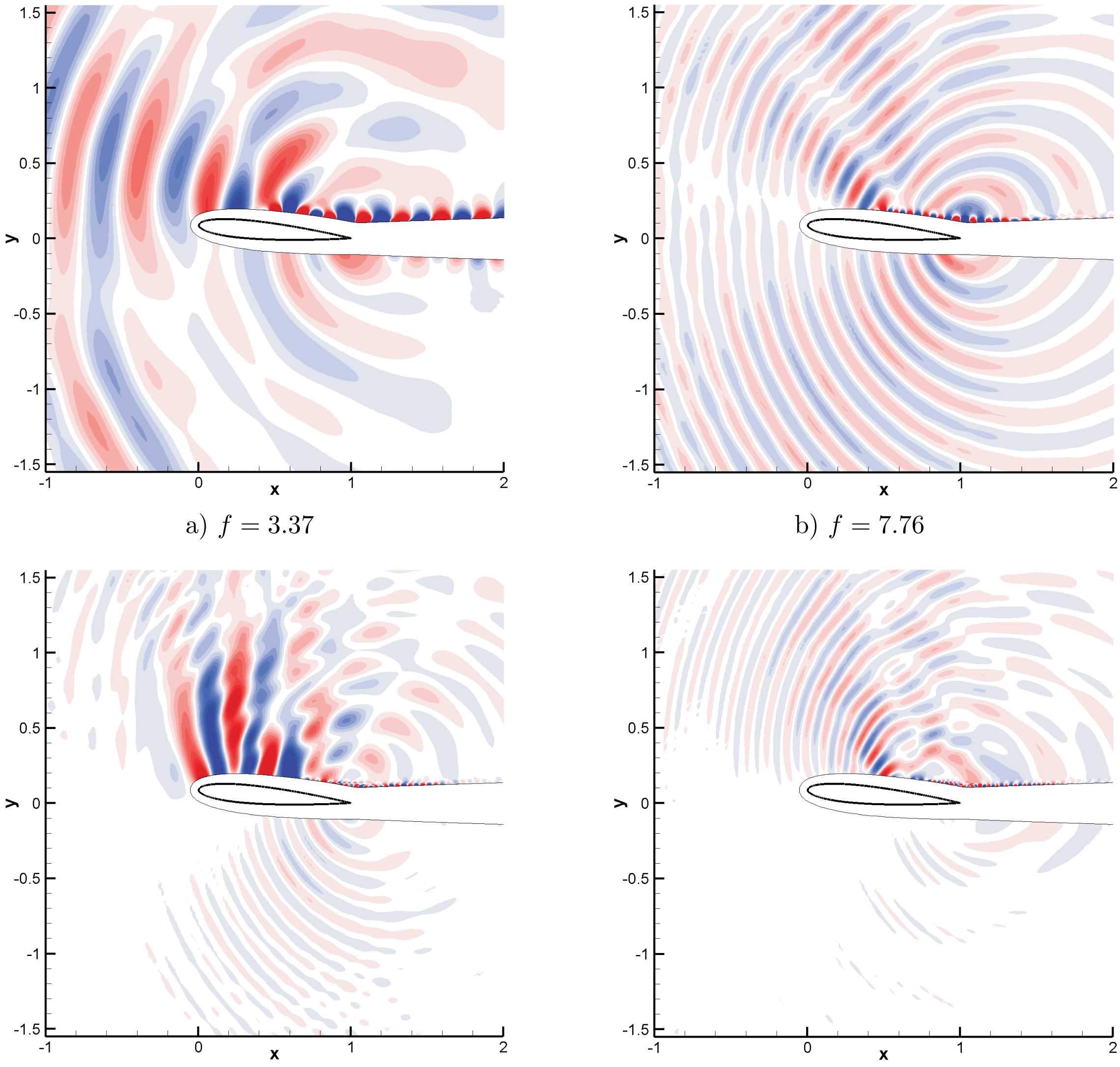

a) $f = 3.37$

b) $f = 7.76$

c) $f = 11.2$

d) $f = 15$

Figure 9.14: Iso-contours of the real part of S_p for case 3DU, plotted over the range $\pm 3 \times 10^{-4}$, for frequencies indicated.

Pressure spectra computed for the acoustic field for case 3DF are unfortunately slightly corrupted due to the transient behaviour described in section 9.2, hence spectra for case 3DU will be discussed first, plotted in figure 9.17. The amplitude of pressure spectra computed for case 3DU appears in general to decrease with increasing frequency. The frequency-averaged modulus for the interval $1 \leq f \leq 4$ exhibits much greater amplitude than the other frequency intervals; in the range $4 \leq f \leq 9$ the frequency-averaged modulus is slightly lower in amplitude, and over intervals $9 \leq f \leq 12$ and $12 \leq f \leq 16$ the modulus is lower still. The directivity of the pressure spectra also changes with frequency. For $1 \leq f \leq 4$ the frequency-averaged modulus appears to exhibit

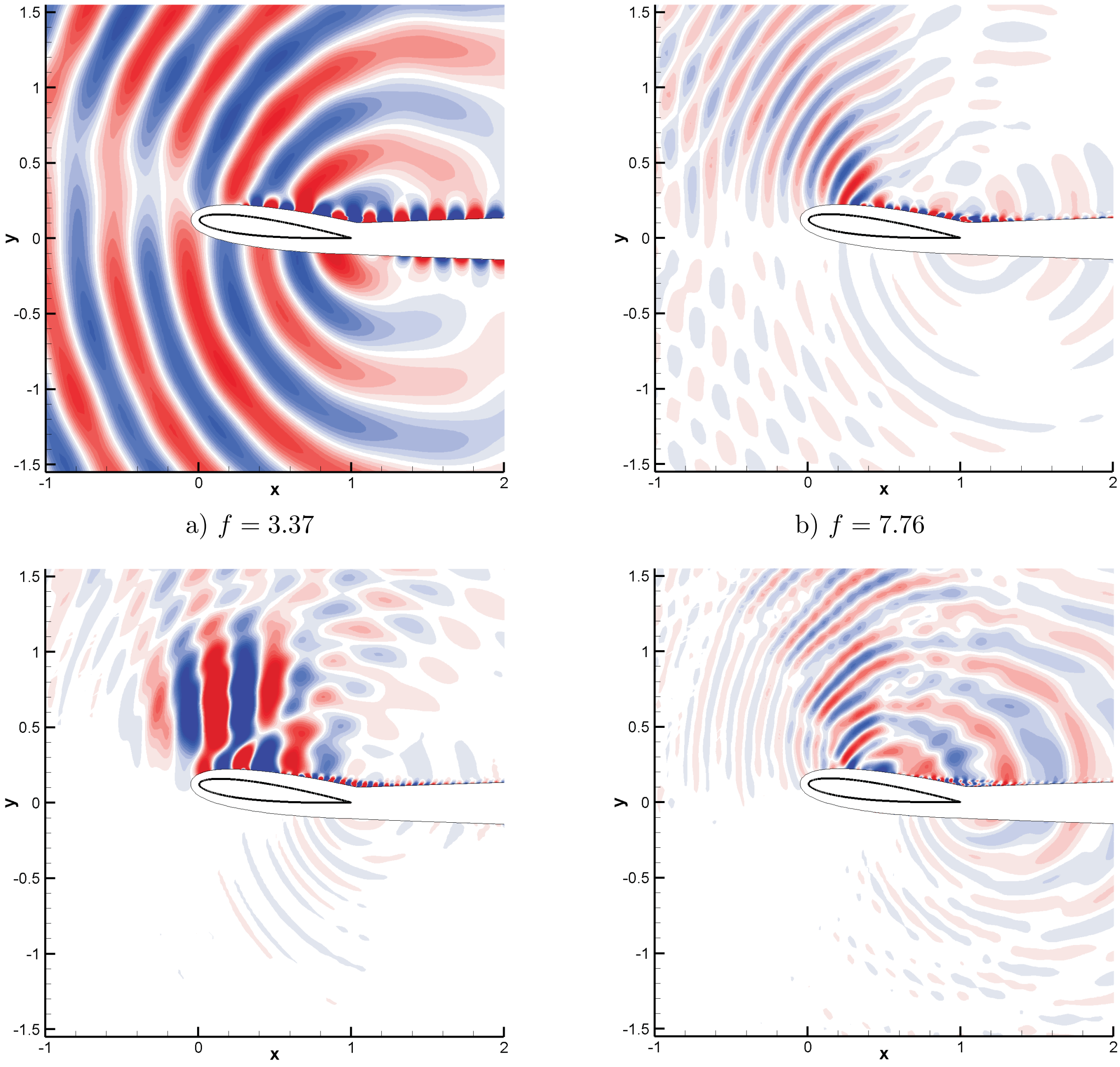

a) $f = 3.37$ b) $f = 7.76$

c) $f = 11.2$ d) $f = 15$

Figure 9.15: Iso-contours of the real part of S_p for case 3D7, plotted over the range $\pm 3 \times 10^{-4}$, for frequencies indicated.

upstream directivity and, for $y > 1$ at least, appears to possess approximately the same amplitude above and below the airfoil. The modulus is a maximum at the airfoil trailing edge, and the iso-contour distribution suggests that the airfoil trailing edge is the dominant source of pressure fluctuations propagating into the free-stream. Indeed, the directivity appears comparatively similar to that of the trailing edge scattering observed clearly in two-dimensions at $\alpha = 5°$ (section 4.4.1), and to trailing edge noise identified for specific frequencies in section 9.5.1. For the higher frequency intervals $9 \leq f \leq 12$ and $12 \leq f \leq 16$, spectra exhibit dramatically different behaviour. At $9 \leq f \leq 12$ there is some evidence of trailing edge noise production below the airfoil, however the frequency-averaged

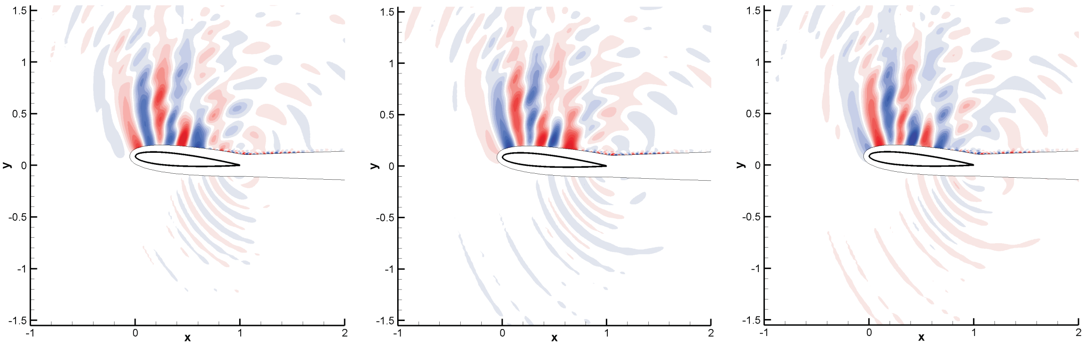

a) $\phi = 0$ b) $\phi = \pi/2$ c) $\phi = 3\pi/2$

Figure 9.16: Iso-contours of fluctuating pressure, p', plotted for case 3DF at the single frequency $f = 11.2$, showing levels over the range $\pm 5 \times 10^{-4}$.

modulus is greatest in amplitude at approximately $x = 0.5$ on the upper airfoil surface. The directivity is highly asymmetric, with the amplitude of the modulus in the freestream being significantly greater above the airfoil than below. The behaviour is even more pronounced at $12 \leq f \leq 16$; almost no trailing-edge noise is observed at these contour levels, and the asymmetry of the spectra is even more striking. The frequency-averaged modulus appears to suggest that over these frequency ranges acoustic waves are primarily being produced in the transition/reattachment region, as observed for $f = 15$ in section 9.5.1. For $4 \leq f \leq 9$ the spectra exhibits a combination of behaviours. There appears to be significant trailing edge noise present and the amplitude of the frequency-averaged modulus appears to be a similar order of magnitude above and below the airfoil, however the directivity appears to be asymmetric.

Case 3DF appears to display the similar trends to case 3DU, however the amplitude of pressure spectra appears smaller for all frequencies. This appears to confirm that the addition of forcing reduces the amplitude of acoustic radiation produced by the flow around the airfoil for this case. Trailing edge noise appears present at significant amplitudes for $f < 10$. As for case 3DF, however, above $f = 10$ the dominant source of pressure fluctuations propagating into the freestream appears to be located on the upper airfoil surface at approximately $x = 0.5$, i.e. the transition/reattachment region, and above $f = 10$ the directivity appears highly asymmetric. Pressure spectra for case 3DF appear corrupted for $1 \leq f \leq 9$, where the effect of the acoustic transient described in section 9.2 can be observed upstream of the airfoil.

Pressure spectra computed from case 3D7 are a similar order of magnitude to those computed from case 3DU, suggesting that a modest increase of incidence affected the amplitude of acoustic radiation far less then the addition of forcing. Again, similar behaviour is observed as for cases 3DU and 3DF, with trailing

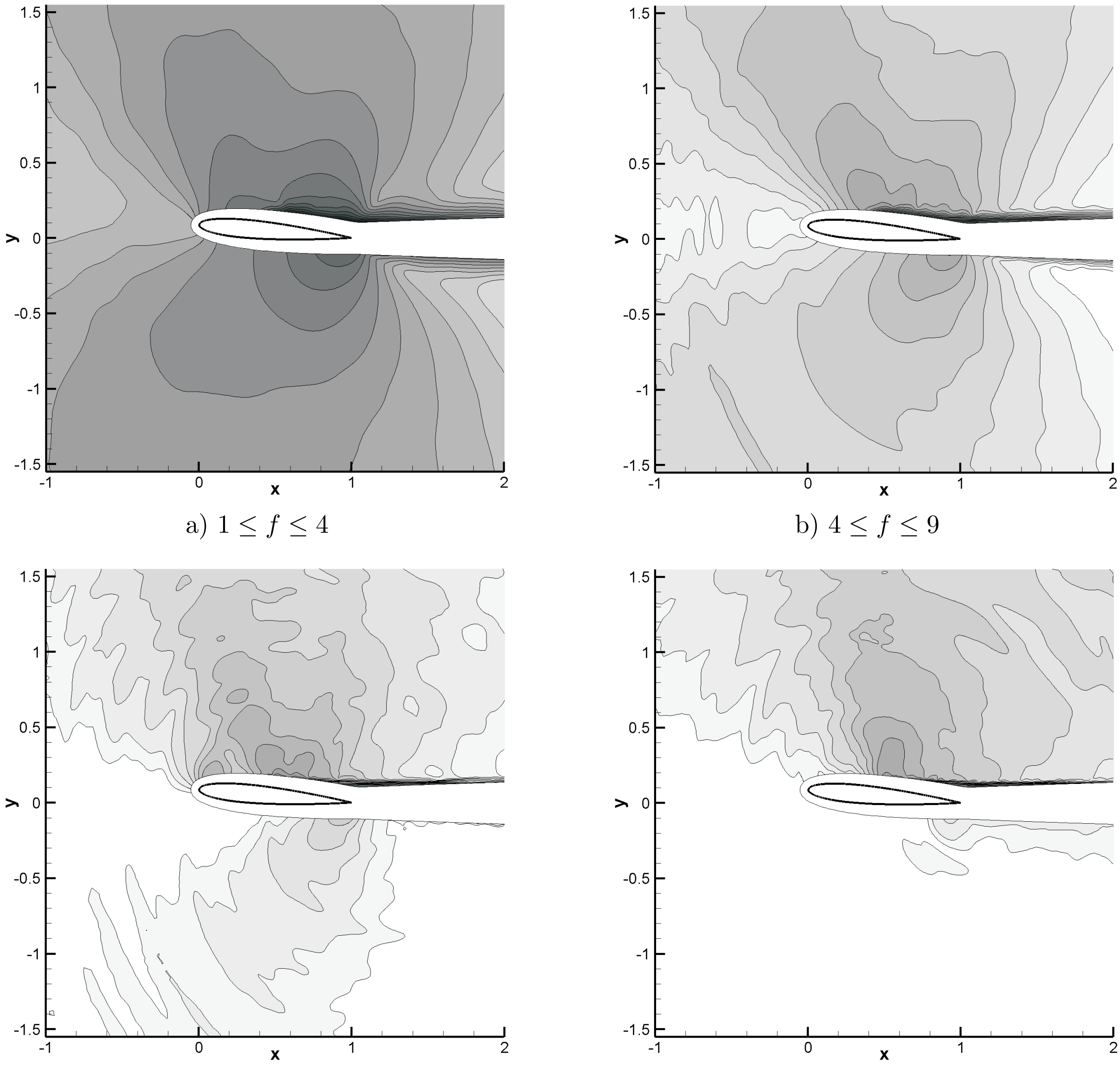

a) $1 \leq f \leq 4$ b) $4 \leq f \leq 9$

c) $9 \leq f \leq 12$ d) $12 \leq f \leq 16$

Figure 9.17: Iso-contours of the frequency-averaged modulus of S_p for case 3DU, plotted for frequencies indicated.

edge noise apparently dominant for $1 \leq f \leq 4$ and noise generated in the transition/reattachment region apparently dominant for $9 \leq f \leq 16$. For case 3D7 the second acoustic source appears to be located slightly further upstream compared to case 3DU, perhaps providing further evidence that this second source of acoustic radiation is indeed associated with the transition/reattachment region.

To summarise, all three cases display similar general trends of behaviour. It appears that for $1 \leq f \leq 4$ trailing edge noise is the dominant acoustic source, whereas for $f > 9$ noise generated in the transition/reattachment region appears to be dominant. For $4 \leq f \leq 9$ trailing edge noise is still the dominant acoustic source, however the effect of the second noise source can still be observed as a change in directivity. The nature of the mechanism by which acoustic radiation is produced in the transition/reattachment region is not known beyond doubt, however it appears likely that the highly unsteady wall shear-stress present in the transition region (see 5, figure 5.12) is likely to be an important source of radiation, as has been found for turbulent channel flow at low Mach number (Hu, Morfey & Sandham, 2003). It would be of interest to determine how the amplitude of acoustic radiation produced in this region scales with Mach number. This would not only help to determine the nature of the acoustic source (e.g. scattering or free-space turbulent fluctuations), but also help to determine the significance of this source in terms of its contribution to airfoil self-noise at different Mach numbers.

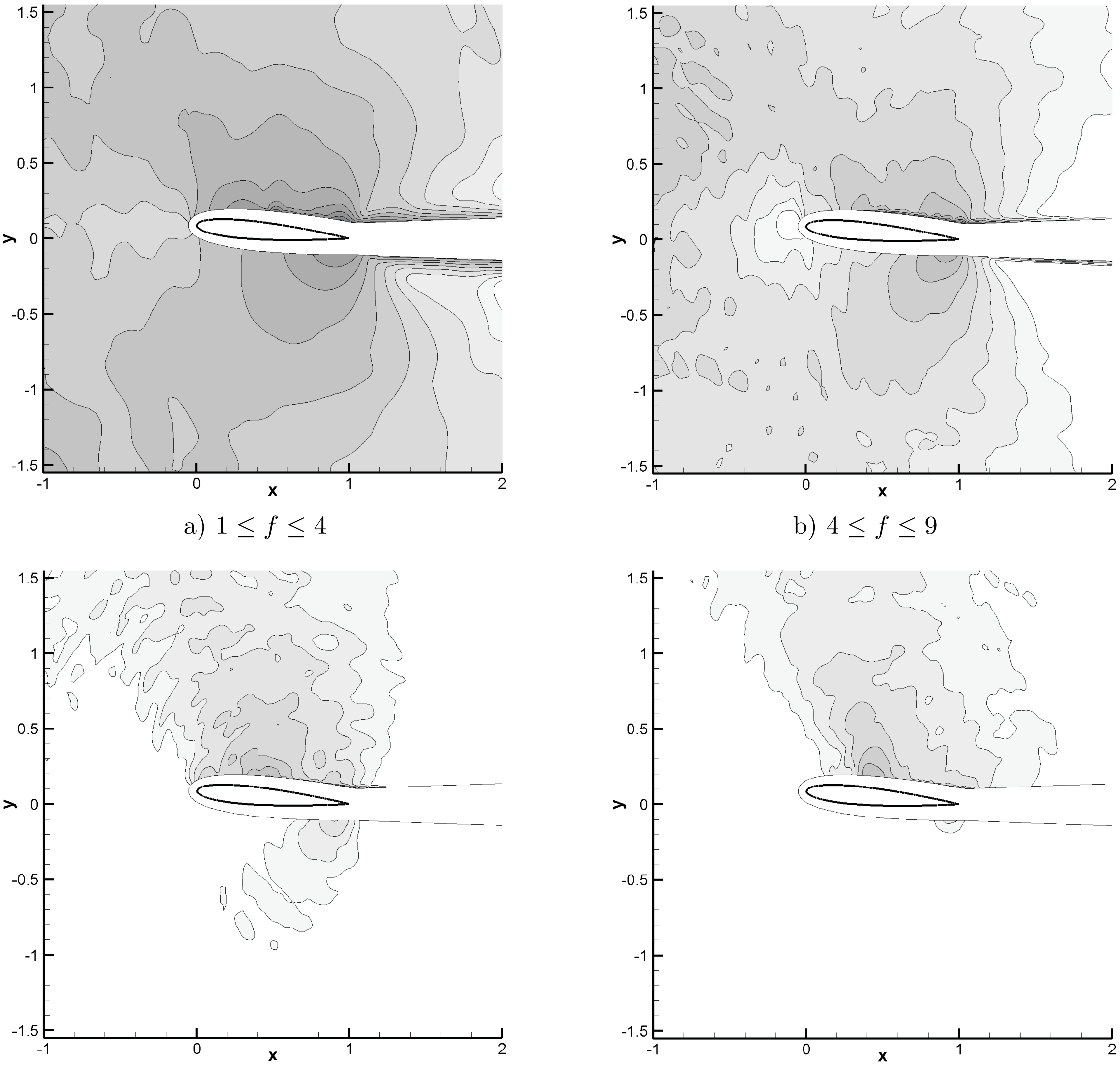

a) $1 \leq f \leq 4$

b) $4 \leq f \leq 9$

c) $9 \leq f \leq 12$

d) $12 \leq f \leq 16$

Figure 9.18: Iso-contours of the frequency-averaged modulus of S_p for case 3DF, plotted for frequencies indicated.

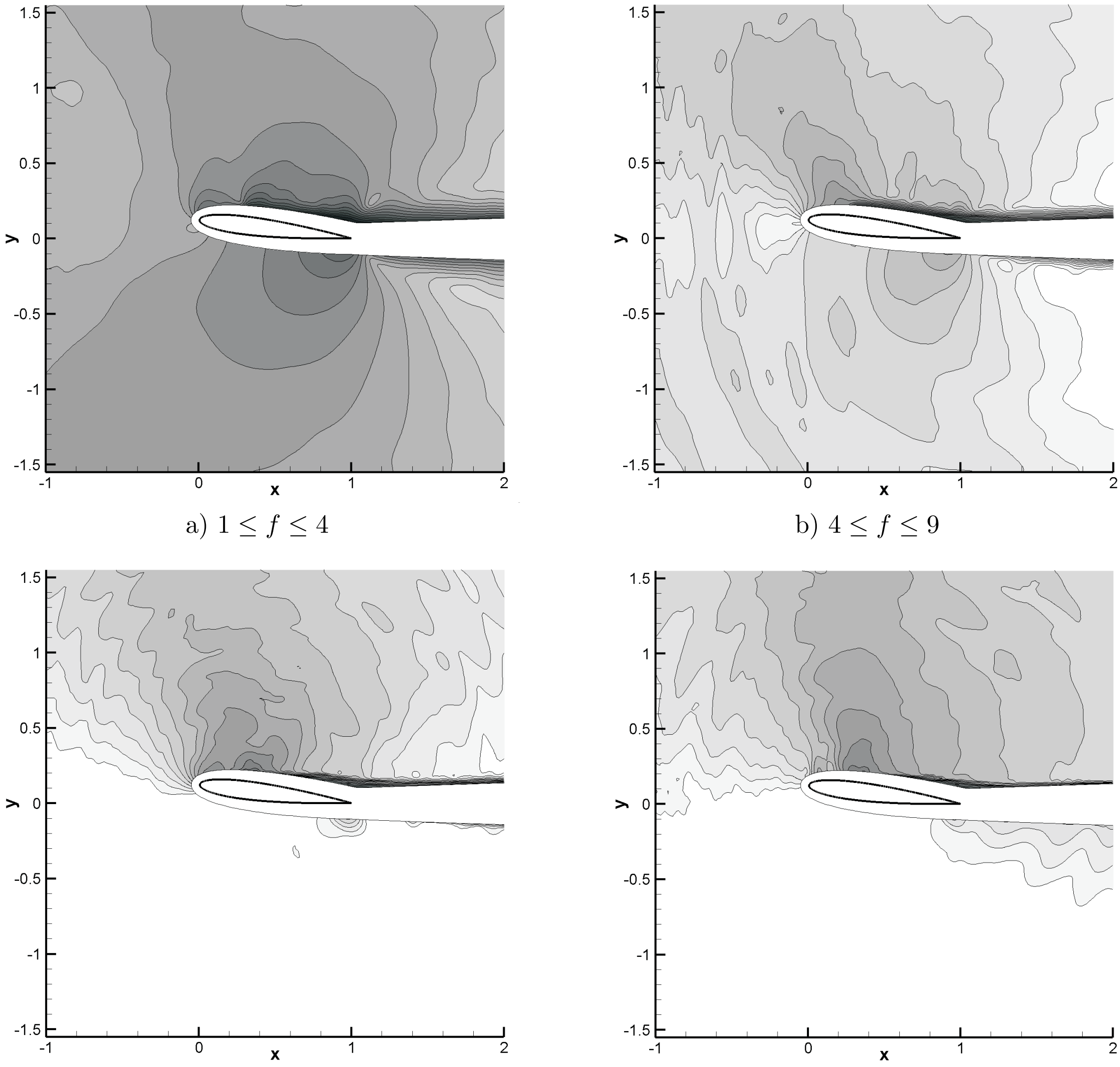

a) $1 \leq f \leq 4$

b) $4 \leq f \leq 9$

c) $9 \leq f \leq 12$

d) $12 \leq f \leq 16$

Figure 9.19: Iso-contours of the frequency-averaged modulus of S_p for case 3D7, plotted for frequencies indicated.

9.6 Discussion of the additional tone at $f = 11.2$

Pressure spectra taken within both the airfoil boundary layer and on the airfoil surface reveal a tonal contribution at $f \approx 11.2$ for all three-dimensional cases. Spectra taken in the acoustic field at this frequency also display unusual behaviour; upstream travelling pressure waves are observed, with wavelength longer than that expected for acoustic waves, which do not appear to be propagating into the free-stream. The origin of this tone appears unclear, and hence will be subject to brief discussion.

It is feasible that additional tones could be caused by an acoustic feedback-loop mechanism involving communication between the airfoil leading-edge and the trailing-edge, as observed in section 7.3. If this were the case, however, one could reasonably expect the frequency of the tone to vary from case to case. Also, the acoustic feedback loop observed in section 7.3 was observed to occur for $f \leq 4$, and evidence in this chapter appears to suggest that acoustic scattering at the trailing edge is most efficient for low frequencies. This appears to discount a leading-edge/trailing-edge acoustic feedback loop, since the additional tones observed occur at higher frequencies than expected for a leading-edge/trailing-edge feedback loop.

A second possibility is that some other form of acoustic feedback loop is present, different to that suggested in section 7.3, for example involving communication between the transition region and the airfoil leading edge. Certainly, acoustic waves are observed to be generated in the vicinity of transition (e.g. see figure 9.15b) and receptivity of the leading edge has been documented for the current case (section 7.3.1). The receptivity process itself will occur most efficiently at a certain frequency, and the energy content of the transitional noise will also be frequency dependent. This could give rise to a preferred frequency that would differ from that associated with a leading-edge/trailing-edge feedback loop. In section 7.3.1 the boundary layer receptivity process was observed to be significant until at least $f = 11$, a value very close to the frequency of the additional tone at $f = 11.2$. If the additional tone were to be the result of a leading-edge/transition feedback loop, this would also explain the noticeable asymmetry observed in the fluctuating pressure field at $f = 11.2$, since the tonal contribution to self-noise would occur only on the upper surface. Furthermore, some similarities exist between noise generated in the transition region and the spatial structure of the additional tone. In particular, noise generated in the transition region appears to propagate in a direction almost normal to the airfoil, and is small in amplitude upstream of the airfoil leading edge (figure 9.15d); in this respect the transitional noise is similar to the additional tone. However, the hypothesis of a leading-edge/transition feedback loop does not explain the comparatively long wavelength of pressure fluctuations associated with the additional tone, and one would still expect the frequency of the tone to vary from case to case, since the structure of the boundary layer in the leading edge region, and hence the receptivity process, will vary.

A third possibility is that the upper airfoil boundary layer exhibits some regularly occurring motion at this frequency, such as a ‘global’ wall-normal flapping of the shear layer, which results in pressure fluctuations in the near-airfoil region. Stability analysis of the time-averaged flowfield of case 3D7 (presented in chap-

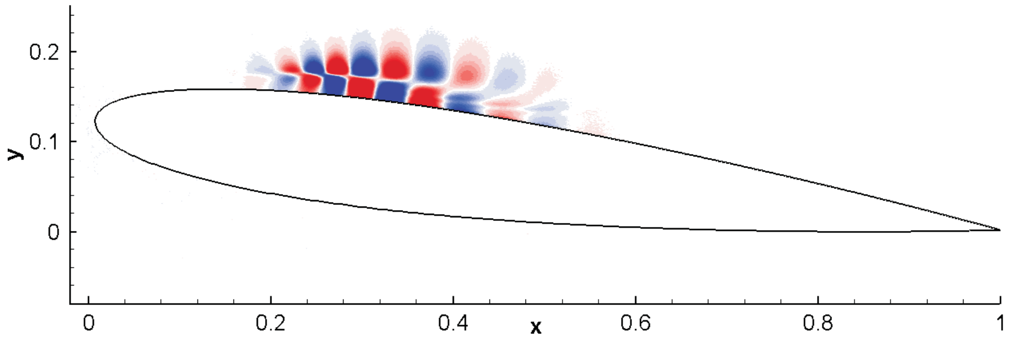

Figure 9.20: Iso-contours of $\nabla\mathbf{U}'$ for the time-averaged flowfield of case 3D7 as described in section 7.3.5, at $t = 8.4$, showing 10 levels over the range $\pm 2 \times 10^{-10}$.

ter 7, section 7.3.5) revealed a very weak form of absolute instability in which the separated region appears to act as an 'oscillator', which could potentially generate a tonal response in the fully developed flow. The oscillatory behaviour observed in section 7.3.5 occurs over a broader frequency range than the tonal contribution observed for three-dimensional simulations however, and when iso-contours of $\nabla\mathbf{U}'$ are plotted (figure 9.20), the flowfield appears dissimilar to that associated with the tone at $f = 11.2$ (e.g. figure 9.14c).

To summarise, the origin of the additional tone appears difficult to determine, however it appears unlikely to be generated by a leading-edge/trailing-edge feedback loop. The concept of a leading-edge/transition feedback-loop appears attractive, however it does not explain the unusual spatial structure of pressure fluctuations at $f = 11.2$ and the resultant implications for wave propagation velocities. At present these phenomena remain unexplained, although it is suggested that the superposition of multiple sources of pressure fluctuations, for example trailing-edge noise, transition noise and pressure fluctuations associated with hydrodynamic behaviour, may result in unexpected behaviour in the Fourier transformed pressure field. It is conceivable, for example, that a standing-wave pattern could be formed under appropriate conditions. Attempts to generate patterns exhibiting long disturbance wavelengths via model problems, e.g. superposing sinusoidal travelling waves and computing the Fourier transform, have not been successful however. It is felt that such studies are inconclusive though, since in the 'real' airfoil flow the free-stream velocity (and hence wave propagation velocity) varies in two-dimensions, and the directivity and phase will vary between acoustic sources. In light of the available evidence, the hypothesis of a leading-edge/transition acoustic feedback loop remains the most feasible mechanism for the additional tones.

9.7 Summary

The acoustic response of three airfoils with separation bubbles has been compared. The overall intensity of sound radiation from the airfoil was found to be a similar order of magnitude for unforced cases at $\alpha = 5°$ and $\alpha = 7°$, however when forcing is introduced at $\alpha = 5°$ the overall intensity of sound radiation decreases by approximately an order of magnitude. This appears to be because the presence of forcing suppresses low frequency events in the turbulent region, which are more effectively scattered than events occurring at high frequency. Hence it appears that the presence of forcing appears to affect the acoustic response of the airfoil more significantly than a modest change of incidence.

Surface pressure spectra suggest that trailing edge noise is significant only for $f \leq 10$, and this appears corroborated by acoustic spectra taken in the free-stream. As well as the expected acoustic scattering at the trailing-edge, a second noise source appears present for all cases; above $f = 10$ trailing edge noise becomes less significant, however acoustic waves continue to be produced in the transition/reattachment region. Noise produced in this region appears to propagate with different directivity to trailing edge noise observed for $f < 10$ and is entirely asymmetric, being produced over only the upper airfoil surface. This second noise source would not be predicted by classical trailing edge theory, and appears an entirely different phenomenon.

Point pressure probes and surface spectra illustrate the presence of discrete tones for all cases. In particular, an additional tone is present at $f = 11.2$ that becomes large in amplitude for $\alpha = 7°$. This tone a associated with unusual pressure-spectra behaviour in the near-airfoil region, that does not correspond to acoustic wave propagation. This additional tone does not appear to generated by the mechanism outlined in section 7.3, and the reason for its presence is not clear.

Chapter 10

Conclusions and future work

The flow around a NACA-0012 airfoil at low Reynolds number has been investigated numerically, in both two and three-dimensions, via a combination of linear stability analysis and direct solution of the compressible Navier–Stokes equations. The application of DNS to complex geometries such as that of airfoil flow has only recently begun to be undertaken, and the current study represents the first comprehensive investigation of airfoil flow at MAV-type Reynolds numbers by direct numerical simulation. Primary topics that have been studied include:

- Investigations of the two-dimensional flow around airfoils at both $Re_c = 10^4$ and $Re_c = 5 \times 10^4$
- A study of the effect of forcing upon the behaviour of a separation bubble formed on an airfoil at incidence
- An investigation of the effect of a modest incidence change upon separation bubble behaviour
- A thorough investigation of the convective and absolute stability characteristics of both forced and unforced separation bubbles formed on airfoils at incidence
- Determination of the mechanism for self-sustaining turbulence observed in unforced separation bubble simulations
- An investigation of the acoustic response of the flow around airfoils with both forced and unforced separation bubbles

10.1 Summary of principal findings

10.1.1 Important results from two-dimensional simulations

At $Re_c = 10^4$ the wake was found to be unstable, ultimately resulting in von-Karman type vortex shedding. At $Re_c = 5 \times 10^4$, a low frequency flapping oscillation was observed at $\alpha = 0°$ over the range $0.5 \leq M \leq 0.8$, which was found to cause fluctuations in the lift-coefficient much greater in amplitude than for the vortex shedding. A series of simulations at varying incidence, at $Re_c = 5 \times 10^4$, $M = 0.4$, illustrated the presence of a laminar separation bubble with vortex shedding. The vortex shedding undergoes a behavioural change at $\alpha \leq 5°$. For $\alpha \leq 5°$ the vortex shedding is near-periodic, and occurs at a single frequency. For $\alpha > 5°$ the vortex shedding is more irregular.

10.1.2 The effect of boundary layer forcing upon separation bubble behaviour

A separation bubble was formed on a NACA-0012 airfoil at $Re_c = 5 \times 10^5$, $M = 0.4$ and $\alpha = 5°$, with explicitly added low-amplitude disturbances to trigger transition to turbulence. When the disturbances are turned off, transition to turbulence was observed to self-sustain for the unforced case, however the presence of forcing was found to significantly alter the behaviour of the laminar separation bubble. The presence of forcing reduces the length of the separation bubble and improves the lift-to-drag ratio by 23%. The turbulence intensity downstream of transition appears to be reduced in the forced case, with lower frequency fluctuations in particular being reduced in amplitude. As a result the acoustic radiation observed in the forced case was around an order of magnitude smaller than for the unforced case. The presence of forcing also alters the developing turbulent boundary layer behaviour; the unforced case exhibited an increased amplitude of fluctuations away from the wall, and the turbulence possessed increased spanwise coherence. Both of the three-dimensional separation bubbles exhibited large variations in skin-friction. At no point downstream of transition was the flow either fully attached or fully separated, suggesting that the concept of a reattachment 'point' is misleading. Comparison of skin-friction PDF's illustrates that time-dependent behaviour of the two-dimensional separation bubble is fundamentally different to that of the three-dimensional bubbles.

10.1.3 The effect of incidence upon separation bubble behaviour

A separation bubble was formed on a NACA-0012 airfoil at $Re_c = 5 \times 10^5$, $M = 0.4$ and $\alpha = 7^\circ$ in order to investigate the effect of a modest incidence change on separation bubble behaviour. A low amplitude perturbation was introduced at initialisation, but no further disturbances were added. Transition to turbulence was observed to occur, and the transition to turbulence self-sustained as at $\alpha = 5^\circ$. The intensity of turbulent fluctuations is similar to the unforced case at $\alpha = 5^\circ$, and the acoustic radiation produced by the flow over the airfoil appears a similar order of magnitude also. Turbulent fluctuations in the developing boundary layer were significantly greater away from the wall than near the wall. For the cases considered, it appears that the addition of forcing affects the characteristics of the turbulence and acoustic radiation more significantly than a modest incidence change.

10.1.4 Stability characteristics of separation bubbles formed on airfoils at incidence

No evidence of local absolute instability could be detected for any of the three-dimensional simulations when performing linear stability analysis of the time-averaged flow field. The same was found to be true of the corresponding two-dimensional simulations. In order to confirm the results of the linear stability analysis, whilst accounting for non-parallel effects, Navier–Stokes simulations were performed using forcing terms to determine the response of the time-averaged flowfield to low-amplitude perturbations. A very weak oscillatory behaviour was observed for simulations at $\alpha = 7^\circ$, however no evidence of absolute instability could be observed that would explain the self sustained transition to turbulence at $\alpha = 5^\circ$. Convective stability characteristics were also investigated. For all cases the most amplified instability wave across the separation bubble was found to be much higher in frequency than the naturally occurring vortex shedding observed in two-dimensions.

10.1.5 An acoustic feedback instability of flow over an airfoil with a laminar separation bubble

Forced Navier–Stokes simulations, investigating the response of time-averaged flowfields extracted from airfoil simulations to low amplitude perturbations, illustrated the presence of an acoustic feedback loop. The resultant behavior may be defined as globally unstable, although no local absolute instability or ‘BiGlobal’ instability was observed. The feedback loop was found to be present for the time-averaged flowfield of two-dimensional simulations at $\alpha = 5°$, $7°$, and $8.5°$, and for the unforced three-dimensional simulation at $\alpha = 5°$. The preferred frequency of the feedback loop is lower than that of the most convectively amplified instability wave over the upper airfoil surface, hence it is suggested that an acoustic feedback loop of this type may potentially act as a frequency selection mechanism for the vortex shedding observed in two-dimensions.

10.1.6 A mechanism for self-sustaining turbulence

A mechanism for the self-sustaining transition to turbulence observed to take place for unforced separation bubbles has been proposed. The mechanism is essentially a secondary instability of the naturally occurring vortex shedding to three-dimensional perturbations, and is driven primarily by two mechanisms. Firstly, three-dimensional perturbations are strongly amplified when they convect into regions of high strain, associated with hyperbolic streamlines, between adjacent vortices. Secondly, perturbations leaving the regions of high strain then extend into regions of strong reverse flow, where the magnitude of reverse flow greatly exceeds that of the time-averaged field. The perturbations are then convected rapidly upstream, and into the strain field associate with the subsequent developing vortex. The instability amplification rates and upstream convection velocities are such that the instability manifests itself in an absolute fashion. The instability appears analogous to behaviour observed in wakes, and may explain self-sustaining transition to turbulence observed in previous studies of separation bubbles. The instability mechanism has important implications for the modelling of laminar separation bubbles, suggesting that if freestream turbulence levels drop below a certain value, the time-averaged transition and reattachment locations will be fixed and not vary with further decreases in freestream turbulence levels.

10.1.7 Acoustic characteristics of separation bubbles formed on an airfoil at incidence

Trailing-edge noise is clearly observed for all three-dimensional simulations, and is found to be the dominant source of acoustic radiation for frequencies below $f = 10$. In addition to the expected trailing edge noise, acoustic radiation was observed to be generated in the transition/reattachment region for all cases. Although evidence of this secondary source is present at lower frequencies, the contribution of the secondary source to radiation generated by the airfoil appears more significant at higher frequencies. For $f > 10$ the secondary source was observed to be the dominant source of acoustic radiation. The second source appears to generate primarily upstream propagating acoustic waves, although there is some evidence that waves with downstream directives are also produced. The second source of acoustic radiation appears unrelated to trailing edge noise, and hence would not be predicted by classical trailing edge theory, however the second source is a significant contributor to airfoil self-noise for the cases studied.

10.2 Recommendations for further study

The present study represents a thorough investigation of the behavior of laminar separation bubbles on airfoils at low Reynolds number, however in performing this study several avenues of further study have been identified.

- The behaviour of short separation bubbles formed on a thin airfoil should be investigated. For such geometries separation bubbles typically grow in length with increased incidence near stall, whereas the bubbles observed in this study decrease in length. Simulating a separation bubble an a geometry exhibiting thin-airfoil type behaviour under similar conditions, e.g similar $Re_{\theta_{sep}}$ or Re_l, would allow any differences in the physics to be investigated.

- Although the presence of forcing dramatically altered the separation bubble behaviour, the forcing was low in amplitude compared to, for example, Alam & Sandham (2000). The amplitude of forcing should be increased by an order of magnitude, and the simulation progressed, in order to determine also the effect of the amplitude of forcing. The transitional behaviour should be monitored in order to determine whether Λ-vortices or other coherent structures are present as for Alam & Sandham.

- Low-frequency flapping of laminar separation bubbles has been observed for $Re_c = 1.3 \times 10^5$ for a NACA-0012 airfoil at $\alpha = 11.5°$, and appears to take the form of periodic bubble growth and bursting (Rinoie & Takemura, 2004). Ideally an attempt should be made to capture this behaviour via numerical simulation as soon as computationally feasible. The phenomenon of bubble bursting is difficult to capture numerically, since it typically occurs as a dynamic process. The low-frequency flapping appears to manifest itself as periodic bubble bursting, and hence if this behaviour could be captured numerically the physics of the bursting process could be scrutinised in detail for the first time.

- As computational power increases simulations with increased complexity will be possible. Micro-air-vehicles typically employ low aspect-ratio wing planforms, and hence it appears likely that direct numerical simulations of an entire MAV wing planform may become feasible within the next few years. A more fundamental study however would an investigation of the effect of aspect ratio upon separation bubble behavior, for a rectangular wing planform. The influence of the finite span upon the fluid dynamics of the separation bubble can be studied, with potential for improving aircraft performance at MAV-type Reynolds numbers.

- The mechanism of boundary layer receptivity to acoustic waves should be investigated. A first step would be to determine if the propagation direction of the acoustic waves influences the receptivity process; if only upstream travelling waves generate boundary layer disturbances this may suggest that 'back-scattering' of acoustic waves is integral to the receptivity process. By subjecting the airfoil flow to single acoustic waves of specified frequency and amplitude, the manner in which the efficiency of the receptivity process varies with frequency may be determined.

- The origin of the unexplained tone observed in three-dimensional simulations at $f \approx 11.2$ should be investigated. Some form of 'BiGlobal' stability analysis could potentially determine whether any global response of the shear layer is responsible for this behaviour, however in the absence of existing BiGlobal code this would not be trivial to perform. In the event of further airfoil simulations being performed, the presence of naturally occurring tones should be investigated.

- The mechanism of noise production in the transition/reattachment region should be investigated. Performing a simulation at similar conditions, but varying the Mach number, would allow the Mach-scaling of the acoustic intensity to be determined. This will potentially enable the nature of the acoustic source to be identified, and will help to determine under what flight conditions the acoustic source is important. Two-dimensional simulations at $\alpha > 5^\circ$ also appear to exhibit more than one acoustic source, hence it is sensible to perform a precursory study in two-dimensions before repeating in three-dimensions as the mechanisms may be similar.

Bibliography

Alam, M. & Sandham, N. 2000 Direct numerical simulation of short laminar separation bubbles with turbulent reattachment. *Journal of Fluid Mechanics* **410**, 1–28.

Allen, T. & Riley, N. 1995 Absolute and convective instabilities in separation bubbles. *Aeronautical Journal* **99** (990), 439–448.

Amiet, R. 1976 Noise due to turbulent flow past a trailing edge. *J. Sound and Vibration* **47** (3), 387–393.

Baragona, M. 2004 Unsteady characteristics of laminar separation bubbles, an experimental and numerical investigation. PhD thesis.

Barkley, D. & Henderson, R. 1996 Three-dimensional Floquet stability analysis of the wake of a circular cylinder. *J. Fluid Mech.* **322**, 215–241.

Bernal, L. & Roshko, A. 1986 Streamwise vortex structure in plane mixing layers. *J. Fluid Mech.* **170**, 499–525.

Bestek, H., Gruber, K. & Fasel, H. 1989 Self-excited unsteadiness of laminar separation bubbles caused by natural transition. *The Prediction and Exploitation of Separated Flow, Roy. Aeronaut. Soc., London* pp. 14–1.

Bouhadji, A. & Braza, M. 2003 Organised modes and shock–vortex interaction in unsteady viscous transonic flows around an aerofoil Part I: Mach number effect. *Computers and Fluids* **32** (9), 1233–1260.

Bourdet, S., Bouhadji, A., Braza, M. & Thiele, F. 2003 Direct Numerical Simulation of the Three-Dimensional Transition to Turbulence in the Transonic Flow around a Wing. *Flow, Turbulence and Combustion* **71** (1), 203–220.

Briggs, R. 1964 *Electron-stream interaction with plasmas*. MIT Press.

Carpenter, M. H., Nordström, J. & Gottlieb, D. 1999 A stable and conservative interface treatment of arbitrary spatial accuracy. *J. Comp. Phys.* **148** (2), 341–365.

Corcos, G. & Lin, S. 1984 The mixing layer: Deterministic models of a turbulent flow. II- The origin of the three-dimensional motion. *J. Fluid Mech.* **139**, 67–95.

Dovgal, A., Kozlov, V. & Michalke, A. 1994 Laminar boundary layer separation: instability and associated phenomena. *Prog. Aerospace Sci* **30**, 61–94.

Drazin, P. G. & Reed, W. H. 1981 *Hydrodynamic stability*. Cambridge University Press, Cambridge, UK.

Drela, M. & Giles, M. 1987 Viscous-Inviscid Analysis of Transonic and Low Reynolds Number Airfoils. *AIAA Journal* **25** (10), 1347–1355.

Eppler, R. & Somers, D. 1980 A computer program for the design and analysis of low-speed airfoils. *NASA TM-80210* .

Ffowcs Williams, J. & Hall, L. 1970 Aerodynamic sound generation by turbulent flow in the vicinity of a scattering half plane. *J. Fluid Mech.* **40** (4), 657–670.

Gaster, M. 1963 On stability of parallel flows and the behaviour of separation bubbles. *PhD thesis, University of London* .

Gaster, M. 1966 The structure and behaviour of laminar separation bubbles. AGARD Conf. *Aeronautical Research Council, RM No. 3595* .

Gaster, M. 1968 Growth of disturbances in both space and time. *Physics of Fluids* **11**, 723–727.

Gaster, M. 1978 Series representation of the eigenvalues of the Orr-Sommerfeld equation. *J. Comp. Phys.* **29**, 147–162.

Gault, D. 1957 A correlation of low-speed airfoil-section stalling characteristics with Reynolds number and airfoil geometry. *NACA Technical Note 3963, Washington, March 1957* .

Gerritsen, M. & Olsson, P. 1996 Designing an Efficient Solution Strategy for Fluid Flows 1. A Stable High Order Finite Difference Scheme and Sharp Shock Resolution for the Euler Equations. *J. Comp. Phys.* **129** (2), 245–262.

Gerritsen, M. & Olsson, P. 1998 Designing an Efficient Solution Strategy for Fluid Flows II. Stable High-Order Central Finite Difference Schemes on Composite Adaptive Grids with Sharp Shock Resolution. *J. Comp. Phys.* **147** (2), 293–317.

Hammond, D. & Redekopp, L. 1998 Local and global instability properties of separation bubbles. *European Journal of Mechanics-B/Fluids* **17** (2), 145–164.

Hannemann, K. & Oertel, H. 1989 Numerical simulation of the absolutely and convectively unstable wake. *J. Fluid Mech.* **199**, 55–88.

Hatakeyama, N. & Inoue, O. 2006 Direct Numerical Simulation of Noise from an Airfoil in a Uniform Flow. *12th AIAA/CEAS Aeroacoustics Conference, Cambridge, Massachusetts* .

Hoarau, Y., Braza, M., Ventikos, Y., Faghani, D. & Tzabiras, G. 2003*a* Organized modes and the three-dimensional transition to turbulence in the incompressible flow around a NACA0012 wing. *J. Fluid Mech.* **496**, 63–72.

Hoarau, Y., Faghani, D., Braza, M., Perrin, R., Anne-Archard, D. & Ruiz, D. 2003*b* Direct Numerical Simulation of the Three-Dimensional Transition to Turbulence in the Incompressible Flow around a Wing. *Flow, Turbulence and Combustion* **71** (1), 119–132.

Horton, H. 1968 Laminar separation in two and three-dimensional incompressible flow. *PhD thesis, University of London* .

Horton, H. 1969 A semi-empirical theory for the growth and bursting of laminar separation bubbles. Aeronautical research council current paper 1073.

Hu, Z., Morfey, C. & Sandham, N. 2003 Sound radiation in turbulent channel flows. *J. Fluid Mech.* **475**, 269–302.

Huang, P., Coleman, G. & Bradshaw, P. 1995 Compressible turbulent channel flows: DNS results and modelling. *J. Fluid Mech.* **305**, 185–218.

Huerre, P. & Monkewitz, P. A. 1985 Absolute and convective instabilities in free shear layers. *J. Fluid Mech.* **159**, 151–168.

Huerre, P. & Monkewitz, P. A. 1990 Local and global instabilities in spatially developing flows. *Ann. Rev. Fluid Mech.* **22**, 473–537.

Ingen, V. 1985 Research on laminar separation bubbles at Delft University of Technology in relation to low Reynolds number airfoil aerodynamics. *Conference on Low Reynolds Number Airfoil Aerodynamics, Notre Dame, IN, Proceedings* pp. 89–124.

Jones, B. 1938 Stalling. *J. Royal Aero. Soc* **38**, 747–770.

Jones, L., Sandberg, R. & Sandham, N. 2006 Direct numerical simulation of an airfoil with unsteady wake. *Proceedings of ECCOMAS CFD 2006, European Conference on Computational Fluid Dynamics., European Community on Computational Methods in Applied Sciences* .

Jones, L., Sandberg, R. & Sandham, N. 2007*a* Direct numerical simulation of the flow around a NACA-0012 airfoil. *5th International Symposium on Turbulence and Shear Flow Phenomena* .

Jones, L., Sandberg, R. & Sandham, N. 2007*b* Direct numerical simulations of forced and unforced separation bubbles on an airfoil at incidence. *J. Fluid Mech.* **(in submission)**.

Kerswell, R. 2002 Elliptical Instability. *Annual Review of Fluid Mechanics* **34**, 83–113.

Kim, H., Lee, S. & Fujisawa, N. 2005 Computation of unsteady flow and aerodynamic noise of NACA 0018 airfoil using large-eddy simulation. *International Journal of Heat and Fluid Flow* .

Kim, J., Moin, P. & Moser, R. 1987 Turbulence statistics in fully developed channel flow at low reynolds number. *J. Fluid Mech.* **177**, 133–166.

Kitsios, V., Kotapati, R., Mittal, R., Ooi, A., Soria, J. & You, D. 2006 Numerical simulation of lift enhancement on a NACA-0015 airfoil using ZNMF jets. *Center for Turbulence Research, Proceedings of the Summer Program* p. 457.

Koch, W. 1985 Local instability characteristics and frequency determination of self-excited wake flows. *Journal of Sound and Vibration* **99**, 53–83.

Krishnan, L. 2005 Dynamics of turbulent spots in a compressible flow. *PhD. Thesis, University of Southampton, U.K* .

Lang, M., Rist, U. & Wagner, S. 2004 Investigations on controlled transition development in a laminar separation bubble by means of LDA and PIV. *Experiments in Fluids* **36** (1), 43–52.

Lawal, A. A. 2002 Direct numerical simulation of transonic shock/boundary layer interactions. *PhD. Thesis, University of Southampton, U.K* .

Lee, B. 1990 Transonic buffet on a supercritical airfoil. *Aeronautical Journal* pp. 143–152.

Lele, S. K. 1992 Compact finite difference schemes with spectral-like resolution. *J. Comp. Phys.* **103**, 16–42.

Leweke, T. & Williamson, C. 1998*a* Cooperative elliptic instability of a vortex pair. *J. Fluid Mech.* **360**, 85–119.

Leweke, T. & Williamson, C. 1998*b* Three-dimensional instabilities in wake transition. *European Journal of Mechanics-B/Fluids* **17** (4), 571–586.

Lian, Y. & Shyy, W. 2006 Laminar-Turbulent Transition of a Low Reynolds Number Rigid or Flexible Airfoil. *36th AIAA Fluid Dynamics Conference and Exhibit* .

Lighthill, M. 1952 On sound generated aerodynamically I. General theory. *Proceedings of the Royal Society of London, Series A: Mathematical and Physical Science* **211A** (1107), 564–587.

Marquillie, M. & Ehrenstein, U. 2003 On the onset of nonlinear oscillations in a separating boundary-layer flow. *J. Fluid Mech.* **490**, 169–188.

Marxen, O. & Henninsdon, D. 2007 Numerical simulation of the bursting of a laminar separation bubble. *AIAA Paper* **2007-538**, 45th Aerospace Sciences Meeting, Reno.

Marxen, O., Lang, M., Rist, U. & Wagner, S. 2003 A combined experimental/numerical study of unsteady phenomena in a laminar separation bubble. *Flow, Turbulence and Combustion* **71** (1), 133–146.

Marxen, O., Rist, U. & Wagner, S. 2004 Effect of spanwise-modulated disturbances on transition in a separated boundary layer. *AIAA J.* **42** (5), 937–944.

Mary, I. & Sagaut, P. 2002 Large eddy simulation of flow around an airfoil near stall. *AIAA Journal* **40** (6), 1139–1145.

Maucher, U., Rist, U. & Wagner, S. 1997 Secondary instabilities in a laminar separation bubble. *Notes on Numerical Fluid Mechanics, edited by H. Korner and R. Hilbig, Vieweg Verlag, Wiesbaden, Germany* **60**, 229–236.

Maucher, U., Rist, U. & Wagner, S. 1998 Transitional structures in a laminar separation bubble. *New Results in Numerical and Experimental Fluid Mechanics II, Proceeds of the 11th STAB/DGLR Symposium, Berlin, edited by W. Nitsche, H.J Heinemann and R. Hilbig* **72**, 307–314.

Maucher, U., Rist, U. & Wagner, S. 2000 Refined interaction method for direct numerical simulation of transition in separation bubbles. *AIAA Journal* **38** (8).

McAlpine, A., Nash, E. & Lowson, M. 1999 On the generation of discrete frequency tones by the flow around an airfoil. *Journal of Sound and Vibration* **222** (5), 753–779.

McCullough, G. & Gault, D. 1951 Examples of Three Representative Types of Airfoil-Section Stall at Low Speed. *NACA TN* **2502**, 1951.

Morin, S. 2002 A combined numerical and experimental study of aerofoil separation bubbles. *PhD. Thesis, University of Southampton, U.K* .

Mueller, T. 1999 Aerodynamic Measurements at Low Reynolds Numbers for Fixed Wing Micro-Air Vehicles. *Development and Operation of UAVs for Military and Civil Applications, course held at the Von Karman Institute for Fluid Dynamics, Belgium, Sept* pp. 13–17.

Owen, P. & Klanfer, L. 1953 On the laminar boundary layer separation from the leading edge of a thin aerofoil. *RAE Rep. Aero* **2508**.

Pauley, L. 1994 Response of two-dimensional separation to three-dimensional disturbances. *ASME, Transactions, Journal of Fluids Engineering* **116** (3), 433–438.

Pauley, L. L., Moin, P. & Reynolds, W. C. 1990 The structure of two-dimensional separation. *J. Fluid Mech.* **220**, 397–411.

Radespiel, J. & Scholz, U. 2007 Numerical and Experimental Flow Analysis of Moving Airfoils with Laminar Separation Bubbles. *AIAA J.* **45** (6), 1346–1356.

Rinoie, K. & Takemura, N. 2004 Oscillating behaviour of laminar separation bubble formed on an aerofoil near stall. *Aeronautical Journal* **108** (1081), 153–163.

Rist, U. 1994 Nonlinear effects of 2D and 3D disturbances on laminar separation bubbles. *Proceedings of IUTAM Symposium on Nonlinear Instability of Nonparallel Flows. Springer-Verlag, New York* pp. 324–333.

Rist, U. & Maucher, U. 2002 Investigations of time-growing instabilities in laminar separation bubbles. *European Journal of Mechanics B: Fluids* **21** (5), 495–509.

Roberts, W. 1980 Calculation of Laminar Separation Bubbles and Their Effect on Airfoil Performance. *AIAA J.* **18** (1), 25–31.

Roger, M. & Moreau, S. 2005 Back-scattering correction and further extensions of amiet's trailing-edge noise model. part 1: theory. *J. Sound and Vibration* **286**, 477–506.

Rogers, M. & Moser, R. 1994 Direct simulation of a selfdmilar turbulent mixing layer. *Phys. Fluids* **6** (2), 903.

Rossiter, J. 1964 Wind-TunnelExperimentsontheFlowoverRectangular Cavities at Subsonicand Transonic Speeds. *Aeronautical Research Council Reports and Memo* **3838**.

Sandberg, R., Jones, L., Sandham, N. & Joseph, P. 2007 Direct numerical simulations of noise generated by airfoil trailing edges. *AIAA Paper 2007–3469* 13th AIAA/CEAS Aeroacoustics Conference, Rome/ May 2007.

Sandberg, R. D. & Sandham, N. D. 2006 Nonreflecting zonal characteristic boundary condition for direct numerical simulation of aerodynamic sound. *AIAA J.* **44** (2), 402–405.

Sandberg, R. D., Sandham, N. D. & Joseph, P. F. 2006 DNS of trailing-edge noise generated by boundary-layer instabilities. *AIAA Paper 2006–2514* 12th AIAA/CEAS Aeroacoustics Conference (27th AIAA Aeroacoustics Conference), Cambridge, Massachusetts.

Sandham, N., Li, Q. & Yee, H. 2002 Entropy splitting for high-order numerical simulation of compressible turbulence. *J. Comp. Phys.* **178**, 307–322.

Sandhu, H. & Sandham, N. 1994 Boundary conditions for spatially growing compressible shear layers. *Report QMW-EP-1100, Faculty of Engineering, Queen Mary and Westfield College, University of London* .

Saric, W., Reed, H. & Kerschen, E. 2002 Boundary-layer receptivity to freestream disturbances. *Annual Review of Fluid Mechanics* **34** (1), 291–319.

Schmid, P., Henningson, D. & Jankowski, D. 2002 Stability and Transition in Shear Flows. Applied Mathematical Sciences, Vol. 142. *Applied Mechanics Reviews* **55**, B57.

Schmidt, S. & Thiele, F. 2003 Detached Eddy Simulation of Flow around A-Airfoil. *Flow, Turbulence and Combustion* **71** (1), 261–278.

Selig, M., Gopalarathnam, A., Giguere, P. & Lyon, C. 2001 Systematic airfoil design studies at low Reynolds numbers. *Fixed and flapping wing aerodynamics for micro air vehicle applications* pp. 143–167.

Shan, H., Jiang, L. & Liu, C. 2005 Direct numerical simulation of flow separation around a NACA 0012 airfoil. *Computers and Fluids* **34** (9), 1096–1114.

Shum, Y. & Marsdent, J. 1994 Separation Bubble Model for Low Reynolds Number Airfoil Applications. *Journal of Aircraft* **31** (4).

Spalart, P. & Strelets, M. 2000 Mechanisms of transition and heat transfer in a separation bubble. *J. Fluid Mech.* **403**, 329–349.

Spalart, P. R. 1988 Direct simulation of a turbulent boundary layer up to $re_\theta =$ 1410. *J. Fluid Mech.* **187**, 61–98.

Tam, C. K. W. & Ju, H. 2006 Numerical simulation of the generation of airfoil tones at a moderate Reynolds number. *AIAA Paper 2006–2502* 12th AIAA/CEAS Aeroacoustics Conference (27th AIAA Aeroacoustics Conference), Cambridge, Massachusetts.

Terzi, D. A. v. 2004 Numerical investigation of transitional and turbulent backward-facing step flows. *PhD. Thesis, The University of Arizona* .

Theofilis, V. 2000 On the origins of unsteadiness and three-dimensionality in a laminar separation bubble. *Philosophical Transactions: Mathematical, Physical and Engineering Sciences* **358** (1777), 3229–3246.

Theofilis, V. 2003 Advances in global linear instability analysis of nonparallel and three-dimensional flows. *Progress in Aerospace Sciences* **39**, 249–315.

Thompson, K. W. 1987 Time dependent boundary conditions for hyperbolic systems. *J. Comp. Phys.* **68**, 1–24.

Thompson, M., Leweke, T. & Williamson, C. 2001 The physical mechanism of transition in bluff body wakes. *Journal of Fluids and Structures* **15** (3), 607–616.

Torres, G. & Mueller, T. 2001 Aerodynamic characteristics of low aspect ratio wings at low Reynolds numbers. *Fixed and flapping wing aerodynamics for micro air vehicle applications* pp. 115–141.

Waleffe, F. 1990 On the three-dimensional instability of strained vortices. *Physics of Fluids A: Fluid Dynamics* **2**, 76.

Wanderley, J. & Corke, T. 2001 Boundary layer receptivity to free-stream sound on elliptic leading edges of flat plates. *J. Fluid Mech.* **429**, 1–21.

Weibust, E., Bertelrud, A. & Ridder, S. 1987 Experimental investigation of laminar separation bubbles and comparison with theory. *Journal of Aircraft* **24** (5), 291–297.

White, F. M. 1991 *Viscous Fluid Flow*. McGraw Hill.

Williamson, C. 1992 The natural and forced formation of spot-like'vortex dislocations' in the transition of a wake. *J. Fluid Mech.* **243**, 393–441.

Williamson, C. 1996 Three-dimensional wake transition. *J. Fluid Mech.* **328**, 345–407.

Windte, J., Scholz, U. & Radespiel, R. 2006 Validation of the RANS-simulation of laminar separation bubbles on airfoils. *Aerospace Science and Technology* **10** (6), 484–494.

Wissink, J., Michelassi, V. & Rodi, W. 2004 Heat transfer in a laminar separation bubble affected by oscillating external flow. *Int. J. of Heat and Fluid Flow* **25**, 729–740.

Wissink, J. & Rodi, W. 2002 DNS of transition in a laminar separation bubble. *Advances in Turbulence IX, proceedings of the Ninth European Turbulence Conference, CIMNE* .

Wissink, J. & Rodi, W. 2003 DNS of a Laminar Separation Bubble in the Presence of Oscillating External Flow. *Flow, Turbulence and Combustion* **71** (1), 311–331.

Yang, Z. & Voke, P. 2001 Large-eddy simulation of boundary-layer separation and transition at a change of surface curvature. *J. Fluid Mech.* **439**, 305–333.

You, D. & Moin, P. 2006 Large-eddy simulation of flow separation over an airfoil with synthetic jet control. *Center for Turbulence Research Annual Research Briefs* pp. 337–346.

Young, A. & Horton, H. 1966 Some results of investigation of separation bubbles. *AGARD CP* **4**, 779–811.

Yuan, W., Khalid, M., Windte, J., Scholz, U. & Radespiel, R. 2007 Computational and experimental investigations of low-Reynolds-number flows past an aerofoil. *Aeronautical Journal* **111** (1115), 17–29.

Yuan, W., Xu, H. & Khalid, M. 2004 Numerical assessment of conventional turbulence models for computing separated low Reynolds number airfoil flows. *RTO-AVT-111 Specialist Meeting, Prague* .

Yuan, W., Xu, H., Khalid, M. & Radespiel, R. 2006 A parametric study of LES on laminar-turbulent transitional flows past an airfoil. *International Journal of Computational Fluid Dynamics* **20** (1), 45–54.